

AD-A230 704

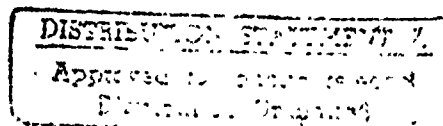
2



DTIC
ELECTE
S D
JAN 16 1991

HIERARCHICALLY-CLUSTERED STRUCTURES:
FORMATION DURING COLLOIDAL PROCESSING
AND EVOLUTION DURING SINTERING

U.S. Army Research Office
Final Report
Contract No. DAAG29-85-K0136



I. A. Aksay and R. Kikuchi, Co-Principal Investigators

December 4, 1990

REPORT DOCUMENTATION PAGE

1a. REPORT SECURITY CLASSIFICATION <u>Unclassified</u>			1b. RESTRICTIVE MARKINGS		
2a. SECURITY CLASSIFICATION AUTHORITY			3. DISTRIBUTION/AVAILABILITY OF REPORT Approved for public release; distribution unlimited.		
2b. DECLASSIFICATION/DOWNGRADING SCHEDULE					
4. PERFORMING ORGANIZATION REPORT NUMBER(S)			5. MONITORING ORGANIZATION REPORT NUMBER(S) <u>ARO 22819.1-MS</u>		
6a. NAME OF PERFORMING ORGANIZATION Advanced Ceramic Materials Laboratory		6b. OFFICE SYMBOL (If applicable)	7a. NAME OF MONITORING ORGANIZATION U. S. Army Research Office		
6c. ADDRESS (City, State, and ZIP Code) University of Washington, FB-10 Seattle, WA 98195			7b. ADDRESS (City, State, and ZIP Code) P. O. Box 12211 Research Triangle Park, NC 27709-2211		
8a. NAME OF FUNDING/SPONSORING ORGANIZATION U. S. Army Research Office		8b. OFFICE SYMBOL (If applicable)	9. PROCUREMENT INSTRUMENT IDENTIFICATION NUMBER <u>DAAG-29-85-K-0136</u>		
8c. ADDRESS (City, State, and ZIP Code) P. O. Box 12211 Research Triangle Park, NC 27709-2211			10. SOURCE OF FUNDING NUMBERS		
			PROGRAM ELEMENT NO.	PROJECT NO.	TASK NO.
			WORK UNIT ACCESSION NO.		
11. TITLE (Include Security Classification) Hierarchically-Clustered Structures: Formation during Colloidal Processing and Evolution during Sintering					
12. PERSONAL AUTHOR(S) I. A. Aksay and R. Kikuchi					
13a. TYPE OF REPORT Final		13b. TIME COVERED FROM 850601 TO 880531		14. DATE OF REPORT (Year, Month, Day) December 4, 1990	
15. PAGE COUNT					
16. SUPPLEMENTARY NOTATION The view, opinions and/or findings contained in this report are those of the author(s) and should not be construed as an official Department of the Army position, policy, or decision, unless so designated by other documentation.					
17. COSATI CODES			18. SUBJECT TERMS (Continue on reverse if necessary and identify by block number)		
FIELD	GROUP	SUB-GROUP			
			Hierarchical structures, colloidal processing, structure evolution		
19. ABSTRACT (Continue on reverse if necessary and identify by block number) The research presented in this report examined the formation and microstructural evolution of colloiddally consolidated systems during sintering. The microstructural evolution of a hierarchically-clustered system was treated as a whole. The main goals were (i) to develop a methodology for predicting the evolution of hierarchically- clustered structures during densification and (ii) to develop experimental techniques for modifying the hierarchical structures through colloidal consolidation techniques. Experimental and theoretical modeling studies showed that all powder compacts eventu- ally approach a steady-state grain-size distribution regardless of the original state of the colloiddally consolidated compact. During densification, all microstructures followed unique paths dependent upon the initial state of the colloidal dispersion (dispersed or flocculated suspensions), but the final microstructure always approached an equilibrium distribution independent of the initial state. Theoretical models also (continued on back)					
20. DISTRIBUTION/AVAILABILITY OF ABSTRACT <input type="checkbox"/> UNCLASSIFIED/UNLIMITED <input type="checkbox"/> SAME AS RPT. <input type="checkbox"/> DTIC USERS			21. ABSTRACT SECURITY CLASSIFICATION Unclassified		
22a. NAME OF RESPONSIBLE INDIVIDUAL Ilhan A. Aksay			22b. TELEPHONE (Include Area Code) (206) 543-2625		22c. OFFICE SYMBOL

19. predicted that an initially narrow grain-size distribution in a dense compact will broaden to an equilibrium distribution over time.

Pressure filtration experiments were performed to study the effect of varying the void fraction upon the microstructural evolution path. The results of modifying the pore network upon the evolution path are discussed in this report.

**HIERARCHICALLY-CLUSTERED STRUCTURES:
FORMATION DURING COLLOIDAL PROCESSING
AND EVOLUTION DURING SINTERING**

*U. S. Army Research Office
Final Report*

for period June 1, 1985 to May 31, 1988

Contract Number DAAG29-85-K0136

**I. A. Aksay and R. Kikuchi
Co-Principal Investigators**

**Department of Materials Science and Engineering; and
Advanced Materials Technology Center
Washington Technology Centers
University of Washington
Seattle, Washington 98195**

December 4, 1990

Accession For	
NTIS CRA&I	<input checked="checked" type="checkbox"/>
DTIC TAB	<input type="checkbox"/>
Unannounced	<input type="checkbox"/>
Justification	
By	
Distribution/	
Availability Codes	
Dist	Availability for Special
A-1	



Contents

1.0 Executive Summary	1
2.0 Introduction	3
3.0 Summary of Research	5
3.1 Preparation and Microstructure Evolution of Hierarchically-Clustered Powders	5
3.1.1 Particle Synthesis and Characterization	5
3.1.2 Particle Packing and Sintering	8
3.2 Evolution of Cellular Structures	14
3.2.1 Microstructural Evolution Modeling	16
3.2.2 Densification Modeling	16
3.3 Modification of Hierarchical Structures	17
3.3.1 Consolidation Through Pressure Casting	17
3.3.2 Rheological Behavior	30
4.0 Discussion	35
4.1 Summary	35
4.2 Conclusions	36
5.0 References	37
6.0 Technical Communications	38
Publications	38
Future Publications	38
Presentations	38

1.0 Executive Summary

This is the final report for the U. S. Army Research Office Contract, number DAAG29-85-K0136, entitled *Hierarchically-Clustered Structures: Formation During Colloidal Solidification and Evolution During Sintering*, which summarizes the work performed during the contract period May 31, 1985 through June 1, 1988 at the Department of Materials Science and Engineering, University of Washington, Seattle, Washington.

Previous studies on the modeling of sintering processes have emphasized two-particle densification and mass transport mechanisms at the micrometer scale. The research presented in this report examined the formation and microstructural evolution of colloiddally consolidated systems during sintering. The microstructural evolution of a hierarchically-clustered system was treated as a whole, and a three-aggregate phase diagram of colloidal systems was introduced which illustrated that colloiddally consolidated powder compacts always display a hierarchical structure of clusters and voids. Our main goals in this program have been (i) to develop a methodology for predicting the evolution of hierarchically-clustered structures during densification and (ii) to develop experimental techniques for modifying the hierarchical structures through colloidal consolidation techniques. In this report we summarize our results in both areas.

Our experimental and theoretical modeling studies showed that all powder compacts eventually approach a steady-state grain size distribution regardless of the original state of the colloiddally consolidated compact. Experiments were performed with nearly monosize colloidal TiO_2 powders. Pore size distribution and the total pore volume of the colloiddally consolidated compacts were varied by controlling the particle interactions in the suspension stage. During densification, all microstructures were found to follow unique paths dependent upon the initial state of the colloidal dispersion, i.e., whether the suspension was dispersed or flocculated prior to consolidation. But the final microstructure always approached an equilibrium distribution independent of the initial state. This observation was important, especially in the subsequent selection of powders for colloidal processing. Currently, it is thought that if monosized particles are packed in an ordered structure, microstructures with a narrow grain size distribution will result after densification. Our experimental findings illustrate that this is not possible due to an eventual broadening of the grain size distribution to a steady state.

To better understand and explain the experimentally observed results, theoretical modeling was performed. The models predicted that in a dense compact, the initially narrow grain coordination distribution will always broaden to an equilibrium distribution over time. The

models also predicted that during densification the microstructural evolution will follow different paths depending on the initial pore size distribution in the compact. These predictions parallel the experimentally-derived results exactly.

If pore size distribution is the controlling factor in microstructural evolution, then modifications to the pore size distribution should allow the evolution of a narrow grain size distribution in the final microstructure. Pressure filtration experiments were performed to study the relationship between pressure and void fraction in colloidal compacts. Changes in the void fraction were monitored using rheological measurements. Significant reductions in the casting rate were observed using pressure filtration. The void fraction was reduced when flocculated suspensions were consolidated, but little effect was observed on dispersed specimens.

Since our microstructural evolution studies indicated that pore volume and pore size distribution play a key role in determining the evolution path during densification, we next examined the modification of the pore network during pressure filtration. These results will be discussed in the following sections of this report.

2.0 Introduction

Hierarchically-clustered structures, developed through colloidal processing, contain first-, second-, and third-generation voids.¹ First-generation voids are the voids within the first-generation clusters of primary particles. Second-generation voids are the voids between the first-generation clusters of particles. Third-generation voids are the voids between the second-generation clusters of particles. In order to determine an optimum processing route that is also economical, it is necessary to understand the formation of hierarchically-clustered structures during the consolidation of colloidal suspensions and the development of these structures as the colloidal compacts are sintered into dense articles.

According to existing theories, a narrow grain size distribution will result from the sintering of compacts composed of particles of a narrow size distribution.² However, the first phase of the experimental portion of this work has shown that a narrow pore size distribution is necessary to produce a narrowly distributed grain size; a narrow particle size distribution is necessary but not sufficient. It is relatively simple, although usually time consuming, to produce a narrow particle size distribution, even with spherical particles. However, packing imperfections similar to the dislocations and vacancies found in crystalline solids lead to a broadened pore size distribution. In addition, due to the formation of hierarchically-clustered structures, it is impossible to form a narrow pore size distribution of any size. The hierarchically-clustered structures that form during consolidation always result in first-, second-, and sometimes third-generation voids, producing bimodal and trimodal pore size distributions causing further deviation from ideal predictions.

The second phase of this work involved the establishment of theoretical models, developed from a statistical mechanics basis, to describe microstructural evolution at the micrometer scale. The first model dealt with the microstructural evolution of a fully dense structure, i.e., grain growth modeling. This model predicted that the initially narrow grain size distribution of a dense compact will broaden during subsequent heat treatments. The second model examined the effects on microstructural evolution in the presence of another phase, in this case, porosity. The densification model predicted that the microstructural evolution will follow different paths which are dependent upon the initial state of the compact, but that the end or stationary state will be the same. However, the end state may be metastable and not necessarily in thermodynamic equilibrium.

Developing processing routes which modify hierarchically-clustered structures and the accompanying pore size distribution will allow a narrow pore size distribution to be achieved during consolidation of colloidal suspensions. Pressure filtration was shown to decrease the void concentration in compacts formed from flocculated suspensions but had little effect on compacts formed from dispersed suspensions. It was also shown that increasing the particle concentration effectively eliminated third-generation voids. Data on the rheological behavior of the colloidal suspension was gathered using dynamic oscillatory techniques and analyzed using the theory of viscoelasticity. These studies will be explained in detail in the following sections.

3.0 *Summary of Research*

3.1 Preparation and Microstructure Evolution of Hierarchically-Clustered Powders

Existing theories suggest that compacts consisting of monosized spherical particles will produce uniformly-sized microstructures with a grain coordination of six; a hexagonal array.³ To test this hypothesis, spherical TiO_2 particles with a narrow particle size distribution were prepared and sintered. This presentation is a summary of C. B. Martin's Master of Science thesis entitled "Preparation and Microstructural Evolution of Hierarchically-Clustered Powders." (Appendix I).

3.1.1 *Particle Synthesis and Characterization*

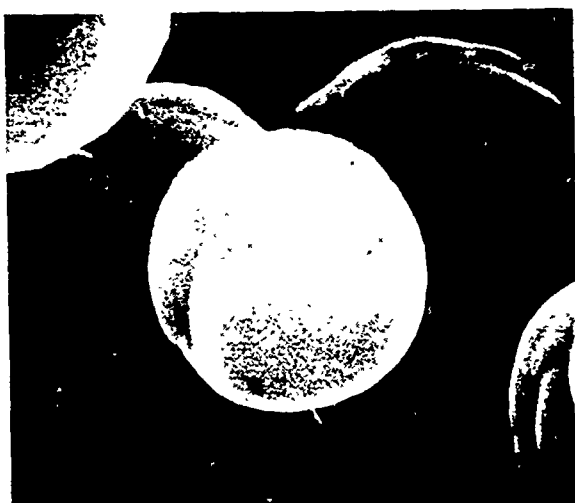
Previous studies have shown that monosized spherical particles of latex and silica will pack in regular arrays constituting colloidal crystals. However, sintering of these compacts does not provide information regarding microstructural evolution since these particles are amorphous. For this reason, crystalline TiO_2 particles were chosen as candidate materials for this study. Crystalline particles will sinter via solid-state sintering mechanisms rather than through viscous flow, and they produce grains and grain boundaries of particular crystallographic orientations whereas amorphous particles sinter into single domain materials without grains or grain boundaries.

TiO_2 particles were produced from titanium salts through the use of ethoxy and chloride ligands. Synthesis was carried out in a dry nitrogen glove box.^a The particles were washed to remove any soluble species and then classified using centrifugation. A surfactant, hydroxypropylcellulose, molecular weight 60,000, was added prior to filtering. The surfactant was shown to reduce agglomeration of the particles. The mean particle size of the powders before classification was 0.5 μm with the surfactant and 0.7 μm without.

The particles formed with the chloride ligands possessed a wide size distribution and were not perfectly spherical (Figure 1). Heterogeneous nucleation on the container surface resulted in a flat surface on each surface particle. This anomaly, coupled with very low yields

^a Model HIE-63-P, Vacuum Atmospheres Company, Hawthorne, California; purchased with contract monies.

(a)

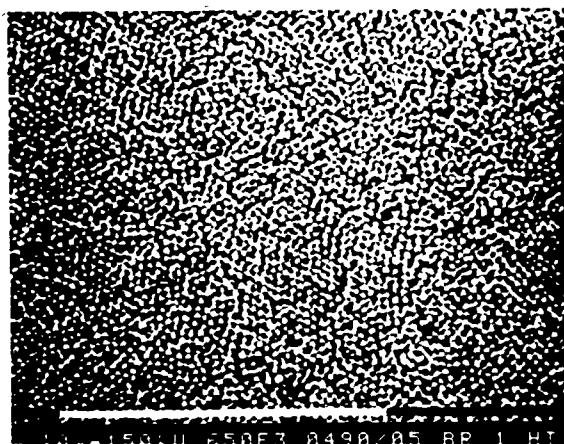


(b)

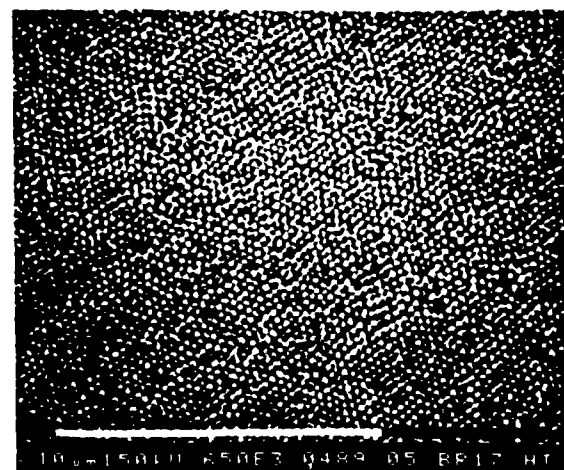


Figure 1. SEM photomicrographs of TiO_2 powder synthesized using TiCl_4 route showing (a) non-spherical particles (bar = 1.0 μm) and (b) broad particle size distribution (bar = 5.0 μm).

(a)



(b)



(c)

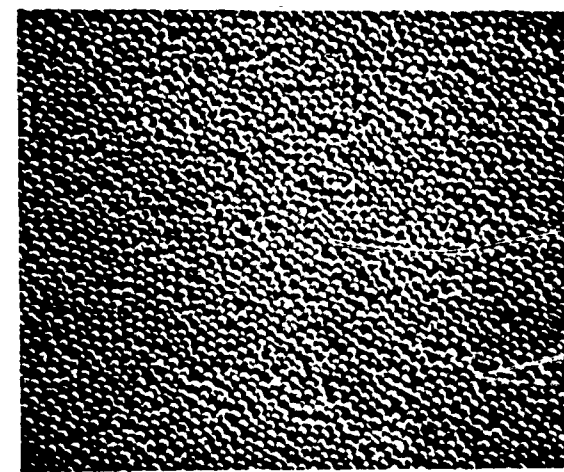


Figure 2. SEM photomicrographs showing the relative domain size achieved through the applied gravitational fields: (a) 1 g, (b) 170 g, and (c) 350 g. Bar = 10.0 μm .

(milligrams per liter of solution), ultimately eliminated the chloride route as a feasible method of producing TiO_2 powders for this study.

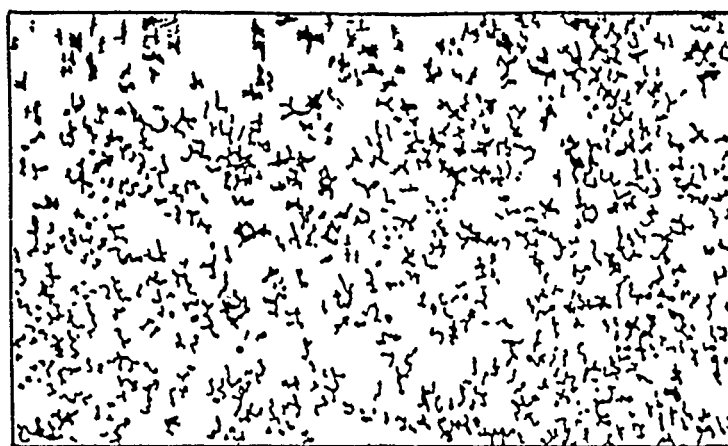
The powders produced with the organometallic (ethoxy) ligands were characterized using x-ray sedimentation and photon correlation spectroscopy (PCS). The chloride powders were characterized with optical and scanning electron microscopy (SEM). Differential thermal analysis (DTA) was used to determine when the particles crystallized and at what temperature the rutile to anatase phase transformation occurred. X-ray diffraction was used to identify the phases. α -alumina was added to the specimens to quantitatively determine the amount of rutile and anatase in the specimens. The powders were shown to crystallize to rutile at 470°C and transform from rutile to anatase at 700°C .

3.1.2 Particle Packing and Sintering

Dispersed suspensions were prepared using doubly distilled water adjusted to a pH of 8 with 0.1 M potassium hydroxide. Flocculation of the particles was induced by adjusting the pH to 5. Both flocculated and dispersed suspensions were compacted by sedimentation with forces of 1, 175, and 350 standard gravities (g's). Figure 2 contains SEM micrographs of the compact surfaces illustrating packing behavior similar to that observed by other researchers for the packing of silica spheres.⁴ The use of higher packing forces (175 and 350 g's) decreased the sedimentation times, resulting in the "quenching" of the colloidal suspension to produce an amorphous packing state. Increasing the packing rate decreased the long-range ordering and the domain size in the compact. This ordering was also shown to be a function of double-layer thickness as predicted by the colloidal phase diagram.⁵

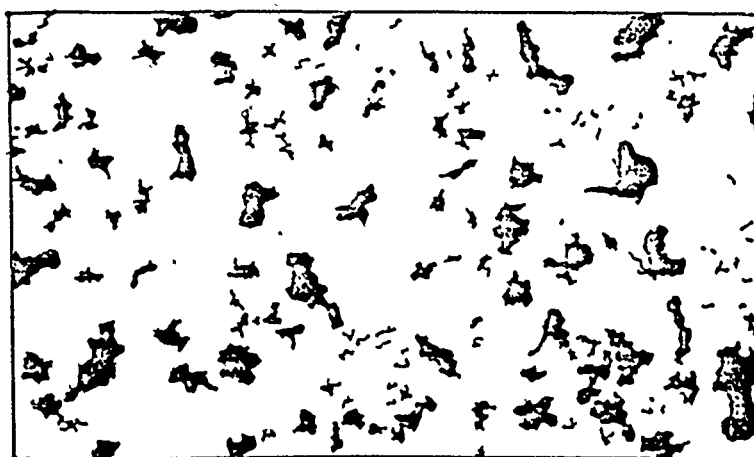
Image analysis of the SEM micrographs was accomplished by tracing the microstructures represented on the micrographs. Figure 3 shows the porosity of a dispersed and a flocculated compact represented as a "negative" image. Analysis of these compact surfaces showed that the dispersed specimen contained first- and second-generation voids, with the second-generation voids comprising approximately 10% of the total surface area analyzed. The flocculated specimen contained second- and third-generation voids, totaling approximately 20% of the total area. These surface pore distributions accurately represented the bulk pore distributions.

Initially, the compacts were isothermally sintered at 1150°C for 5 min. Observation of the compact surfaces showed surface grain growth, implying that the densification had entered the intermediate stage of the sintering regime. After 30 min at 1150°C , no remnant of the original packing structure was observed. In order to observe the initial stage of sintering behavior, the



a

1.0 μ m



b

1.0 μ m

Figure 3. Tracings of photomicrographs illustrating the pore distribution (in black) for a dispersed (a) and a flocculated (b) specimen. Bar = 1.0 μ m.

temperature was reduced to 1050°C. Holding times for the sintering experiments were 0, 5, 10, and 30 min. Shrinkage of the compact was determined through the use of microhardness indents on the compact surface prior to heat treatment. The indents also served as markers to study the microstructural evolution on the surface of the compact.

To observe the effect of time during isothermal heat treatments on the surface sintering behavior, specimens with indenter marks were placed directly in a tube furnace hot zone. The specimens were removed after a predetermined time and rapidly cooled to room temperature. These specimens were carbon-coated (using a sputtering technique) then observed with SEM. After observation, the carbon coating was removed by low-temperature heat treatments in air and the process repeated.

Particle coarsening occurred when the compacts were sintered at 1050°C in both the flocculated and dispersed compacts. The coarsening was initially caused by the local particle packing density and coordination; then, as the particle grew and approached the domain size, by domain coordination. As the sintering time was increased, the grain size distribution broadened and tended to a bimodal distribution.

Initial studies focused on the densification and grain growth behavior of the compact surface. Both the dispersed and the flocculated specimens exhibited normal grain growth when held at 1150°C for times less than 10 h. After 10 h, abnormal grain growth began, splitting the grain size distribution in dispersed specimens. In the flocculated compacts, grain growth stabilized after 2 h due to the pinning effects of the intergranular pores (Figure 4).

Although the original particle size distribution was narrow, during densification the grain size distribution always broadened. In addition, the grain size distribution did not reflect the morphology of the grains. Figure 5 illustrates the large variation in grain shape on the sintered surfaces, including the equiaxed nature of abnormally large grains found in the dispersed specimens. The exponential time dependence of grain growth during isothermal sintering was determined to be 0.48 for the dispersed specimen and 0.54 for the flocculated specimen.

Comparison of the surface microstructure with the bulk microstructure showed the mean bulk grain size to be slightly larger than the mean surface grain size for the dispersed specimen and significantly larger for the flocculated specimen (Figure 6). Densification occurred without

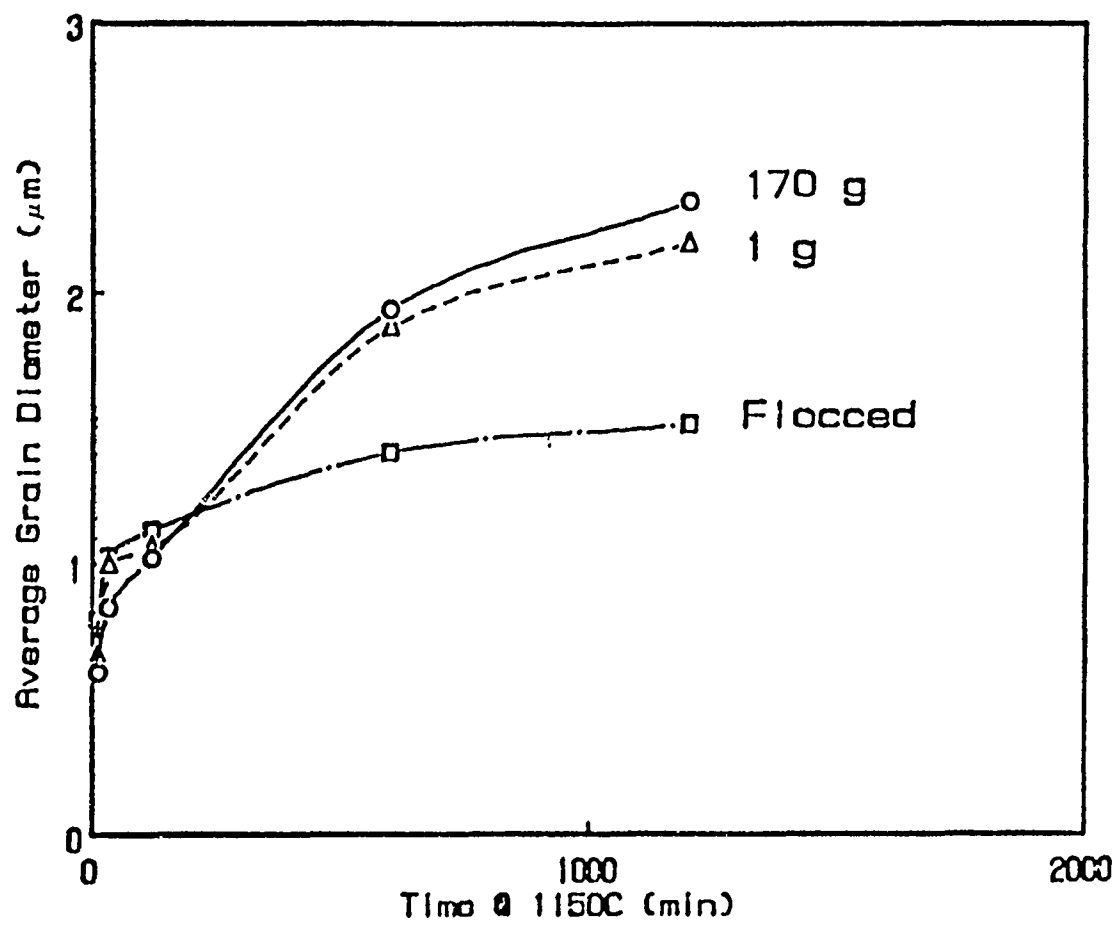


Figure 4. Mean grain size distribution versus sintering time for dispersed and flocculated specimens.

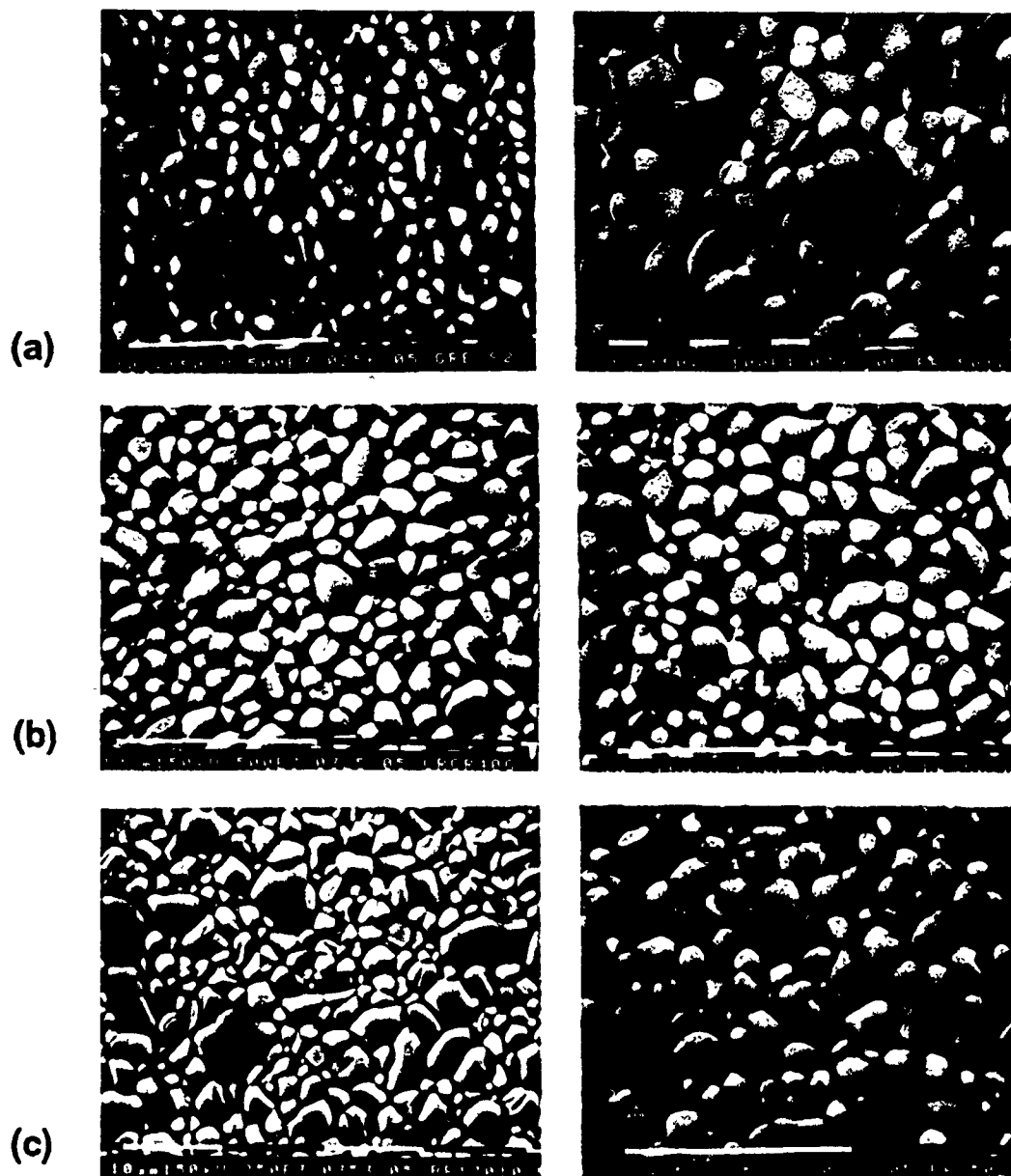


Figure 5. SEM photomicrographs illustrating surface grain shapes for specimens consolidated at 170 g. The compacts were sintered at 1150°C for (a) 10 minutes, (b) 2 hours, and (c) 10 hours.

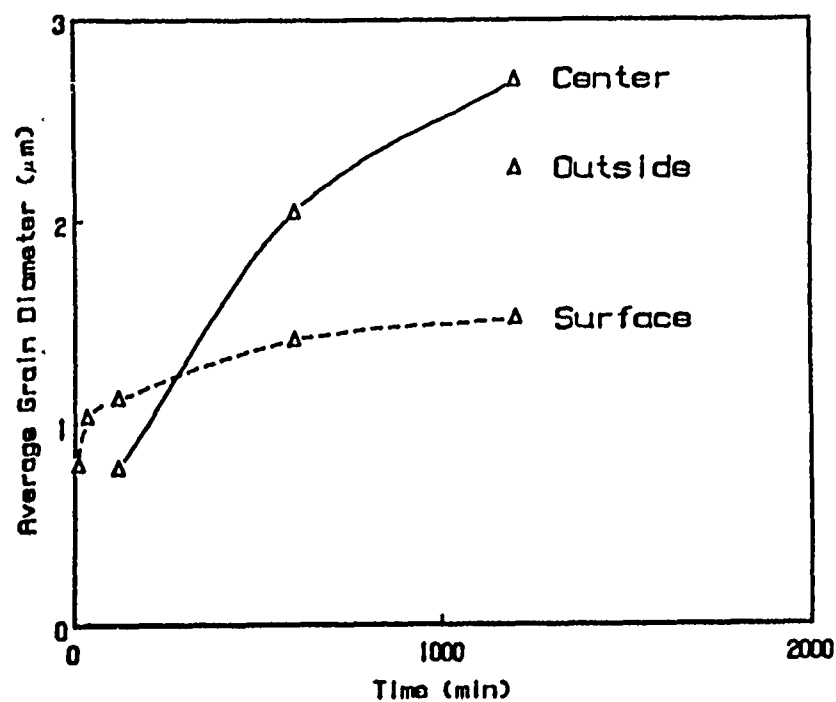
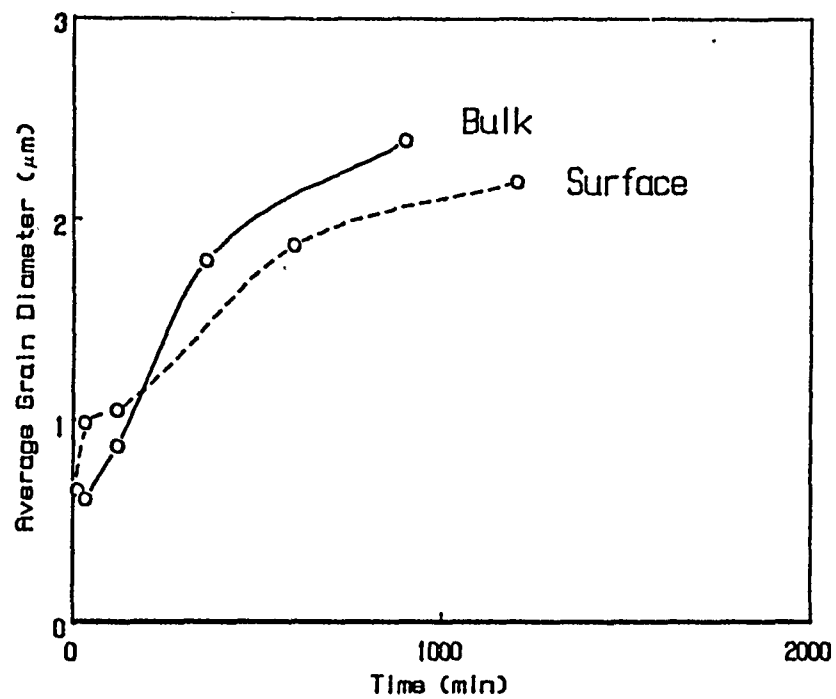


Figure 6. Mean grain size vs. sintering time for (a) dispersed and (b) flocculated specimens consolidated at 170 g and sintered at 1150°C.

grain growth at lower temperatures in the ordered compact. The flocculated compact exhibited grain growth and pore coalescence during similar heat treatment. This suggested that these microstructures could not be compared until the porosity was eliminated and that microstructural evolution followed different paths (Figure 7).

3.2 Evolution of Cellular Structures

Two questions have emerged which summarize microstructural evolution in real systems: (i) Is there an equilibrium structure which all green compacts approach during heat treatment regardless of the initial green state? and (ii) Do these microstructures evolve along separate paths? In order to answer these questions, two calculation methods, the Cluster Variation Method (CVM) and the Path Probability Method (PPM) were adopted. This section is a summary of S. K. Fukuda's Ph.D. dissertation entitled "The Evolution of Cellular Structures" (Appendix II).

The CVM is an approximation method that models the interactions between particles more accurately than the pair approximation method for determining the equilibrium state of the system. The PPM is an extension of the CVM that calculates the most likely path the system will follow to attain the equilibrium state. The CVM was first applied, with fairly good agreement, to calculate the equilibrium (steady state) cell coordination distribution (CCD) for a soap froth; the development of structures between particles was the critical issue of the work on froths.

To keep these calculations within reasonable limits, certain restrictions were adopted. Without these restrictions, the number of variables would have increased geometrically, exceeding the hardware capacity and time limits of our computer system. The restrictions do not negate the validity of the results in answering the proposed questions. The following restrictions applied:

- 1) two-dimensional structures were analyzed, and
- 2) the analysis used the zero limit of energy over temperature, which reduced the principle of minimizing free energy to one of maximizing the system topologic entropy.

The second restriction meant that the coordination of the grains would be analyzed rather than the grain size distribution. It was shown in later research that grain size distribution alone was not sufficient to describe the microstructure. To fully describe the microstructure,

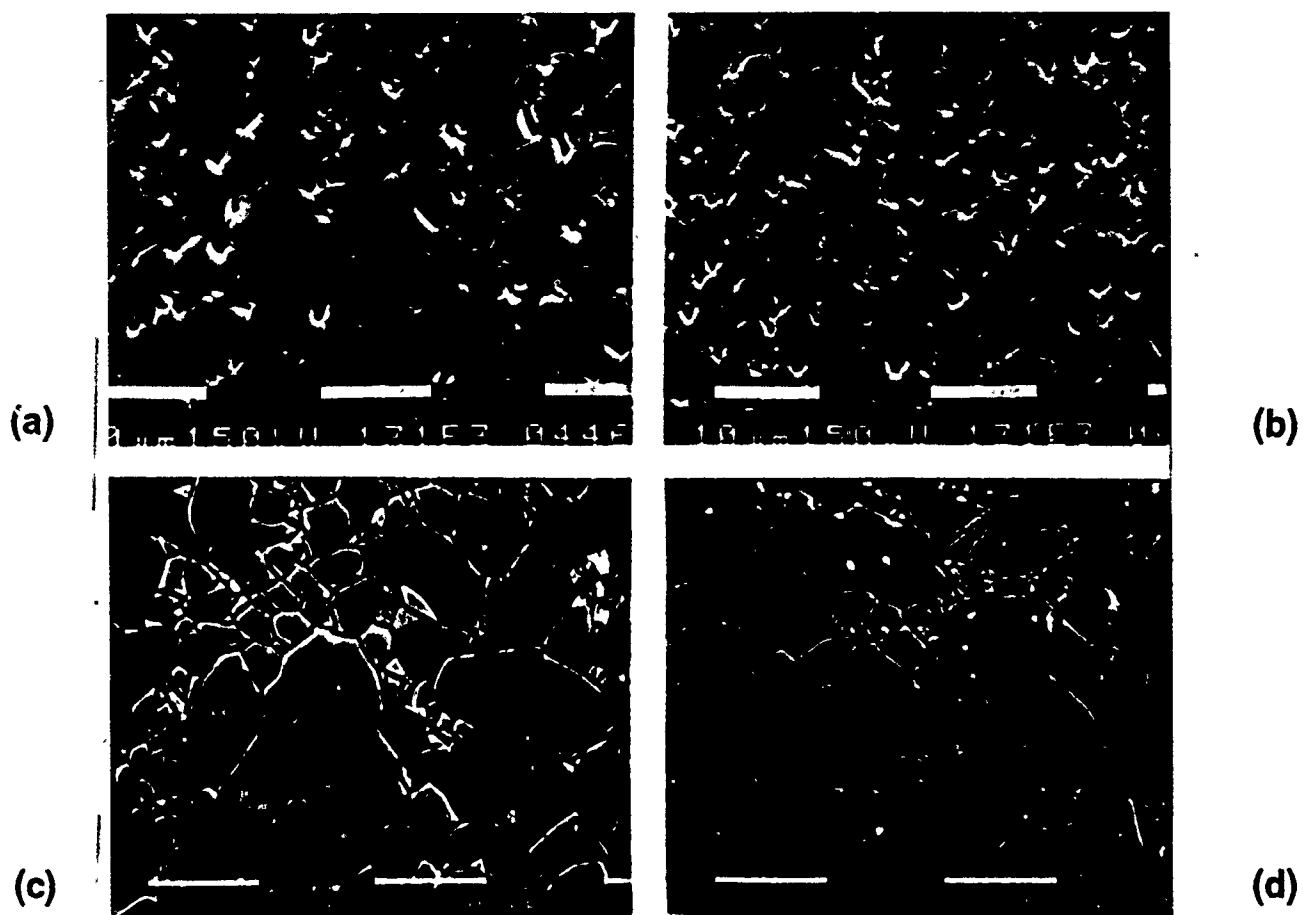


Figure 7. SEM photomicrographs representing the microstructures of the (a) center and (b) edge of a flocculated specimen and the (c) center and (d) edge of a dispersed specimen consolidated at 170 g and sintered at 1150°C for 20 hours.

grain size distribution, pore size distribution, and grain coordination distribution were found to be required.

3.2.1 Microstructural Evolution Modeling

Model 0 was developed to analyze grain growth starting from an initially dense microstructure with a narrow grain distribution. Calculations were conducted to determine the path the microstructural evolution would follow over time. To describe this evolution, two processes must be considered: the neighbor exchange, termed a T1 process, and the cell elimination process, or T2 process, illustrated in Figure 8. The T1 process conserves the number of vertices, edges, and cells and is symmetric in time. The T2 process erodes and eliminates a three-sided cell by the three neighboring cells. This process results in a reduction of vertices, edges, and cells.

Figure 9 shows the effect of time on the CCD distribution which started from an initial narrow distribution of 6. As time increases, the CCD is shown to broaden. The development of the CCD of a single phase structure (no porosity) undergoing only T1 processes was described using the CVM and PPM. The calculations show that the cellular structures have an equilibrium CCD and will develop the equilibrium CCD along one of two possible evolutionary paths, as illustrated in Figure 10. Renderings of the structures along the evolutionary path are illustrated in Figure 11. The initial state of the structure is shown in Figure 11a. Model 0 was then expanded to include both T1 and T2 processes (renamed Model 1) and resulted, for all practical purposes, in identical conclusions: the distribution broadens over time.

3.2.2 Densification Modeling

Model V is a three-point approximation of a two-phase microstructure. The second phase in this case, porosity, allows densification to be studied. This model only allows T1 processes to occur. One of the variables is "chemical potential," which is an undetermined multiplier which sets the number density of cells in the system. Using this variable, the equilibrium density of the structure can be calculated.

The CCD for the fully dense structure is identical to those obtained through Model 0. Partially dense structures were shown to shift from a most probable CCD of 6 to a CCD of 5, mainly due to the effects of pores which have a coordination of 4 or more.

Figure 12 shows the effective density of the structure as a function of time, similar to time density profiles for actual sintered compacts. As time increases, the cell coordination distribution broadens, as illustrated in Figure 13 where $t=5.0$ corresponds to the dense state.

This model can also predict the pore coordination distribution at various densities. Figure 14 illustrates that as the effective density of the specimen decreases, the void number density decreases, implying that the specimen is undergoing grain growth.

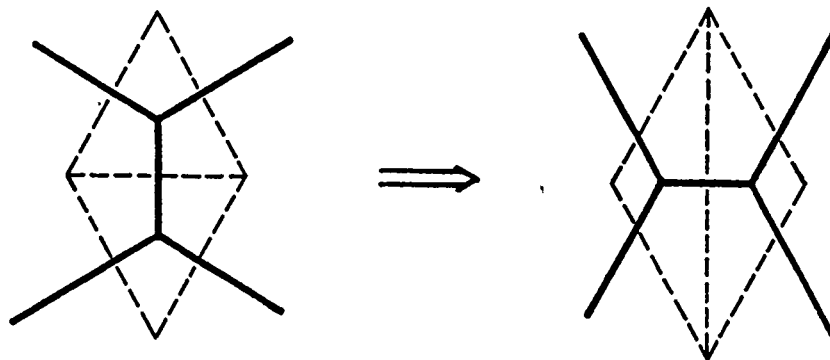
Finally, Model V predicts that the structures evolve along different paths dependent upon the initial state of the specimen. This state is a function of pore coordination distribution and pore number density. This also shows that structure density is not sufficient to fully characterize the structure.

3.3 Modification of Hierarchical Structures

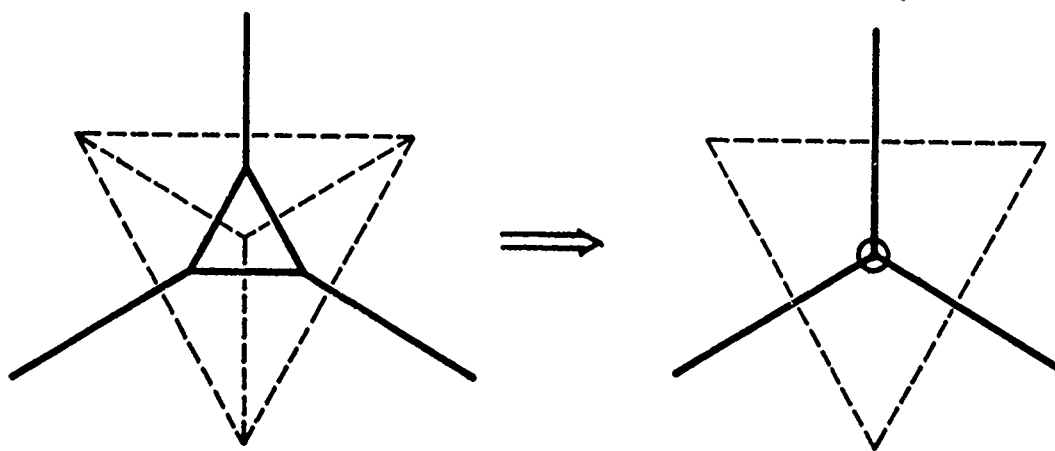
To further improve densification of colloiddally processed materials, it is beneficial to understand not only the formation but also the modification of the hierarchical structure of consolidated compacts. Our previous studies have shown that enhanced densification results in compacts of a broad pore size distribution when compared to compacts with second and third-generation voids. The purpose of this work was to examine the modification of hierarchical structures through plastic deformation and to study the rheological aspects of hierarchical structures in suspensions. The following is a summary of S. I. Kim's Ph.D. dissertation entitled "The Modification of Hierarchical Structures and Rheological Behavior of Aqueous, Ceramic Particle Systems" (Appendix III).

3.3.1 Consolidation Through Pressure Casting

The excessively long times often required for the consolidation of ceramic articles from colloidal suspensions can result in problems such as particle segregation, phase separation, and a decrease in the stability of the suspension. Increasing the consolidation rate can reduce these problems. This can be accomplished by the application of pressure during the casting process itself. The most common filtration medium for consolidation is plaster of Paris which provides a nominal pressure, through capillary suction, of 18 pounds per square inch (psi). Any pressure greater than 18 psi will produce a decreased casting time.



Neighbor Exchange Process



Cell Elimination Process

Figure 8. T1 and T2 topological processes used for PPM and CVM calculations.

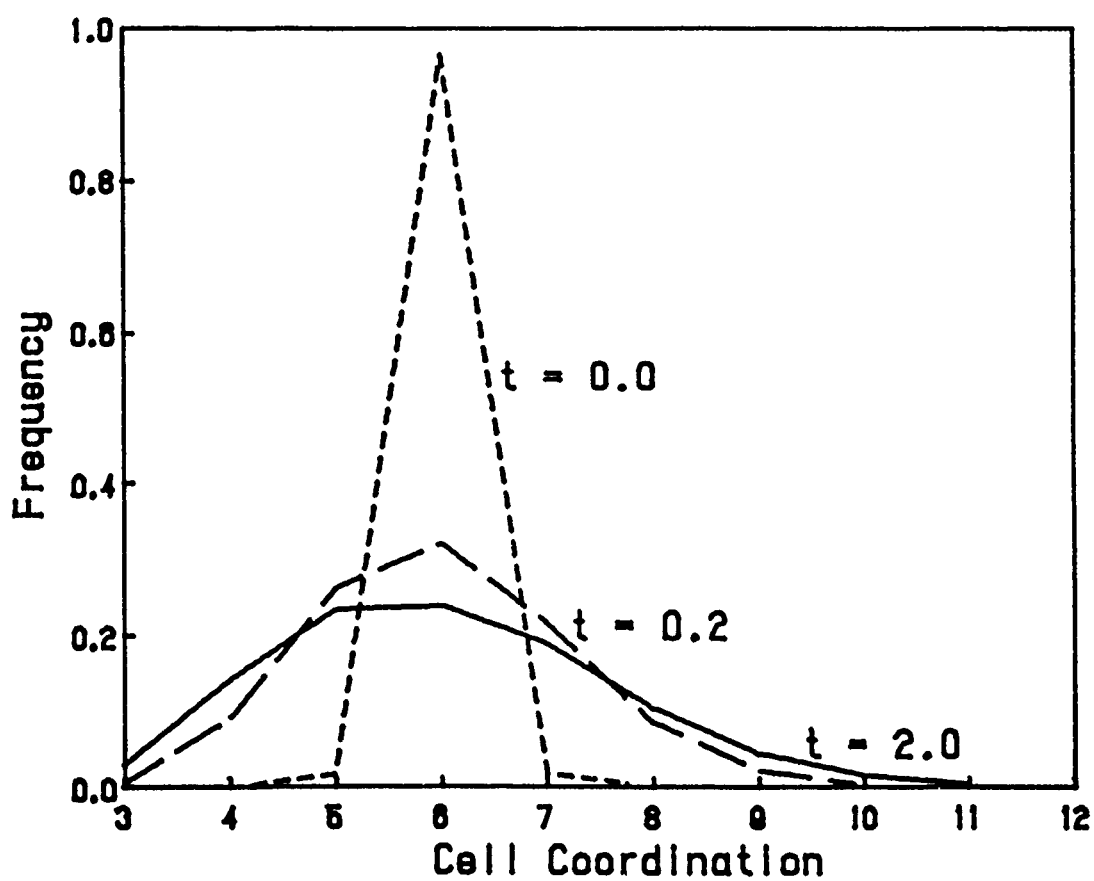


Figure 9. Broadening of the cell coordination distribution calculated with increasing time for a dense microstructure.

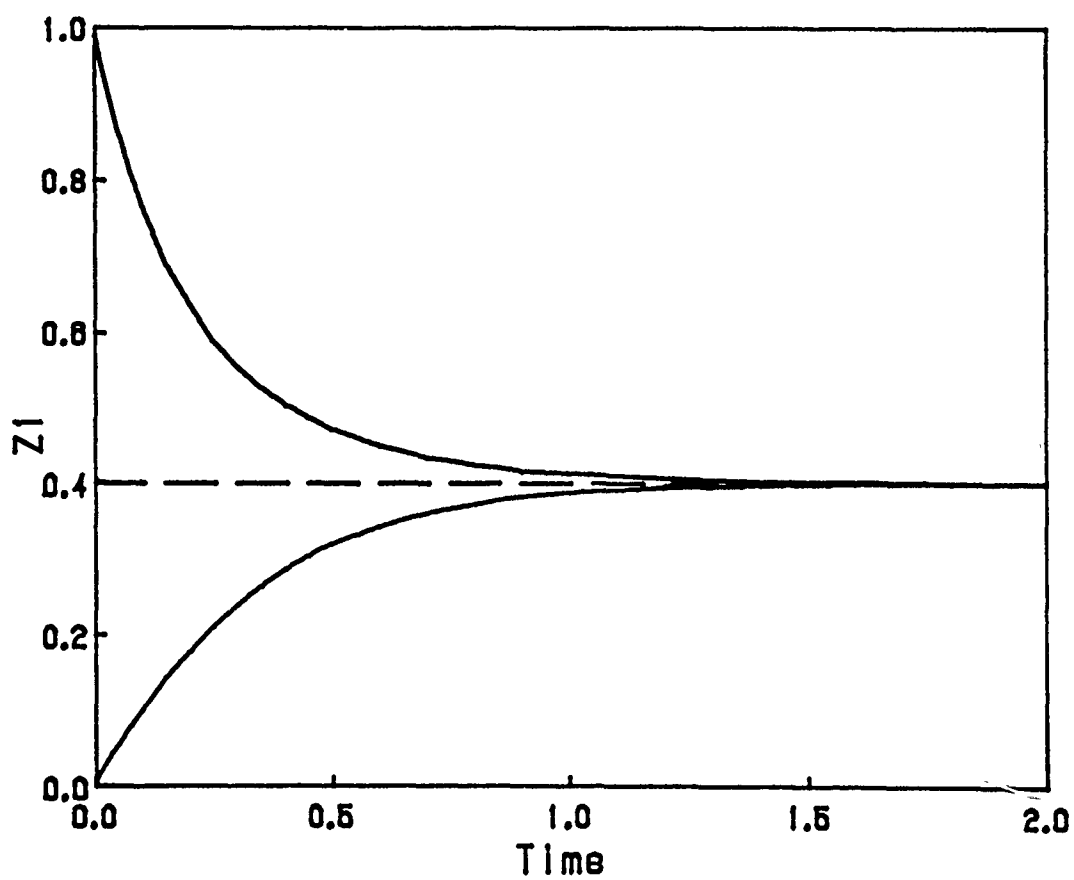


Figure 10. The evolutionary paths along which cell coordination distributions approach equilibrium.

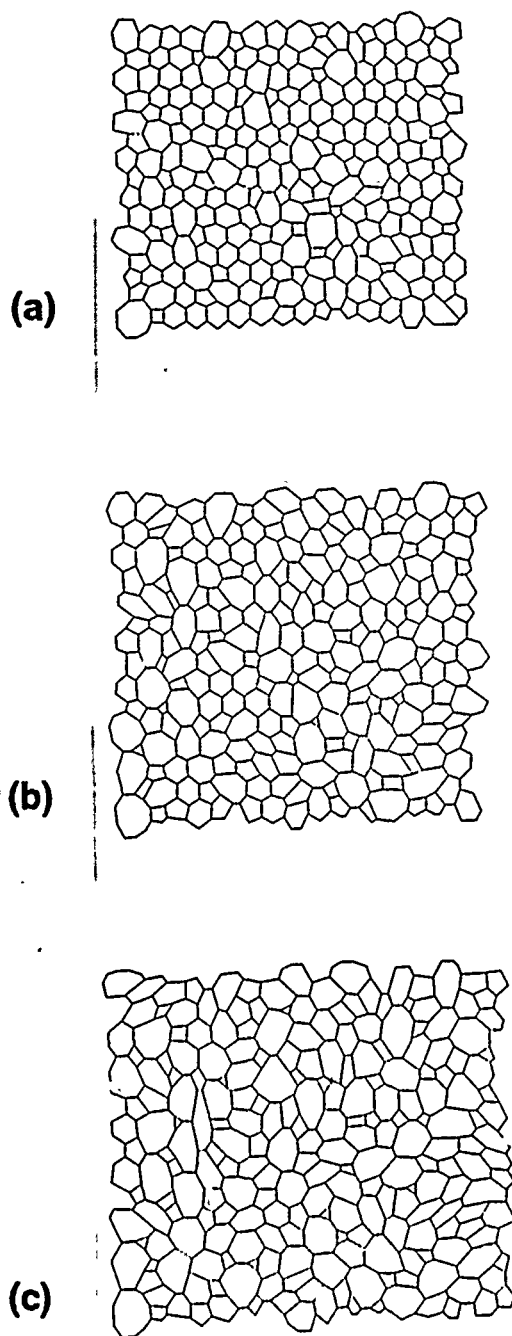


Figure 11. Computer-generated renderings of cellular structures at (a) $t=0.0$, (b) $t=0.2$, and (c) $t=2.0$ illustrating a broadening of the cell coordination distribution.

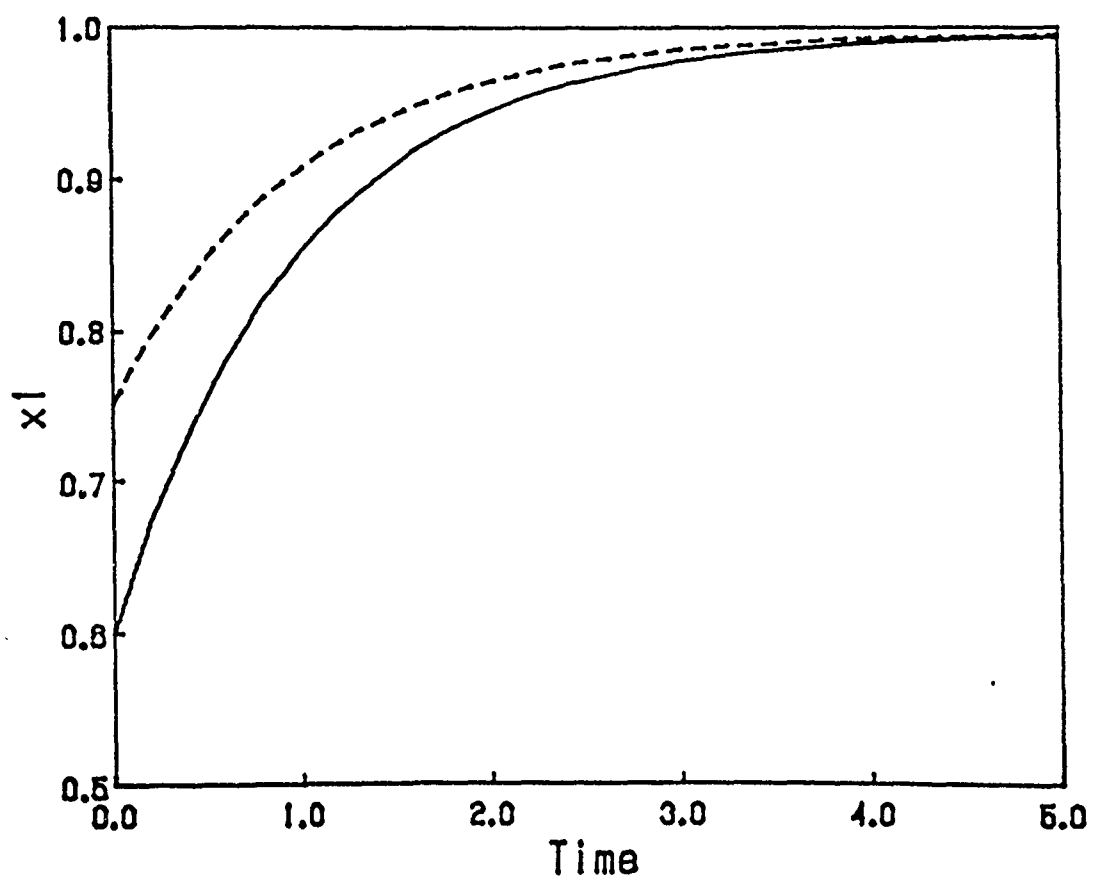


Figure 12. Calculated density of a cellular structure as a function of time.

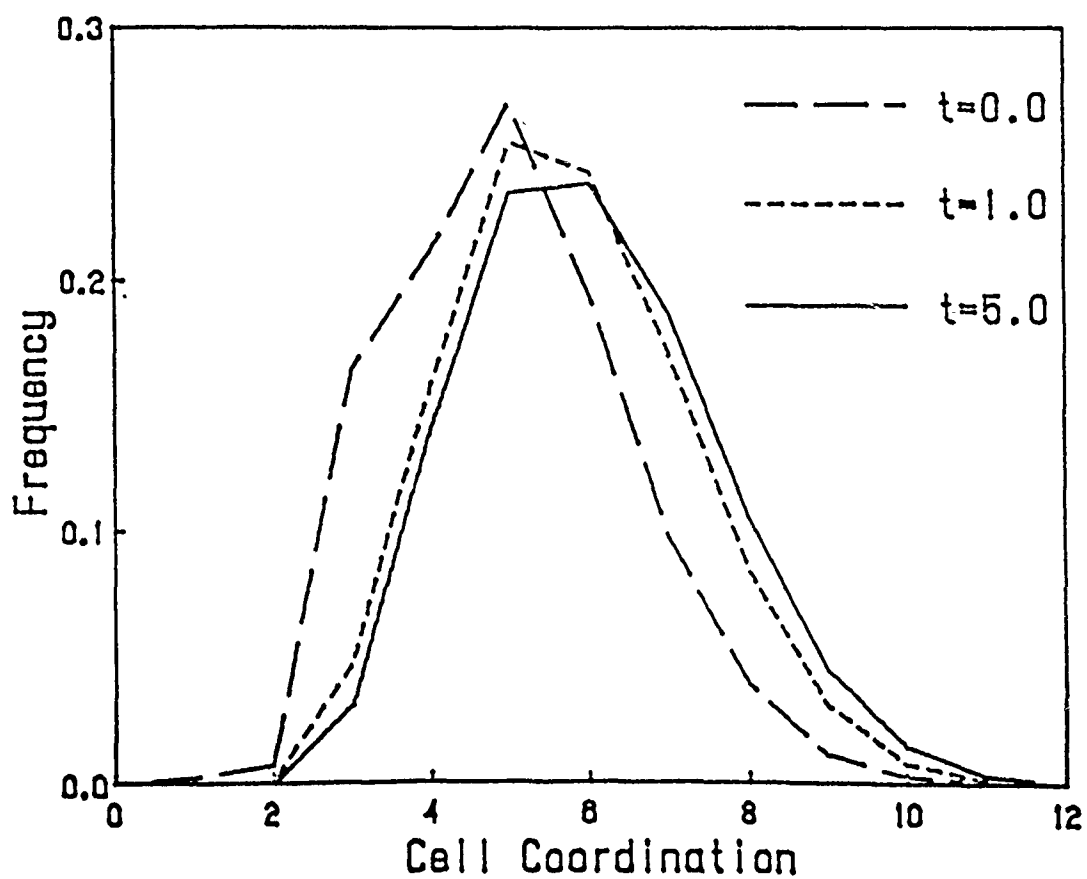


Figure 13. Broadening of the CCD during densification as a function of time. A dense state is represented by the time $t=5.0$.

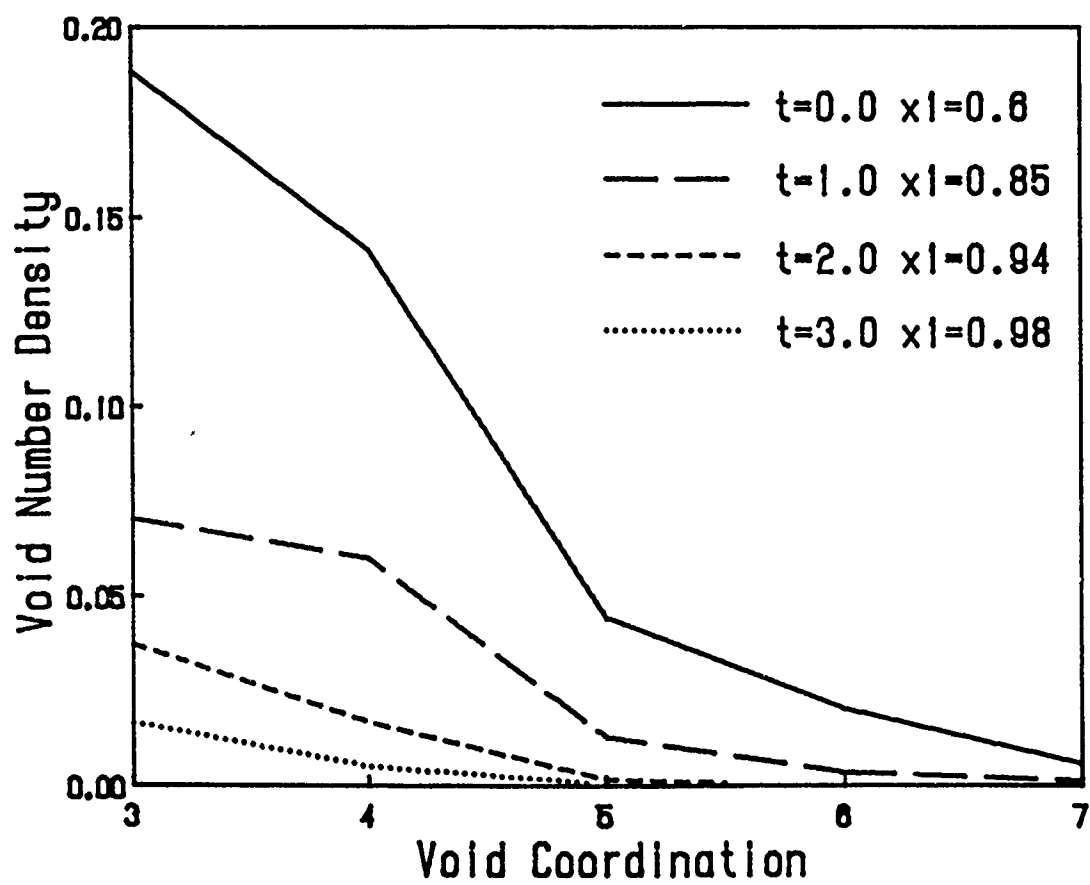


Figure 14. Change in the void number density during densification of a cellular structure.

Electrostatically-stabilized dispersed suspensions containing 40 volume percent alumina^b were prepared at pH 3.0. Sodium hydroxide was added to these suspensions to adjust the pH to values of 7.0, 7.5, and 8.5 and force the system to flocculate. Flocculated suspensions containing less than 15 volume percent alumina would segregate prior to casting, leaving a clean water layer above the settled cake. Because of this, 15 volume percent suspensions were always used.

Samples were cast using a pressure filtration apparatus, illustrated in Figure 15, consisting of a Lexan tube,^c a 0.1 μm Millipore filter,^d and a gas-tight plug. The plug prevented the pressurized gas from dissolving into the suspension during casting and forming decompression bubbles upon the release of pressure. The Lexan cylinder allowed the suspension height to be monitored during the consolidation process.

The casting rate for the dispersed suspension increased significantly as the filtration pressure was increased (Figure 16). The casting time required to produce a given thickness was shown to be inversely related to pressure (Figure 17), corresponding to theoretical models of casting behavior.

Pressure casting of flocculated suspensions produced greater densities at higher pressures. This was due to the loosely packed structure of the flocculated suspensions; compaction ends when the applied pressure matches the strength of the colloidal structure. Figure 18 shows the effect of increased pressure on compact porosity. Dispersed suspensions are not affected by increasing the filtration pressure because the structure of the ordered compacts has already obtained its highest possible packing density.

To provide detailed analysis of the microstructure and the decay of voids at different times during the pressure filtration, simulations of the compaction stages at different times were prepared by varying the concentration of solids in suspensions. These specimens were freeze-dried to preserve the structure and analyzed with SEM. Specimens containing only 5 volume percent alumina contained third generation voids. Increasing the solids loading to 45 volume percent was sufficient to eliminate these voids.

^b AKP-30, Sumitomo Chemical Company, Osaka, Japan.

^c General Electric Company, Schenectady, New York

^d Catalog #VCWP 04700, Millipore Filter Company, Bedford, Massachusetts

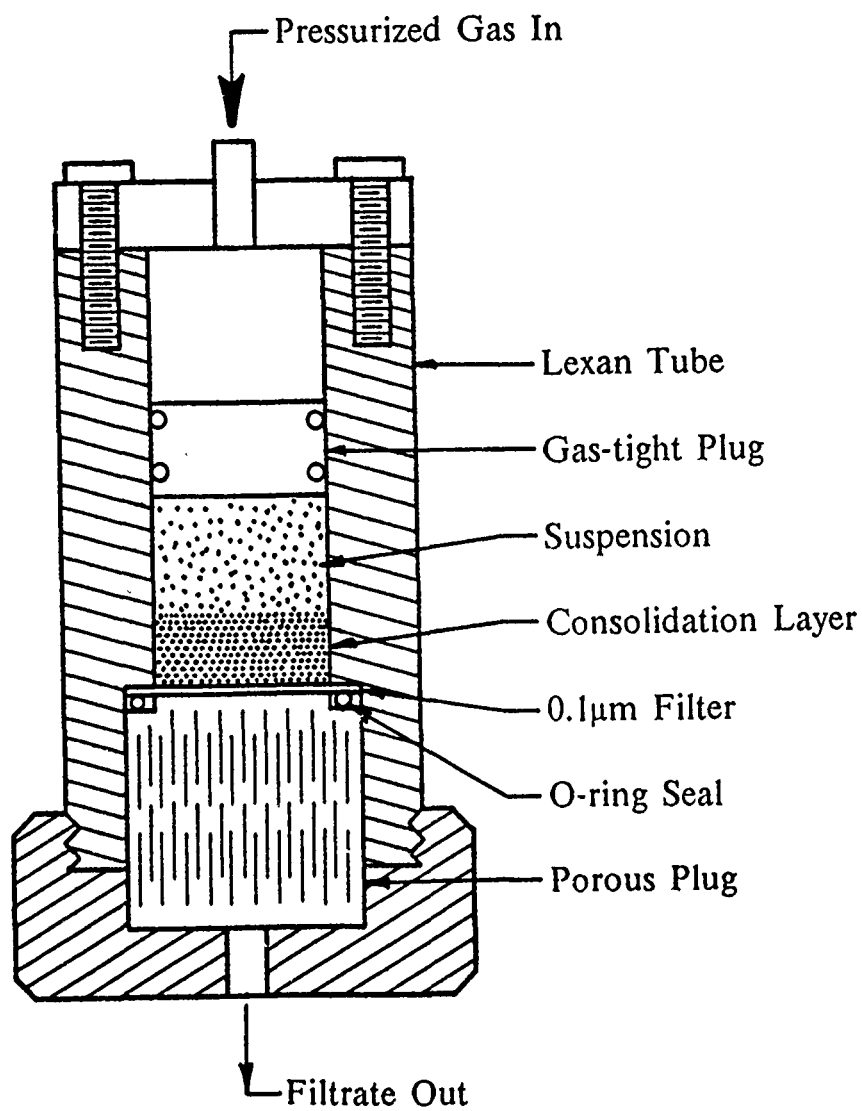


Figure 15. Schematic diagram of the apparatus constructed for use in pressure filtration experiments.

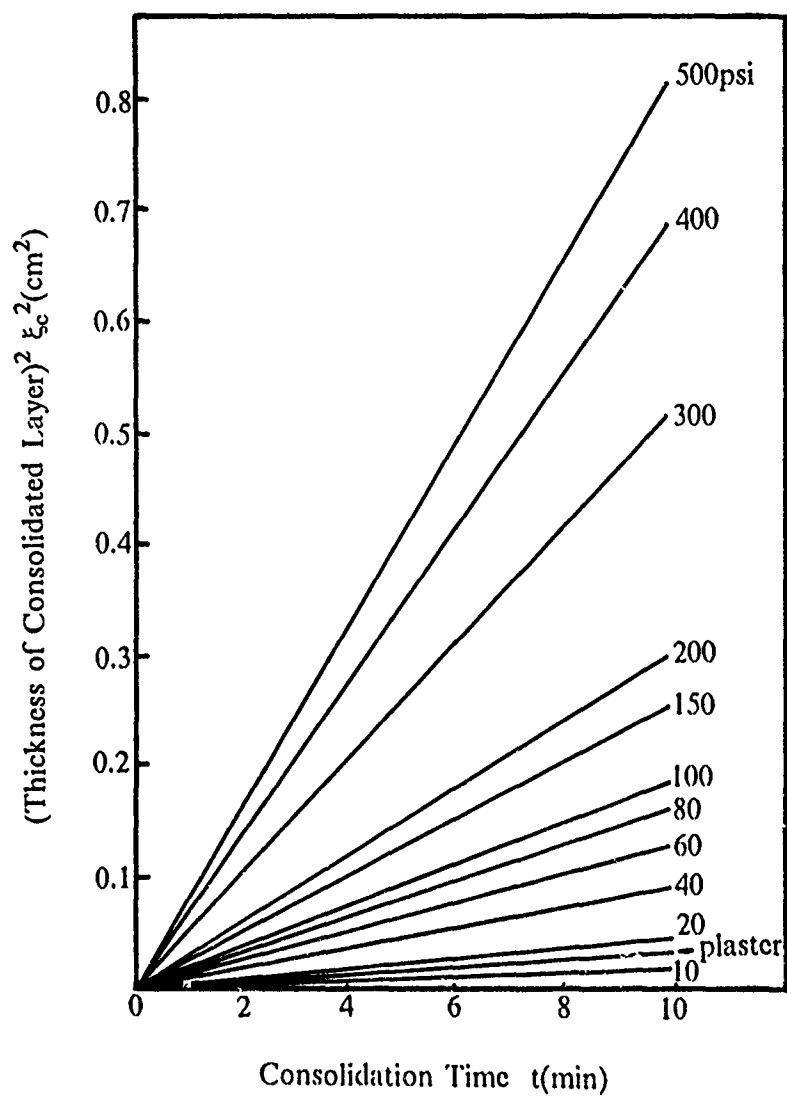


Figure 16. Consolidated cake height as a function of consolidation time. Increased slope indicates increased casting rate.

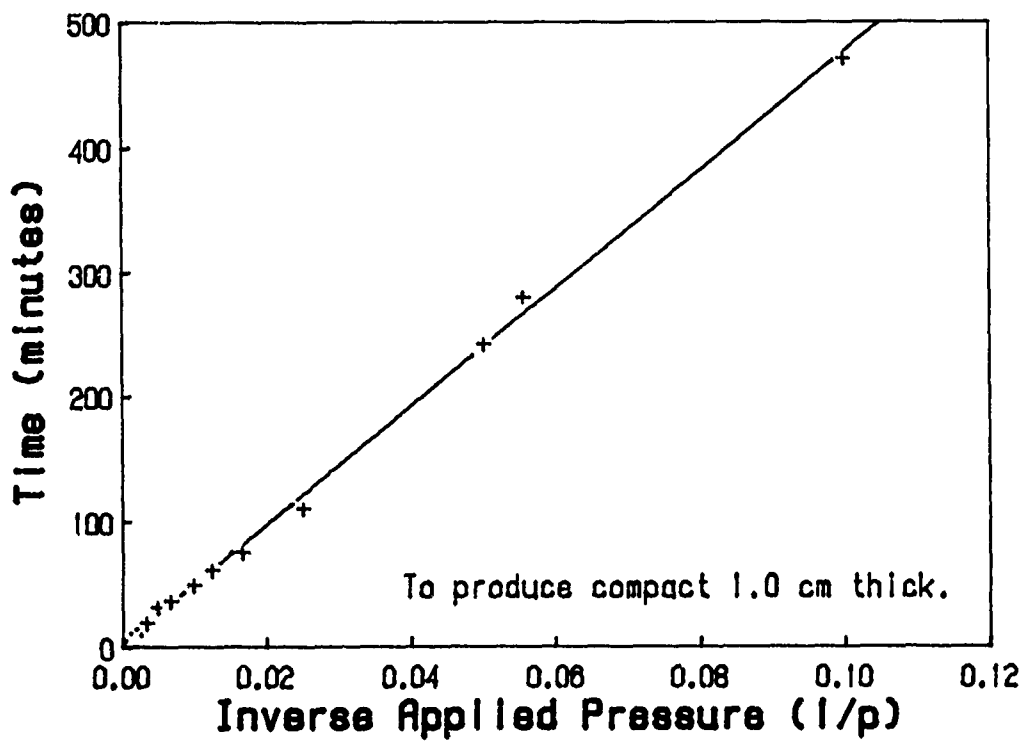


Figure 17. The time required to produce a cake one centimeter in height is inversely related to applied pressure corresponding to filtration theories.

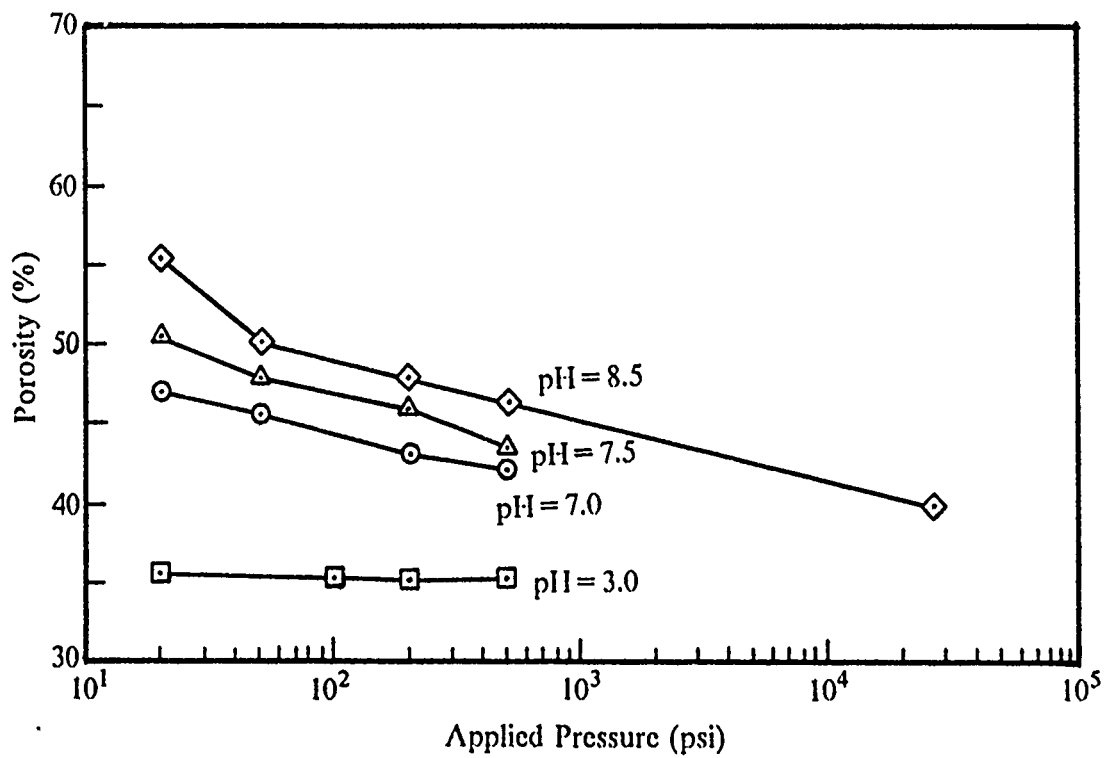


Figure 18. Decrease in porosity observed in flocculated specimens (high pH) as pressure is increased. Dispersed specimens (pH=3.0) are unaffected by increased pressure.

Confined compression tests were performed on the pressure-filtered compacts prepared from the flocculated suspension having a pH of 8.5. After the initial consolidation at 20 psi, the pressure was increased to 50 psi, the decrease in compact height recorded, then the pressure was returned to 20 psi. This test was continued at pressures up to 500 psi. In each case, the specimen remained at the final compaction height, i.e., the compact exhibited plastic behavior.

In order to understand the observed behavior and monitor the structural changes, rheological measurements were performed. These measurements, described in the following section, identify the onset of plastic deformation and regions of linear viscoelastic behavior, helping to characterize the properties of the colloidal suspensions.

3.3.2 Rheological Behavior

Colloidal suspensions possess a very weak structure which can easily be modified with the application of small stresses. These suspensions exhibit viscoelastic behavior through which plastic deformation can occur.

The rheological properties of suspensions of α -alumina (0.4 μm) and boehmite^e (150 Å mean particle size) suspensions were studied because they represent an idealized system of similar chemical composition. The effect of particle size on the rheological properties could also be quantitatively analyzed using dynamic testing. α -alumina has been extensively studied. Boehmite exhibits viscoelastic, plastic, and viscous deformation and can easily form a gel at relatively low concentrations.

The alumina was electrostatically stabilized as described above. Boehmite suspensions were prepared in concentrations from 1 to 10 volume percent with nitric acid, mixed, then classified to eliminate large agglomerates. The remaining suspension was adjusted to the desired pH with sodium hydroxide solution to produce dispersed suspensions (pH 3.5) and flocculated suspensions (pH 5.6).

Rheological measurements, in the form of dynamic oscillatory tests, were conducted using a Rheometrics Fluid Spectrometer.^f Lissajous patterns were constructed from the rheology data to describe the stress-strain behavior of the suspensions. Stress relaxation was also studied

^e Catapal D, Vista Chemical Company, Houston, Texas.

^f Model 8400, Rheometrics, Inc., Piscataway, New Jersey.

through the application of a fixed strain. The stress relaxation of the specimen was then monitored as a function of time. In addition, the microstructure formed in the colloidal suspensions was examined using SEM analysis of freeze-dried specimens.

SEM analysis of freeze-dried specimens of a flocculated (pH 5.6) 3 volume percent boehmite suspension shows a three-dimensional network structure. At a fixed oscillation rate (0.7 radians/second) and up to 3.75% strain, the specimen has a constant storage and loss modulus, meaning the specimen exhibits linear viscoelastic behavior and no structural breakdown. At a constant storage modulus, energy is stored and recovered during oscillations. A constant amount of energy is dissipated through the suspension as heat, producing a constant loss modulus. From these measurements, a Lissajous pattern (Figure 19) was constructed which illustrates the linear relationship between stress and strain and no hysteresis.

Above 3.75% strain, the structure breaks down and the storage modulus decreases. This structural breakdown results in the formation of smaller structures which become dispersed in the liquid medium, increasing the loss modulus. This transition of strain-independent to strain-dependent behavior marks the onset of plastic deformation and flow. Figure 20 is a Lissajous pattern describing the stress-strain relationship and the energy dissipation of the specimen during deformation. The large hysteresis indicates that the suspension has lost its characteristic yield point and now exhibits plastic behavior. As strain is increased above 5.75%, the storage modulus remains constant and the loss modulus increases and the specimen exhibits viscous deformation behavior. At this point (above 5.75% strain), the original internal structure is completely destroyed and a new equilibrium structure is formed.

The dispersed boehmite suspension (5 volume percent, pH 3.5) exhibits completely different behavior. The stress required to destroy a network structure is below the detection level of the rheometer and the suspension simply behaves as a viscous fluid. The inability of the suspension to support even a minute strain suggests that the suspension lacks any network structure.

The behavior of the boehmite suspension was explained using a modified scaling theory which assumes that the system does not act as individual particles but as a system composed of clusters. The size of the cluster decreases as particle concentration increases. As the cluster size decreases, the yield strain of the cluster (and of the specimen) decreases and the modulus of the specimen increases. The predictions of the modified scaling theory satisfactorily explain the experimentally-observed behavior and are in good agreement with other simulations.

The rheological behavior of the alumina suspensions is considerably different. Due simply to the size difference between the alumina and the boehmite particles, the attractive energy

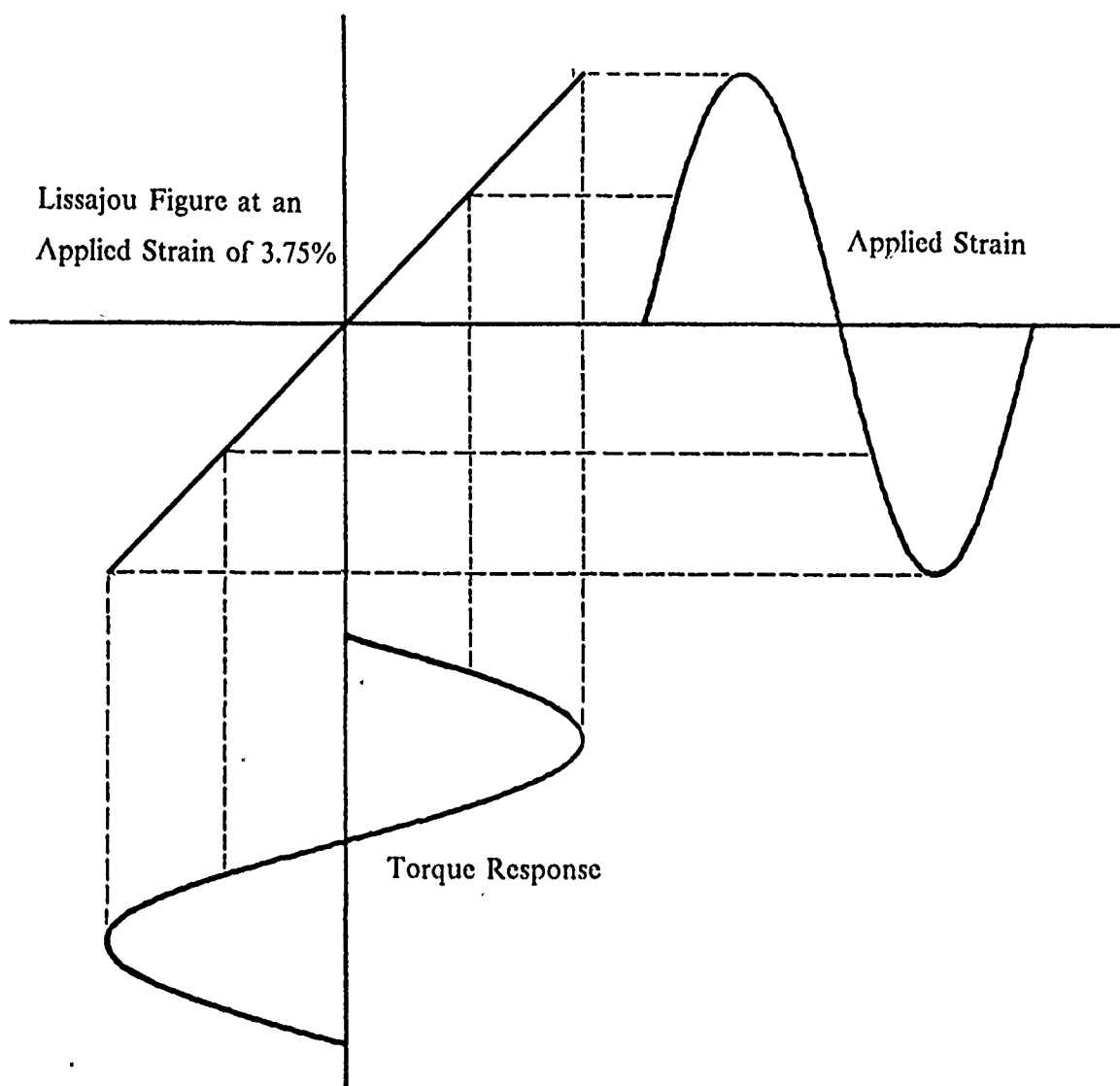


Figure 19. A Lissajou figure for a boehmite suspension exhibiting linear viscoelastic behavior denoted by the linear relationship between applied strain and torque response.

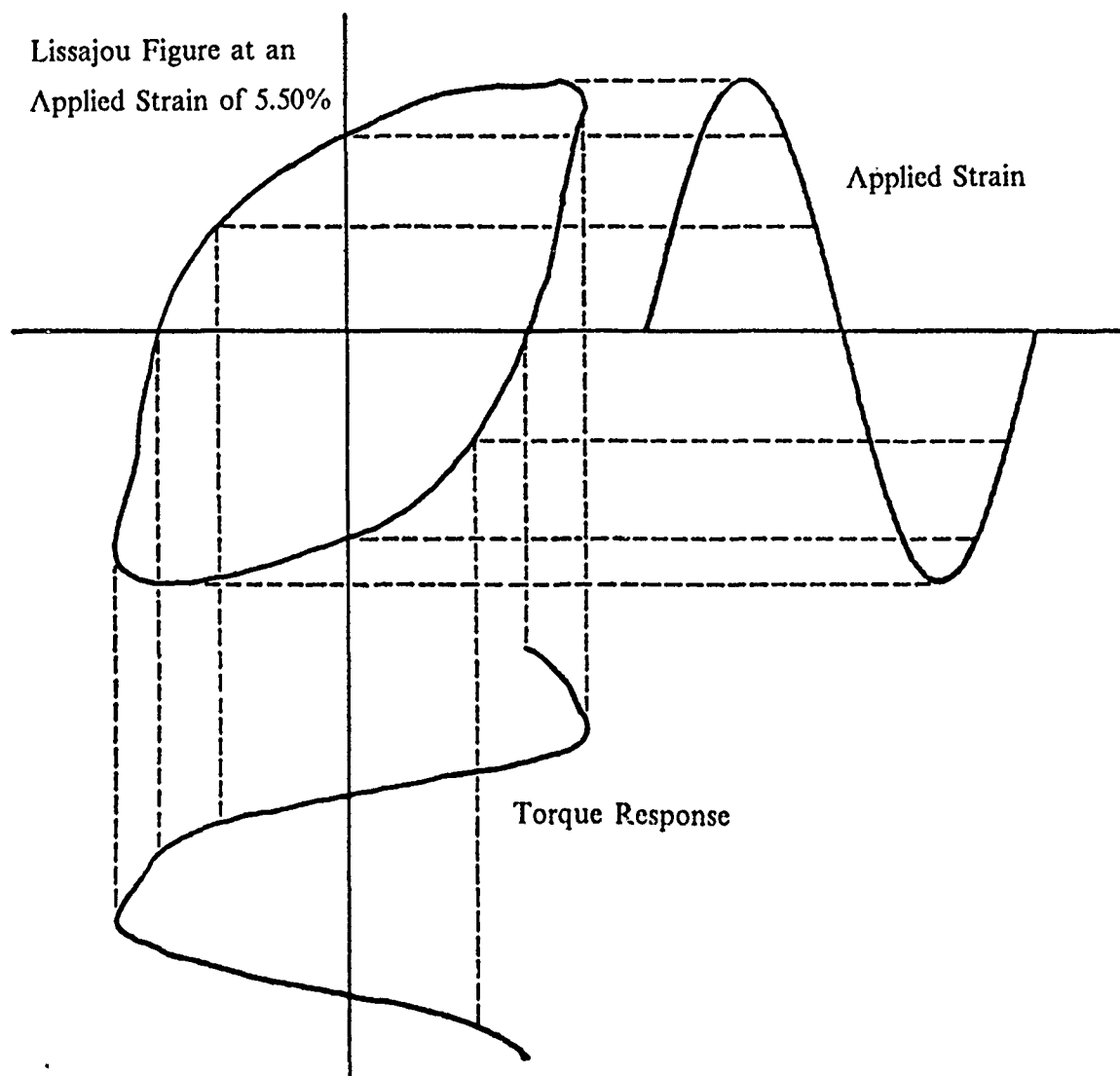


Figure 20. A Lissajou figure for a boehmite suspension exhibiting plastic behavior denoted by the large hysteresis resulting between the applied strain and the torque response.

between a pair of alumina particles is almost six orders of magnitude greater than the attractive energy between two boehmite particles. But when the volume concentration of particles present in a suspension is similar, the total energy of the boehmite suspension is much greater than that of micron-sized alumina particles. This means the boehmite suspension will exhibit elastic properties at much lower concentrations than the alumina suspension.

The micron-sized alumina suspensions do not exhibit any linear viscoelastic behavior was observed in the boehmite suspension. The storage modulus increases rapidly and the yield strain decreases with increasing particle concentration.

4.0 Discussion

4.1 Summary

In order to evaluate existing sintering and microstructural evolution theories, narrowly-distributed spherical TiO_2 powders were synthesized using established organometallic and inorganic precursor routes. The powders produced through organometallic routes with an *in situ* steric stabilizer possessed the ideal properties. Compacts were produced from dispersed and flocculated suspensions and their densification behavior was studied. The grain-coarsening behavior was a function of the packing configuration. Specimens were subjected to isothermal heat treatments for various times to allow the observation of the densification behavior on the surface of the compacts. After sufficient time, abnormal grain growth was observed in the dispersed specimens. The flocculated specimens exhibited time-independent normal distributions for the same heat treatments, apparently due to pinning of the grain boundaries by pores.

Contrary to theoretical predictions for sintered microstructures, TiO_2 will not produce uniform microstructures even when starting with narrowly-distributed spherical powders. This suggests that, from a densification viewpoint, the use of narrowly-distributed powders offers no advantage in the colloidal processing of ceramics. This broadening of the distribution is apparently due to the anisotropic properties of the particles themselves since they possess crystallographic orientations. Ideally, the pore size distribution should be narrow and similar in size to the grain size. This is very difficult to achieve because hierarchically-clustered structures develop upon consolidation of the compact from the colloidal suspension.

Modeling of the densification and grain growth processes have shown that microstructures evolve along different paths but approach the same equilibrium structure regardless of the initial particle distribution. This implies that the final microstructures are essentially independent of the processing route provided that the equilibrium structure can be obtained.

Modification of the hierarchy of the structure to further narrow pore size distribution can lead to enhanced densification. One method of destroying this structure is through the application of pressure during filtration, which also results in substantial increases in the consolidation rate. The void fraction of flocculated specimens can be reduced through pressure filtration, but no advantage in terms of decreased void concentration was observed for dispersed specimens.

Boehmite suspensions exhibit regions of linear viscoelastic behavior at given constant strains. Increasing the solids concentration decreases this region exponentially. The rheological

properties of boehmite can be accurately described through the use of a modified scaling theory. Unlike boehmite, micron-sized alumina suspensions do not exhibit a linear viscoelastic region.

4.2 Conclusions

Preparing compacts from narrowly-distributed powders is not sufficient to produce a narrow grain size distribution in the final microstructure; a narrow pore size distribution is also required. If a narrow pore size distribution can be obtained, it is still possible that a narrow grain size distribution will result. Even if a narrow grain size distribution is obtained, the distribution will always broaden if subjected to subsequent heat treatments sufficient to allow grain growth to occur.

The implications of this work can be applied to the fabrication of ceramic whisker- or fiber-reinforced ceramic composites. A multiphase material, i.e., a material containing inclusions, will attempt to achieve the equilibrium size distribution. If the inclusions are chemically similar, interactions between the matrix and the included phase may effectively eliminate the inclusions, reverting to a single phase material. If the matrix and inclusion can be isolated, perhaps through the use of a coating or diffusion barrier, the matrix and the inclusion will attain an equilibrium grain size distribution independently, allowing subsequent use at higher temperatures.

5.0 References

1. I. A. Aksay, in *Advances in Ceramics*, Vol. 9, edited by J. A. Mangels and G. L. Messing (American Ceramic Society, Columbus, Ohio, 1984) p. 94-104.
2. E. A. Barringer, R. Brook, H. K. Bowen, in *Sintering and Heterogeneous Catalysis*, edited by G. C. Kuczynski et al. (Plenum Press, New York, 1984), pp. 1-21.
3. E. Barringer, et al., in *Ultrastructure Processing of Ceramics, Glasses, and Composites*, edited by L. L. Hench and D. R. Ulrich (Wiley, New York, 1984), pp. 315-333.
4. M. F. Yan, R. M. Cannon, H. K. Bowen, U. Chowdhry, "Effect of Grain Size Distribution on Sintered Density," *Mater. Sci. Engr.*, **60**, 275-281 (1983).
5. M. A. Occhionero, J. W. Halloran, in *Sintering and Heterogeneous Catalysis*, edited by G. C. Kuczynski et al., (Plenum Press, New York, 1984), pp. 89-102.

6.0 Technical Communications

Publications

S. I. Kim and I. A. Aksay, "Effect of Pressure and Interparticle Energy on the Structure of Hierarchically-Clustered Solids," to be submitted to *J. Am. Ceram. Soc.*

Future Publications

1. S. K. Fukuda, R. Kikuchi, and I. A. Aksay, "On Uniform Packing," to be submitted.
2. S. K. Fukuda, R. Kikuchi, and I. A. Aksay, "PPM Calculation of the Topological Development of Cellular Structures Prior to Grain Growth," to be submitted.
3. S. K. Fukuda, R. Kikuchi, and I. A. Aksay, "PPM Calculation of the Topological Development of Cellular Structures During Densification," to be submitted.
4. S. K. Fukuda, R. Kikuchi, and I. A. Aksay, "The Evolution of Cellular Structures."
5. S. I. Kim, W.-H. Shih, and I. A. Aksay, "Structure-Property Relationships in Pressure Filtration."

Presentations

1. S. I. Kim, W.-H. Shih and I. A. Aksay, "Rheological Behavior of a Nanometer-Sized Particle System," presented at US/Japan Workshop, October 1988.
2. S. I. Kim, W.-H. Shih and I. A. Aksay, "Rheological Behavior of a Nanometer-Sized Particle System," presented at the 90th Annual Meeting, American Ceramic Society, May 1988.
3. S. I. Kim and I. A. Aksay, "Rheological Behavior of Nanometer-Sized Particulate Systems," presented at the 40th Pacific Coast Regional Meeting, American Ceramic Society, October 1987.

4. S. I. Kim and I. A. Aksay, "Effect of Pressure and Interparticle Energy Upon Colloidal Systems," presented at the 39th Pacific Coast Regional Meeting, American Ceramic Society, October 1986.
5. S. I. Kim and I. A. Aksay, "Pressure Filtration of Colloidal Systems," presented at the 37th Pacific Coast Regional Meeting, American Ceramic Society, October 1984.

APPENDIX I

Corrie B. Martin*

*Preparation and Microstructure Evolution
of Hierarchically-Clustered Powders*

M.Sc. Thesis

Department of Materials Science and Engineering,
University of Washington,
Seattle, Washington

1988

* Currently Vice President in Charge of Operations, SSC, Inc., Bothell, Washington 98011.

Preparation and Microstructure Evolution
of Hierarchically Clustered Powders

by

CORRIE B. MARTIN

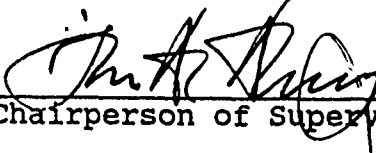
A thesis submitted in partial fulfillment
of the requirements for the degree of

Master of Science in Ceramic Engineering

University of Washington

1988

Approved by



(Chairperson of Supervisory Committee)

Program Authorized

to Offer Degree Material Science and Engineering

Date _____

Master's Thesis

In presenting this thesis in partial fulfillment of the requirements for a Master's degree at the University of Washington, I agree that the library shall make its copies freely available for inspection. I further agree that extensive copying of this dissertation is allowable only for scholarly purposes, consistent with "fair use" as prescribed in the U.S. Copyright Law. Any other reproduction for any purposes or by any means shall not be allowed without my written permission.

Signature_____

Date_____

Table of Contents

	Page
1.0 INTRODUCTION	1
2.0 BACKGROUND	4
2.1 Spherical Powders	4
2.2 Particle Packing	6
2.2.1 Particle Interactions	6
2.2.2 Colloidal Crystals	8
2.2.3 Flocced Particle Systems	15
2.3 Microstructure Evolution	15
2.3.1 Particle Coalescence Grain Growth and Pore Behavior During Sintering	16
2.3.2 Grain Growth in Dense Compacts	22
2.3.2.1 Closed Form Models	22
2.3.2.2 Computer Simulations	35
3.0 EXPERIMENTAL	40
3.1 Particle Synthesis	40
3.1.1 Ethoxy Ligand	40
3.1.2 Chloride Ligand	41
3.2 Particle Characterization	42
3.3 Particle Packing	42
3.4 Compact Characterization and Sintering	43
3.4.1 Image Analysis and Microstructure Characterization	44
4.0 RESULTS AND DISCUSSION	45
4.1 Particle Synthesis	45
4.1.1 Particle shape and size	45
4.1.2 Densities	48
4.1.3 Calcination	51
4.2 Particle Packing	53
4.3 Sintering	60
4.4 Grain Growth	66
4.4.1 Surface	66
4.4.2 Bulk Microstructure	74
5.0 SUMMARY AND CONCLUSIONS	88
5.1 Summary	88
5.2 Conclusions	90
6.0 BIBLIOGRAPHY	91
7.0 APPENDIX: Abnormal Grain Growth	97

List of Figures

	Page
Figure 1. Particle pairwise potentials in electrostatic, steric and electrosteric systems.	9
Figure 2. Order disorder phase transitions in latex suspensions ³³ .	10
Figure 3. Relative osmotic pressure changes in polydisperse particle systems ³⁹	12
Figure 4. Crystallization rate in a particle system as a function of volume fraction solids ⁸ .	14
Figure 5. Pore growth and shrinkage regimes for equilibrium dihedral angle and coordination number ¹¹ .	18
Figure 6. Particle coarsening as a function of density ^{44,20} .	21
Figure 7. Representation of grain faces, edges, and corners.	24
Figure 8. Soap bubble froths showing Euler's relationship.	25
Figure 9. Loss of a triangular face in three dimensional space.	31
Figure 10. Unit operations of neighbor exchange and disappearance of a triangular face in 2 dimensional grain growth.	36
Figure 11. X-ray sedigraph of as prepared insitu stabilized and unstabilized TiO ₂ powders.	46
Figure 12. Inorganic salt derived TiO ₂ powder.	47
Figure 13. FTIR absorbance peak of HPC surfactant on TiO ₂ powders.	49
Figure 14. Intraparticle shrinkage in the surface of the 170 g ordered compact during crystallization at 780°C (bars = 10 μm).	50

Figure 15. DTA runs for the stabilized and unstabilized powders.	52
Figure 16. Relative crystallinity for applied centrifugation fields of 1g, 170g, and 350g (bar = 10 μm).	55
Figure 17. Top and fracture surfaces of ordered and flocced compacts.	57
Figure 18. Negative of the top surfaces (Fig 17) enhancing voids.	59
Figure 19. Void size distribution from Figure 18.	61
Figure 20a. Initial and intermediate stages of sintering in the ordered 170 g compact surface (bar = 1 μm).	63
Figure 20b. Initial and intermediate stages of sintering in the flocced compact surface (bar = 1 μm).	64
Figure 21a. Normalized surface grain size distributions in the 1 g ordered compact.	67
Figure 21b. Normalized surface grain size distributions in the 170 g ordered compact.	68
Figure 21c. Normalized surface grain size distributions in the flocced compact.	69
Figure 22. Mean grain size vs. time for the distributions in Fig 21a,b,c.	70
Figure 23. Micrographs of surface grain shapes for 170 g and flocced compacts at various times	73
Figure 24. Mean grain size growth in the 170 g and flocced compact crosssections.	75
Figure 25. Mean grain size at different positions in the 170 g sample	77
Figure 26. Mean grain size at different positions in the flocced sample.	78

Figure 27. Micrographs at different positions in the flocced and 170 g ordered cases.	79
Figure 28. Ordered (1050°C) and flocced(1150°C) at 2 and 10 hours.	80
Figure 29. Pore size distributions for 170 g ordered during sintering at 1050°C.	82
Figure 30. Pore size distribution for the flocced specimen during sintering at 1150°C. two different temperatures for similar densities.	83
Figure 31. Bulk grain size distributions of the ordered 170 g compact.	85
Figure 32. Bulk grain size distributions of the flocced compact.	86
Figure A1. Fracture surface of 170 g compact after after nonisothermal sintering at 1150°C.	98

List of Tables

Normalized Surface Grain Distributions	72
Normalized Bulk Grain Distributions	84

Acknowledgments

I would like to thank Dr. Ilhan Aksay for introducing the concepts of colloid and ceramic science, and for providing guidance in my research over the period of my undergraduate and graduate education. A special thanks goes to Mr. Chan Han for his friendship and advice throughout the present and past projects. In addition, I would like to express appreciation to Dr. Scott and Dr. Fishebach for their time and the use of their laboratory equipment. As always, the support of family, friends, and associates over the period of research and thesis preparation has been indispensable.

This work was supported under the Army Research Office Contract DAAG29-85-K-0136.

1.0 INTRODUCTION

Submicrometer powders are used in materials processing to enhance sintering rates and to yield fine grained microstructures. A question arises as to whether or not submicrometer powders are the only prerequisite in the evolution of the final microstructure. The unsintered compacts resulting from the consolidation of powders always consist of two phases, particles and pores. One school of thought is that monosized particles are essential in the development of microstructures with a narrow grain size distribution and with a minimum degree of grain growth. However, in a "monosized" particle system the, the pore size distribution can vary from a narrow to very broad width depending upon the processing routes used. The relative importance and effect of the pore size distributions^{1,2,3} and particle size distributions^{4,5,6} on an evolving microstructure would seem to be in question. Thus the goal of the work presented in this thesis is to examine the relative importance of a controlled pore size distribution on a resultant microstructure. It will be illustrated that in a monosized particle compact the pore size distribution plays a key role on the evolution of a microstructure during sintering.

Monosized particles can be synthesized and then packed into various particle-pore configurations by manipulating the particle-particle interactions⁷ and particle mobility during compact formation⁸. Careful control of the system parameters can yield colloidal crystals with well defined narrow pore distributions or a broad spectrum of pore sizes⁹.

Pore size effects on microstructure during sintering were illustrated by Exner¹⁰ to be quite pronounced with pore

shrinkage and pore growth occurring in the same compact. While some portions of a compact may exhibit pore shrinkage, pores in other regions can grow resulting in anisotropic strains and particle rearrangement. The densification and particle coarsening are concurrent processes and as such the compact can exhibit inhomogeneous particle and grain growth as a direct consequence of particle rearrangement¹¹. By extension of previous studies^{10,11} in to the models proposed by Yan⁴ it should be evident that the time evolution of microstructure during densification is highly dependant upon the initial particle-pore state.

After a critical relative density, a growth process transition from particle coarsening to grain growth is expected¹². During grain growth in a porous compact two scenarios are possible, normal or breakaway grain boundary motion¹³. Normal grain growth is considered a process in which pores remain at grain junctions and boundaries and subsequently disappear by diffusion to vacancy sinks at grain grain boundaries and dislocations. Breakaway motion, or abnormal grain growth, is represented by intragrainular porosity. Grain boundary pinning by pores during the final stages of sintering is a critical phenomena since a slight inhomogeneity in pore distribution may result in abnormal grain growth¹⁴. It is evident that fully dense microstructures may vary substantially in their grain size distribution dependant upon previous processing.

Grain growth models have been derived for single phase fully dense metal and ceramic systems which should apply to the evolving microstructure being followed in this introduction. Grain growth models have evolved from that first proposed by Harker and Parker¹⁵ which considered growth to be independent of size to that of Kurtz and Carpay¹⁶ with it's relationship between size and shape. All

models and subsequent observations show a time independent grain size distribution as well as an approach to equilibrium. However, what is not explained is the evolution of the time independent grain size distribution.

As early as 1956, Kikuchi¹⁷ illustrated that in cellular structures, cell or grain size distribution is determined by entropy considerations. Two recent models have also been introduced in an attempt to explain the observed distribution^{18,19}. Both models resort to topological aspects of polycrystalline grain arrays in the determination of a configurational entropy term. The problem in experimental confirmation is to start with microstructure of relatively low configurational entropy and observe the evolution to the time independent distribution.

The study presented in this thesis was initiated as part of an Army Research Office supported project on the development of a methodology for predicting the evolution of hierarchically clustered colloidal structures. The hypothesis of the work was that monosize particles, even in colloidal consolidation, do not yield monosized grain distributions in a sintered compact. Instead, the microstructure evolution is mainly controlled by the initial pore size distribution. the work presented in the following sections attests to the validity of this hypothesis.

2. BACKGROUND

Spherical powders are produced from solutions by several well established techniques all of which yield a slightly different product in terms of size, size distribution, shape, and thermal behavior. From these powders the most appropriate can be chosen for fabrication of particle compacts. Control of particle-particle interactions and particle mobility can yield various configurations of particles and pores ranging from colloidal crystalline arrays to ill defined particle flocs. Densification of the compacts will follow the three stages of initial, intermediate, and final sintering concomitant with particle coarsening and grain growth. The continued stages of microstructure evolution will follow via the grain growth processes.

2.1 Spherical Powders

Packing of powders will depend on their size, size distributions²⁰, shape, structure²¹, surface chemistry²², and environment²³. In addition to packing considerations behavior on drying and heat treatment is critical in terms of densification and porosity, or chemical and thermodynamic behavior.

An examination of systems yielding easily characterized packing geometries spans both organic and inorganic compositions. Synthesis of Latex spheres which can be stabilized by both steric and electrostatic interactions are well known^{24,25} and a great deal of work has been done on ordering such lattices, but no crystallization occurs in these systems and hence no grain growth effects are seen on heating³. Similar studies on SiO_2 by the Stobber²⁶ process are numerous; unfortunately these easily characterized and

producibile spherical powders sinter via viscous flow with an absence of grain boundaries. It is clear that crystalline powders must be used; however, it is not necessary to have as synthesized crystalline powders.

Phase transformation, from amorphous to crystalline, of units in a packed lattice may be acceptable if drastic rearrangement of the lattice does not occur. In the case of wet chemical synthesis of TiO_2 ^{5,27} amorphous precipitates are formed which show three transformations²¹ and substantial intra and interparticle shrinkage on heating; but these particles do not indicate drastic rearrangement of packing configuration. Hydrothermal treatment of the amorphous TiO_2 powders in boiling water induces crystallization²⁸, but also results in particle breakdown and subsequent abnormal grain structure.

Insitu transformation may be avoided by working with powders which are crystalline prior to packing. Matijevic²⁹ investigated the formation of TiO_2 from ionic solution which showed x-ray diffraction peaks in the as synthesized state. However, yields were very small with a mean size of 1 micrometer and a standard deviation of + 0.3 micrometers. Aerosols³⁰ have also been produced by hydration of Ti salts and alkoxides in a gas stream which have a wide distribution and are amorphous in the as prepared state. Gold sols³¹ have been produced in the submicron range (4000 Å) which are crystalline but are considered "globular" as opposed to spherical.

Probable systems are reduced by the study parameters to either the TiO_2 or Gold system. Both systems can be electrostatically stabilized, show relative monodispersity, can be crystallized, and have been shown to form colloidal crystals^{32,30}. Solid state sintering is expected in both

cases with subsequent grain growth behavior controlled by similar processes.

Once powders are synthesized the particle-particle interaction potentials can be controlled to yield a variety of particle-pore configurations². In order to illustrate the goals of this study a range of particle packings and pore size distributions are needed.

2.2 Particle Packing

In order to attempt correlations between sintering and densification stages an easily controlled green states are desirable. Colloidal crystal or polycrystalline particle packing is one extreme, where the structure consists of domains, inter, and intra domain pores^{1,2}. On the other extreme is a highly flocced powder compact consisting of the same monosized particles, but a substantially larger hierarchy of pores. Therefore, a prime objective is to control particle interactions and form both well packed colloidal polycrystalline and flocced green bodies from the synthesized powders.

2.2.1 Particle Interactions

Relative radial position of colloidal particles with respect to one another is attributed to interaction potentials between particles due to either steric³³, electrostatic³⁴, or electrosteric stabilization. Steric and electrostatic interactions can be considered in terms of trapping in potential wells in dilute cases³⁵ or hard sphere interactions for concentrated suspensions. Particle approach distance in electrosteric interactions can occur in a potential well or as a hard sphere interactions depending on concentration and potential determining characteristics.

Electrostatic potentials result from adsorption of potential determining ions on a surface with a concomitant formation of a cloud of neutralizing ions. DLVO theory describes the electrostatic forces arising from such an ion cloud - particle configuration where both attractive and repulsive forces are present. The total interaction forces between two particles is represented by the sum of the distance derivatives of the energies:

$$1) \quad \frac{dU}{dr} = \frac{dU_{at}}{dr} + \frac{dU_r}{dr}$$

where U_{at} is the attractive energy, U_r is the repulsive energy, and dr is the differential distance.

Repulsive forces can result from steric, electrostatic, or electrosteric interactions. For the case of spherical particles energy of attraction is given by²³:

$$2) \quad U_{at} = -\frac{A}{6} \left[\frac{2a^2}{R^2 - 4a^2} + \frac{2a^2}{R^2} + \ln \left(\frac{R^2 - 4a^2}{R^2} \right) \right]$$

where A is Hamaker's constant, a is the particle radius, and R is the center to center particle separation. Electrostatic repulsive energy is given by:

$$3) \quad U_r = 2\pi\epsilon\epsilon_0 a \zeta^2 \left(\frac{\exp(-\kappa(R-2a))}{1 + (R-2a)/2a} \right)$$

where ϵ and ϵ_0 are the dielectric constant of the medium and permittivity of vacuum respectively, ζ is the surface potential, and κ is the characteristic inverse Debye-Huckel length. The above formula represents U_r for low ζ and large $\kappa(R-2a)$ values, where $1/\kappa$ is an indicator of the counter-ion cloud thickness given by:

$$4) \quad 1/\kappa = \left[\frac{\epsilon \epsilon_0 RT}{F^2 \sum c_i z_i^2} \right]^{1/2}$$

where R is the gas constant, T is the absolute temperature, F is the Faraday constant, c_i and z_i are the concentration and charge number of the ions in the dispersion.

Steric repulsion results from entropic and enthalpic changes in free energy due to polymer-polymer interactions as particles with adsorbed surfactants approach one another. As was mentioned previously a combined repulsion energy can result from electrosteric interactions which is a combination of the polymer and ion cloud interactions. The shape of the radial electrostatic and electrosteric potentials are illustrated in Figure 1 in which it is apparent that a potential well is possible for the combined case. Also shown is the presence of a secondary minimum in the electrostatic potential curve the depth of which is dictated by equation 1.

The critical point to be considered here is the manipulation of parameters affecting both attractive and repulsive energies to form desired particle packing configurations. Long range ordering in electrosteric and electrostatic interactions may occur by trapping in the secondary minimums at low particle concentrations and low potentials or by strictly repulsive potentials at higher particle concentrations and steric interactions.

2.2.2 Colloidal Crystals

Hachisu³⁶, using colloidal latex suspensions, observed order-disorder phase transitions (Figure 2) which varied

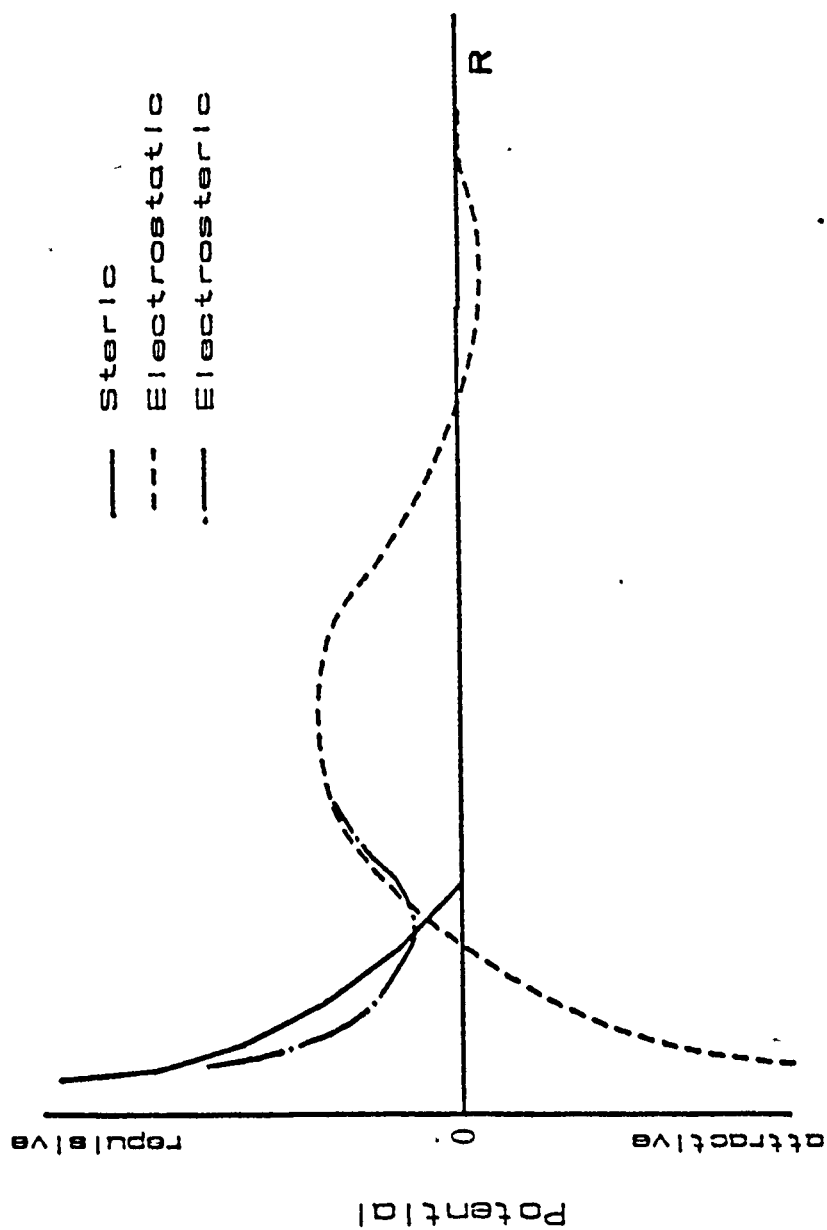


Figure 1. Particle pairwise potentials in electrostatic, steric and electrosteric systems.

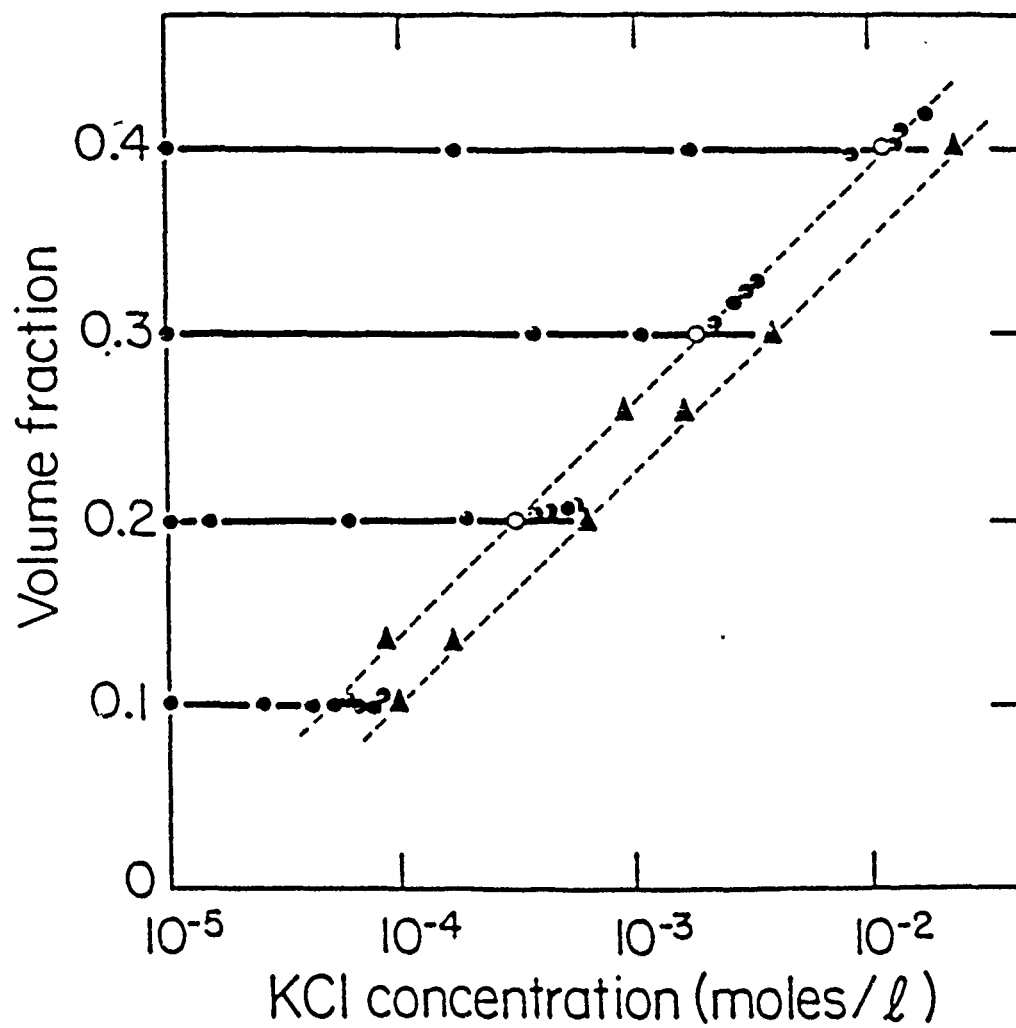


Figure 2. Order disorder phase transitions in latex suspensions³³.

with particle and electrolyte concentration. Models³⁷ and further measurements³⁸ relating the experimental results to variables of pressure and particle concentration predict essentially the same results for formation of colloidal crystals. A critical volume fraction for the transition of ≈ 0.50 was observed; however, pressure at the transition varied with respect to electrolyte concentration. Pressure variations with electrolyte concentration are reconciled by an effective particle diameter:

$$5) \quad a^* = a + \lambda/\kappa$$

where λ is a parameter evaluated from measured lattice parameters along the coexistence boundary and $1/\kappa$ is the Debye-Huckel length. As a^* increases pressure will increase, with fixed particle number density, proportional to $8a^{*3}$.

Pressure effects are also realized in terms of polydispersity³⁹ where it is predicted that structure is disrupted in both the repulsive potential and secondary minimum potential dominated cases. For repulsive potential domination, i.e. high concentrations, pressure changes depend on a^* (effective diameter) which in turn is dictated by the Debye-Huckel length (κ^{-1}). Figure 3 indicates relative pressure changes for a polydispersity factor δ and normalized double layer length κa . In all cases pressure is increasing with polydispersity, but decreasing pressure changes with increasing double layer thickness are predicted due to a transition from hard sphere to soft sphere particle-particle interactions. As κa decreases, the effective particle of size a^* becomes more and more elastic and therefore able to take up strain due to particle misfit. This double layer effect is fortuitous in that a finite

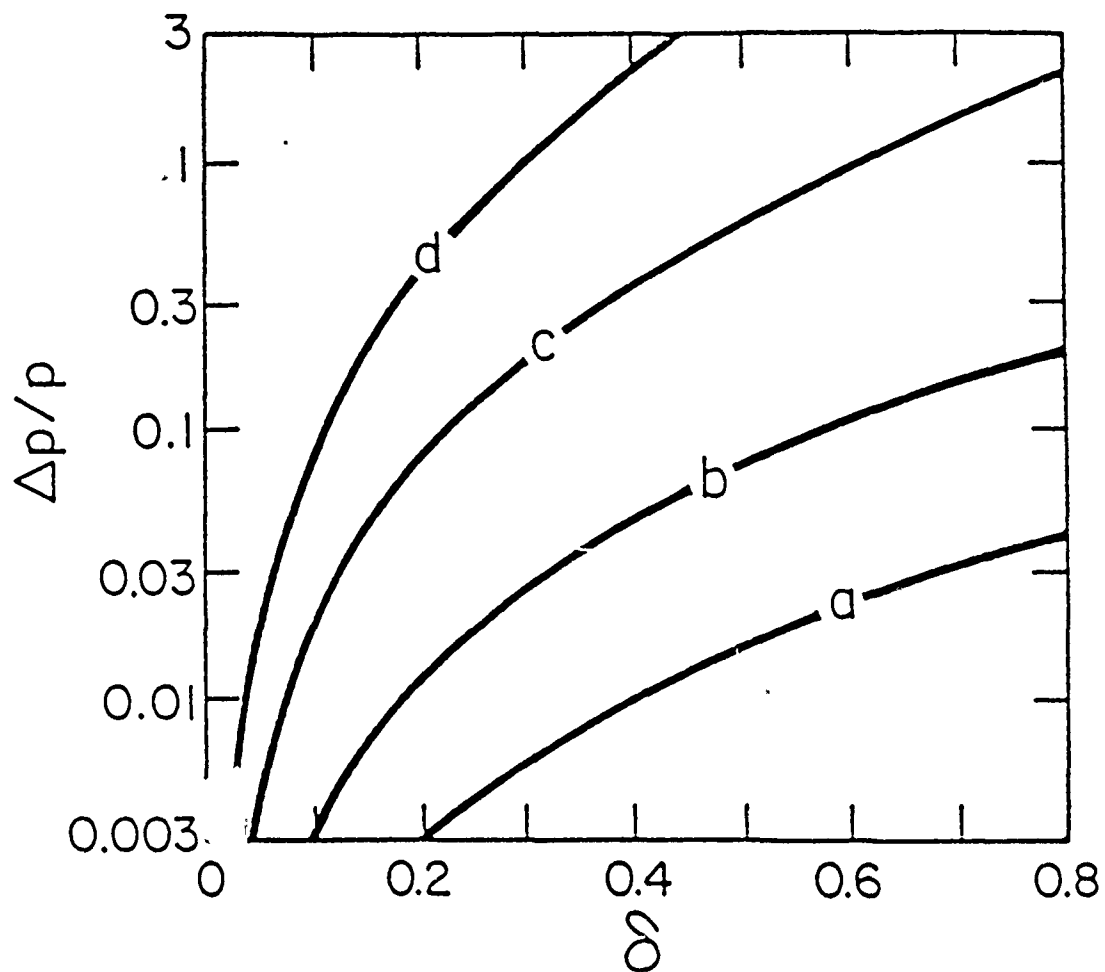


Figure 3. Polydispersity effect on the osmotic pressure of an electrostatically stabilized dispersion for (a) $\kappa a = 5$; (b) $\kappa a = 10$; (c) $\kappa a = 25$; $\kappa a = 50$ ³⁹.

amount of polydispersity is always present in real particle systems. Qualitative work on nucleation and growth in colloid systems has been carried out on the SiO_2 system^{2,40} in terms of particle size and applied centrifugal fields. As the settling rate is increased by centrifugation, the domain size of the colloid polycrystalline array decreases. For constant settling rate the domain size increases with particle size in the submicrometer range. Recently a model has been proposed⁴¹ for sterically stabilized SiO_2 in nonaqueous systems. Predictions based on this model tend to follow the qualitative work and are explained in terms of particle motion due to diffusion and applied fields effects.

The applied field in this case being gravity, or centrifugal acceleration, and the driving force for diffusion being the free energy gradient between the colloidal liquid and colloidal crystalline states. In fact crystallization in colloids is analogous to the same effect in glasses where the mobility control is due to quenching below a temperature where atom rearrangement no longer occurs in a measurable time period. In the case of colloidal crystallization quenching is achieved by increasing the volume fraction of solids to a degree where particle diffusion is retarded. Figure 4 shows the effect of volume fraction solids on crystallization rate in the critical fraction range where colloidal crystallization is known to occur. If the particle system passes through this crystal growth region quickly, via particle mobility in an applied field, the final fraction crystallized is small. The abscissa represents a particle velocity determined by the product of a chemical potential difference and a self-diffusion coefficient. In an ideal case the self diffusion coefficient is dependent upon the volume fraction of solids. Effective parameters for the formation of colloidal crystals

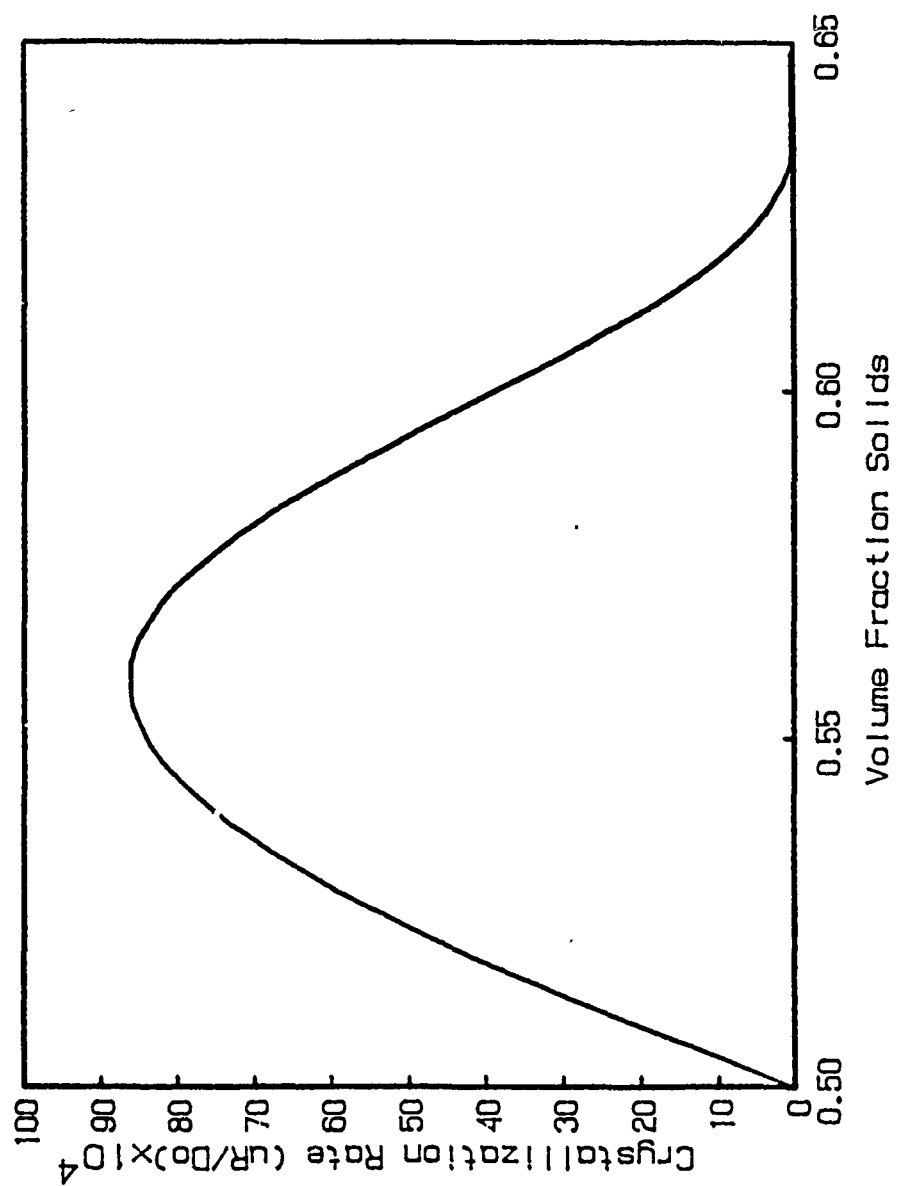


Figure 4. Crystallization rate in a particle system as a function of volume fraction solids⁸.

are particle-particle interactions and particle concentration. Fortunately processing of a flocced powder compact follows along the same lines as the well packed arrays.

2.2.3 Flocced Particle Systems

Similar to the colloidal crystal formation particle separation is controlled via repulsive and attractive potentials. In a colloidal suspension the particles exhibit Brownian motion resulting in particle particle collisions. By reducing the repulsive potential the particle system is dominated by attractive forces causing extremely close range particle contacts and a high rate of flocculation. Due to the high rate of particle contacts resulting in successful trapping in primary minima particle agglomerates are formed²³. Rearrangement of the particles within the agglomerates is difficult and the loosely packed particle agglomerates now become the packing units for powder compact formation⁴².

Once the particle agglomerates are formed they exhibit increased size, with subsequent reduced self diffusion, and increased gravitational forces. These affects yield a poorly packed structure with a large variance in pore size and agglomerate size distributions.

The two extremes of particle packing are producible from the same monosized particles by the manipulation of pairwise potentials and particle concentrations. Using the particle compacts produced in both the flocced and ordered states as starting points the role of both particles and pores on subsequent microstructures during sintering and grain growth can be observed.

2.3 Microstructure Evolution

The stages of microstructure evolution during sintering are described by pore and particle behavior. In fact powder compacts can be considered two phase systems during densification, one phase being pores and the other particles. Sintering and growth processes occurring in the two phase body will show a continuous change in dominance as the relative amount of porosity decreases. Similar to other two phase systems the spatial distribution and solubility of one phase in another may have profound effects on the microstructure. As the porosity approaches a critical concentration a single phase system is approached in which grain boundary movement is the dominant process in microstructure changes. Several models and controlling mechanisms have been proposed over the last forty years to explain the grain growth observed in dense polycrystalline materials. The main aspects to be addressed are pore affects as well as particle and grain size distribution evolution.

2.3.1 Particle Coalescence, Grain Growth, and Pore Behavior During Sintering

Coble¹³ designated sintering as the pore shape change, pore shrinkage, and grain growth in particle compacts during heat treatment. The structure evolution was broken down into three stages. Neck growth between particles represents the first stage followed by an intermediate stage of equilibrium dihedral angles between solid and vapor with interconnected porosity. The final stage of sintering starts with the advent of closed porosity and can occur in two scenarios, that of abnormal grain growth due to uneven distribution of grain junction porosity or normal growth by pinning of all grain junctions by pores. Abnormal grain growth is indicated by intragrainular porosity in the final microstructure. Sintering was treated as a vacancy diffusion mechanism with

the pores as the source and grain boundaries as the sinks. Models based on an idealized grain shape of the tetrakaidecahedron using both bulk and grain boundary diffusion were derived for closed and interconnected porosity. All models in the study indicated an inverse third power relation of densification to grain growth.

Subsequent experimental data on grain growth during sintering supported the model's $t^{-1/3}$ proportionality to grain size. The bulk diffusion model best fit the observed results with a log time dependence and a variation in densification rates with temperature which was dependant on the diffusion coefficient. Also apparent from this study was the grain size and distribution dependence on initial porosity. The suggestion was made that grain growth was dependant upon porosity.

Kingery and Francios¹¹ derived a theoretical relationship for pore growth and shrinkage with the variables of equilibrium dihedral angle and pore coordination number. Assuming a tetrakaidodecahedron grain shape they related the number of grains surrounding a pore with the pore:grain size ratio and extended this to pore shrinkage and growth fields. They predicted, as shown in Figure 5, that pore stability could occur over the pore:grain size ratio ranges of 0 to 1.5 for equilibrium dihedral angles of 80° to 160° . On either side of the equilibrium pore growth and shrinkage regimes are predicted. In addition to the grain growth in Coble's¹³ experiments the observation of a constant pore-grain configuration was noted which was used to related grain boundary motion to pore motion and coalescence. This work emphasizes the importance

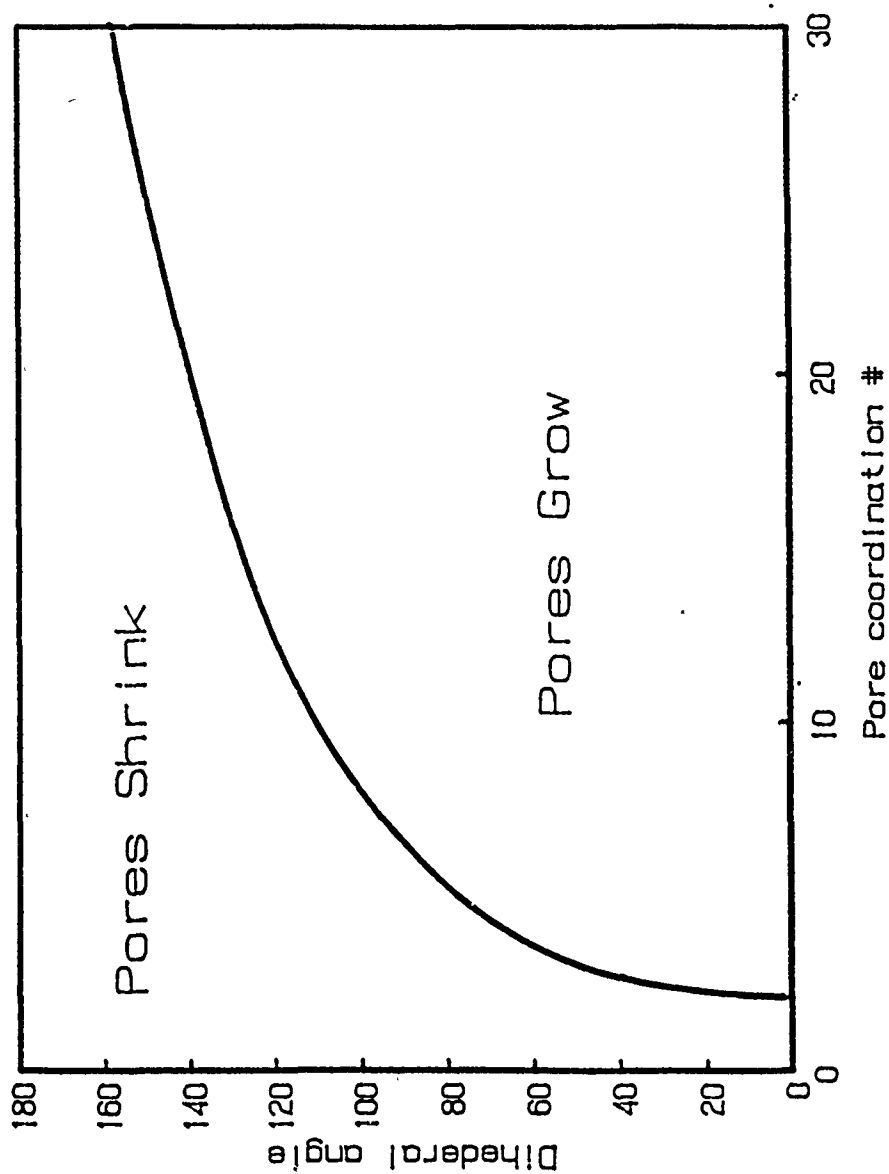


Figure 5. Pore growth and shrinkage regimes for equilibrium dihedral angle and coordination number α_1 .

of the size, coordination number, and dihedral angle of a pore in a developing microstructure.

Exner et al⁴³ observed pore growth and shrinkage in a planar arrangement of copper spheres. Exner's conclusion was that the initial packing of the uniform spheres will dictate the evolution of pores during sintering. Smaller trivalent pores in regions of regular arrangement were observed to disappear, whereas the larger pores grew by particle rearrangement stemming from inhomogeneous stress distributions in the shrinking body. The specific perimeter (=perimeter/area) of the larger pores formed upon particle rearrangement were observed to decrease with time while that of smaller pores increased which indicated smaller pores shrink while pores of a certain size grow. Pore particle arrangements were shown to approach an equilibrium angle :

$$6) \quad \alpha = 180 - 360/n$$

where n is the coordination number of the pore. This formula is the one used by Kingery¹¹ in the derivation of the pore growth-shrinkage regimes. These observations illustrate that the initial packing of a monosized spherical powder system are of prime importance in the time-temperature evolution of microstructure.

Lange⁹ extended early work in the experimental observation of agglomerated Al_2O_3 powder systems during sintering. The growth of pores with $R > R_c$ was observed during the initial stages of sintering while pores with $R < R_c$ shrank. R_c is a critical coordination number which defines the inflection point between convex and concave pore surfaces for a given dihedral angle. As the compact densified all pores were observed to decrease in size and R (coordination number), but it was noted that this was not a

smooth transition. Large pores were observed first to grow in size and R due to particle rearrangement and local densification of agglomerates, then to decrease in size and R (coordination number). The decrease in R was attributed to support of grain growth in relatively dense regions of the compact.

Sintering studies of TiO_2 powders synthesized from metallorganics yielded results showing three distinct regimes of sintering which are discerned by changes in rates of linear shrinkage⁴⁴. Particle coarsening was shown to be independent of temperature, but strongly dependant on density as depicted in Figure 6. This behavior illustrates the effect of a second phase inclusion, i.e. pores, on the grain growth behavior during densification. It should be noted that this behavior is dependant on the initial packing of the compact⁴⁵. The conclusion of this study was that grain growth and especially abnormal grain growth was suppressed and particle rearrangement was eliminated by the use of a well packed, monosized, spherical particle system.

Yan's⁴ models for coarsening during densification of electronic ceramics were based on three rate limiting processes for particle growth and two rate limiting processes for densification. Large variations in the coarsening for similar densities were predicted for most cases, but only in the evaporation/condensation and surface diffusion cases were the initial pore and particle sizes important.

Kimura et al⁴⁶ followed the sintering and microstructure evolution in Al_2O_3 powders of different agglomerate size, a well dispersed and a highly flocculated state. Their results indicate that sintering is hindered in the flocculated state, but the sequence of microstructure development was independent of the initial packing state of

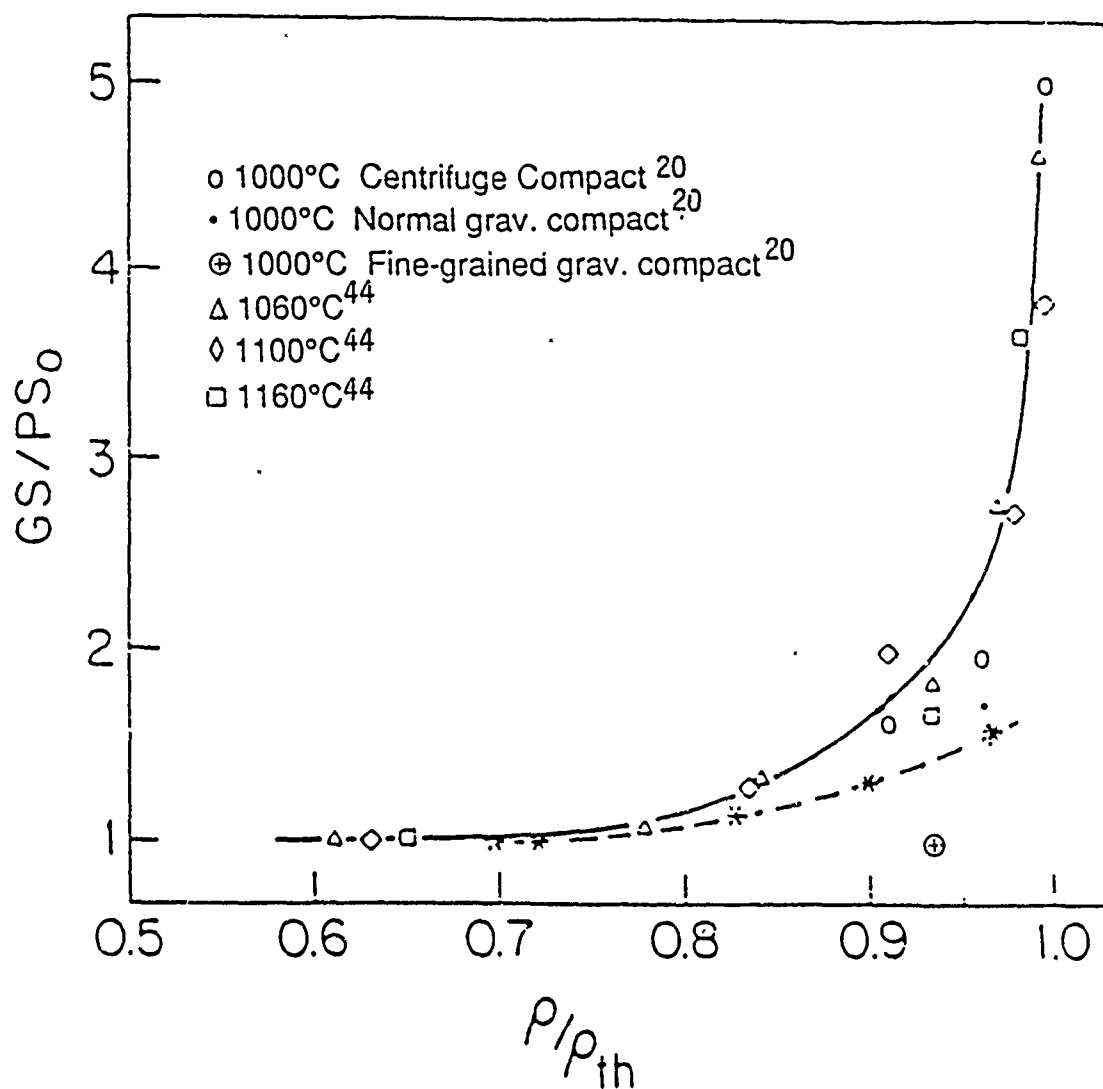


Figure 6. Particle coarsening as a function of density where Δ , \diamond , and \square represent the same compact at different temperatures; \circ , \bullet , \oplus represent decreasing pore hierarchy; \oplus and $*$ represent ordered structures similar to this study

the particle system. That is, a specific microstructure was obtained at a lower temperature and time for the well dispersed initial particle state, while the same microstructure evolved at a longer time or higher temperature for the flocculated initial state. As observed by previous investigators an increase in grain growth occurred as the compact reached 90% of theoretical density in both the flocced and disperse cases and the standard deviation of the grain size distribution increased with average grain size.

After sintering the densification and particle growth gives way to grain growth via grain boundary motion. In this regime the system is single phase and the parameter usually associated with the boundary motion is boundary curvature related to surface tension and grain coordination number.

2.3.2 Grain Growth in Dense Compacts

Various models in conjunction with experimental studies have been applied to metal and ceramic systems. Initial investigations followed grain shape or size related growth and more recently relationships between grain size and shape have been used. Computer simulations based on random jumps on grid systems are the most recent additions to grain growth studies. One prominent aspect of all models is a time independent grain size distribution which is also observed experimentally. In the following review the two dimensional analogs of grain growth will predominate, but the transfer of the two dimensional results to three dimensions has been extensively covered and will not be elucidated upon.

2.3.2.1 Closed Form Models

In the last stage of sintering pores diffuse out leaving a single phase polycrystalline body. A similar grain

configuration is seen in metal systems after recrystallization and it is in the metal systems after recrystallization of cold worked specimens. Most studies on grain growth have been carried out using this system. In either system, ceramic or metal, the causality of grain growth will be the same; the driving force for grain growth in a polycrystalline arrangement is the minimization of grain surface area.

Harker and Parker¹⁵ attributed the ability of a grain to grow as shape and not size dependant, where the triple point angle was given as the measure of stability. The stable configuration of grains in a space filling polycrystalline material was given with the stipulation that only three grains meet at an edge and four grains at a corner. Figure 7 is a representation of a grain separated from the matrix and illustrates faces, edges, and corners. This requirement dictated one of two equilibrium grain configuration, one a rhombic dodecahedron the other derived from the first splitting and rotation of the former. The correlation found between grain growth and triple point angle in fact turned out to be a proof of the surface tension affect, given as the initial stipulations, for an equilibrium grain structure.

Smith⁴⁷ introduced the relationship between grain shape and surface tension and space filling requirements of a dense, single phase, polycrystalline body. Euler's law in two dimensions

$$7) \quad P - E + C = 2$$

is used to describe space filling requirements of polygons where P, E, and C are the number of polygons, edges, and corners respectively. In this special case the area outside

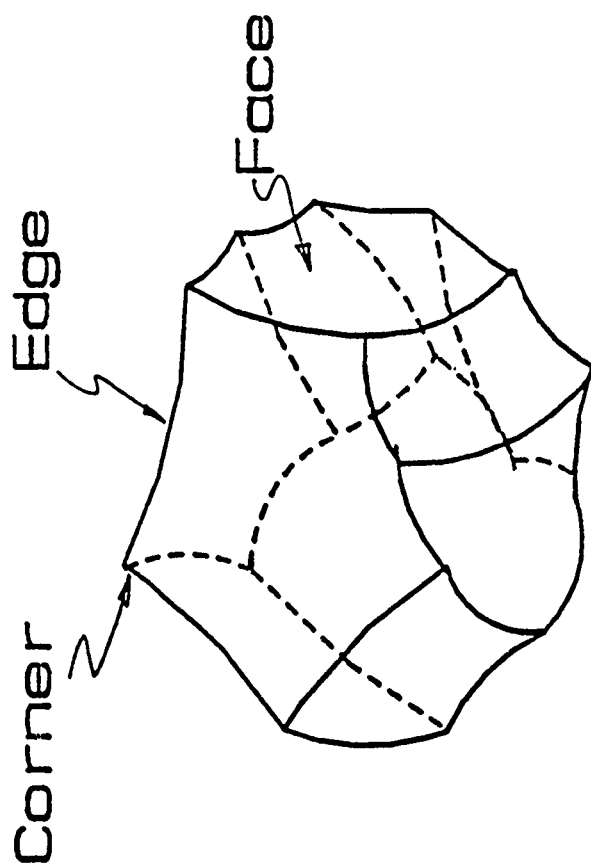


Figure 7. Representation of grain faces, edges, and corners.

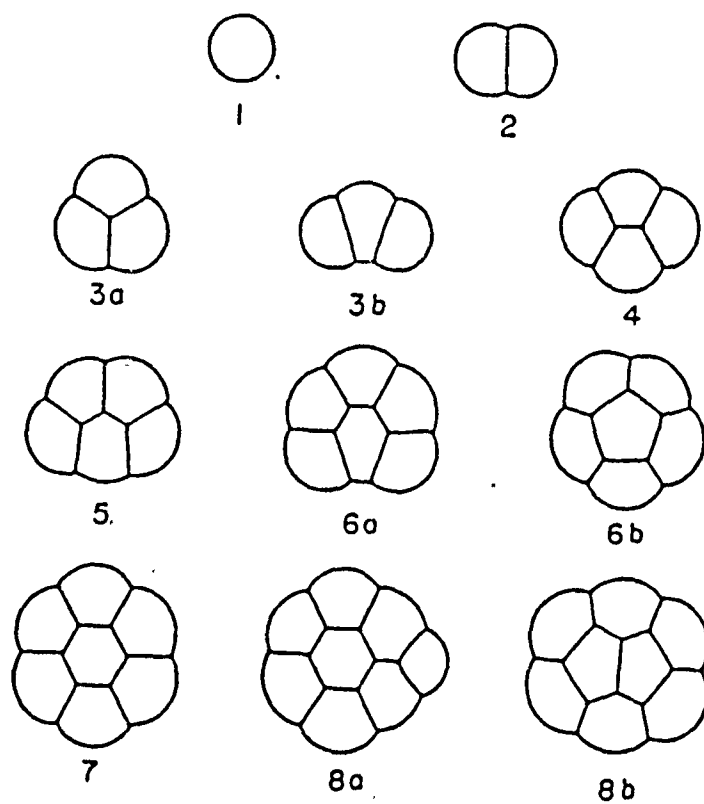


Figure 8. Soap bubble froths showing Euler's relationship.

the array of polygons is considered as one polygon. An illustration of Euler's relationship is given in Figure 8 for aggregates of bubbles. A simplification results when the requirement that every edge joins two corners and every corner has three edges; therefore, a form of Euler's law is:

$$8) \quad E = \Sigma(nP_n)/2$$

for an infinite array where P_n is the number of grains of n sides. Considering the boundary as one grain leads to a closed system equation of

$$9) \quad E = \Sigma(nP_n)/2 + E_b/2$$

where E_b is the number of edges at the boundary. This relationship when substituted into equation 8 yields

$$10) \quad \Sigma(6-n)P_n - E_b = 6.$$

This extends the ideas for the basis of grain growth to include both topological and physical aspects of a polycrystalline array.

The curvature of a grain boundary will result from the topological and physical constraints. That is for polygons with number of sides less than 6 a positive curvature is imposed to obtain the equilibrium 120° angle at the grain corner (in two dimensions). Similarly for more than 6 sides a negative curvature is required for surface tension equilibrium. The pressure difference leading to diffusion of atoms across a grain boundary is inversely proportional to the radius of curvature, and proportional to the surface energy.

Since the earlier work of Harker and Parker did not consider topological constraints the equilibrium grain,

Rhombic Dodecahedron, fit the physical-space filling criteria. Introducing topological constraints in addition to physical constraints requires an equilibrium grain in the form of a Tetrakaidecahedron. In this ideal configuration grain boundary curvature still exists but is minimized and the grain conforms to the basic requirements of space filling, surface tension, and topology.

Beck⁴⁸ reported the time invariant standard deviation of the grain size and shape distributions for the isothermal grain growth of aluminum. Feltham⁴⁹ showed that Beck's data followed a lognormal distribution and used this finding and the time invariance of the standard distribution in his model of grain growth. A third postulate introduced was the linear relationship between grain size and shape which was experimentally shown to be true for tin⁴⁹ and has been known to exist as Lewis's Law in natural systems obeying space filling and surface tension requirements⁵⁰.

The change in diameter of a grain was related to the curvature of the boundary⁴⁹ by atom movement from one grain to another:

$$11) \quad dD_i/dt = (K\gamma/\rho) \exp(-H/kT)$$

where K is a system constant, γ is the specific grain boundary energy, H is the activation energy for grain boundary self diffusion, and ρ is the radius of curvature. Considering an equiaxed polygon and assuming some critical grain side number n^* such that grains with greater n will grow and grains with n less than n^* will shrink a function of the ratios of n is:

$$12) \quad f(n/n^*) = r_i/\rho_i = \sin [\pi/6(1-n^*/n)]/\sin [\pi/6(n^*/n)]$$

where r_i is the radius of the equiaxed grain and ρ_i is the radius of curvature. Equation 12 should be recognized as the same function used by Kingery and Francios¹¹ in the derivation of pore growth and shrinkage regimes. The product of 12, a rate or shape factor, and 11, a rate, supplies the first approximation of growth for grains of radius r_i ($=D_i/2$).

$$13) \quad dD_i^2/dt = Kf(n^*/n)$$

The value n^* is taken as the most probable number of sides in a distribution which in an ideal planar array conforming to physical, topological, and space filling requirements is six. Using the linear relation between most probable grain size and n , the number of sides, as well as the assumption of a log normal distribution equation 13 can be rewritten as

$$14) \quad dD_i^2/dt = K \ln(D_i/D^*).$$

For time invariance of the distribution and standard deviation the ratio D_{\max}/D^* is a constant which for Feltham was 2.5. Integration of equation 14 and substitution of the time invariant D_{\max}/D^* leads to

$$15) \quad (D^*)^2 - (D_0^*)^2 = K\lambda t \exp(-H/kT)$$

where K is the constant from 13, λ is a variable of the initial distribution at time $t=0$, D_0^* is the most probable grain size at time $t=0$, and D^* is the immediate most probable grain size.

Hillert⁵¹ started with the assumption that grain boundary velocity was proportional to the size of the grain:

$$16) \quad dR/dt = \alpha M \gamma (1/R^* - 1/R)$$

where M is the grain boundary mobility, α is a dimensionless constant, γ is the grain boundary energy, and R^* is a critical radius defining the boundary between positive and negative growth. Using the relationship

$$17) \quad n = 6 + 6\alpha(R/R^* - 1)$$

where n is the number of nearest neighbors, and determining the average value of n for an array :

$$18) \quad \bar{n} = 1/N \sum n = 6 + 6\alpha(R/R^* - 1).$$

Recall that $\bar{n} \approx 6$; therefore it can be seen that $R = R^*$. The constant α was determined as 0.5 by fixing a boundary condition that $R=0$ for $n=3$, for two dimensions. When grain growth approaches a steady state, the growth of R^* was given as:

$$19) \quad d(R^*)^2/dt = KM\gamma$$

and the limiting value of R_{\max}/R^* was given as 2. A result of this treatment is that abnormal grain growth may occur in systems to reduce the standard deviation of distributions which lie outside the limiting value of R_{\max}/R^* . The distribution of individual grain sizes was given as

$$20) \quad P(u) = 2(e)^{\beta} \beta u / (2 - u)^{\beta+2} \exp[-2\beta/(2 - u)]$$

where $u = R/R^*$, β is given as 2 for two dimensions and 3 for three dimensions. It should be noted that a distribution is

preordained by assuming the limiting value $u=2$ and that this value is less than that given by Feltham as $u=2.5$.

A model for grain growth in aluminum which is completely devoid of a Euclidean base was introduced by Rhines et al⁵². Using topological factors or grain shape, it was found that grain volume increased in direct proportion with time and that the ratio corners:faces:edges was constant. A "topological-Euclidean" expression is introduced in the measurement $1/N_V$, or average grain volume, but is reconciled in that volume is independent of all other parameters both Euclidean and topological. The approach of grain shape to an equilibrium configuration of a tetrakaidecahedron⁴⁷ is said to be a local response of the system to surface tension forces, that is forming coordinations of three for edges and four for corner of grains. Long range response is the term given to grain growth in the absence of further significant shape change.

The driving force for grain growth, as has been mentioned previously, is differential pressures across surfaces caused by curvatures. Curvatures of faces and edges will always occur for the equilibrium grain shape, or more concisely for grains approaching this shape. Positive and negative curvatures of grain faces have been shown to exist as a direct function of grain shape (see equation 12), hence defining positive and negative growth. A "structural gradient" was introduced which related total grain curvature M_V , grain surface area S_V , and number of grains/unit volume N_V :

$$21) \quad \sigma = M_V \cdot S_V / N_V$$

where it has been shown that both M_V and S_V decrease with grain growth. For the near equilibrium tetrakaidecahedron σ

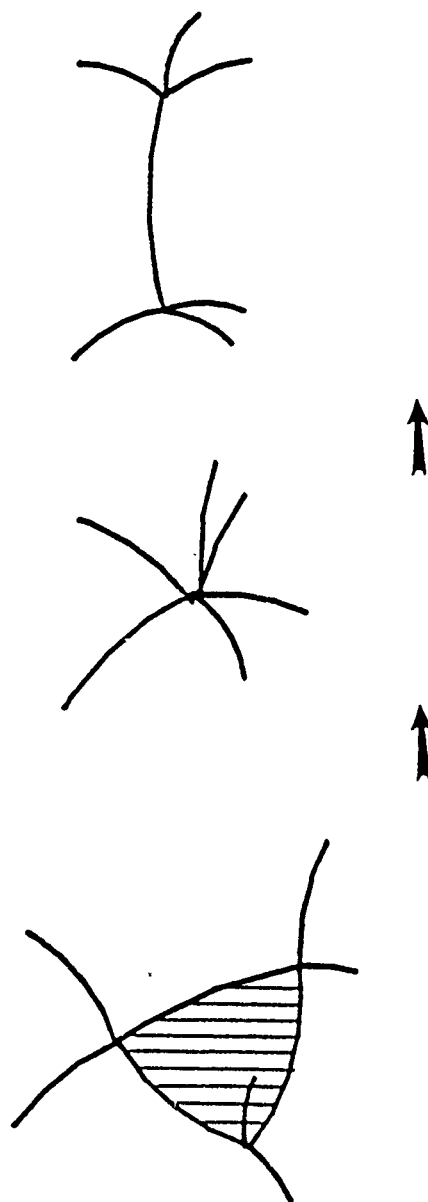


Figure 9. Loss of a triangular face in three dimensional space.

would approach zero, i.e. $M_v \rightarrow 0$, but in the experimental portion of the study σ was found to be 1.33.

Grain growth was assumed to be the stepwise losses of triangular faces, illustrated in Figure 9, in the system causing changes in nearest neighbors and since the distribution was observed to be time invariant the net loss of grains must coincide with the constant ratios observed, i.e. 6:7:12 for the features corners:faces:edges. The loss of common triangular faces was shown to also regenerate triangular faces, thus the number of triangular faces is independent of time. A grain boundary movement rate can be determined and the number of grains lost per unit volume after each sweep of the boundary through the volume determined. The number of grains lost per unit volume is a constant ϕ .

Volume transfer on the loss of one average grain is related to the grain boundary velocity and ϕ :

$$22) \quad \phi \mu \gamma M_v S_v / N_v$$

where μ and γ are the mobility and surface tension respectively. Considering that the volume lost on disappearance of one grain is transferred equally to all others the volume increase in average grain size is

$$23) \quad \phi \gamma \mu M_v S_v / N_v^2$$

and the volume increase per unit time is

$$24) \quad \phi \gamma \mu \sigma t / N_v$$

where σ is the structural gradient defined in equation 21. Therefore, a grain growth law for volume increase in the average grain is given as

$$25) \quad 1/(N_v)_t - 1/(N_v)_0 = Kt$$

where N_{v0} is the initial number of grains per unit volume, K is a constant, and t is time.

Kurtz and Carpay¹⁶ used constraints of topology, spacefilling, surface tension, and scaling used by previous investigators^{47,49,52}. By introducing the breakdown of grains into topological classes, each with a lognormal distribution similar to that of the overall grain shape and size distributions, a more rigorous analysis of grain growth is obtained. They found that growth is controlled by rate of loss of grains from the lowest topological class ($n=3$ for planar and $f=4$ for spatial) and that to maintain the time independent distribution the growth rate for each class is different and is also time independent. Relationships between the size and shape parameters is given:

$$26) \quad D_{n,med}/D_{med} = (n/n_{med})^b$$

where $D_{n,med}$ and D_{med} are the median grain sizes in the topological class n and the overall distribution respectively and b is a dimensionless exponent ($= 1$ for planar cases). The derivative result of equation 26 is

$$27) \quad dD_{n,med}/dt = (n/n_{med})^b dD_{med}/dt.$$

Therefore, once a knowledge of median grain growth, dD_{med}/dt , is known class grain growth is determined. An

equation essentially the same as those obtained by previous investigators is given

$$28) \quad D_{med,t_1}^2 - D_{med,t_0}^2 = G_{med}(t_1 - t_0)$$

where G_{med} is a growth constant of the system.

Experimental evidence of the assumptions and results of the theoretical work of Kurtz and Carpay was obtained by observations in the Ni-Zn Ferrites. The proposed lognormality of both size and topology parameters, as well as their relationship, were shown to fit observed data quite well.

Louat⁵³ proposed the random motion of grain boundaries in grain growth where the change in grain size results from fluxes from neighboring grains. The assumption of a common rate constant, irrespective of size, and fluxes which are proportional to the populations from which they arise leads to an equation which is analogous to the diffusion equation:

$$29) \quad \delta f / \delta t = (B \delta x^2) \delta^2 f / \delta x^2$$

where $B \delta x^2$ relates to the grain boundary mobility and f is the distribution of grain sizes of linear measurement x . Using a boundary condition of $f(0) = 0$ the required solution is:

$$30) \quad f(x,t) = Cx(At^{1.5})^{-1} \exp(-x^2/4At)$$

where C is a constant representing $f(x,0)$ and A is a rate factor independent of both t and x . The resultant grain growth equation for linear intercepts is given as

$$31) \quad N(t) = Ct^{-0.5}$$

where N is the number of intercepts.

In all the models reviewed similar grain growth laws were obtained, this is not surprising since most were based on the time invariant grain size distribution and a shape or size factor. Even Laout's⁵³ results are dependant upon the relative fluxes relating to the relative frequency of a grain in a distribution. The question of grain boundary motion due to the driving force represented by pressure differentials across a curved boundary have been eliminated in computer simulations of grain growth. Resultant grain size distributions and growth equations are similar to those already covered.

2.3.2.2 Computer Simulations

Computer simulations of grain growth have been carried out based on relative free energy changes in a polycrystalline array due to random element motion and topological unit operations. The similarity in both cases resides in assignment of relative energies to metric or topological characteristics. Alterations are allowed to the configuration followed by recalculation of the energy change to determine the thermodynamic probability of the alteration.

Fortes and Ferro⁵⁴ set out 2 dimensional structures based on the topological and physical constraints previously mentioned⁴⁷. They described two basic topological transformations, or unit operations, which could occur and still maintain the system within its configurational constraints. The unit operations are neighbor switching and triangular grain disappearance, which are illustrated in Figure 10 for the three dimensional case. It has been shown

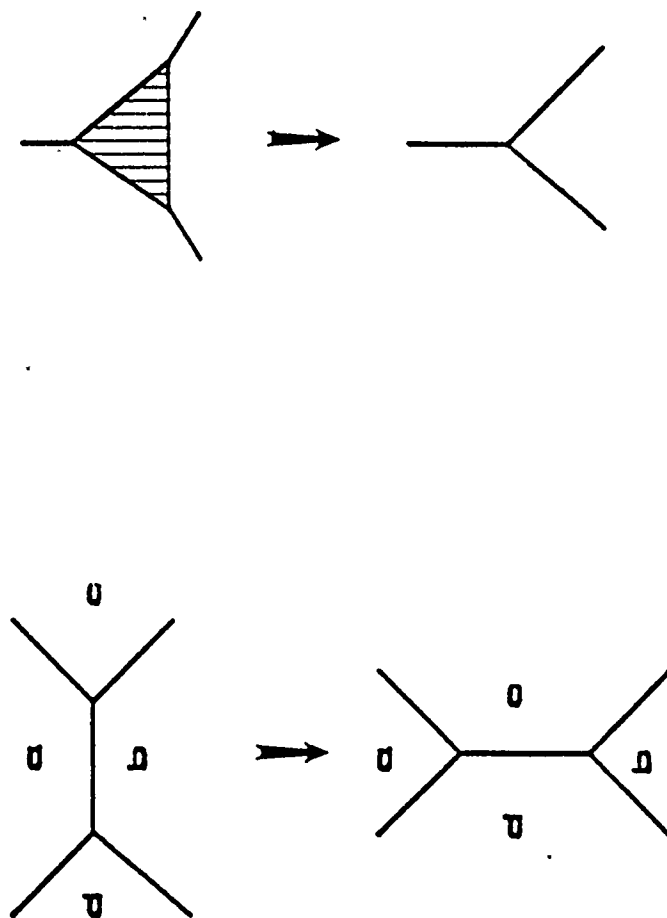


Figure 10. Unit operations of neighbor exchange and disappearance of a triangular face in 2 dimensional grain growth.

that all topological transformations can be represented by the two unit operations.

Thermodynamics of growth were addressed by defining the surface free energy of a structure as:

$$32) \quad A = L\eta + V\nu$$

where L is the length of edges, V is the number of vertices, η and ν are the excess free energies, with respect to the bulk, associated with L and V . Anisotropies in specific free energies are not considered. For any configuration there will be in general a neighboring configuration of a lower energy, but still having the same topology restrictions. The path of configuration change will follow the greatest rate change of A , the free energy, which was shown to coincide with the resultant force vector of trivalent vertices. The driving forces for mobility in two dimensional arrays were reduced to resultant vectors of the vertices by assuming straight grain edges.

Using the basis laid down by Fortes and Ferro⁵², Soares et al⁵⁵ produced a computer simulation of grain growth based on the edge mobility and neglecting the driving force due to curvature. Starting from a random planar network conforming to the topological and physical constraints⁴⁷, stepwise movements of vertices and subsequent unit operations produced a steady state regime of growth after an initial incubation period. The distribution of n , number of edges to a face, was not time independent as reported in experimental work and closed form models, but the average grain area growth was proportional to $t^{1/2}$.

Anderson et al⁵⁶ used a Monte Carlo, or random motion, method to simulate grain growth. Grains were set out on a lattice and each lattice point within the grain was assigned

a number corresponding to the grain orientation "Q". Reduction of the number of nearest neighbors with different orientations is the driving force for grain boundary motion. The transition of a lattice point from one orientation to another is given by a the probability W:

$$33) \quad W = \begin{cases} \exp(-\Delta G/kT) & \Delta G > 0 \\ 1 & \Delta G < 0. \end{cases}$$

where ΔG is the energy change for the orientation range. A resultant boundary velocity is:

$$34) \quad v = C[1 - \exp(-\Delta G/kT)]$$

where C is a grain boundary mobility. It was found that the grain boundary energy was only weakly grain orientation dependant and was treated as isotropic, but microstructure evolution was strongly dependant on the number of orientations when Q was less than thirty six.

Power law growth and a time independent distribution occurred after an initial transient stage. The distribution when normalized to a mean radius was not lognormal, but was skewed to larger ratios and was in relatively good agreement with Louat and Hillert. Lewis's law relating topological and metric quantities was found to occur in this simulation and the distribution of grain edges was normally distributed. In general it was found that large grains did not grow, but some showed steady shrinkage while other fluctuated in size. Grains below a certain size always shrank. Two regimes of power law growth were given:

$$35) \quad (D)^{8/3} - (D_0)^{8/3} = Bt$$

for short times and for long times

36) $D^{8/3} = Bt.$

A conclusion was drawn that the grain growth consisted of both a directed grain velocity, i.e., small grains shrink, and a random walk procedure which was exhibited by larger grains driven.

For all models and experiments covered the main differences are in the processes assumed to occur during grain growth. There is a tendency for the time invariant normalized distribution to change shape from investigator to investigator, but the general consensus is that the curves are very similar. Exponents of time, in the grain diameter-time proportionality, tend to lie between $1/3$ to $1/2$.

The cause of the observed time independent distribution is not covered by any of the grain growth models, but is an intrinsic part in all of them.

3.0 EXPERIMENTAL

Particles were synthesized from solutions of titanium salts with both ethoxy and chloride ligands. The route yielding the most monosized particle in the required size range was used to produce the powders for subsequent investigation. As prepared powders were clarified for size and purified to remove solubilized ions which would affect particle-particle potential fields. Purified monosized particles were packed under various centrifugal fields, dried, calcined, and sintered. Resulting microstructures from the treatments were analyzed for grain size distribution on the surface and interior.

3.1 Particle Synthesis

3.1.1 Ethoxy Ligand

Reactions were carried out using both batches. All reactions were carried out under prepure N_2 . A standard bulk reaction consisted of: preparing separate solutions of the water (0.45 M) and titanium tetraethoxide (0.15 M) in dry, 200 proof, ethanol; filtering both reaction solutions through a 0.22 micron filter; and simultaneously pouring both solutions into a stirred reaction vessel.

Powders synthesized in the presence and absence, designated here after as HPC and H_2O respectively, of an insitu steric stabilizer were compared. Insitu stabilization was by the addition of Hydroxypropylcellulose, MW 60,000, in a concentration of 3.5 mg /cc (based on the total solution volume)²⁷. In all the reactions the surfactant was included in the titanium tetraethoxide-ethanol solutions prior to filtering.

The as produced powders were washed and partially classified by four iterations of the sequence: centrifugation, decantation of the supernatant and redispersion in distilled water at pH 8. Doubly distilled water with an initial pH of 5.6 was treated with 0.1 M KOH to increase the pH to 8, initial ion concentration of the water was not measured. Centrifugation was initially at 1700 g's (g=acceleration due to gravity at the surface of the earth) and the settled cake discarded to remove the larger flocs. In subsequent centrifugations the supernatant was discarded to reduce smaller particles.

3.1.2 Chloride Ligand

TiCl_4 was dissolved in 12 M hydrochloric acid to a concentration of approximately 1 M. Because of the high vapor pressure of TiCl_4 the concentration of the mother solution was calibrated against a prepared standard. The standard was made by dissolving 0.25 g of titanium in molten sodium pyrosulfate producing titanium peroxide, cooling the melt, and dissolving the fused mass in 2 M sulfuric acid to known concentrations. Absorption of light in the 400-420 nm range was plotted as a function of titanium peroxide concentration. A sample of the mother solution was reacted with hydrogen peroxide and the light absorption measured and compared with the standard.

Solutions of 0.106M titanium tetrachloride in 5.76 M HCl were prepared with the addition of H_2SO_4 in the ratio to give $[\text{SO}_4^{2-}]:[\text{Ti}^{4+}] = 1.9$. The solutions were placed in teflon capped bottles kept at 98°C for 17 days (constant pressure and volume). No further treatment of the products was necessary.

3.2 Particle Characterization

Particle size analysis on the as prepared organometallic route suspensions was done by x-ray sedigraph and photon correlation spectroscopy (PCS) in the stabilized suspensions. The usual requirement of approximately 2 v/o suspensions were not enough to reduce x-ray transmission to acceptable levels and a relatively high concentrations of particles were needed. Size analysis on the chloride route was by SEM observation of dried dilute suspensions. The classified suspensions were sized by SEM and optical microscope observations.

Differential Thermal Analysis (DTA) runs were carried out on the as synthesized powders to determine the temperatures for the onset of expected phase changes. Runs were carried out in flowing air at heating rates of 25°C per minute to 1000°C. X-ray diffractometry of the as prepared powders, and at various heat treatments, was used to determine crystallization extent and phases present. Crystallization was by non isothermal heat treatment in air at 780°C for times in excess of 3 hours^{2,39}. Subsequent changes in phases upon isothermal sintering were also monitored. Synthesized powder was mixed at a constant weight fraction with α -Al₂O₃ powder of roughly the same crystallite size to give approximate quantitative data on phases present.

3.3 Particle Packing

The washed ethoxy derived powders were classified using centrifugation to reduce the width of the size distribution and the number of multi particle clusters. Particle suspensions of approximately 5 v/o were prepared from the tetraethoxide derived powders and were adjusted in pH and

ion concentration using 0.1 M KOH and HCl solutions. If it was necessary ion concentrations were adjusted using 0.1 M KCl solutions and ion exchange techniques with H and OH specific resins. Settling of the particles, to determine the degree of dispersity, at an interface was observed using a settling chamber on a metallographic microscope³¹.

Compacts for grain growth studies were fabricated by settling in tilted petri dishes for one week in the case of 1 g samples and centrifugation in centrifuge tubes for the 170 g and 350 g samples. Flocculated specimens were prepared by adjusting the pH to approximately 5 followed by sedimentation at 1 g. The clear supernatant was withdrawn as far as possible without disturbing the surfaces and the remaining moisture removed by evaporation. In all cases the compacts cracked into very small pieces with the cracks running in planes perpendicular to the top of the cake.

No attempt was made at any time to control the carbon dioxide content in the suspension or to monitor the pH change over the period of settlement or drying.

3.4 Compact Characterization and Sintering

Pieces of the powder compacts were indented with a micro hardness indenter using zero load. Arrays of indents were used as gauges for shrinkage measurements and locating marks during subsequent observations. The indented compacts were calcined at 780°C for three hours, carbon coated (≈ 200 Å), and the surface of the crystalline powder compact microstructure observed using a Scanning Electron Microscope (SEM). Carbon coated compacts were decoated at 750°C in an open tube furnace and isothermally sintered, in the same tube furnace, at 1050°C and 1150°C for time intervals from

five minutes to thirty minutes, after the thirty minute sinter nonisothermal heating with a 50°C per minute ramp rate was used. At each time interval the samples were recoated and observed with the SEM at the same position on each sample followed by a similar decoating and sintering. For times longer than thirty minutes non-isothermal heating cycles were employed with a $50^{\circ}\text{C}/\text{min}$ ramp rate to temperature.

Unindented control samples were also prepared, in a similar manner, using the same techniques as above, to indicate possible transient thermal and carbon coating effects in the 1150°C set of samples. Cross sections of the control samples were prepared to observe and possibly correlate surface and bulk microstructure evolution. Thermal etching of the one micrometer diamond polished cross sections was at 1000°C for one hour preceded by a ramp rate of 50°C per hour and followed by characteristic furnace cooling.

3.4.1 Image Analysis and Microstructure Characterization

High contrast images were produced by tracing micrographs of the emerging microstructure onto transparencies. These images were analyzed by a Cambridge/Imanco unit for equivalent spherical grain and pore diameter distributions as well as relative quantities of each feature. Both grain growth on the surface and in the control sample cross sections were analyzed for size and distribution changes over the periods studied. The number of grains sampled ranged from 400 to 1000 depending on grain size. Total area sampled for pore size distributions was restricted by resolution of the pores.

4.0 RESULTS AND DISCUSSION

4.1 Particle Synthesis

The physical properties of the powders produced using both the ethoxy and chloride ligands has been well covered in investigation concerned particularly with particle synthesis^{27,29,32}. Only the variations between the different routes will be discussed here.

4.1.1 Particle shape and size

In all cases where the ethoxy ligand was used the predominate particle shapes were spherical; size, size distribution, surface texture, and number of agglomerates varied with the different processing methods. Figure 11 is an x-ray sedigraph plot for the bulk reactions with and without surfactants. A mean particle size of 0.5 micrometers is seen for the HPC surfactant particles as well as a shift to an almost lognormal distribution. The particles produced without surfactant show a mean particle size of 0.7 micrometers in a normal distribution. In the case where no surfactant was used time between reaction and washing was found to be critical in the sense that the continued presence of unreacted species caused particle agglomeration. On the other hand stable suspensions were established by surfactant additions and did not require the immediate wash due to the stabilization of all the precipitated species by the surfactant.

Hydrolysis using the chloride ligand yielded spherical particles with a relatively wide distribution when compared to the organic precursor powders. Figure 12 is a representative sample of the powder produced at 17 days at

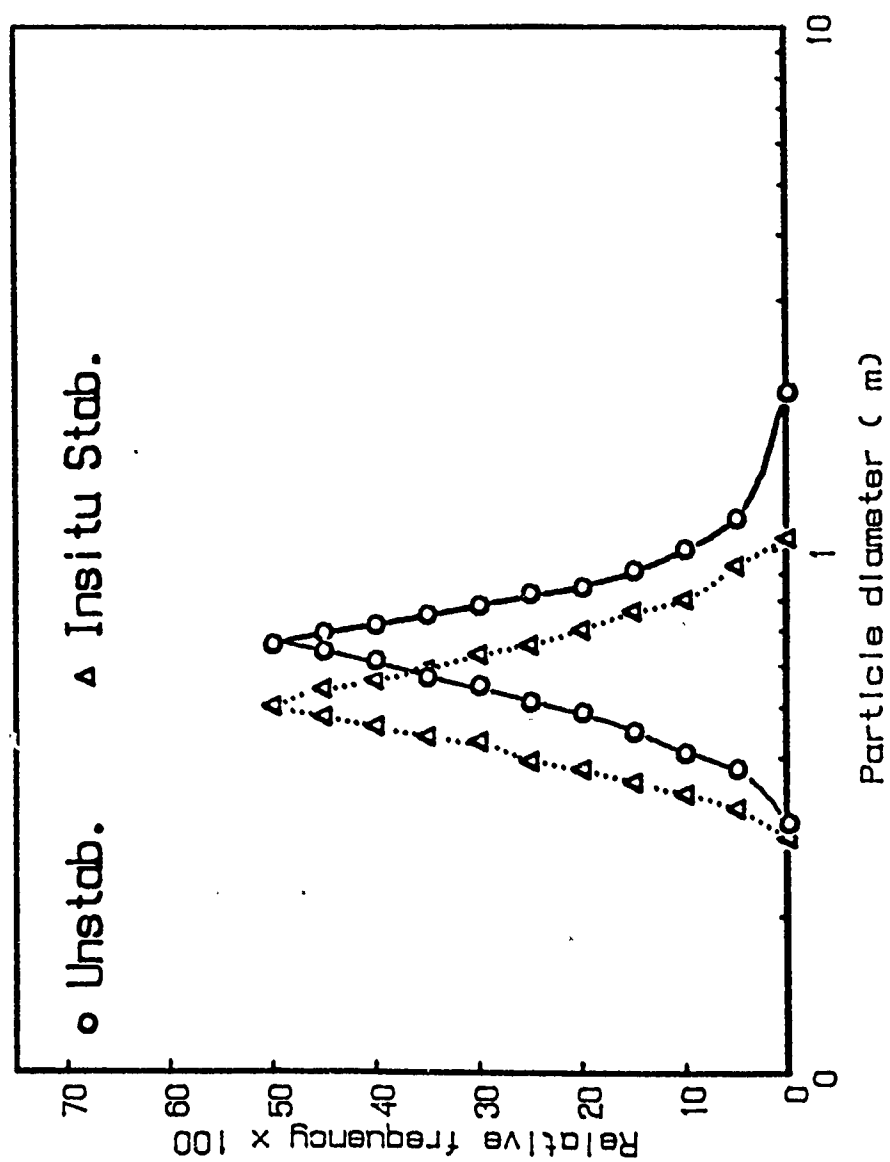
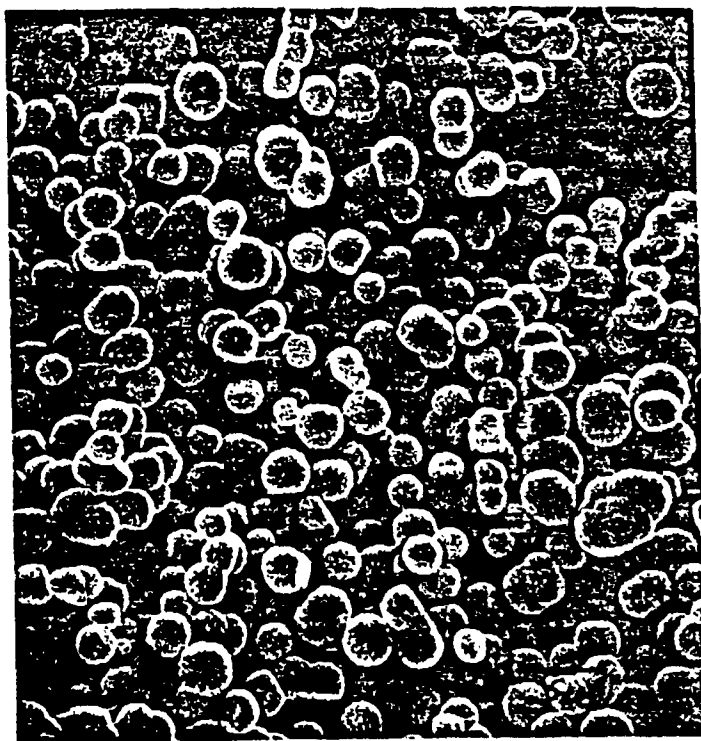
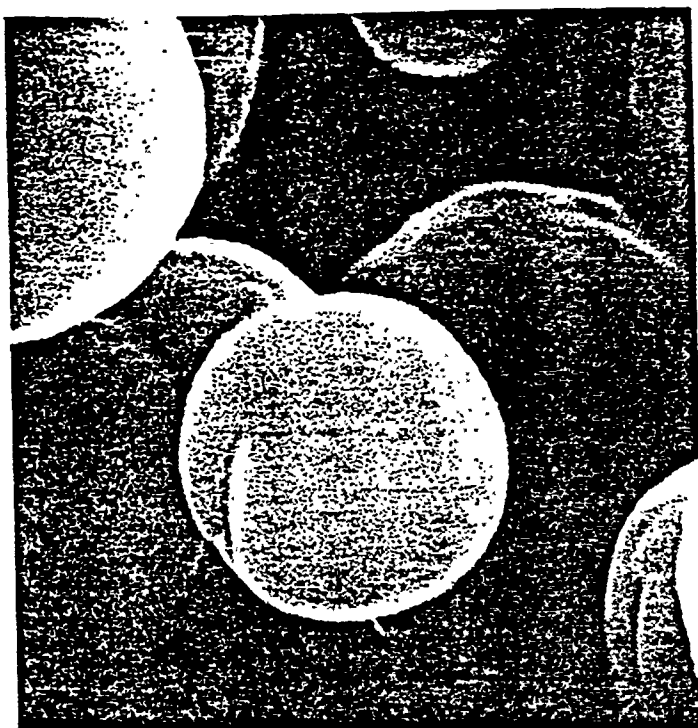


Figure 11. X-ray sedimentation of as prepared insitu stabilized and unstabilized TiO_2 powders.

Figure 12. TiO_2 powder derived from TiCl_4 .



$\approx 98^{\circ}\text{C}$ illustrating the width of the size distribution. Also apparent in this figure are the flat faces, one per particle, which is indicative of heterogeneous nucleation on the reaction vessel wall. In most cases it was noted that liquid removed from the bulk contained little or no particles and that most of the particles adhered to the vessel wall. Reasonable explanations are an inordinate number of nucleation sites on the vessel wall or a disproportionate ratio of reaction vessel surface to volume. The wide size distribution observed could result from either of the above in that a small number of nucleation sites which were not of equal potential would cause simultaneous growth and nucleation. At this stage of the experimental procedure the chloride precursor route was dropped as a possibility due to very low yields (milligrams per liter), large size distributions, and the characteristic single facet spheres.

4.1.2 Densities

The literature sources give the densities of the ethoxy precursor powders as 3.1 gm/cc for the bulk reaction and 2.56 gm/cc for the insitu stabilized powders. This discrepancy would lead one to think that the surfactant becomes an inherent part of the growing particle, as opposed to allowing reactant species to diffuse through a surfactant layer to the core²⁷. Evidence for surfactant inclusion is seen in the continued FTIR (Fourier Transform Infra Red) absorbance peak at 1050 cm^{-1} , illustrated in Figure 13 after repeated washing in distilled water.

Barringer³² reported a particle shrinkage between dried amorphous and crystalline state of 0.34 micrometers diameter to 0.3 micrometers diameter, while Jean and Ring²⁷ reported a size change of 0.35 to 0.23 micrometers in diameter. This

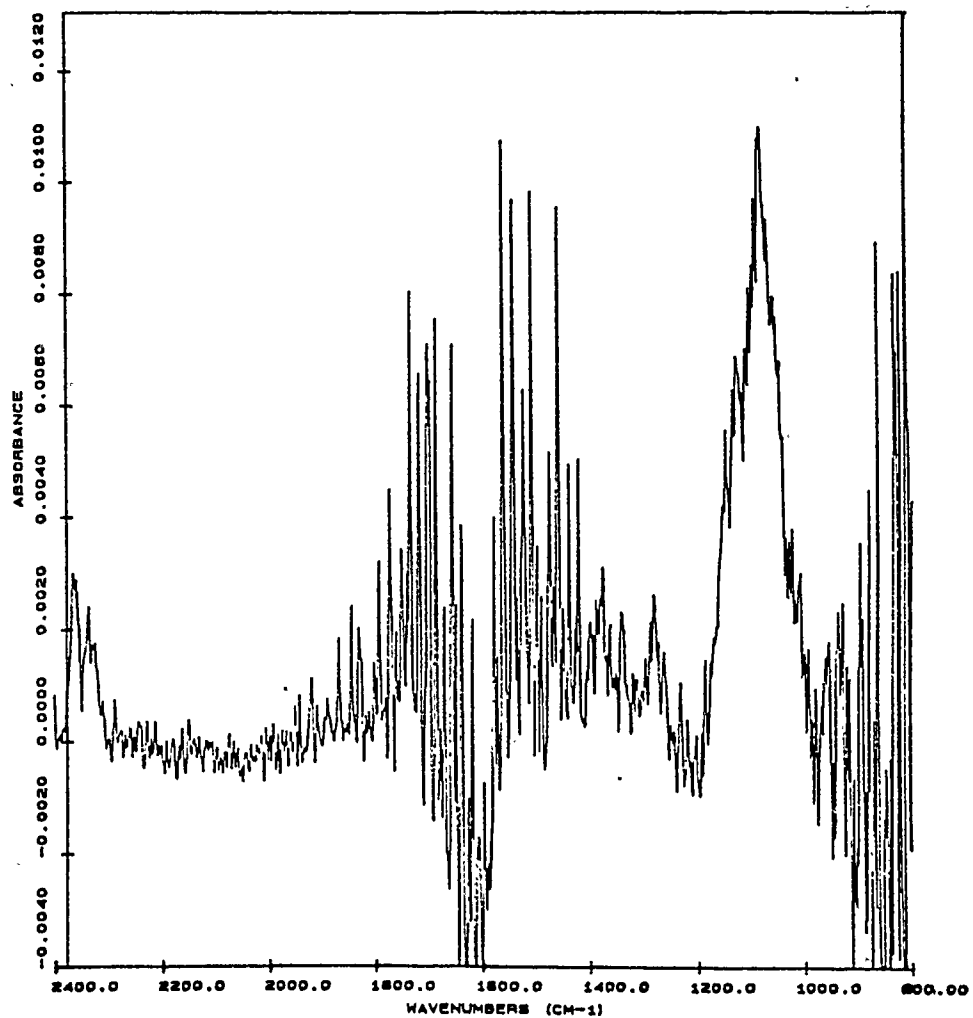
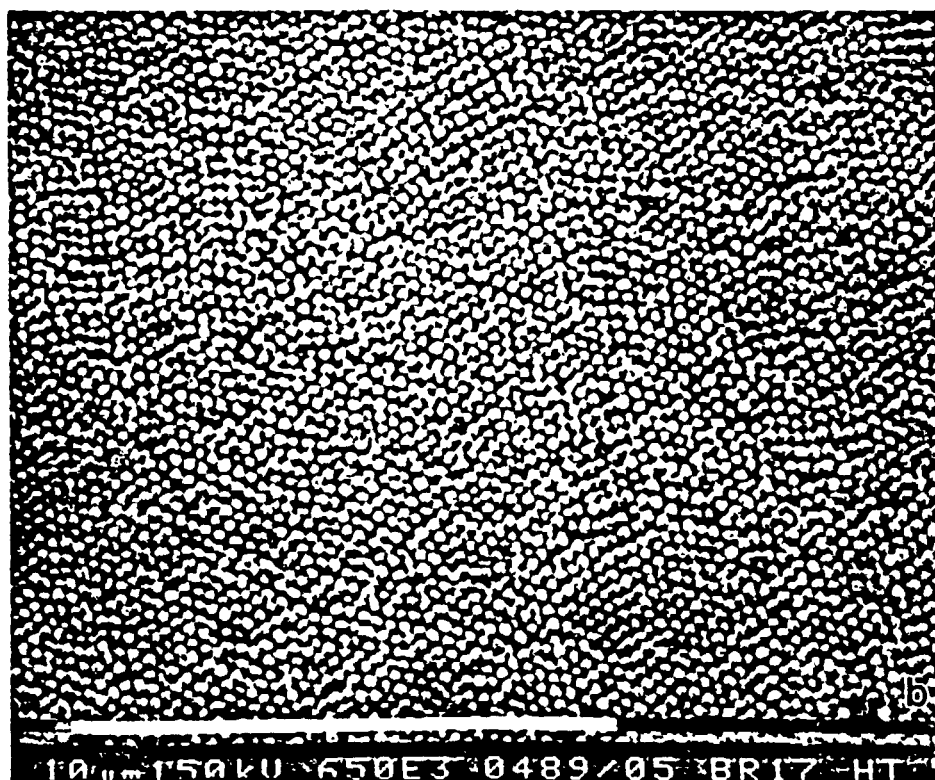
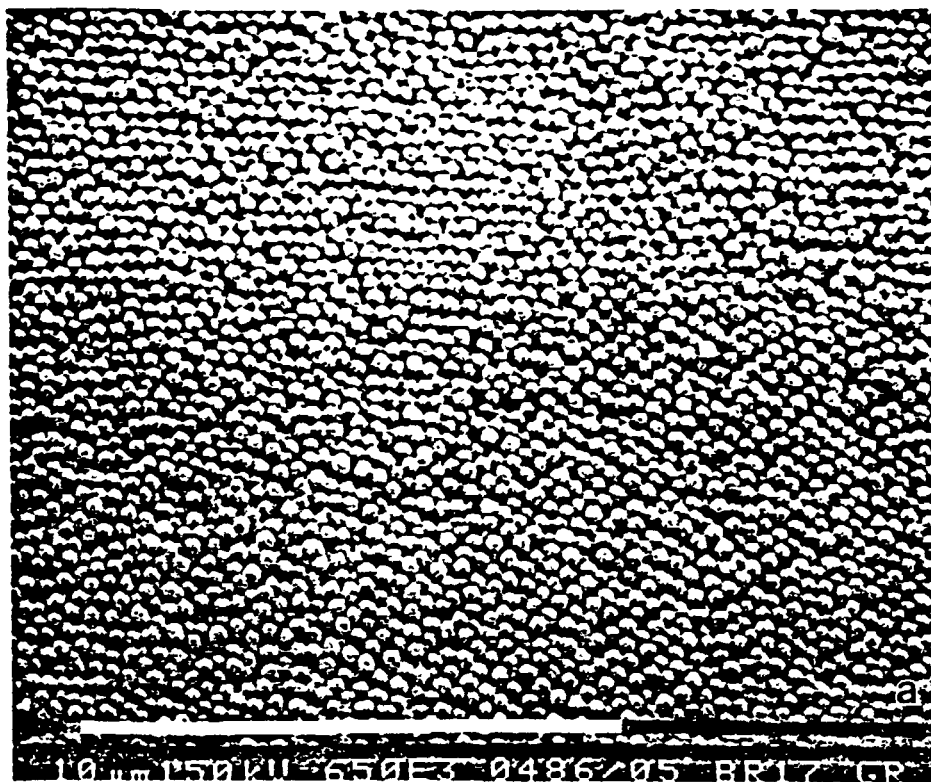


Figure 13. FTIR absorbance peak of HPC surfactant on TiO₂ powders.

Figure 14. Intra and interparticle shrinkage on top ordered surface of 170 g compact during heat treatment at 780°C a) green amorphous compact and b) crystalline powder (bar = 10 μ m).



variation in the particle densities was observed in the calcining of settled powder compacts. Figure 14 illustrates the difference in the dried and crystallized powders produced by the inclusion of an insitu stabilizer. In view of these discrepancies it is highly probable that the two powders are not similar at all in their initial state nor in their thermal behavior.

4.1.3 Calcination

Differential Thermal Analysis runs on the insitu stabilized and unstabilized particles showed no variation in the onset temperatures of crystallization and transformation. Figure 15 is a comparison of the DTA runs of the two powders showing the crystallization temperature of 470°C and anatase to rutile transformation of 700°C . Both powders have essentially the same transformation onset behavior, but a variation in the rate of transformations apparent. The downward slope of the differential scan is due to machine calibration, but it also indicates a change in heat capacity and thermal conductivity of the sample which follows from increasing crystallite size and intra particle sintering. Comparison of the curves in Figure 15 shows a relatively different slope between the HPC stabilized and unstabilized powders.

Sullivan and Cole⁵⁷, in their study of colloidal titania, showed that it is possible to have substantial variance in the unit cell and crystallite size for powders processed using the same precursor, but slightly different routes. X-ray diffraction carried out on the insitu stabilized powders at 780°C for three hours and six hours showed no Anatase phase or change in relative peak intensities between the two times. No change in peak intensities were observed for a sample heat treated at 780°C

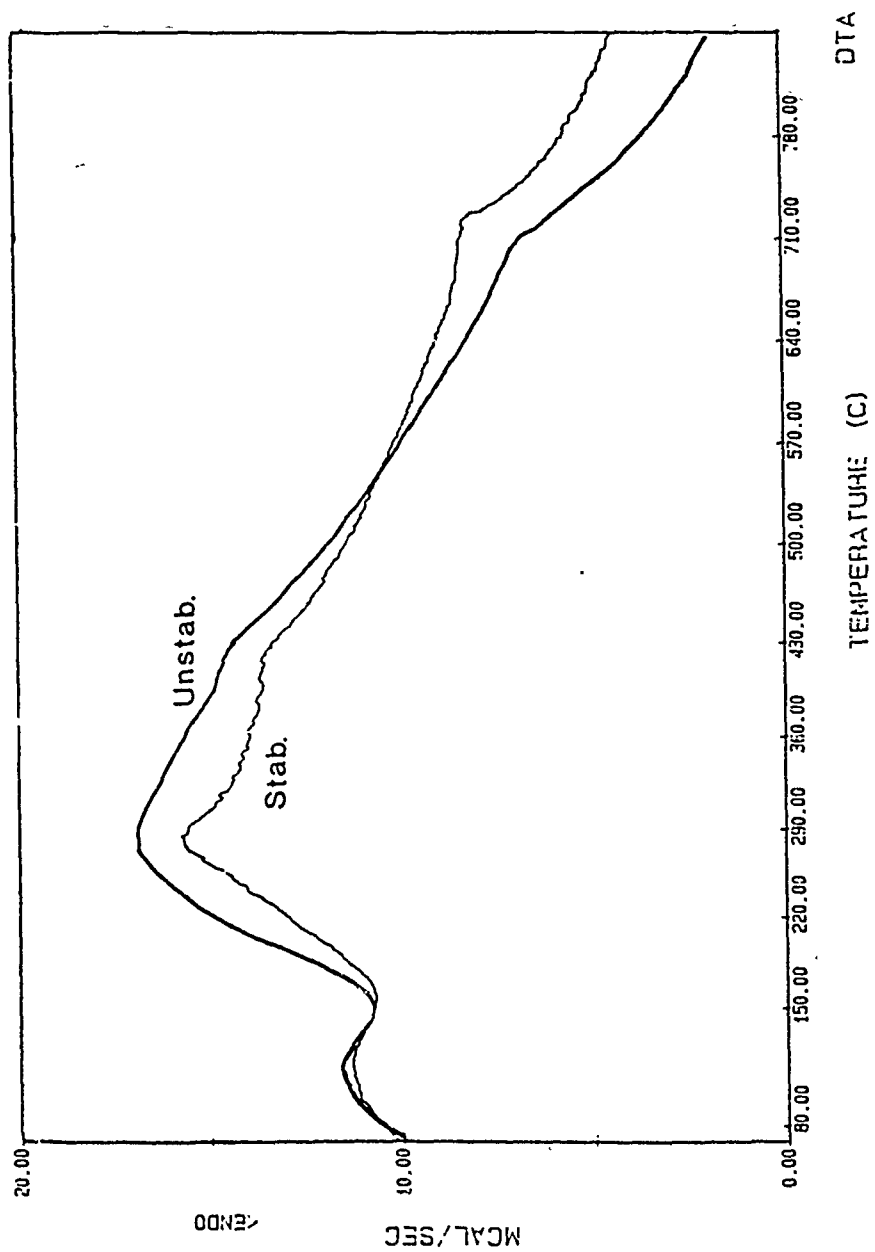


Figure 15. DTA runs for the stabilized and unstabilized powders.

for 3 hours followed by an isothermal heat treatment at 1150°C for 10 minutes. Relative peak shifts which would indicate the presence of an expanded or well formed lattice were not evident.

Other than the change in relative densities between the stabilized and unstabilized particles the powders are essentially the same.

4.2 Particle Packing

Settling observations, using a metallographic microscope³¹, of the unclassified particle systems showed that the number of particle agglomerates in the powders synthesized without surfactant was far greater than those synthesized with surfactant. Complete elimination of agglomerates by the classification procedure was observed only in the stabilized powders. Classification of the unstabilized powders resulted in the elimination of large agglomerates, but the presence of doublets, triplets, and a slightly wider distribution were still evident. Long range ordering in either classified powders was not observed, but a large number of particle coordinations of 6 were noted in the particle plane parallel to the cover slip. The lack of long range order in this portion of the work was due to immediate adsorption of some particles to the cover slip. When similar experiments were repeated with 0.7 micrometer diameter SiO_2 and 0.3 micrometer diameter latex particles no absorption occurred and long range ordering was observed.

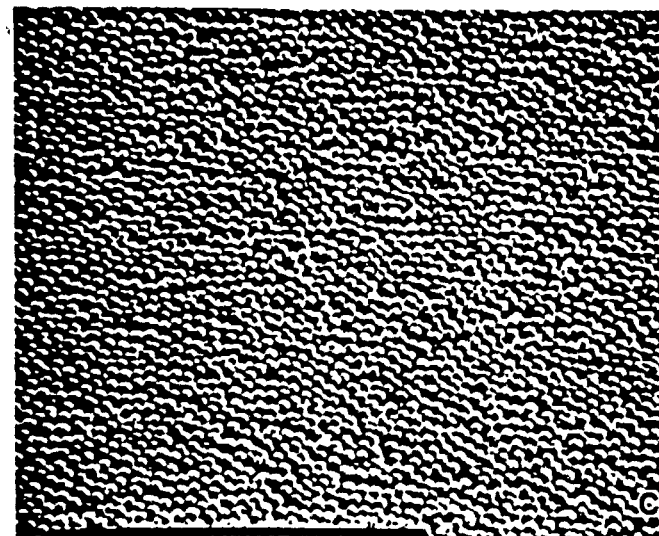
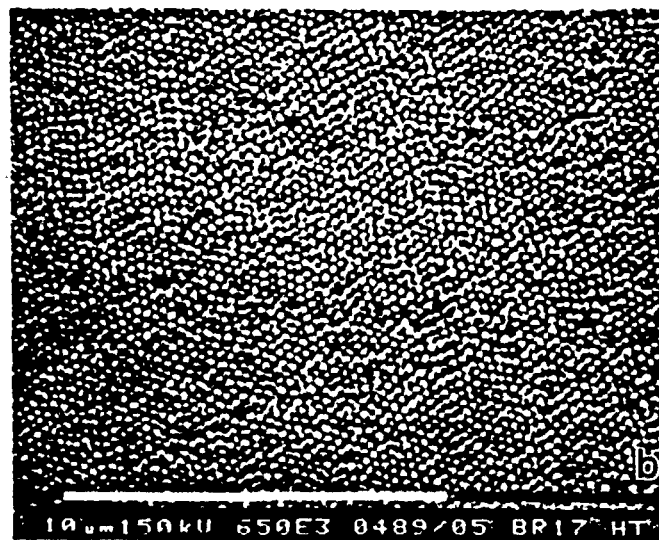
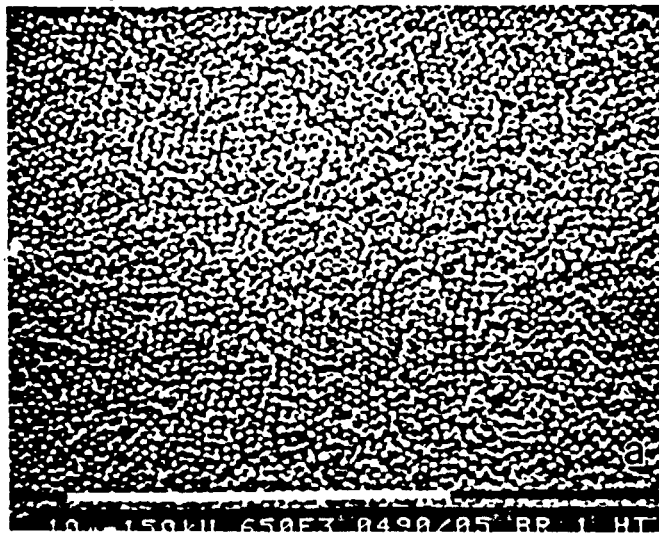
Differences in the degree of packing between stabilized and unstabilized particles were not readily discernible, but the amount of time required to reduce the size variance for nonsurfactant powders was far greater than that for the in situ stabilized powders. This is expected from the

observation of a log normal curve for the size distribution of the HPC powders as opposed to the normal distribution of the H₂O powders. From these continuous distributions it is expected that the HPC powders will show a smaller variance in the classified powders. Based on the ease of synthesis and seemingly very similar thermal behavior subsequent experimental work was solely on the insitu stabilized powders.

Variations in particle packing by applied centrifugal fields and particle size effects have been noted for the monosized silica sphere system^{1,41,42}. By increasing the applied field the domain size has been shown to decrease and the amorphous like packing of the suspension becomes quenched into the final particle compact. This behavior is represented in Figure 16 for 1 g, 175 g, and 350 g settling fields, where the crystalline nature of packing becomes most evident at the intermediate force of 175 g. In fact domain size is controlled by the rate at which the particle system moves through the density regimes which support crystallite nucleation and growth⁴¹. That is by increasing the original concentration the time that the compact in the centrifuge tube experiences a particle density less than that of a critical density for growth is decreased. Or similarly by increasing the settling field (g force) the time the compact experiences a particle density less than a critical density is also decreased. Therefore, it is possible to quench a particle system into an amorphous state by passing through the particle density regimes in which the particle exhibits a the mobility required for nucleation and growth of a crystalline configuration.

Packing observed at the intermediate gravitational force of 170 g could be the result of a large $1/\kappa$ which is not substantially depressed under the centrifugal

Figure 16. Relative degrees of colloidal crystallinity for the applied gravitational fields of a) 1 g, b) 170 g, and c) 350 g (note that sample (c) is not heat treated as are the others) (bars = $10\mu\text{m}$).

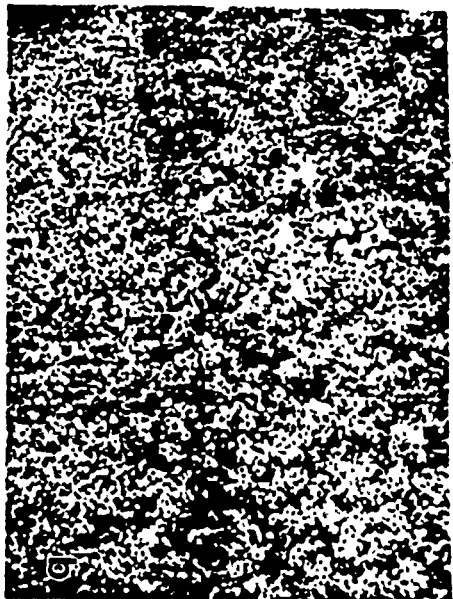
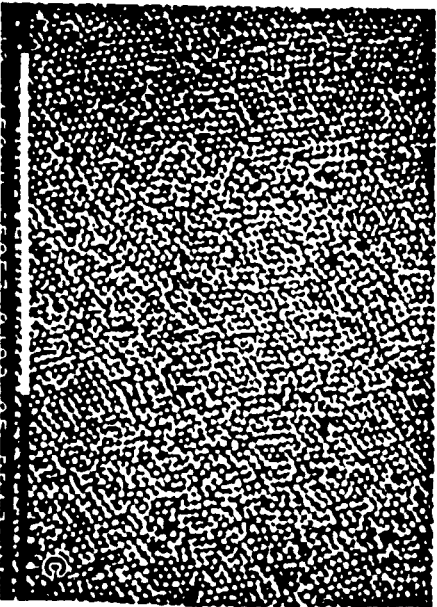
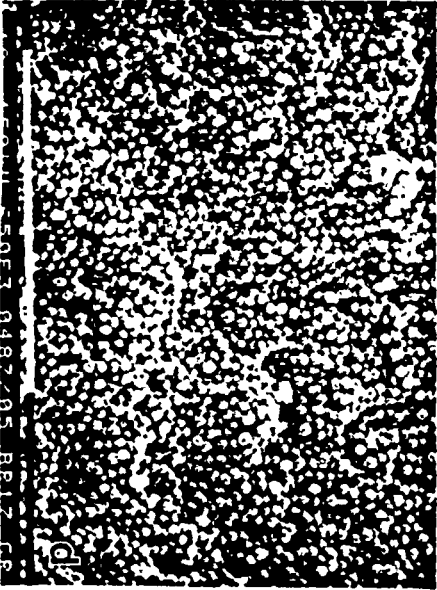


acceleration. In such a case the particle suspension is brought quickly into the high crystallization regime (Figure 2) and the time spent in the high high crystallization range is greater than either the 1 g or 350 g compacts. Past theoretical work has indicated that polydispersity in a particle system will also lead to a packing disorder over certain ranges of size variance²⁰. It was found that the effect of polydispersity was to increase the osmotic pressure of the ordered phase, or a tendency towards disorder. Decreasing the double layer thickness for constant polydispersity also increased the osmotic pressure. When dealing with a polydisperse system it would therefore make sense to work in the low electrolyte concentration range where lower pressure changes with polydispersity are predicted. Barringer³² found that the higher electrolyte regimes reduced the volume of ordered phase and gave a δ value of ≈ 0.13 .

In line with experiment³² and established theory²⁰ our observation was that ordering took place only in systems which were extensively washed with distilled water in the low electrolyte, basic pH range. The particle systems will never approach flocculation in the primary minimum due to the irreversible absorption of surfactant causing short range repulsive potentials²³. Jean and Ring²⁷ estimated the steric barrier to be ≈ 200 A, while the position of the electrostatic primary maximum is estimated at 2000 A³². Hence, flocculation may occur in a secondary potential well formed from electrosteric interactions.

In order to illustrate the green microstructure effects on sintered microstructure evolution, a flocced specimen and a relatively well ordered specimen are compared. The top and fracture surfaces for the two compacts are represented in Figure 17 where the relative packing and hierarchy^{1,2} of

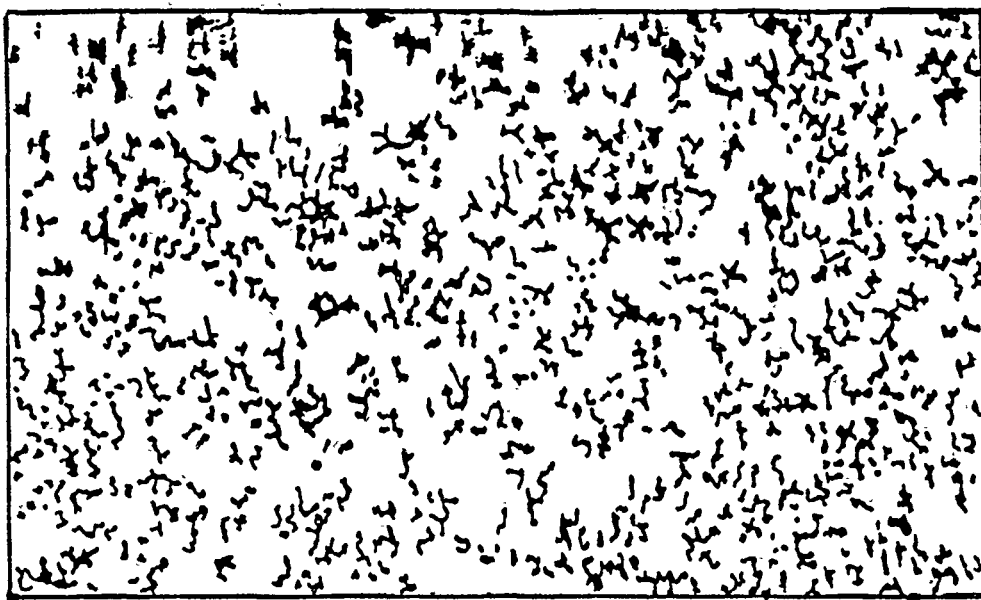
Figure 17. Top and fracture Surfaces of the flocced and 170 g ordered compacts a) fracture flocced, b) top surface flocced, c) top surface ordered, and d) fracture ordered (bar = $10\mu\text{m}$ except (b)).



voids becomes most evident on the top surface of the dried powder compacts. In this case the particle size and chemistry is identical between the two cases; however, number and distribution of void sizes is substantially different. Figure 18 is a comparison of the microstructures in Figure 16 in which the voids are represented by the black areas and dense particle packing units are white. The equivalent spherical diameter distributions vs. the percent frequency per total area are given in Figure 19 and are representative of a hierarchy of voids in the two compacts. A_t represents the total area of the sample used in obtaining the data in Figure 19. Based on the total area A_t it was found that 10 area percent of the ordered compact is in second generation voids and over 20 area percent of the flocced sample is in voids of the second and third hierarchy. Smaller first generation pores are common to both packings and are not represented in the pore size distributions, similarly not all the second generation voids appear in the negative of the flocced case. At this stage it was assumed that these surface packings were representative of the relative packing, this is substantiated in subsequent sintering studies.

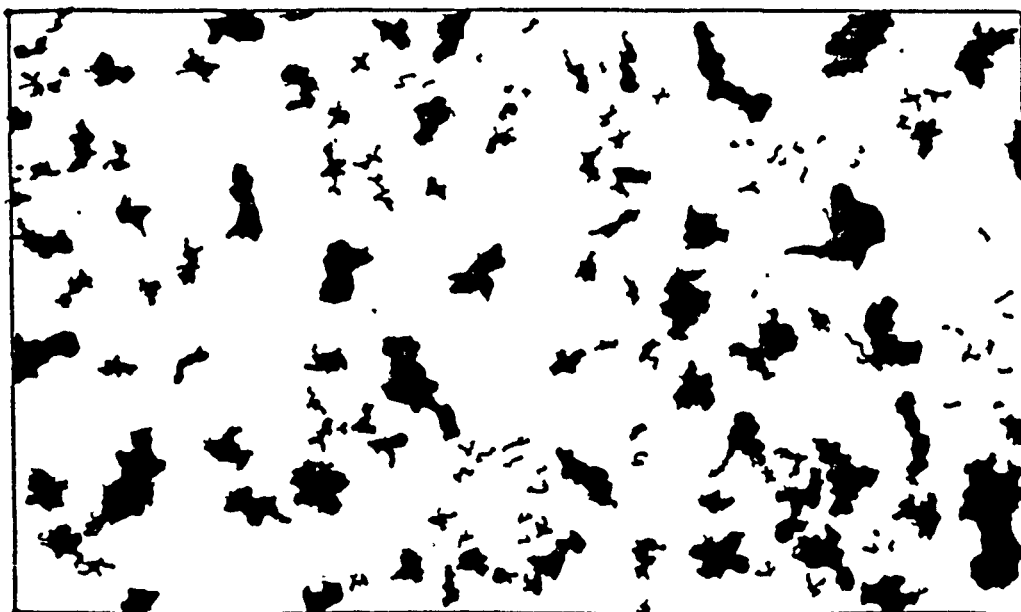
Insitu crystallization of the powder compacts yielded similar packing as observed in the green amorphous state. The expected intra-particle densification is illustrated in Figure 14 which shows a substantial increase in porosity, but no rearrangement of particles relative to one another is observed. Edelson²¹ reported a bulk shrinkage of 87 volume percent on sintering to full density with only 40 volume percent due to inter particle sintering. This indicates

Figure 18. Negative of top surfaces in Figure 17 showing enhanced voids a) ordered b) flocced (bar = $1\mu\text{m}$).



a

1.0μm



b

1.0μm

substantial intraparticle densification during the crystallization and initial low temperature sintering. Packing densities on the order of 60 volume percent in the ordered case and 45 volume percent in the flocced case are estimated from the area under the curves in Figure 19. This estimate is made with the assumption that first generation voids will account for approximately 25 to 30 volume percent of the total porosity and that there is direct mapping from area to volume fractions.

4.3 Sintering

Measurements of the microhardness indents indicated a linear shrinkage of 16 % in the first 5 minute isothermal sintering at 1150°C. The linear shrinkage is related to the relative volume change by

$$37) \quad \Delta\rho/\rho_{th} = ([1-\Delta l/l]^{-3} - 1)$$

where $\Delta l/l$ is the relative linear shrinkage and $\Delta\rho/\rho_{th}$ is the relative volume change. Using equation 37 a volume change of 31 % between the initial crystalline packed and the sintered compact is obtained. For sintering times greater than 5 minutes large variations in relative linear shrinkages were obtained, including linear expansion. Due to the anomalous results only the initial measurement can be used to indicate that a large proportion of the sintering occurs in very short times for the ordered compact. Shrinkage data on the flocced compact were not taken due to indent collapse upon sintering.

Surface grain growth was observed to occur within the first 1150°C sintering time period (5 min) in all compacts; hence the intermediate stages of sintering has been well

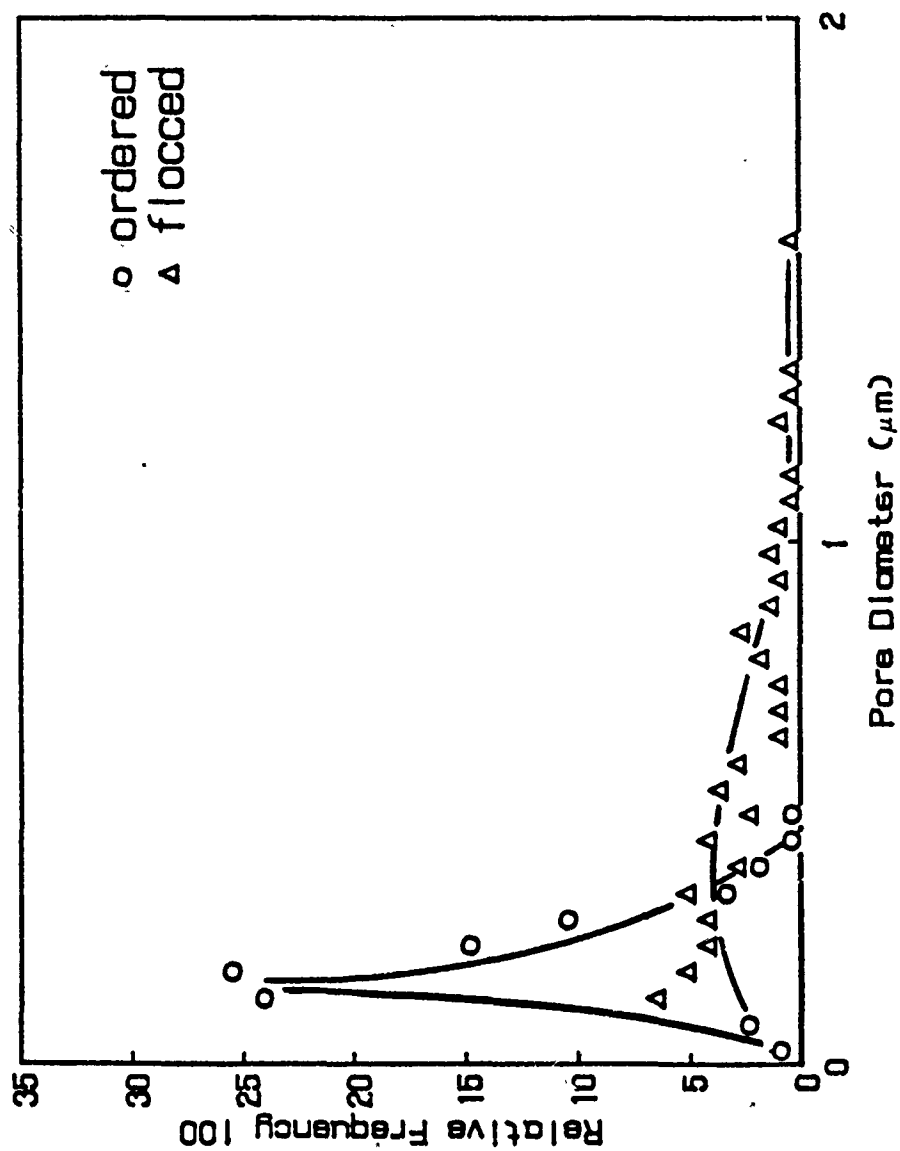


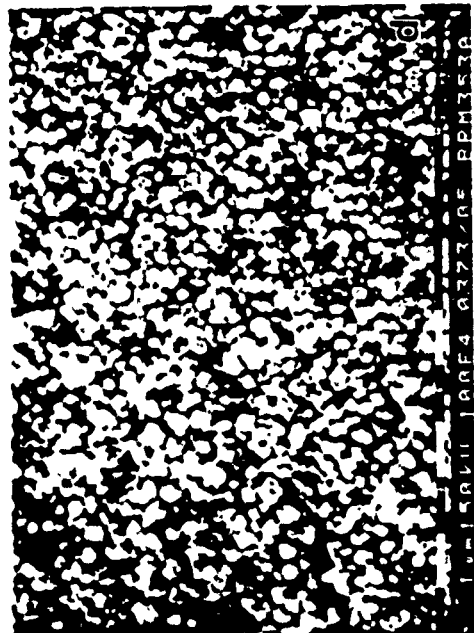
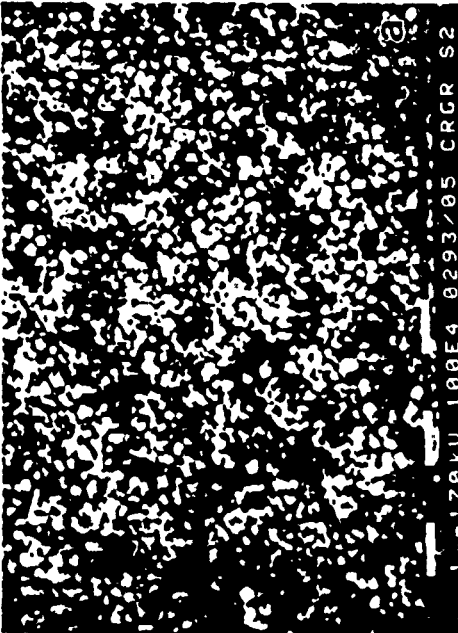
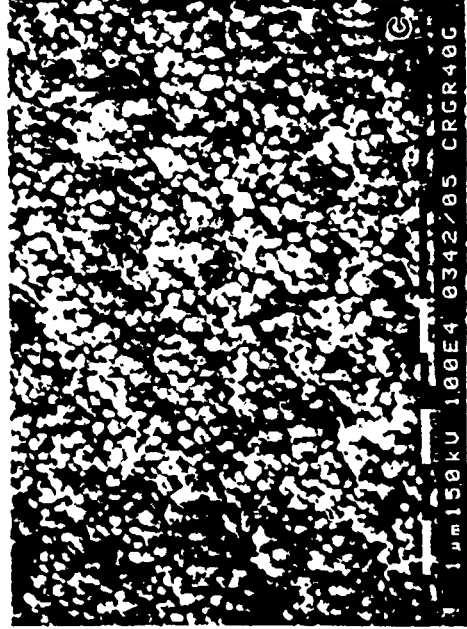
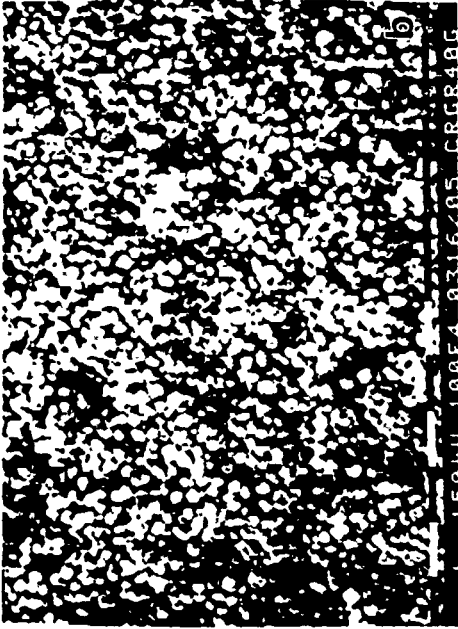
Figure 19. Void size distribution from Figure 18.

established. In the case of the 1 g and 175 g ordered green structure no remnant of the original packing was observed after an initial sintering time of 30 minutes at 1150°C. In order to observe what occurred in the original stages of sintering the temperature was reduced to 1050°C and similar samples run for the same time periods. Considering the work of Barringer⁴⁴, Vergnon⁵⁸ and others in which similar processes are seen to occur over the sintering regimes for different isotherms the 1050°C samples should be representative of the intermediate sintering at higher temperatures. Since the initial phase of sintering had already been fairly well established during the crystallization step the microstructure observed cover the transition from initial into and partially through the intermediate stage. Figure 20 illustrates the breakdown of the packed particle units by particle rearrangement over a period of 30 minutes for the flocced and dispersed samples. The particle coarsening in each case is obvious as is the evolution of a particle/grain size distribution which is wider than the original. This illustrates that the coarsening is not uniform in the well ordered compact even though the initial green packing would be expected to give areas of homogeneous particle growth resulting in an area of uniform hexagonal grains.

From Figure 20 it becomes clear that particle coarsening occurs in both the flocced and ordered cases and is of the same magnitude in each case. The micrographs indicate that the overall densities of both compacts cannot be the same. Based on these two observations it can be said that the particle coarsening is dependant upon local particle densities and coordinations. Coarsening and grain growth will be dependant on domain coordination as the particle/grain size approaches the domain size.

Figure 20a. Initial and intermediate stages of sintering in the 1 g surface at 1050°C for a) 0 min, b) 5 min, c) 10 min, and d) 30 min (bar = 1 μ m).

Figure 20b. Initial and intermediate stages of sintering in the flocced surface at 1050°C for a) 0 min, b) 5 min, c) 10 min, and d) 30 min (bar = 1 μ m)



Work by Exner⁵⁹ on planar arrangements of copper spheres indicates that only the higher coordination number voids grow and the ordered regions remain intact which is contrary to the phenomena observed here. Anisotropy in sintering in the vicinity of the free surface of the compact could be used to explain particle rearrangement on the surface. However, similar experiments⁶⁰ on surfaces of 3 dimensional compacts did not show a substantial rearrangement of surface structure by bulk movement during the initial stages of sintering.

An explanation for the rearrangement of a titania system similar to the present study was given by Edelson²¹ in terms of particle substructure in which the initial particles were not single domains. These polydomain particles give rise to interparticle grain growth in isolated regions which in turn cause further particle rearrangement. Interparticle grain boundary motion, as covered by Exner⁵⁹, in porous ceramics will only occur at times when the vapor-solid equilibrium surface tension requirements of the boundary are energetically less favorable than the change resulting from boundary motion.

A further point should be noted in that the porosity and pore sizes between the ordered and flocced samples are quite different through intermediate sintering as illustrated in Figure 20. In the initially ordered compact the pore size distribution grows, but remains fairly evenly distributed over the range studied. The flocced sample also exhibits pore growth on the same order of size, but the initially wide distribution of sizes increases. In addition to the wider pore size distribution in the flocced case the presence of relatively large areas of high density domains are also noted. The advent of pore growth in the intermediate stages of sintering has been covered by various

investigators^{9,60,61} using mercury porosimetry with the conclusion that intra-agglomerate sintering causes inter-agglomerate pore growth. As the coarsening and grain growth occurs the coordination number of the pores decreases to the point where the pore shrinks and densification is completed or the pores become stable⁹.

Both compacts, flocced and ordered, during intermediate sintering can be envisaged as consisting of domains. Only the relative size of domains, the coordination number, and the pore size between compacts is different. As pointed out by Lange⁹ and Han⁶² the size of these dense domains and their growth rate is of prime importance in subsequent microstructure evolution in that these dense volumes can now support normal grain growth by grain boundary movement.

4.4 Grain Growth

4.4.1 Surface

All compacts illustrated normal grain growth on the surface over the first 10 hours, but as the normalized grain size distributions, depicted in Figure 21, indicate there is an evolution of a second mode throughout the total observed period. The most prevalent secondary growth is observed in the 175g sample at times in excess of 10 hours. When the mean grain size is plotted vs time for the three compacts it can be seen that the initial surface evolution follows the same trend in all cases (Figure 22). However, at 2 hours the initially highly ordered compacts show continued growth while the flocced compact tends to stabilize.

In the literature reviewed two investigations dealt with observations of thin sections^{62,63} in which almost planar grain boundary motion was used in the evaluation of growth parameters. Ikegami⁶⁴ reported a $t^{1/3}$ for MgO

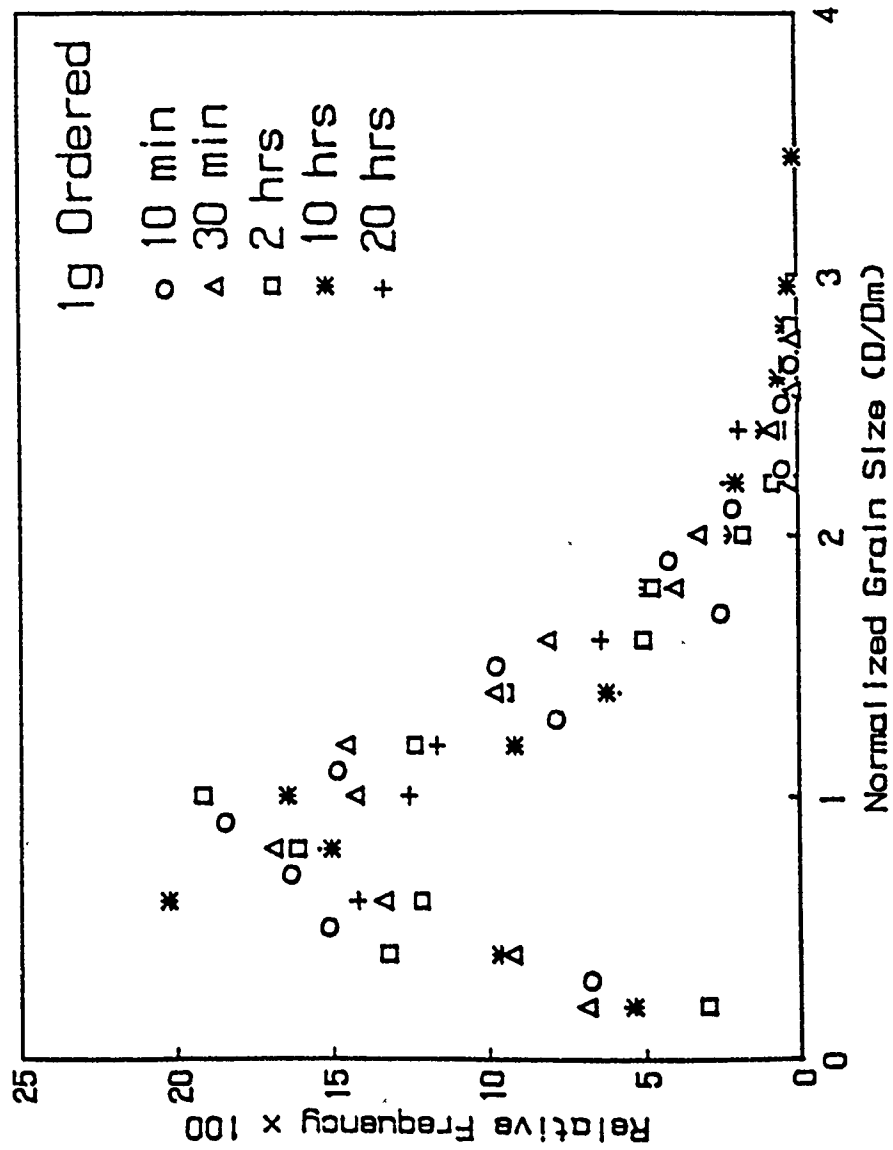


Figure 21a. Normalized surface grain size distributions in the 1 g ordered compact.

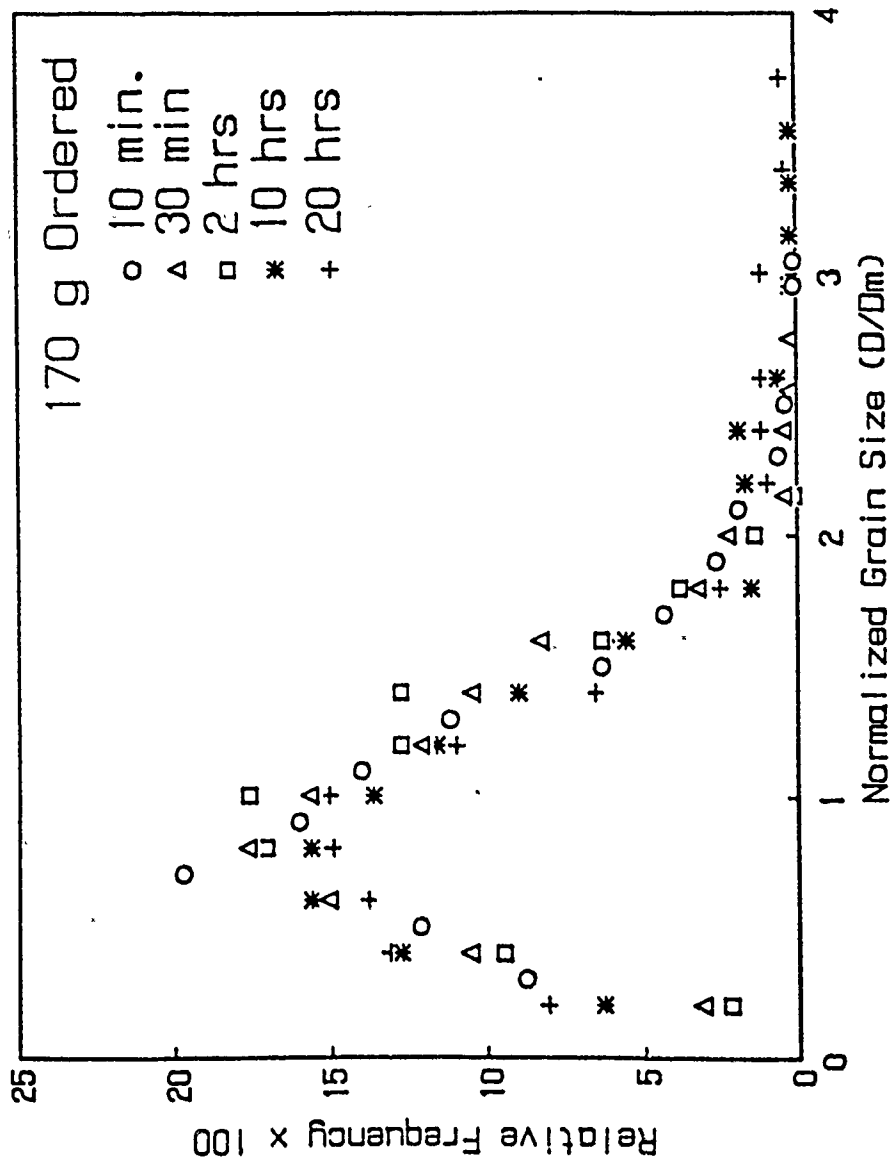


Figure 21b. Normalized surface grain size distributions in the 170 g ordered compact.

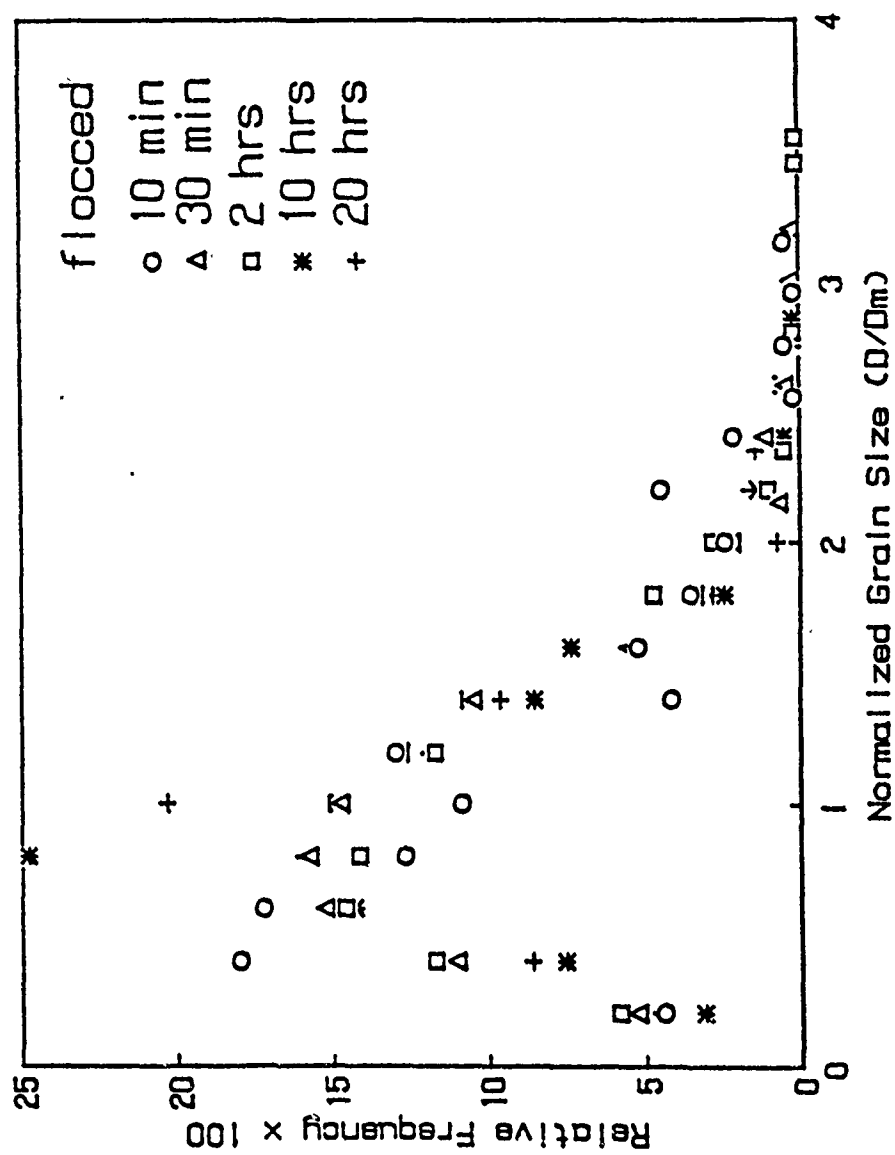


Figure 21c. Normalized surface grain size distributions in the flocced compact.

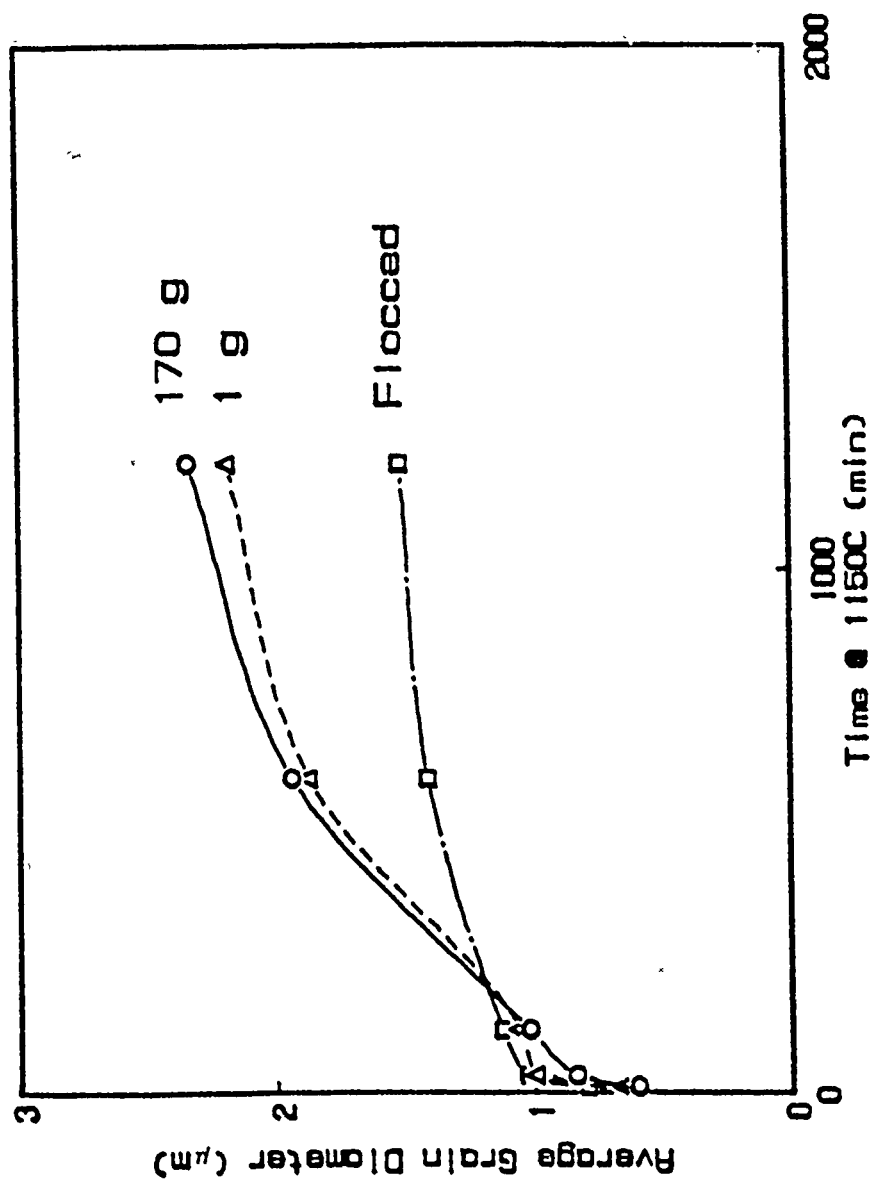


Figure 22. Mean grain size vs. time for the distributions in Fig 21a,b,c.

relationship for grain growth while Hott⁶³ found $t^{1/2}$ behavior in BeO. In addition the BeO was observed to stabilize after a period of 20 hours. Two different exponents in the grain growth equation are observed for the initially ordered state that of $1/5$ for times less than 10 hours and $1/3$ for times greater than 10 hours. A time exponent of $1/5$ applied to the flocced case over the range of time studied. In most investigations the possible edge effects, or free surface effects, are circumvented by sampling bulk regions which are deemed independent of free surfaces. It has been mentioned in passing that a time exponent on the order of $1/2$ is expected for regions close to surfaces⁶⁴. There is evidence of slight porosity on the surface of the flocced state up to 2 hours which does not occur in either of the ordered cases. A period of pore stabilized grain growth would explain the evidently restrained growth for up to 2 hours, but the continued low order growth should not occur. This behavior indicates a restraint of boundary movement by other than local forces, i.e. pore pinning in the bulk.

Most grain growth models, as mentioned in section 2.3.2, are based on the time independent normalized distribution which for the most part is represented here. It should be noted that models predict a maximum size grain which vary from 2.0 to 2.5 times the mean grain size ' D_m ' whereas some experiments⁶⁵, including the present one, exhibit largest grain sizes on the order of $3D_m$. Table I lists the arithmetic mean grain sizes, standard deviations, and number of grains sampled for the distributions in Figures 21 and 22.

The distribution shapes are similar to that given by Hu⁶⁵ for bulk grain growth, that is they are not lognormal but skewed to larger normalized sizes when plotted on a log

scale. One substantial deviation from the time independence is for 10 minutes in the flocced compact which moves back to the expected behavior over the next time interval. As time proceeds the advent of a second mode is observed in all

Table I
Normalized Surface Grain Distributions

	10 min	30 min	2 hrs	10 hrs	20hrs
1g ord					
D_m	0.61	0.84	1.02	1.94	2.3
σ	0.47	0.49	0.48	0.55	0.55
N	694	789	526	556	308
170g ord					
D_m	0.66	1.00	1.06	1.90	2.2
σ	0.55	0.46	0.42	0.62	0.64
N	590	479	570	447	379
flocced					
D_m	0.8	1.03	1.12	1.40	1.52
σ	0.6	0.50	0.52	0.45	0.48
N	360	595	727	433	348

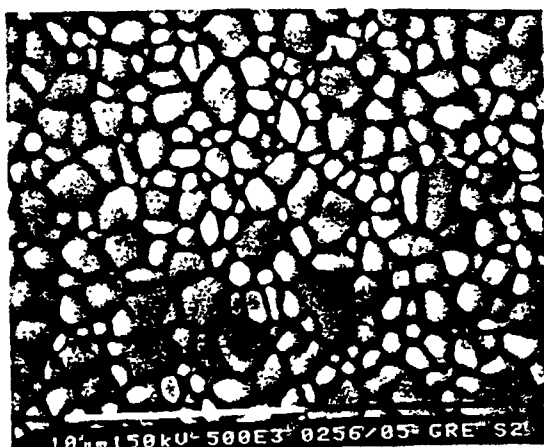
D_m is the mean grain size in micrometers, σ is the standard deviation, and N = number of grains.

powder compacts, which represents the only other deviation from the expected distributions.

To illustrate the grain shape, which is not evident in the distributions, Figure 23 consists of micrographs taken at various times for the flocced and 170 g ordered case. The deviation of the flocced microstructure from a time independent distribution at 10 minutes is apparent from the grain shape. At longer times the abnormal shapes are not encountered in the flocced case, but abnormally large equiaxed grains appear in the 170 g compact. Hillert⁵¹

Figure 23. Micrographs of surface grain shapes for the 170 g ordered and flocced compacts sintered at 1150°C for a) 10 minutes, b) 2 hours, and c) 10 hours (note scale changes).

Ordered



Flocced



a



b



c



hypothesized an abnormal growth followed by a return of the microstructure to the observed time independent distribution. Whether or not the observed behavior is a result of departure and return to an equilibrium distribution in shape or size has not been determined beyond doubt.

It is well known that surface phenomena are not representative of the bulk behavior of a material. This is due to the predominance of the vapor-solid interface at the surface as opposed to the solid-solid interface in the bulk as well as a possible insoluble intrapore gas. For the case of grain growth an additional aspect of the area available for flux should show a considerable effect on the variations between growth on the surface and in the bulk. Since the surface and bulk are not separate entities, nor is fracture indicated between the surface and bulk, the characteristics of the surface and bulk must be interdependent to a great extent. In this case an apparently unprecedented stable grain system on the surface will be shown to result from bulk microstructure effects.

4.4.2 Bulk Microstructure

As was mentioned in the previous section the relationship between surface and bulk microstructure has rarely been addressed. With the advent of as-formed non-machined surfaces, thin substrates, and surface treatments of ceramics relationships between bulk and surface microstructure should be considered critical in design.

Comparison of the control specimens surface microstructure with that of the characterized surfaces showed a fairly good correlation. A slight increase in size for the resintered surfaces as compared to the control can be attributed to a slight nonisothermal period which is

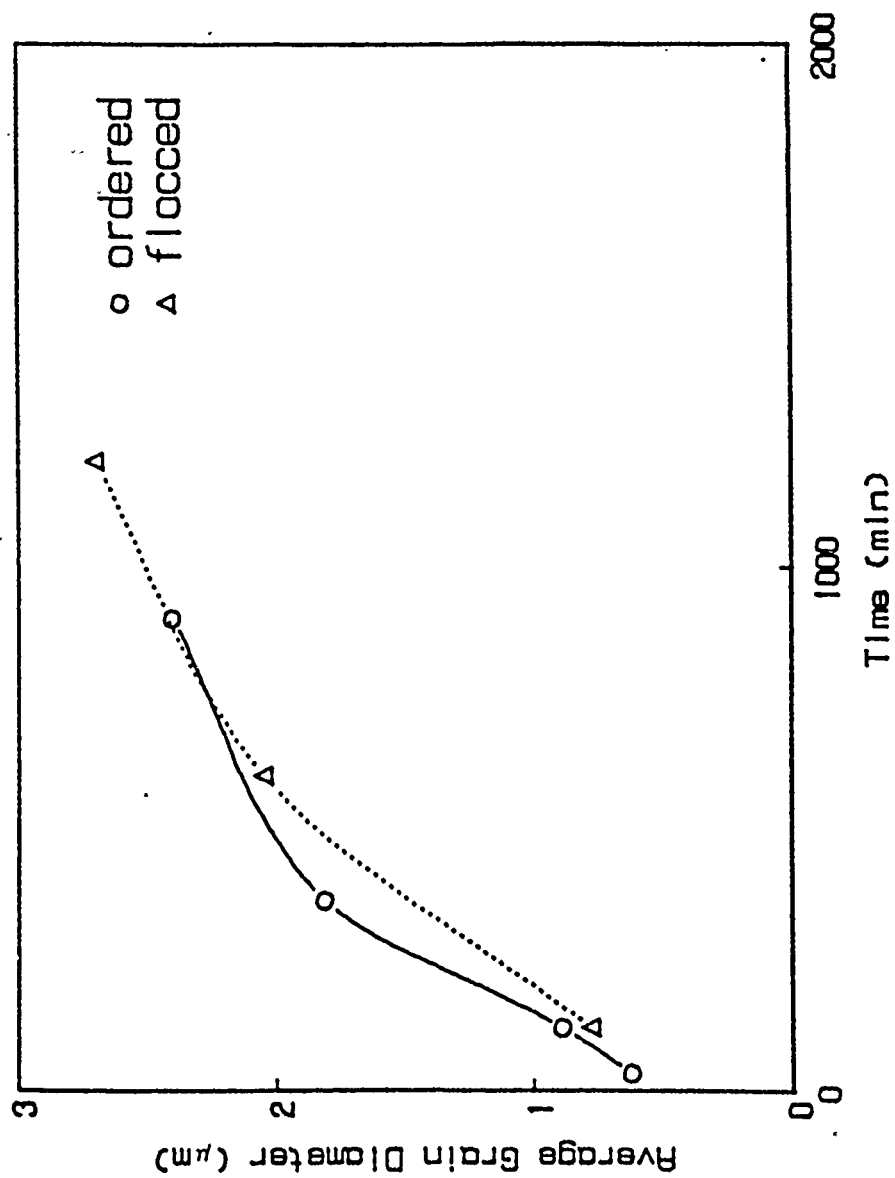


Figure 24. Mean grain size growth in the 170 g and flocked compact crossections.

inherent in any "isothermal" process. Due to the size of the specimens the transient heat transfer effects are deemed to be negligible and as mentioned previously the transient time is relatively short.

Mean grain size vs time is represented in Figure 24 for the 170 g ordered and flocced compacts. Depth of the 1 g ordered specimens was small enough so that edge effects could not be ignored; therefore, 1 g crosssections were not characterized. Curve fitting yielded a time exponent to the simplified growth equation:

$$D_m = Kt^n$$

where n is 0.48 for the ordered case and 0.54 for the flocced case. In essence the time exponent is 0.5 for both cases.

Gradients of porosity and grain size were evident in the cross-sections with the flocced compact exhibiting the greater of the two. Figures 25 and 26 illustrate the grain size gradients for the 170 g and flocced cross-sections where it is obvious that there is a substantial difference between the two cases. These figures are extensions of Figures 22 and 24 in that the diameter of the spherical equivalent mean grain size is given with respect to time at various positions in the cross-section. Grain growth on the ordered compact surface is only slightly retarded when compared to the bulk. However, there is a large grain size decrease from the center to the surface for the flocced case.

What is not evident in the figures is the porosity existing in the flocced compact. Figure 27 is a set of micrographs through the flocced and ordered compact for 20 hours at 1150°C. The far left edge of the left micrograph is the edge of the compact represented previously in Figure 23. It is evident that pore pinning is a dominant process in the

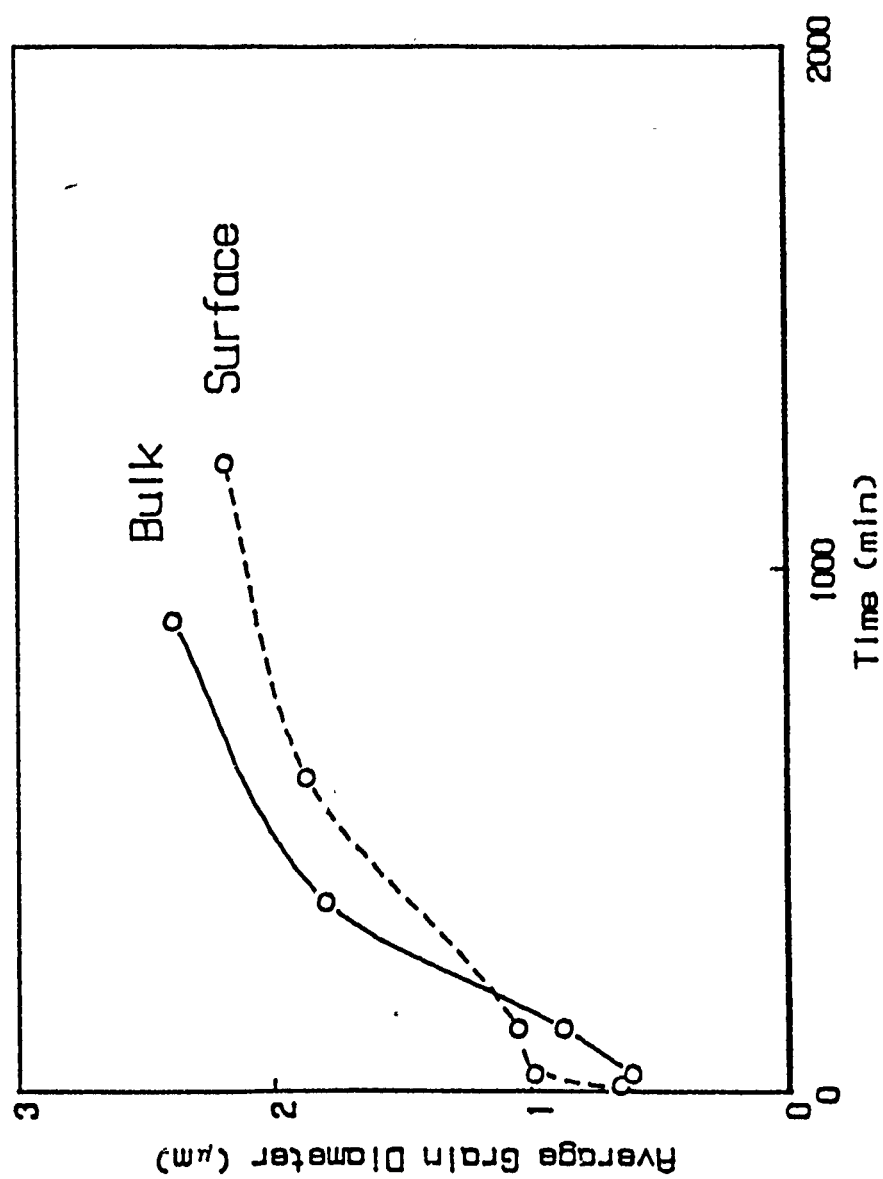


Figure 25. Mean grain size at different positions in the 170 g sample

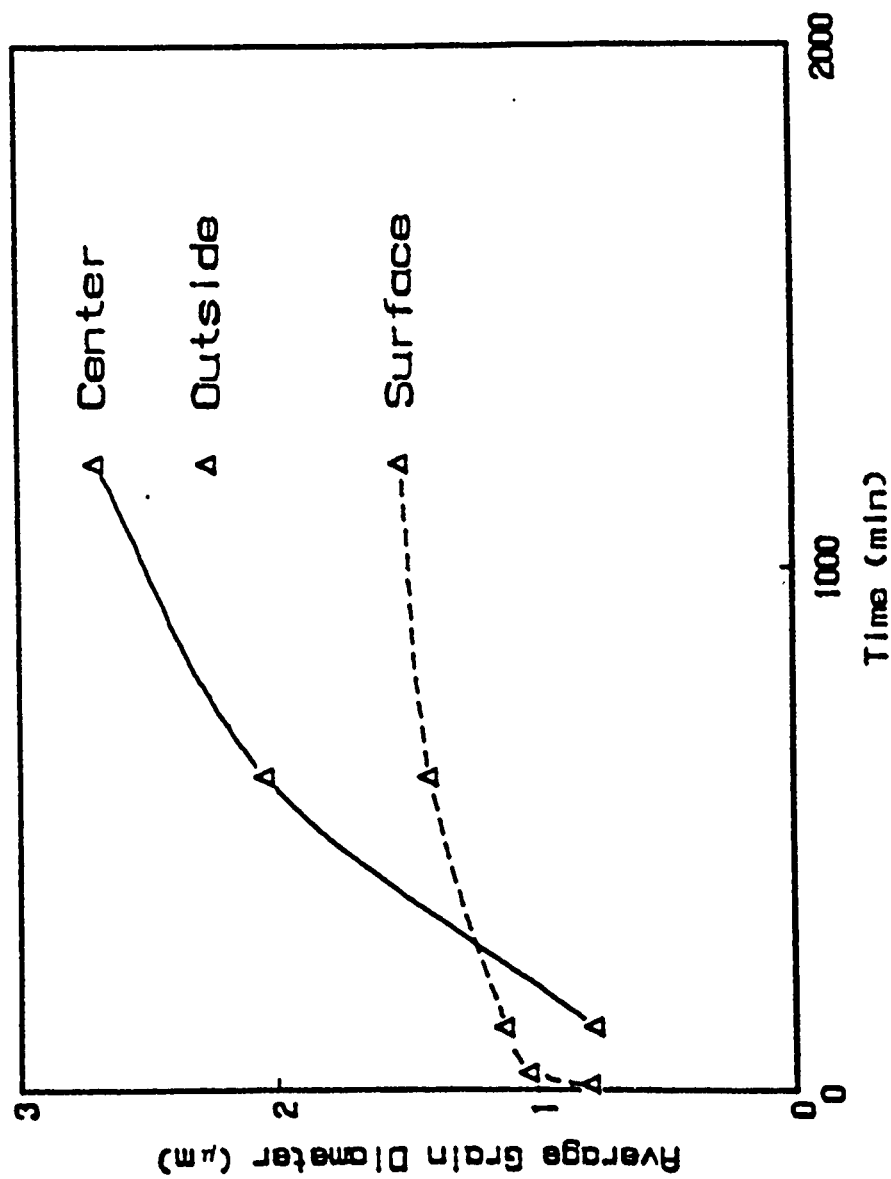


Figure 26. Mean grain size at different positions in the floc sample.

Figure 27. Micrographs of the a) center and b) edge of the flocced sample at 20 hours, and of the c) center and d) edge of the 170 g ordered sample (bar = $10\mu\text{m}$).

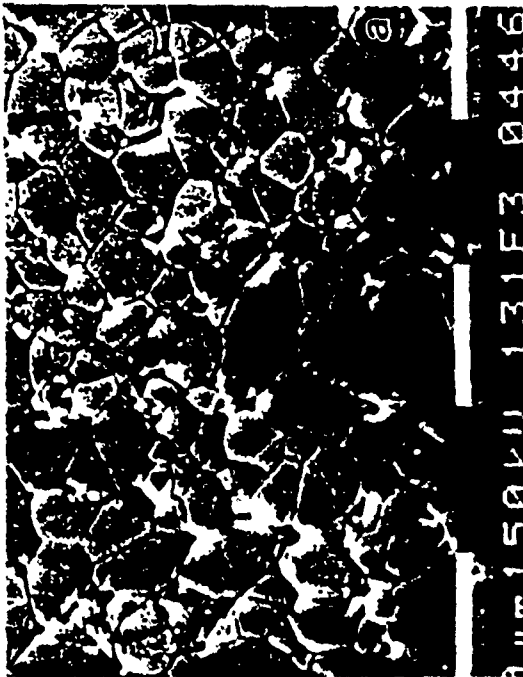
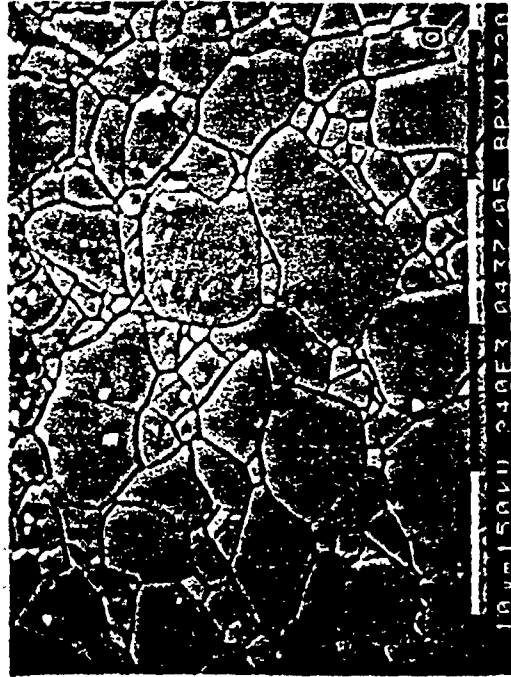
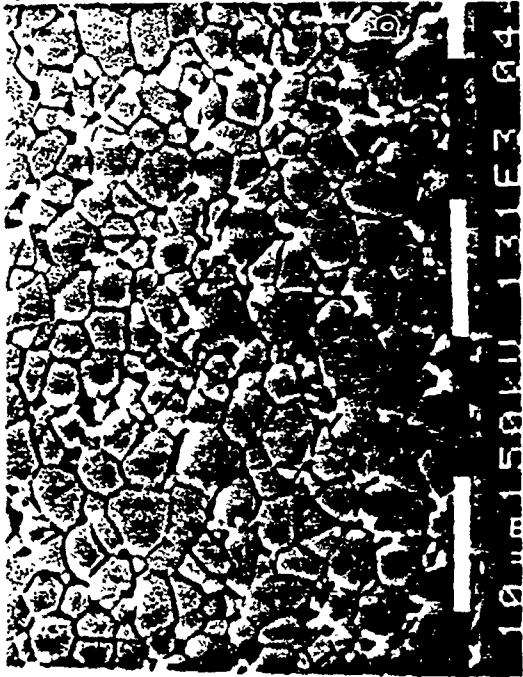
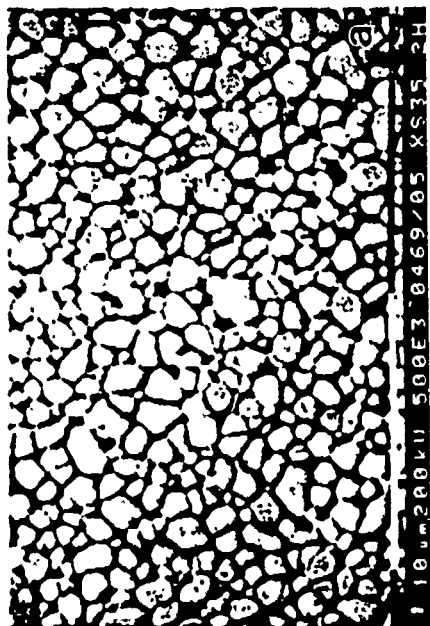
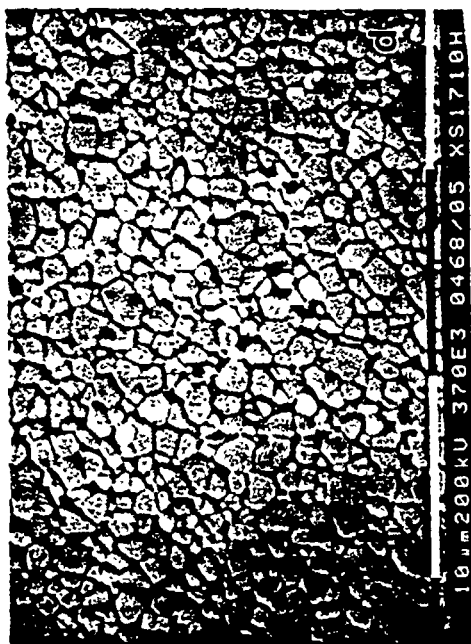
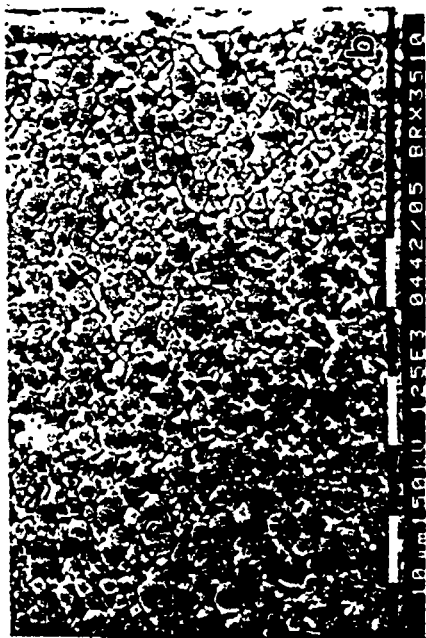


Figure 28. Flocced sample sintered at 1150°C for a) 2 hours and b) 10 hours, Ordered 170 g sample sintered at 1050°C for c) 2 hours and d) 10 hours (bar = 10 μ m).



flocced case over the periods of time covered in this study. Crosssections of the ordered compact after sintering for 30 minutes at 1150°C show that all porosity has been eliminated. In order to determine relative microstructures evolution between the two cases this porosity difference must be eliminated.

At lower temperatures the ordered compact will not densify even for long times. Figure 28 represents this behavior for 2 and 10 hours at 1050°C in the ordered case and at 1150°C in the flocced case. At 2 hours the microstructures are very similar in terms of porosity and grain size. Upon further heat treatment to 10 hours the pore size and grain size of the ordered compact has remained relatively constant; porosity in the flocced compact has remained constant while the grain size has doubled. Image analysis on the crosssections in Figure 28 indicate a difference in relative density of only 2%, but the grain size in the flocced case is on the order of 2 times greater than the ordered compact grain size.

In the ordered case densification without grain growth appears to occur at low temperatures while the flocced sample shows grain growth with pore coalescence. The degree of pore shrinkage and pore coalescence are exhibited in Figures 29 and 30 where the pore size distribution vs. time for the two compacts in Figure 28 are illustrated. It is seen that the pores in the ordered compact shrink while those in the flocced case shift the mean to larger sizes and also broaden the distribution. Since this type of behavior would indicate that the temperature range lies within two regimes. In one regime densification occurs without grain growth, in the other regime pore coalescence takes place with little densification. Therefore, it is questionable as to whether or not the two microstructures can be compared at

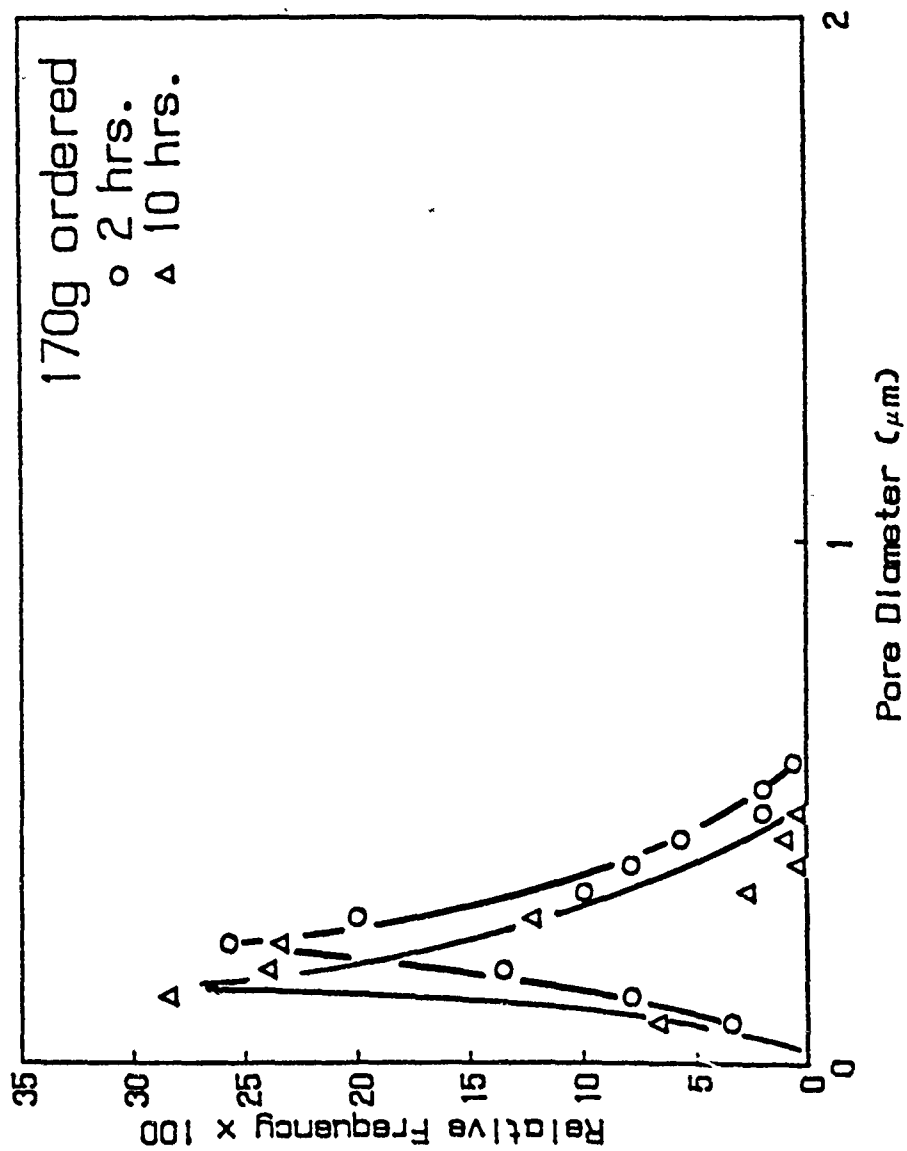


Figure 29. Pore size distributions for 170 g ordered during sintering at 1050°C.

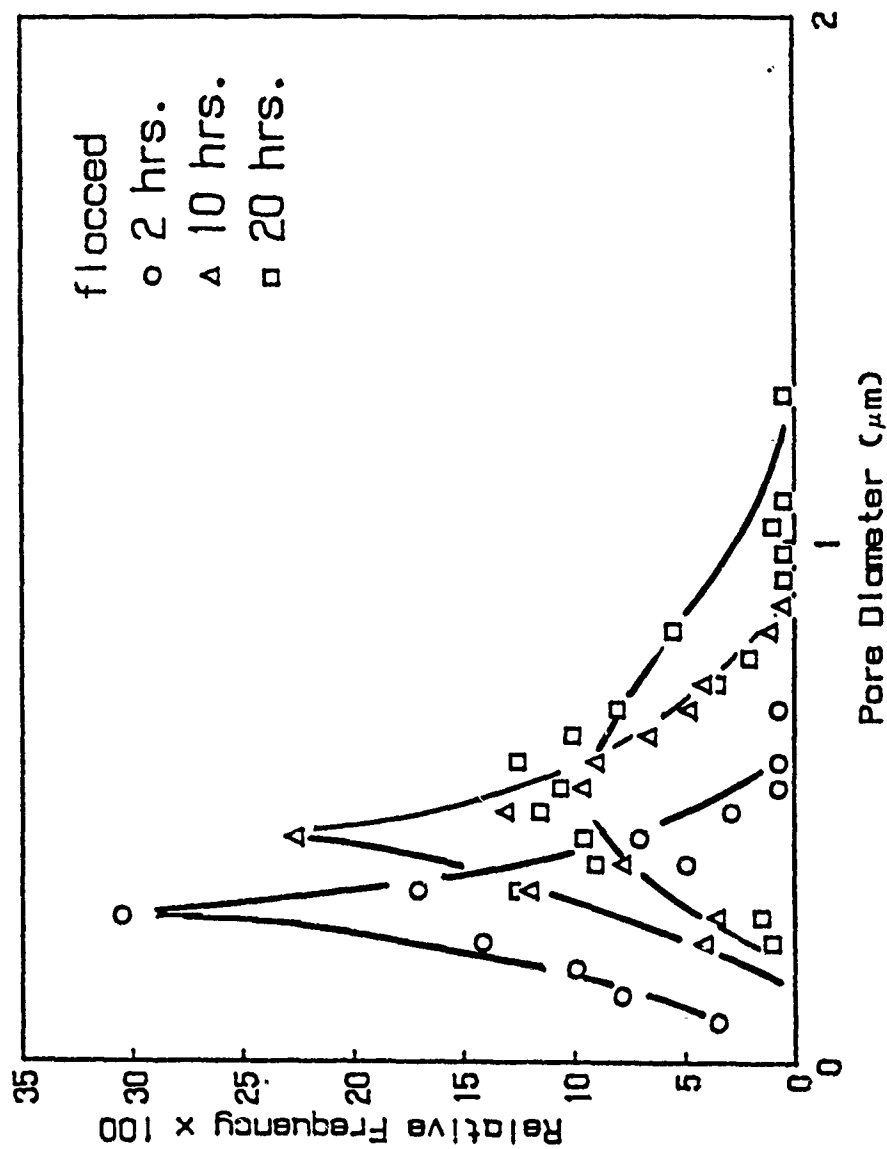


Figure 30. Pore size distribution for the flocked specimen during sintering at 1150°C. two different temperatures for similar densities.

The equivalent spherical grain size distributions, normalized to the arithmetic mean (D_m), are illustrated in Figures 31 and 32 for the ordered and flocced compacts respectively. It is evident that the initially ordered structure does not follow a time independent distribution while the flocced grain size distribution appears very time invariant. The microstructures at 20 hours are illustrated in Figure 27 where it becomes apparent that the porosity plays an important role in stabilizing the distributions. Pores in the flocced compact show a tendency to coalesce and do not appear to separate from grain boundaries and junctions indicating sufficient pore mobility, but also substantial pore control of the microstructure. Table II summarizes the data for the distributions in Figures 31 and 32 and illustrates the steady increase in the standard deviation in the ordered case.

Table II
Normalized Bulk Grain Distributions

	30min	2hr	6hr	10hr	15hr	20hr
170g ordered						
D_m	0.63	0.88	1.81	-	2.40	-
σ	0.57	0.79	0.90	-	0.94	-
N	300	445	619	-	450	-
flocced (center)						
D_m	-	0.79	-	2.15	-	2.72
σ	-	0.42	-	0.53	-	0.64
N	-	400	-	1000	-	500
flocced (edge)						
D_m	-	0.79	-	2.05	-	2.26
σ	-	0.42	-	0.48	-	0.48
N	-	400	-	1000	-	708

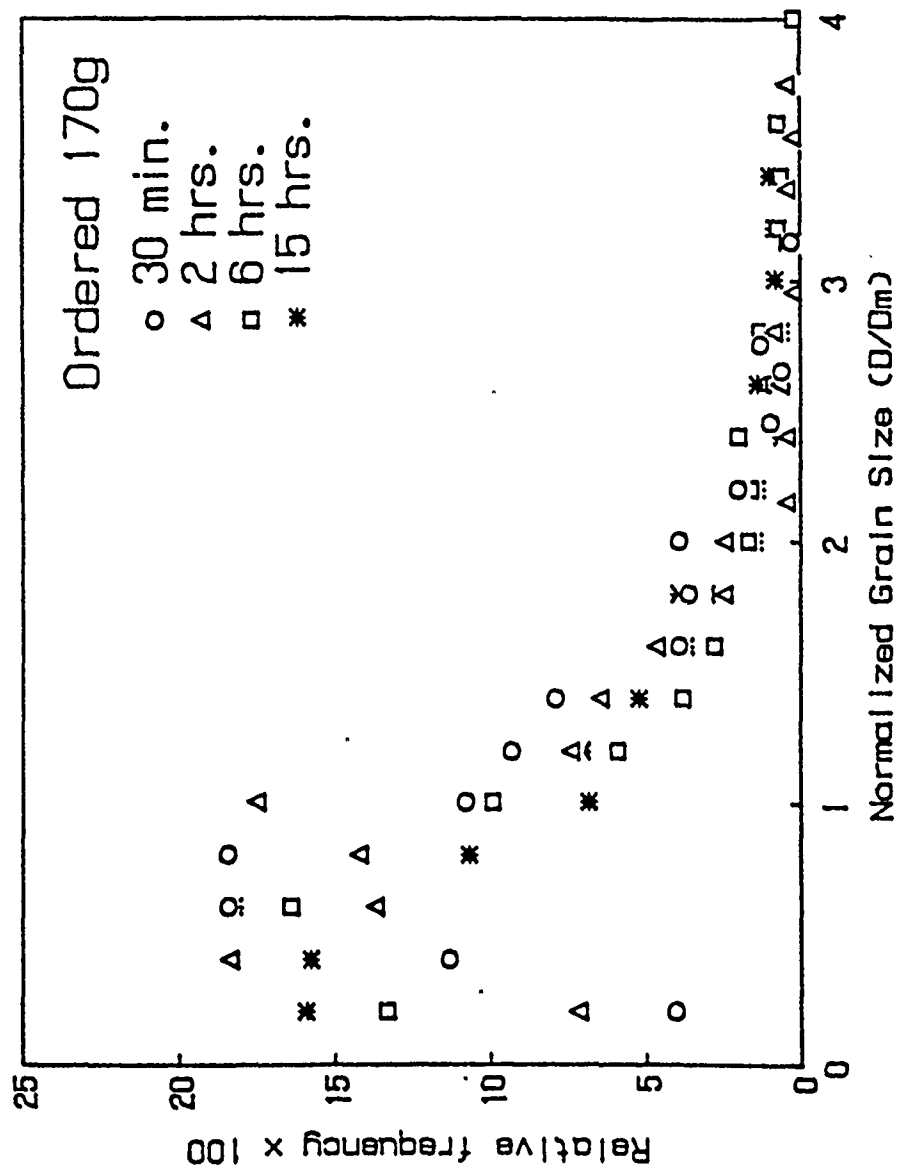


Figure 31. Bulk grain size distributions of the ordered 170 g compact.

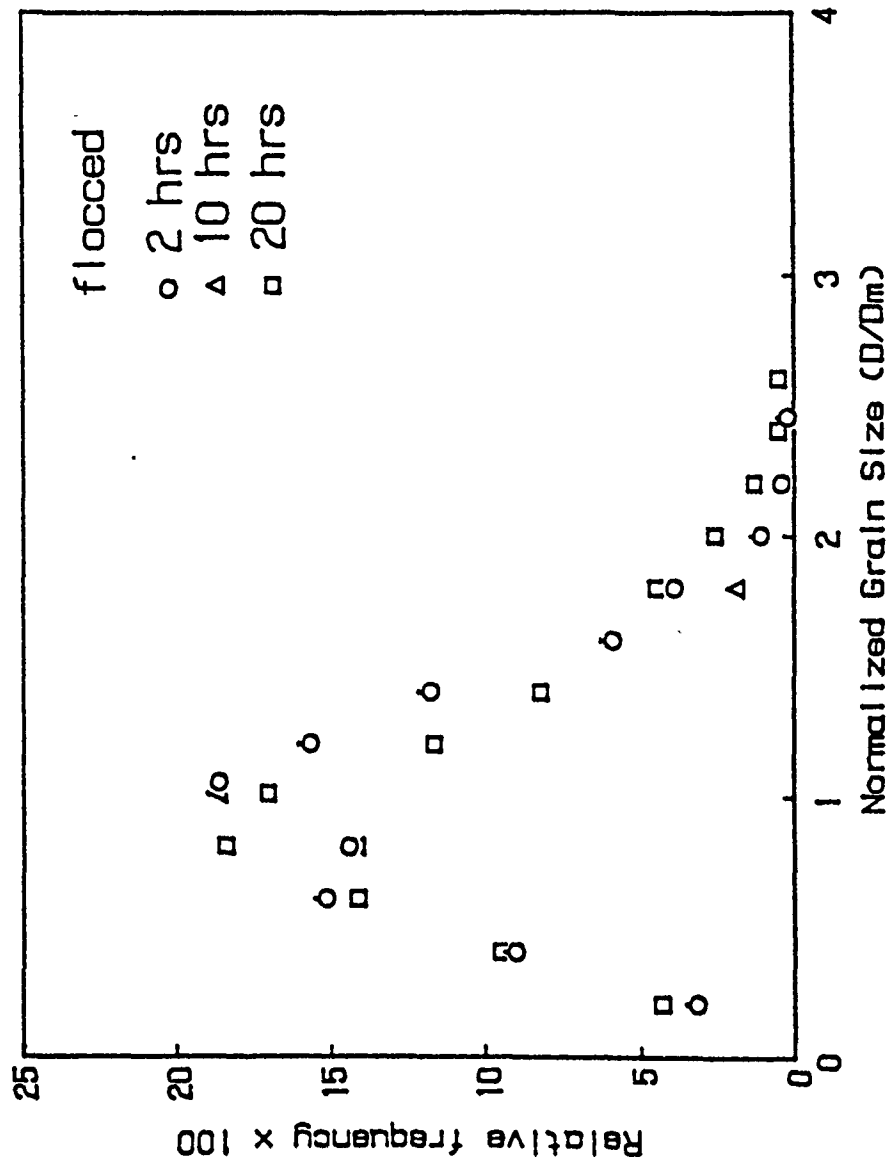


Figure 32. Bulk grain size distributions of the flocxed compact.

D_m is the mean grain size in micrometers, σ is the standard deviation, and N is the number of grains sampled. However, it should be noted that this is not unimodal broadening but is a shift to the bimodal abnormal grain growth stage.

5.0 SUMMARY AND CONCLUSIONS

5.1 Summary

In theory particle packing consisting of isotropic packing of perfect spheres and iso-coordinated voids will yield a stable monosized size distribution of grains upon sintering. Real systems approaching a narrow size distribution of particles and pores have been prepared with colloidal latex, silica, and recently titania. During sintering the presence of a slight deviation in isotropy of either pores or particles distributes itself through the microstructure by stress gradients which yields a finite grain size distribution as an end product.

Submicron titania powders were synthesized by precipitation techniques from both organic and inorganic metal ligand solutions. Inorganic precursors produced a particle distributions which were unusable in subsequent portions of the study. Routes using organic ligands produced particles which were of narrow size distribution and in usable particle concentrations. Insitu stabilized synthesis routes yielded the best distribution and size results of the organic ligand precursor processes.

Powder compacts were prepared in both the well dispersed and flocculated states by varying the electrostatic interaction potentials. Presence of steric stabilization was still apparent in the relatively dense packing of the "flocced" particle systems. Colloidal crystal formation was observed on the surface of the dispersed cakes; contours of packing indicated that this particle configuration extended into the compact.

Small samples of the compacts were first crystallized and then sintered by both isothermal and nonisothermal

techniques. It was found that abnormal grain growth occurred in cases where isothermal sintering was not used for the initial sintering periods. Further, it was deduced that the abnormal growth was instigated by growth of nuclei formed during the low temperature (1000-1100°C) transient times and that the nucleation - growth sequence was particle packing dependant. Reproduction of specific nucleation - growth sequences was difficult.

Evolution of surface microstructure was observed, in the absence of the abnormal growth), by a reiteration: sintering, carbon coating, observation, carbon sublimation, and resintering. Short time observations of the surfaces indicated the evolution of areas exhibiting short range hexagonal grain structure which were disrupted or included in larger grains at slightly longer times. After full surface density was attained a time independent normalized distribution was observed for short time periods with the advent of a bimodal distribution at longer times. Very stable normalized grain size distributions for the flocced case were observed.

Bulk microstructure evolution was characterized by sectioning of control samples sintered to the same total time as the reiterated surface samples. Evidence of pore stabilized and pore controlled microstructure evolution regimes were observed and linked to the surface microstructure. Time dependant normalized distributions were observed in the bulk due to growth of the large size tails. Conversely time independent bulk normalized distributions were apparent in the flocced case over the time periods observed. The regions of normalized distributions time dependence can be linked to the dominating mechanisms regimes of pore drag, grain boundary motion, or breakaway grain boundaries.

5.2 Conclusions

In theory, monosized spherical particles arranged in manner resulting in monosized pores should yield a narrow grain size distribution upon sintering. The breadth of the grain size distribution is expected to broaden with time to an equilibrium distribution which is then time independent.

The particle and pore size distribution required for experimental validation of the proposed equilibrium grain size evolution are hard to attain in normal practice. Hence, a narrow grain size distribution in solid state powder processing is extremely unlikely due to the inherent hierarchical clustering in the green state. In this study it was observed that a broad distribution of grain sizes evolves during sintering and is well established upon complete densification.

Particle rearrangement, pore growth, and particle coarsening during sintering are dictated by local particle density, not by compact bulk density. If the pore distribution cannot be controlled as closely as the particle distribution throughout a compact any benefit of "monosized" particles is largely negated during sintering.

Particle-pore systems with initially different hierarchies do not follow the same microstructure evolution path during sintering and grain growth. It has not been substantiated in this study whether or not the evolution paths converge at some point in the time-temperature domain.

6.0 BIBLIOGRAPHY

- 1) B. Allman, "Polycrystalline Colloids and Their Implications on Microstructure Evolution," MSc. Thesis, UCLA 1983.
- 2) I. Aksay and C. Shilling, Chapter 34 in Ultrastructure Processing of Ceramics, Glasses, and Composites, Ed. by L. Hench and D. Ulrich, J. Wiley & Sons, NY, 1984.
- 3) B. Kellet and F. Lange, "Influence of Particle Arrangement on Sintering," in Science of Ceramic Chemical Processing. Edited by L. Hench and D. Ulrich. Wiley & Sons, New York, 1986.
- 4) M. Yan, "Microstructural Control in the Processing of Electronic Ceramics," Mat. Sci. Eng., [48] 53-72 (1981).
- 5) H. Barringer and H. Bowen, "Formation, Packing and Sintering of Monodisperse TiO_2 Powders," J. Am. Cer. Soc., 65 c199-201 (1982).
- 6) G. Chol, "Influence of Milled Powder Particle Size Distribution on Microstructure and Electrical Properties of Sintered Mn-Zn Ferrites," J. Am. Cer. Soc., 54[1] 34-39 (1971).
- 7) I. Aksay and R. Kikuchi, "Phase Equilibria in Colloidal Systems", in Science of Ceramic Chemical Processing, Edited by L. Hench and D. Ulrich. Wiley & Sons, New York, 1986.
- 8) K. Davis and W. Russel, "A Model of Crystal Growth in the Sedimentation and Ultrafiltration of Colloidal Hard Spheres," unpublished work, Dept of Chem. Eng., Princeton Univ.
- 9) F.F. Lange, "Sinterability of Agglomerated Powders," J. Am. Cer. Soc., 67[2] 83-89 (1984).
- 10) H.E. Exner, Principles of Single Phase Sintering, Rev. Powd. Metal. Phys. Cer., 1 (1979).
- 11) W.D. Kingery and B. Francios, Sintering and Related Phenomena, Edited by G.C. Kuczynski, N. Hootan, and G.F. Gibbon, Gordon and Breach, NY (1967).

- 12) T.K. Gupta, "Possible Correlation Between Density and Grain size During Sintering," J. Am. Cer. Soc., 55[5] 276-277 (1972).
- 13) R.L. Coble, "Sintering Crystalline Solids I & II," J. Appl. Phys., 32[5] 787-799 (1964).
- 14) R.J. Brook, "Pore Boundary Interaction and Grain Growth," J. Am. Cer. soc., 52[1] 56 and 339 (1969).
- 15) D. Harker and E. Parker, "Grain Shape and Grain Growth," Trans. A.S.M., 34 156-201 (1945).
- 16) S. Kurtz and F. Carpay, "Microstructure and Normal Grain Growth in Metals and Ceramics. Parts I & II," J. Appl. Phys., 51[11], I 5725-5744, II 5745-5754, (1980).
- 17) R. Kikuchi, "Shape Distribution of Two Dimensional Soap Froths," J. Chem. Phys., 24[4], 861 (1956).
- 18) E. Carnal and A. Mocellin, "A Topological Model for Plane Sections of Polycrystals," Submitted to Acta. Metal..
- 19) S. Fakuda, R. Kikuchi, and I. Aksay, "Hierarchically Clustered Structures", Work in progress Univ. of Washington, 1987.
- 20) L. Edelson, "The Role of Particle Substructure in the Sintering of Monosized Titania," MSc. Thesis, UC Berkeley, 1986.
- 21) E. Matijevic, "Colloid Stability and Complex Chemistry", J. Coll. Int. Sci., 43 [2] 217-245 (1973).
- 22) J. Overbeek, "Recent Developments in the Understanding of Colloid Stability", *ibid*, 53 [2] 408-422 (1977).
- 23) J. Goodwin et al, Coll. Poly. sci., 252 464- (1974).
- 24) R. Ottewill et al, "The Preparation of PMMA Lattices in Non-Aqueous Media", Coll. Surf., 17 67-78 (1986).
- 25) W. Stober, A. Fink and E. Bohn, "Controlled Growth of Monodisperse Silica Spheres in the Micron Range," J. Coll. Int. Sci. 26, 62, (1968).

- 26) J. Jean and T. Ring, "Nucleation and Growth of Monosized TiO_2 From Alcohol Solutions," *Langmuir*, 2 251-255 (1986).
- 28) R. Heistand II, Y. Oguri, H. Okamura, W. Moffat, B. Novich, E. Barringer, and H. Bowen, "Synthesis and Processing of Submicrometer Ceramic Powders", in Science of Ceramic Chemical Processing. Edited by L. Hench and D. Ulrich. Wiley & Sons, New York, 1986.
- 29) E. Matijevic, M. Budnik, and L. Meites, "Preparation and Mechanism of Formation of Titanium Dioxide Hydrosols of Narrow Size Distribution", *J. Coll. Intf. Sci.*, 61 [2] 302-311 (1977).
- 30) M. Visca and E. Matijevic, "Preparation of Uniform Colloidal Dispersions by Chemical Reactions in Aerosols", *J. Coll. Intf. Sci.*, 68 [2] 308-319 (1979).
- 31) S. Okamoto and S. Hachisu, "Ordered Structure in Monodisperse Gold Sol", *J. Coll. Intf. Sci.*, 62 [1] 172-181 (1977).
- 31) E. Barringer, "The Synthesis, Interfacial Electrochemistry, Ordering and Sintering of Monodisperse TiO_2 Powders," Ph.D. Thesis, MIT, 1983.
- 32) A. Kose and S. Hachisu, "Kirkwood-Alder Transition in Monodisperse Lates I. Nonaqueous Systems", *J. Coll. Int. Sci.*, 46[3] 460-469 (1974).
- 33) I. Langmuir, "The Role of Attractive and Repulsive Forces in the Formation, " *J. Chem. Phys.*, 6[12] 873-896 (1938).
- 35) I. Efremov, "Periodic Colloidal Structures," in Surface and Colloid Science, edited by E. Matijevic, Wiley & Sons, NY, 1976.
- 36) Hachisu et al, "Kirkwood-Alder Transition in Monodisperse Latexes II. Aqueous Latexes of High Electrolyte Concentration", *J. Coll. Int. Sci.*, 46 [3] 470-476 (1973).
- 37) C. Barnes et al., "Order/Disorder Transitions in Concentrated Electrocratic Dispersions", *J.C.S. Faraday Trans. II*, 89, 136-148 (1978).

- 38) K. Takano and S. Hachisu, "Pressure of Kirkwood-Alder Transition in Monodisperse Latex", J. Chem. Phys., 67 [6] 2604-2608 (1977).
- 39) E. Dickinson, "Polydispersity and Osmotic Pressure of Stable Ordered Colloidal Dispersions", J. Chem. Soc., Faraday Trans. II, 75, 466-473 (1979).
- 40) J. Kielbauch, "Compaction and Sedimentation Behavior of Silica Powders as a Function of Particle Size", BSc. Thesis, Univ. of Washington, 1986.
- 41) K. Davis and W. Russel, "A Model of Crystal Growth in the Sedimentation and Ultrafiltration of Colloidal Hard Spheres", to be published.
- 41) I. Aksay, "Microstructure Control Through Colloidal Consolidation," in Forming of Ceramics, Adv. in Ceramics vol. 9, 1984.
- 43) H.E. Exner, G. Petzow, and P. Wellner, "Extension of Sintering Theories to Real Systems", Material Science Research Vol. 6, edited by Kuczynski (1973).
- 43) E. Barringer, R. Brook, and H. Bowen, "The Sintering of Monodisperse TiO_2 ", Mater. Sci. Res., 16, 1-21 (1984).
- 45) R.L. Coble and T.K. Gupta, "Intermediate Stage Sintering", in Sintering and Related Phenomena, edited by G. C. Kuczynski, et al, Gordon and Breach, NY (1967).
- 46) T. Kimura, Y. Matsuda, M. Oda, and T Yamaguchi, "Effects of Agglomerates on the Sintering of Alpha- Al_2O_3 ", Cer. Int., 13 27-34 (1987).
- 46) C. Smith, "Grain Shapes and Other Metallurgical Applications of Topology," in Metal Interfaces, 64-113, ASM Cleveland 1952.
- 48) A. Beck, Phil. Mag. Suppl., 3, 245 (1954).
- 48) P. Feltham, "Grain Growth in Metals," Acta Metall., 5 97-105 (1957).
- 50) N. Rivier and A Lissowski, "On the Correlation Between Sizes and Shapes of Cells in the Epithelial Mosaics", J. Phys. A:Math. Gen. 15, L143-L148, (1982).

- 51) M. Hillert, "On the Theory of Normal and Abnormal Grain Growth", *Acta Met.* 13, 227-238, (1965).
- 52) F. Rhines and K. Craig, "Mechanism of Steady-State Grain Growth in Aluminum", *Met. Trans.* 5, 413-425, (1974).
- 53) N.P. Louat, "On the Theory of Normal Grain Growth", *Acta Metall.*, Vol. 22, 721-724 (1974).
- 54) M. A. Fortes and A.C. Ferro, "Topology and Transformation in Cellular Structures", *Acta Metall.*, 33[9] 1697-1708 (1985).
- 55) A. Soares, A. Ferro, and M. Fortes, "Computer Simulation of Grain Growth in a Bidimensional Polycrystal", *Scripta Metall.*, 19 1491-1496 (1985).
- 56) M.P. Anderson, D.J. Srolovitz, G.S. Grest, and P.S. Sahni, "Computer Simulation of Grain growth I & II", *Acta Metall.*, 32[5] 783-802 (1984).
- 57) W. Sullivan and S. Cole, "Thermal Chemistry of Colloidal Titanium Dioxide," *J. Am. Cer. Soc.*, 42[3] 127-133 (1959).
- 58) P. Vergnon, F. Juillet, M. Astier and S. Teichner, "Sintering of Ultrafine Particles of Anatase and Delta Alumina", in *Science of Ceramics* vol. 5, British Ceramic Society.
- 58) H.E. Exner, "Principles of Single Phase Sintering," *Rev. Powd. Metal. Phys. Cer.*, 1 (1979).
- 61) O. J. Whittemore, Jr., and J. Sipe, "Pore Growth During the Initial Stages of Sintering", *Powder Tech.*, 9, 159 (1974).
- 60) C. Han, I. Aksay, and O.J. Whittemore, in *Advances in Material Characterization II*, ed. by R.L. Snyder, R.A. Condrate, Sr. and P.F. Johnson, Plenum 1985.
- 62) A.C. Hott and R.L. Eichelberger, "A New Transmitted Light Hot Stage", in *Sintering and Related Phenomena*, edited by G.C. Kuczynski, N.A. Hootan, and C.F. Gibbon, Gordon and Breach 1967.

- 63) T. Ikegami and Y. Moriyoshi, "Evaluation of Grain Growth Parameters", J. Am. Cer. Soc., 68 [11] 597-603 (1985).
- 64) R.C. Lowrie and I.B. Cutler, "The Effect of Porosity on the Rate of Grain Growth in MgO", Discussions in Sintering and Related Phenomena edited by G.C. Kuczynski, N.A. Hootan, and C. F. Gibbon, 1967.
- 65) H. Hu, "Grain Growth in Zone Refined Iron", Can. Met. Quart., 13[1] 275 (1974).

7.0 APPENDIX : Abnormal Grain Growth

It was hoped to arrive at an activation energy for grain growth by using 1200°C and 1100°C samples as well as the 1150° data. However, extensive abnormal grain growth was observed in the lg and flocced samples when sintered at 1200°C, as illustrated in Figure A1. While working with the insitu stabilized powders this type of sintering phenomena was noted in a variety of circumstances. If the initial crystallization and isothermal sintering steps are replaced by non isothermal sintering of the amorphous powders abnormal grain growth as illustrated is guaranteed. In fact by the methods attempted in this study the absence of isothermal sintering results in these flowing type grains regardless of powder state. Possibility of impurities have been discounted by resynthesis of powders using new precursors and slightly different processes. From initial work on the unstabilized powders it would appear that the insitu stabilization manifests itself in some structural aspect of the powder. The powders processed without surfactant yielded normal microstructures during preliminary work. As stated previously no difference in the DTA runs is apparent, neither is there a difference in the stabilized powder structure caused by the isothermal sintering step.

The original work on HPC²⁷ powders indicates that high grain boundary mobility was observed. Hiestand²⁸ found the same type of microstructures when the unstabilized particles were hydrothermally treated. Upon hydrothermal treatment the

Figure A1. Fracture surface of 170 g compact after nonisothermal at 50°C/min to 1150°C followed by cooling. Note the large grain (arrowed) in a small grain matrix (bar = 10 μ m).



spherical agglomerates broke down to the primary particle size; when sintered the extremely fine powders yielded large textured grains. From the observations of Hiestand and the fact that the abnormal growth does not exist in nonstabilized particles, a plausible explanation of the abnormal growth lies in the initial processing.

Observations of fracture surfaces indicate that only certain sites in the compacts, nuclei, give rise to the abnormal growth in an otherwise normal microstructure. These nuclei are not apparent in the 170g microstructure at any temperature after the crystallization and isothermal sintering steps. In the case of the remaining powder compacts the concentration of nuclei are in the bulk, not at the surface of the samples and growth tends to be along an interface, as seen in Figure A1, in an otherwise submicron size grain structure. Large grains with a surface texture resembling the initial particle packing occurring at short times, after long periods the texture disappears the grain surfaces flatten out.

All qualitative observations indicate a nucleation and growth behavior which is highly dependant on particle packing. The insensitivity of a well packed system to this abnormal growth is probably due to the high number of nucleation sites for the process which in the growth regime impinge on each other and hence do not grow. In a less well packed system the number of nuclei are less and there is no hindrance to growth through the microstructure. There is also a dependence on the physical state of the particles, i.e. crystalline or amorphous. It would be a difficult task to isolate a nucleation point prior to its growth to ascertain if in fact it were crystalline, phase and lattice constant, or amorphous. Evidence that the nucleation is at a lower temperature than 1150°C is seen in the presence of

nuclei at 1050°C in a fracture surface of a flocced compact sintered for 5 minutes. By passing through the nucleation range at a sufficiently high rate abnormal growth is avoided as is seen in the microstructure studies. Conversely, by residing in the nucleation regime for even a very short period areas of abnormal growth are seen. The time variation in sintering between 750°C and 1150°C was on the order of 15 seconds with a probable variation of 5 seconds. Whether or not an amorphous phase or an abnormal crystalline phase present was not discernible by x-ray diffraction.

APPENDIX II

Steven K. Fukuda*

The Evolution of Cellular Structures

Ph.D. Dissertation

Department of Materials Science and Engineering,
University of Washington,
Seattle, Washington

1988

* Currently Associate Professor in the College of Ceramics at State University of New York, Alfred, New York 14802.

© Copyright by
STEVEN K. FUKUDA
1988

The Evolution of Cellular Structures

by

STEVEN K. FUKUDA

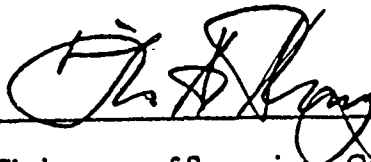
A dissertation submitted in partial fulfillment
of the requirements for the degree of

Doctor of Philosophy

University of Washington

1988

Approved by



(Chairperson of Supervisory Committee)

Program Authorized

to Offer Degree

Materials Science and Engineering

Date

August 15, 1988

In presenting this dissertation in partial fulfillment of the requirements for the Doctoral degree at the University of Washington, I agree that the Library shall make its copies freely available for inspection. I further agree that extensive copying of this dissertation is allowable only for scholarly purposes, consistent with "fair use" as prescribed in the U.S. Copyright Law. Requests for copying or reproduction of this dissertation may be referred to University Microfilms, 300 North Zeeb Road, Ann Arbor, Michigan 48106, to whom the author has granted "the right to reproduce and sell (a) copies of the manuscript in microform and/or (b) printed copies of the manuscript made from microform."

Signature

Steven K. Jorde

Date

15 AUG 88

University of Washington

Abstract

THE EVOLUTION OF CELLULAR STRUCTURES

by Steven K. Fukuda

Chairperson of the Supervisory Committee: Professor Ilhan A. Aksay
Materials Science and Engineering

This work extends the application of the Cluster Variation and Path Probability Methods to the description of cellular structures. Both methods are used to describe how 2-dimensional cellular structures develop a common stationary cell coordination distribution. Although all structures develop to a common stationary state, the evolution of each structure to the stationary state is unique. The results for both fully dense and partially dense cellular structures are presented. The fully dense system is relevant to the development of the cell coordination distribution prior to normal grain growth. The partially dense system is relevant to the densification (sintering) behavior of partially dense ceramic compacts.

TABLE OF CONTENTS

	<i>Page</i>
List of Figures	iv
List of Tables	vi
List of Abbreviations and Terms	vii
Chapter 1: Introduction	1
1.1 Motivation	1
1.2 Method of Attack	5
1.3 Scope	6
Chapter 2: Background	9
2.1 Classical Grain Growth Theories	9
2.2 Simulations	11
2.3 Metric-Topological Correlations	14
2.4 Topological Theories	16
2.5 Stochastic Theories	16
2.6 Summary	17
Chapter 3: CVM, PPM, and Model-0	20
3.1 Dual Space	21
3.2 2-D Topological Processes	23
3.3 CVM & PPM for Model-0	25
3.3.1 Model-0 State Variables	26
3.3.2 Entropy	29
3.3.3 Maximum Entropy	29

TABLE OF CONTENTS (Cont.)

	<i>Page</i>
3.3.4 CCD Calculation	31
3.3.5 F-0 Description	31
3.3.6 State-Path Equations	34
3.3.7 F-0 Results and Discussion	35
3.4 Summary	43
Chapter 4: Model-V	44
4.1 E-V Description	44
4.2 E-V Results and Discussion	49
4.3 F-V Description	52
4.4 F-V Results and Discussion	57
Chapter 5: Model-VI	69
5.1 E-VI Description and Results	69
5.2 F-VI Description	75
5.3 F-VI Results and Discussion	79
Chapter 6: Summary	88
References	94
Appendix A: Model-V Program Source Code	97
Appendix B: Model-VI Program Source Code	115

LIST OF FIGURES

<i>Figure</i>	<i>Page</i>
1. Effect of Dispersion on Green Microstructures	3
2. Examples of Microstructural Evolution	4
3. Comparison of Stationary CCDs	19
4. Dual Representation of a Cellular Structure	22
5. 2-D Topological Processes	24
6. Z1 vs. time	36
7. Evolution of the Model-0 CCD	37
8. Model-0 Dual & Real Rendering at $t=0.0$	40
9. Model-0 Real Space Rendering at $t=0.02, 2.0$	41
10. Model-V Effect of CHM on Equilibrium CCD	50
11. Model-V Effect of R21 & R31 on Equilibrium CCD	51
12. Model-V Relation of State and Path Variables	54
13. Model-V X1 vs. time	59
14. Model-V Evolution of the CCD	61
15. Model-V CCD μ	62
16. Model-V Evolution of the VCD	63
17. Model-V Evolution of the Void Density Dist.	65
18. Model-V Evolution of S/k, BCHM, and BGP	66
19. Model-V State Trajectories on the z1-x1 Plane	67
20. Model-VI 1-Point S.V. & the T1 and T2 Process	74
21. Model-VI S/k vs. x1	76
22. Equilibrium CCD for Emie-VI and Emie-0	77

LIST OF FIGURES (Continued)

<i>Figure</i>		<i>Page</i>
23.	Model-VI Relation of State and Path Variables	80
24.	Model-VI X_1 vs. time	84
25.	Model-VI Evolution of the CCD	85
26.	Model-VI State Trajectories on the x_2 - x_1 Plane	87
27.	Comparison of CCD to other works	89
28.	Comparison of VCD to an alumina structure	91

LIST OF TABLES

<i>Number</i>		<i>Page</i>
1.	Model-0 State Variables	27
2.	Model-0 Reduction Relations	27
3.	Model-0 Cell Coordination	32
4.	Model-0 Path Variables	33
5.	Model-V Three point State Variables	45
6.	Model-V Reduction Relations	46
7.	Model-V Path Variables	53
8.	Model-V Path Reduction Relations	55
9.	Model-V State-Path Equations	56
10.	Model-V T0 State-Path Reduction Relations	58
11.	Model-VI Three point State Variables	70
12.	Model-VI Subcluster State Variables	72
13.	Model-VI State Reduction Relations	73
14.	Model-VI 3-point Path Variables	78
15.	Model-VI Path Reduction Relations	81
16.	Model-VI State-Path Equations	82
17.	Model-VI T0 State-Path Reduction Relations	83

LIST OF ABBREVIATIONS AND TERMS

CCD Cell Coordination Distribution

CHM The variable provided to the CVM calculation that in effect sets the stationary value of the point state variables. In the PPM calculations, CHM is defined as the ratio of the forward to reverse T2 process.

CVM Cluster Variation Method

d average linear intercept

Euler's Relation In 2-dimensions, Euler's relation requires that the average number of edges per cell equal 6 for a cellular structure that fills the plane and has only vertices with coordination 3.

GSD Grain Size Distribution

Lewis law An experimental correlation relating the cell area to the cell coordination.

The Lewis law has the form, $R = a(n-2)$, where a is a constant, n is the cell coordination, and R is the equivalent circular radius of the cell.

n grain growth exponent (chapter 2). The exponent in the equation

$$R = \alpha t^n$$

where R is the average grain size and t is the time.

n cell coordination

NGS Normalized Grain Size The ratio of the equivalent circular radius of a cell to the averaged equivalent circular radius of all cells.

NIM Natural Iteration Method.

Perimeter law A correlation relating the cell perimeter to the cell coordination. The perimeter law has the same form as the Lewis law.

LIST OF ABBREVIATIONS AND TERMS (Cont.)

PPM Path Probability Method

von Neumann's growth equation Equation developed by von Neumann that relates the cell growth rate to the cell coordination. The equation has the form,

$$dR/dt = a(n-6)$$

where a is a constant, n is the cell coordination, R is the equivalent circular radius of the cell, and t is time.

μ The second central moment of the CCD

ACKNOWLEDGEMENTS

The author wishes to express sincere appreciation to Professor Ryoichi Kikuchi for his assistance and guidance on the calculational techniques used in this work. He has also provided the author with an exemplary role model of a scientist. The author also wishes to express sincere appreciation to Professor Ilhan A. Aksay for providing his time and guidance in directing this research. Finally, the author thanks Jerry Garcia for showing him the location of square one (DARKSTAR).

The author also acknowledges the financial support provided by Kenneth M. and Naoe Fukuda, the FELIXERNIEGROUP, and the U.S. Army Research Office under grant number DAAG29-85-K-0136, "Hierarchically Clustered Structures: Formation During Colloidal Processing and Evolution During Sintering".

DEDICATION

To Naoe and Kenneth Masaru Fukuda for their constant love and support, I dedicate this work with all my love. To Felix and Ernie for their companionship and support through trying times, this work is also for you.

CHAPTER 1. INTRODUCTION

1.1 Motivation

The goal of ceramic processing is to produce a product with the most desirable properties in the most efficient manner. Desirable properties and efficient processing can be viewed as external constraints by the processor, and both parameters are usually determined by the product's targeted market. The processor takes a list of desirable properties and uses his/her materials science background to translate these usually macroscopic properties into a list of candidate materials and desirable microscopic properties. The problem is now more clearly defined and is reduced to moving in an efficient manner from starting materials and a set of possible processing techniques to a final product that has the most desirable microscopic properties.

Although several processing routes are available, one of the most widely followed paths is particulate processing. This processing path has three major steps where the starting materials, usually in the form of small particles, are mixed, consolidated, and heat treated. Since these steps are sequential, the processor would like to understand how each step affects the final state. Then we can choose the appropriate processing techniques in order to meet our objectives. For example, if the heat treatment step erases the effects of the previous steps, then the processor can choose the most cost effective route for the first two steps and concentrate on

optimizing the heat treatment. More likely is the case where all three steps affect the final state and the choice of the processing route becomes more difficult since we must now find a route that gives us the desired final state while retaining the desirable properties from the previous step. An example of this is the processing of a dense alumina body from a bimodal distribution of alumina particles. If the mixing step is incomplete, the consolidated compact will undergo differential densification during heat treatment and the compact will warp or will generate microcracks in the final structure. If the mixing is complete but the consolidation is poor, the effect of mixing may be negated because the particles segregate during consolidation resulting in a poor final product.

Figures 1 and 2 show microstructures that are typical of the colloidal processing route.¹ Figure 1 presents silica particulate compacts consolidated from flocculated (Fig. 1a) and dispersed suspensions (Fig. 1b) and illustrate the range of green microstructures that can be engineered in the mixing and consolidation stage of the processing path. Figure 2 presents alumina microstructures for two consolidated compacts as they evolve from a particulate structure to a fully dense monolithic body. The left column of Fig. 2 shows the evolution of a compact that was consolidated from a dispersed suspension whereas the right column of Fig. 2 shows the evolution of a compact consolidated from a flocculated suspension. The micrographs of Fig. 2 appear to support the hypothesis that the initial structure of the compact affects the densification behavior and may also affect the "final" structure attained by the compact. Although Fig. 2 cannot quantitatively support or reject the hypothesis that different structures evolve along unique paths, it leads us to the central question of this work. Specifically, we attempt to answer two questions about the heat treatment step: 1) is there an equilibrium (or steady state) structure that all green compacts approach

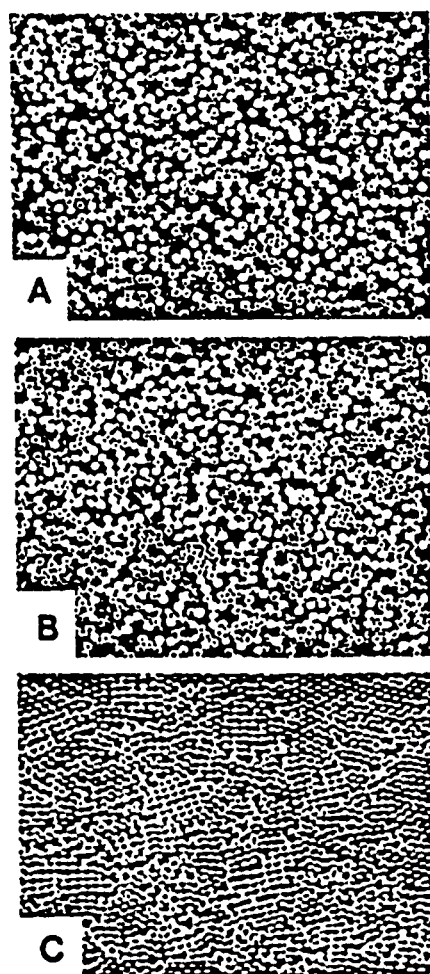


Figure 1. Micrographs of silica spheres consolidated from flocculated (a) and dispersed (b) suspensions illustrating the range of initial structures prior to densification.

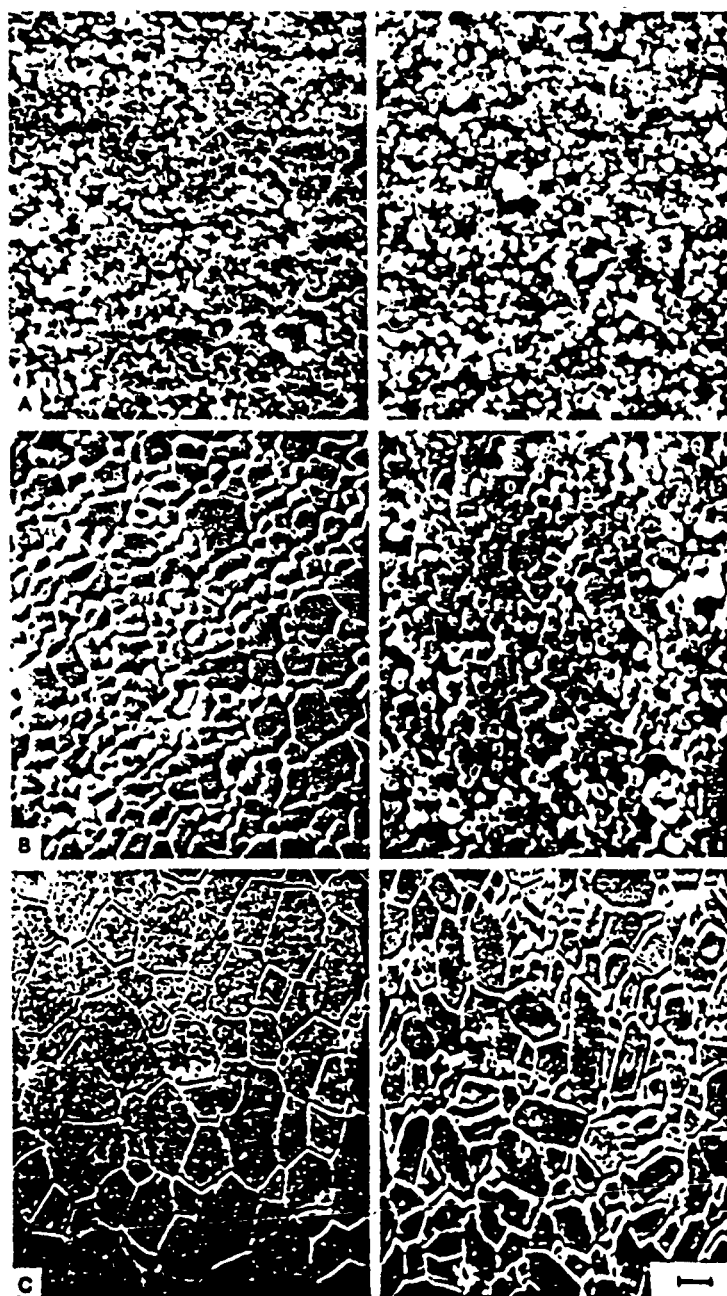


Figure 2. Micrographs of alumina sections at various stages of densification illustrating the structural evolution of particulate compacts from partially dense structures to fully dense bodies. The left column of micrographs began with a compact consolidated from a dispersed suspension while the right column began with a compact consolidated from a flocculated suspension.

during the heat treatment step, and 2) are the paths followed by the microstructure distinct?

The work presented in this dissertation hopefully contributes to the understanding of how the heat treatment step affects the final structure and the structures produced by the mixing and consolidation steps. In addition, the results of this work is relevant to the discussion of the effect of grain size distribution and initial green density on the final density of the ceramic body. For example, Barringer et al. demonstrated that monosized spherical submicron powders could produce fine grained fully dense structures at substantially lower temperatures than is common in practice.^{2,3} Yan et al. also concluded that monosized particle distributions are required to produce dense fine grained structures by deriving the conditions for pore separation from grain boundaries.⁴ Occhionero and Halloran concluded that the initial (green) density affects the pore size distribution and also affects the density where grain growth commences.⁵ The discussion of the relevance of this work to the literature cited above is postponed until Chapter 6.

1.2 Method of Attack

The questions posed above require a calculational technique that can determine an equilibrium structure and that will provide the path that a structure will follow to that equilibrium structure. The calculational methods chosen for this work were the Cluster Variation Method (CVM)⁶ and the Path Probability Method (PPM).⁷ The CVM is an approximate method that takes into account the interactions more accurately than the pair approximation in determining the equilibrium state of a system. The PPM is an extension of the CVM that allows one to calculate the most likely path that the system will follow toward the equilibrium state. The CVM was

first applied to cellular structures in 1956 by Kikuchi ⁸ where he was able to calculate for a soap froth the equilibrium cell coordination distribution (CCD) that was in fairly good agreement with the available experimental data. The results of Kikuchi's soap froth analysis indicated that the answer to the first question posed in the previous section was affirmative. Kikuchi asked the second question but left it unanswered due to the lack of a method to analyze it of how these structures developed in time. This question provided the starting point for our investigation.

1.3 Scope

Although the motivation for this work stems from very practical needs, several restrictions have been applied that require more care in the application of the results to real systems. However, these restrictions do not in any way negate the validity of the results in terms of answering the questions posed previously. The restrictions applied to this study are as follows.

First, only two-dimensional cellular structures are considered in this study. This restriction was used to keep the problem focused on the goal of this research while minimizing the mathematical clutter associated with an additional dimension. Although the CVM and PPM are capable of handling three dimensional systems, it is at the cost of a geometric increase in the number of variables and equations that must be solved. For reasons argued below, this additional cost is not warranted since the two-dimensional analyses presented in the following chapters satisfy the questions stated previously.

Second, the analyses use the zero limit of energy that reduces the principle of minimizing free energy to one of maximizing the system "topologic" entropy. This restriction does not affect the validity of our analysis because the topological

properties of a cellular system are independent of the metric properties of the system. The interaction energies depend on the geometry of the system but the CCD is purely topological and should be independent of the system geometry. This is supported by the very similar structures exhibited by two-dimensional soap froths, polycrystalline planar sections, columnar basaltic formations, and undifferentiated cellular arrangements in cucumbers.⁹ These structures span several length decades and operate under different growth mechanisms but exhibit similar CCDs.

A simple dimensional analysis of the boundary energy and the entropy terms show that the topologic entropy is of order 1 while the grain boundary and surface energy terms divided by temperature are many orders of magnitudes larger than the entropic term and provides the driving force for densification of particulate compacts. Since the boundary energy terms are much larger than the topological entropy of mixing, why do the systems mentioned above develop similar CCDs? This interesting question is not addressed in this work, but the approach by Rivier described in the next chapter offers the most promise toward understanding how the system topology affects the system free energy.¹⁰

By restricting this study to the topological behavior of cellular structures, we give up the possibility of predicting direct grain growth and densification rates since both are metric dependent quantities. This trade-off is serious in terms of practical applications of microstructural development but does not affect the question of unique evolution paths. If the topological evolution of cellular structures is shown to be distinct, then the question is answered regardless of the geometric considerations.

The remainder of this dissertation is arranged as follows. Chapter 2 is a brief summary of the grain growth and densification theories in the current literature. The CVM and PPM are described in Chapter 3, and the analysis for the first model

(Model-0) is presented and is used to illustrate how CVM and PPM are applied. The densification model (Model-V) and the full grain growth model (Model-VI) are presented in Chapters 4 and 5, respectively. The CVM calculations for Model-0 and Model-VI are essentially the same as Kikuchi's 1956 calculations. The PPM calculations for Model-0 and Model-VI are the extensions to Kikuchi's work. The densification model (Model-V) is original and was developed while debugging Model-VI. Chapter 6 concludes this dissertation with a short discussion comparing the results of the PPM analysis with available experimental data and also discusses some of the unresolved and "curious" questions uncovered during the course of this work.

CHAPTER 2

BACKGROUND

A short review and summary of the various grain growth theories found in current literature is included for two reasons. First, two of the three models that are the core of this dissertation represent fully dense systems, and the evolution of these systems is interpreted as the initial behavior of systems undergoing grain growth. Second, this review of material allows us to place this dissertation into its proper context with respect to the existing body of knowledge.

2.1 Classical theories

The "classical" theories of grain growth are contained in the papers by Feltham,¹¹ Hillert,¹² Louat,¹³ and Rhines and Craig.¹⁴ The first three papers are mean field theories in that the growth rate of the "average" grain is calculated and grain size distributions (GSD) are examined. Feltham assumed a log-normal grain size distribution that was time-invariant and concluded that the grain growth exponent, n , was 0.5. He also found that the maximum normalized grain size (ratio of the maximum grain radius to the average grain radius) was 2.5.

Hillert and Louat both used the continuity condition of the grain size distribution function, $f(R,t)$, of the form

$$(df/dt) + (dj/dR) = 0 \quad (1)$$

where j is the flux of the grain distribution. Hillert used a flux that was proportional to the velocity of the grain boundary motion which in turn was proportional to the curvature of the grain boundary. Louat used a flux of the form of Fick in which the grain boundary diffused. Both methods produced a grain growth exponent of 0.5 but obtained different grain size distributions and maximum normalized grain sizes. Hillert obtained a GSD that peaked at a normalized grain size (NGS) of 1.0 was skewed toward a NGS of 0.0 and had a maximum NGS of 2.0. Hillert also observed that a 5-7 coordinated grain pair acted similar to a dislocation in a perfect hexagonal lattice and that the rate of the dislocation climb was related to grain growth. This also resulted in a parabolic growth law assuming that the defect concentration was constant. The defect concentration, c , was defined to be the number of defects (average coordination difference from 6) per grain and was determined to be 0.75.

Louat obtained a GSD that was similar to the log-normal distribution assumed by Feltham but which fit the experimental data closer than the log-normal distribution. Louat's GSD did not exhibit a cutoff but rapidly went to 0 for large sizes.

Rhines and Craig focused on three-dimensional topological features of polycrystalline aluminum and developed a rate equation for the average volume per grain. They found a grain growth exponent of 0.33 based on true volume and a value of 0.43 based on mean intercept measurements which agreed with the values of the Exxon simulation described in section 2.2 below. In their reply to a comment by Louat and Morral, Rhines and Craig made two points that are still valid today. First, they pointed out that the soap froth model did not behave like the observed polycrystalline growth. Second, they observed that the grain radius determined from the grain volume was fundamentally different from the grain radius taken from planar

sections in that the latter was shape dependent while the former was shape independent.

2.2 Simulations

Monte Carlo simulations of grain growth were reported in a series of papers by Sahni-et-al. (referred to hereafter as the Exxon group).¹⁵⁻¹⁷ Their simulation used 200 x 200 square and triangular lattices with periodic boundary conditions to model two dimensional grain growth. Each lattice point was assigned a number between 1 and Q which represented the "grain orientation" of the lattice point. A Monte Carlo time step (MCS) was defined as N microtrials where N was the number of lattice points in the simulation. A microtrial consisted of randomly choosing a lattice site and the new trial orientation, calculating the energies of both configurations (using the Potts Hamiltonian), and choosing the configuration with the lowest energy ($T=0$). The most important findings of the Exxon group with respect to this work are as follows. First, they found that the grain size distribution was time invariant and was not log-normal. Second, the grain growth exponent, n , was 0.42 instead of 0.5. Third, the grain size distribution had a maximum cutoff around $2.7\bar{R}$ where \bar{R} was the mean grain size. Fourth, the grains appeared to obey a perimeter law, $R = a(n-2)$, where n is the grain coordination and a is a constant. Finally, they obtained the cell coordination distribution (CCD) for the simulations and observed that the CCD was also time invariant.

The Exxon group extended their simulations to three dimensions¹⁸ and reported that the normalized grain size distributions were time invariant. The distributions obtained from the simulations fit the experimental distributions better than the log-normal or Hillert's distributions and were in agreement with Louat's

distribution. The group also reported that the average growth exponent, n , obtained from three different techniques (volume, cross-sectional area, and cord length measurements) was identical to within a standard deviation. The growth exponent was smaller ($n=0.37$) than the exponent derived in the two-dimensional case ($n=0.41$) but both were within the range of growth exponents determined from experimental data. The similarity of the growth exponents obtained from different methods indicates that the simulated structures were compact and could be assumed to be spherical. This last result seems to contradict the results that Rhines and Craig obtained via serial sectioning in which the growth exponent derived from volume measurements was different from that derived from chord length measurements. While these three dimensional simulations are not directly applicable to the present research, it is encouraging in terms of using planar section measurements to estimate three dimensional quantities.

Weaire and Kermode¹⁹⁻²¹ also simulated a two-dimensional soap froth but used a different method than that used by the Exxon group. Their work was motivated by the work of Smith²² and Aboav²³ in which opposing conclusions were drawn from the same data set. Smith concluded that the CCD evolved to a time-invariant distribution and that the average cell area grew linearly in time. Aboav used a larger portion of the data set generated by Smith and concluded that there was no stable CCD and that the average linear intercept, d , and the second central moment of the CCD, μ , increased linearly in time.

The simulations of Weaire and Kermode involved a two step process consisting of a diffusion step in which the cell areas were adjusted by allowing the diffusion of gas across the cell boundary followed by a local relaxation of the vertices. During the relaxation step, the boundary length was tested for a T1 or T2 process.

The T1 and T2 processes are the basic topological processes in a two-dimensional space and are described more fully in the next chapter. The simulation consisted of 100 cells with periodic boundary conditions and was allowed to proceed until only 40 cells remained. The results of the simulations seem to agree with Aboav's findings in that μ increased with time and the CCD also changed with time. They also concluded that Lewis' law (an experimental correlation between cell area and cell coordination) did not hold for the soap froth. The question of the asymptotic behavior of the soap froth was left unanswered because of the small simulation size.

Wejchert, Weaire, and Kermode ²⁴ also reported the results of a Monte Carlo simulation of a two-dimensional soap froth. The simulation was essentially identical to the Exxon simulation with the exception of an additional term in system energy. The additional term weighted the cell energy such that each cell grew to its "target area". The target areas were calculated for each cell using von Neumann's growth equation ²⁵ at each time step. They were able to reproduce the Exxon results by neglecting the target area term. When the target area term was included, they calculated a grain growth exponent of 0.49 and a stable CCD in accordance with the conclusions of Smith.

Soares, Ferro, and Fortes ²⁶ (hereafter referred as the Portuguese group) simulated two-dimensional grain growth based on a driving force different from that used by the Exxon group or by Weaire and Kermode. The Portuguese group assumed straight grain boundaries and allowed the grain vertices to relax under the action of line tensions that acted along the grain boundaries. The simulation was initiated on a random Voronoi network and the vertices were allowed to relax. A T1 process occurred when a shrinking edge reached a critical length, at which time the edge was replaced by an edge perpendicular and at the midpoint of the initial edge. A T2

process occurred when one edge of a three coordinated cell dropped below the critical length, at which time the cell was replaced by a vertex. The direct use of the topological unit processes in the simulations by the Portugal group also made the simulations distinct from the Exxon and Weaire and Kermode simulations.

Although the simulation was completed for a very small number of cells (48 grains), they observed the following results. First, the CCD broadened with time. Second, the second moment of the CCD increased with time with no indication that it would reach a stationary value. Third, the grain growth exponent was estimated to be near 0.5. The strength of the results should be reduced because of the very small simulation size. The Portuguese group also noted that the stationary second moment observed by Weaire and Kermode was probably due to the balance between the two topological processes where the T1 process increases the second moment, whereas the T2 process decreases the second moment. This is incorrect since the PPM calculations presented in later sections show that the second moment reaches a stationary point with the T1 process.

2.3 Metric-Topology Correlations

Beenakker published two analyses of soap froth evolution that focused on trying to understand the correlation between the cell area and the cell coordination. In his first theory,²⁷ Beenakker used a mean field theory approach in which he minimized the free energy of the froth assuming regular polygons, and used the constraint that the average cell coordination was 6. The results of this analysis indicated that the correlation between normalized cell area and cell coordination did not follow the linear behavior according to Lewis' law but increased very rapidly for large coordination. A second result indicated that the scaled distribution of cell areas

against the cell coordination alternately broadened and collapsed. Beenakker attributed the behavior of the distribution to the assumption that the cell surface energy was the dominant mechanism in the development of the area-coordination correlation.

Beenakker's second analysis^{28,29} used von Neumann's cell growth equation with additional terms to account for the diffusion process. Beenakker also generalized the growth equation to a distribution that depended on the cell area, coordination, and time. The results of his second analysis indicated that the cell area-coordination correlation was not fully described by the Lewis or by the perimeter law. He did find that the scaled normalized cell area distribution was time independent in the long time limit and was very similar to the distribution obtained by the Exxon group. He also showed that the grain growth exponent was 0.5 and that topological constraints did not modify the mean field value. He attributed the Exxon group's lower grain growth exponent to be due to the small grain size relative to the spacing of the simulation lattice. The CCD obtained from Beenakker's analysis was sharply peaked at coordination 6.

Marder³⁰ also used von Neumann's growth equation with a distribution function dependent on cell area, coordination, and time. He modified the equation to account for the rate that a cell of a given area would gain or lose an edge. His results showed a linear increase of cell area with time, an area-coordination correlation that did not follow a Lewis or a perimeter law, and a stable CCD at long times. The behavior of μ is curious in that it increased rapidly to 5 (corresponding to the beginning of the scaling regime) and then decreased to a value of around 4.

2.4 Topological Theories

Rivier and Lissowski¹⁰ showed that Lewis' law relating the average area of an n coordinated cell was a result of maximizing the entropy of the coordination distribution under the constraints of fixed total area and topology (i.e. average coordination is 6). Rivier and Lissowski concluded that structures that did not exhibit Lewis-type behavior must be under constraints in addition to the space-filling requirement. In a later paper, Rivier³¹ incorporated an additional correlation between cell perimeters and coordination and found that the perimeter law resulted in a higher entropy than the Lewis law. He also showed that the grain size distribution obtained from his CCD and the perimeter law matched the GSD generated by the Exxon group.

Mocellin and his coworkers in Switzerland^{32,33} (the Swiss group) also used topological arguments to derive the CCD for two-dimensional cellular structures. Their analysis followed the effect of the T1 and T2 processes on the CCD and they were able to generate a CCD that was very similar to Kikuchi's results. Their analysis also produced conditions for the stability of the CCD that related the T1 and T2 rates to the CCD. The model had one adjustable parameter (the ratio of the T1 to T2 process rates or the probability of the three coordinated cell) and had defect concentrations in the range from 0.7 to 0.75 and second moments of the CCD in the range from 3.0 to 4.0.

2.5 Stochastic Theories

A recent paper by Pande³⁴ used a stochastic approach to model grain growth. This paper presented a very clear explanation of the distributions used to model the GSD and gave the clearest perspective on the current confusion of comparing

experimental data to derived distributions. Pande began with a Langevin type equation containing a "deterministic" term that modeled the drift of the boundary due to curvature and a "noise" term that represented the randomness (or, our lack of knowledge of the details) of the system. This resulted in a Fokker-Planck partial differential equation that was solved and found to be a modified Rayleigh distribution. This distribution results in a grain growth exponent of 0.5. The distribution can be generalized by a transformation of the grain size variable in order to recover grain growth exponents less than 0.5 (to match experimental data and recover the Ostwald ripening case). However, the physical motivation for choosing the appropriate transformation was not clear.

Pande's most interesting comments concerned the comparison of grain size distributions. First, he concluded that the modified Rayleigh distribution derived from a stochastic approach to grain growth was very similar to the log-normal distribution. Second, and most important, the experimental data fit the log-normal distribution as well as the modified Rayleigh distribution, i.e. the "noise" in the data completely swamped the minor differences between the two distributions.

2.6 Summary

The current state of grain growth theories can be characterized as confused. The grain growth exponent is predicted to be 0.5 although most experimental data show values for n to be less than 0.5. This difference should not be taken seriously since the problems associated with obtaining an experimental value of n (i.e. obtaining a large enough sample size over several decades of growth) prevent a final experimental judgment of the various grain growth theories. This also applies to the predicted shape and asymptotic behavior of the grain size distribution. Of the research

presented in this section, the work of Pande and Rivier are the most significant in that they represent the two most general approaches to the problem. Pande's work is significant because he explicitly treated grain growth as a stochastic process. Rivier's work is significant because he started from the topological requirements of a space filling network and used maximum entropy to produce a GSD. He was also able to attach a physical motivation for the occurrence of either Lewis or perimeter correlations.

Figure 3 shows the CCDs produced by the Exxon and Swiss groups along with the CCD produced by Marder. Two CCDs obtained from experimental data are also shown in Fig. 3. The first experimental distribution is from Aboav's paper that was based on Smith's soap froth data on 1372 cells. The second experimental distribution was obtained by the author and was based on 277 grains from a planar section of polycrystalline alumina. The final distribution in Fig. 3 was from the results of the Ernie-VI calculation described in chapter 5.

The research described in this section was concerned with the behavior of a fully dense cellular structure in the scaling regime where the CCD was stationary and the structure increased in size in a self-similar fashion. The research presented in the following sections attempts to describe how structures develop the stationary CCD prior to self-similar growth.

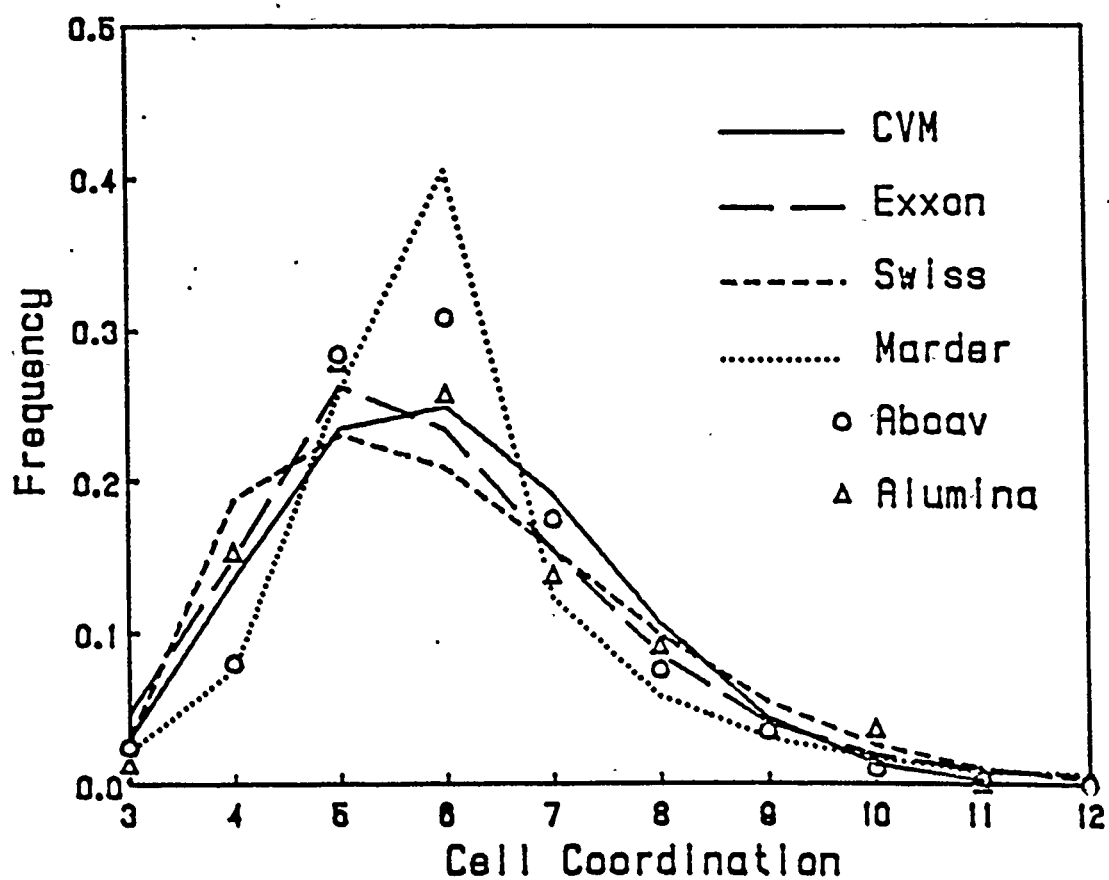


Figure 3. Comparison of Cell Coordination Distributions

CHAPTER 3

CVM, PPM, AND MODEL-0

The Cluster Variation Method (CVM) and Path Probability Method (PPM) are described in this chapter. The general description of the CVM is given in Kikuchi's 1951 paper ⁶ and the PPM is described in Kikuchi's 1962 paper. ⁷ Both methods are approximate calculations; the accuracy of the calculation is dependent on the size of the largest cluster used in the calculation. Occurrence probabilities of the cluster and subcluster configurations (called state variables in CVM and path variables in PPM) are combined to form an entropy expression that counts the number of ways of distributing the clusters and subclusters onto a lattice of the user's choice. The entropy term is incorporated in the free energy of the system and the free energy is minimized under a set of constraints including cluster normalization, subcluster relations, and cluster topological restrictions. In the analyses presented below, only the entropy term is maximized (zero limit of the energy to temperature ratio). The discussion rationalizing the maximum entropy approach is postponed until Chapter 6. The CVM performs this maximization once on the state variables to calculate the equilibrium distribution of clusters within the system. The PPM performs this maximization on the path variables at each time step in order to calculate the most probable path that the system will follow. The path variables are integrated to calculate the state variables at each time step. The analysis for Model-0 is presented

in this chapter in order to illustrate how the CVM and the PPM are applied to cellular structures. Before presenting the Model-0 calculations, the next two sections discuss the dual representation of cellular structures and the possible two-dimensional topological processes.

3.1 Dual Space

A cellular structure is represented by a graph consisting of a set of points and edges. Each edge is terminated by a point at each end and each point can have an arbitrary number of edges terminating at the point. Each edge represents a boundary separating two adjacent cells and the number of edges that enclose a cell is the coordination of that cell. For cellular structures of interest here, each point (or vertex) has three terminating edges and therefore represents a triple point where three cells are adjacent to each other. Figure 4 is taken from Kikuchi ¹ and shows a cellular structure represented by the solid lines.

The structure outlined by the dashed lines in Fig. 4 is called the dual representation of the cellular structure and is used by the CVM and PPM. In the dual representation, each point represents a cell, each edge represents a boundary, and each triangle (3-point cluster) represents a triple point. The number of edges terminating at a point in the dual space represents the coordination of that cell. This dual representation contains all the topological information of the real cellular structure but does not contain any information about the geometry of the real structure. This is because the mapping of the real space edge length to the dual space edge length is undefined. In the real cellular structure, the edge represents a boundary and its length represents the physical boundary length, whereas in the dual representation, the length

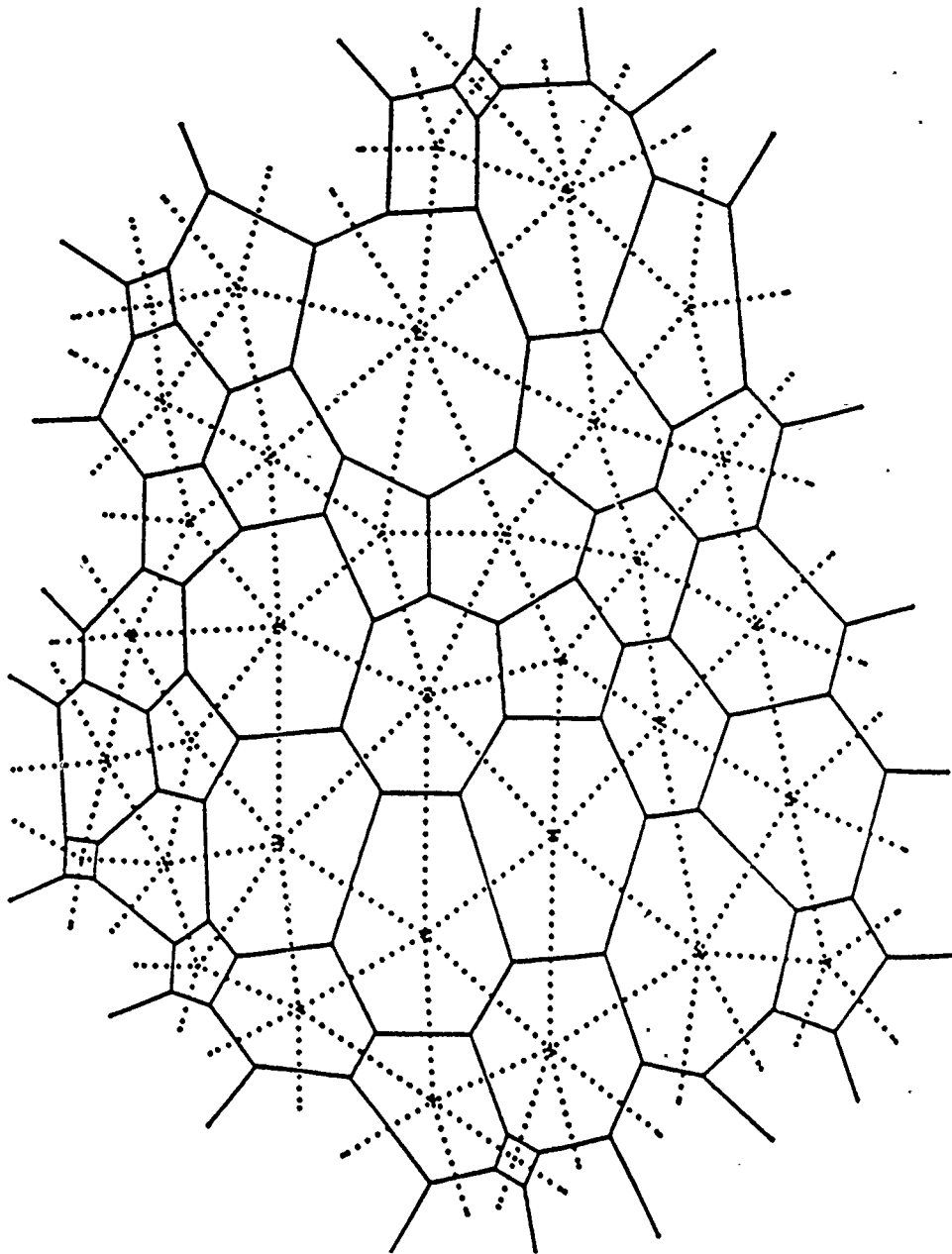


Figure 4. Example of a cellular structure (solid lines) and the dual representation of the structure (dashed lines).

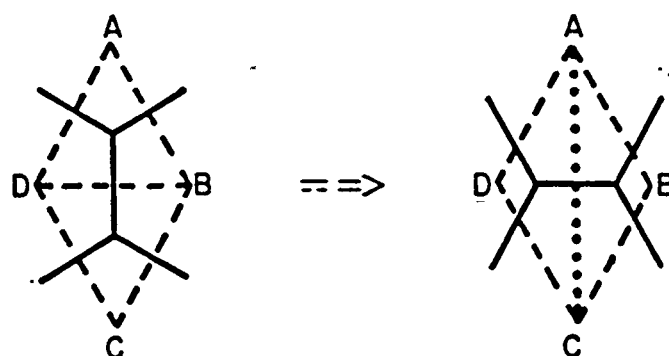
of the edge has no physical interpretation and the edge merely indicates the existence of adjacency.

Since the dual representation is used by the CVM and PPM, this work is restricted to the topological evolution of cellular structures as was mentioned in the introduction. The choice of the dual representation was not arbitrary but is actually required due to the current limitations of the CVM and PPM. The limitation arises because cellular structures are, in general, random structures, but the CVM and PPM are lattice calculations. The choice of the dual representation enables us to deform the structure into a regular lattice arrangement and thereby use the power of the CVM and PPM to calculate the behavior of the cellular structure. A more detailed discussion of the CVM and PPM calculations is delayed until section 3.3 on the CVM/PPM entropy formulation.

3.2 Topological Unit Processes in Two-dimensions

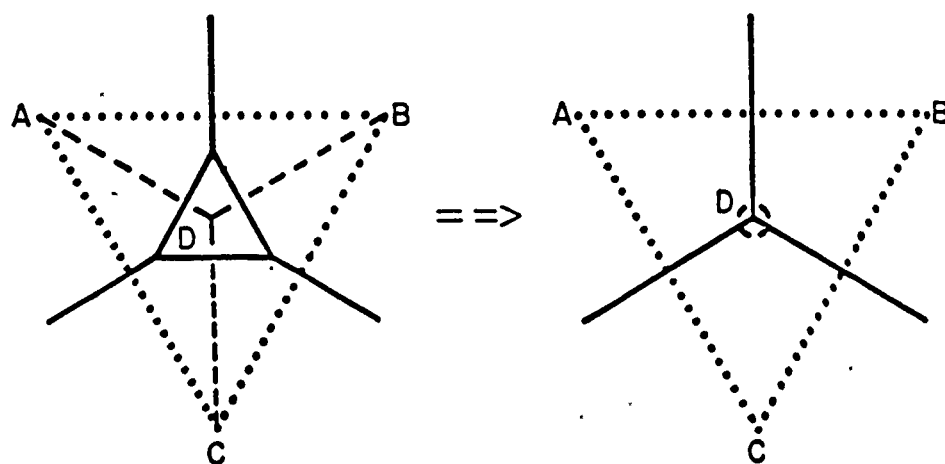
This section describes the unit processes by which two-dimensional cellular structures topologically transform. We can describe the topological evolution of a cellular structure by the change in the number and arrangement of the vertices, edges, and cells that compose the graph. These changes can be accomplished by two primitive processes called the T1 and T2 processes, as shown in Figure 5.

The T1 process is a neighbor exchange process whereby two adjacent cells become separated by the two cells that were previously adjacent to both cells. This is illustrated in Fig. 5a where initially adjacent cells B and D become separated and initially separated cells A and C become neighbors. The T1 process conserves the number of vertices, edges, and cells in the graph and is symmetric in time.



(a)

T1 Process: Neighbor Exchange



(b)

T2 Process: Cell Elimination

Figure 5. Illustrations of the two topological process in the 2-D plane.

The T2 process erodes and eliminates a three sided cell by its three neighboring cells. This process is shown in Fig. 5b by the elimination of cell D. The process results in the reduction of 2 vertices, 3 edges, and 1 cell. The reverse process results in the creation of a three sided cell and the addition of 2 vertices, 3 edges, and 1 cell. Both the forward and reverse process are included since they are valid topological processes. The physical interpretation of the forward and reverse T2 process introduces a bias that favors one direction over the other but this discussion is postponed for a later chapter.

Mitosis (cell division) can be considered a generalization of the T2 process since the change in the number of vertices, edges, and cells are the same as the T2 process but the restriction of operating on a three sided cell is relaxed to include cells with more than three edges. Cell division is not considered in this work since the resulting structure produces a triple point configuration with a very large turning angle (180°) and is energetically unfavorable for structures such as soap froths and polycrystalline planar sections.

We should also note that if the graph covers the plane, we know from Euler's Rule that the average number of edges per cell is exactly 6. This is shown by noting that each edge is shared by two cells, each vertex terminates 3 edges, and each edge is terminated by two vertices. If the graph does not cover the plane (i.e. the graph contains interior holes or is finite and we do not consider the space external to the graph to be a large cell), the average number of edges per cell will be less than 6.

3.3 CVM & PPM for Model-0

The major steps in both the CVM and PPM are 1) the definition of the state (path) clusters and subclusters, 2) the formulation of the entropy (path function)

appropriate to the order of the calculation and the chosen lattice, and 3) minimization of the free energy (maximization of the entropy). An additional step in the PPM is the integration of the path variables to determine the trajectory of the system in state space. Each of these steps is described below using Model-0 as an example of the procedure.

Model-0 is a 3-point approximation of a single phase structure on a triangular lattice and is equivalent to Kikuchi's first model.¹ The PPM calculation of Model-0, F-0, restricts the topological evolution of the structure to the T1 process. In order to distinguish the CVM and PPM calculations for each model, F-? is used to refer to the PPM calculation of Model-? and E-? is used to refer to the CVM calculation of Model-? where ? represents the specific model i.e., 0, V, or VI. The 3-point approximation means that the largest cluster used in the calculation is a 3-point cluster (triangle). The term single phase means that there is only one type of point variable represented by the cell and that every lattice position is occupied by that point variable. Remember that in the dual representation, the point represents a cell. The triangular lattice was chosen for the calculations since it automatically satisfies Euler's theorem for two-dimensions.

3.3.1 Model-0 State Variables

The state and path variables represent the probability of occurrence for that particular cluster. Only two 3-point state variables are required for Model-0 and are shown in Table 1 by the full triangle, z_1 , and the partial triangle, z_2 . The two types of 2-point (pair) state variables are the full pair, y_1 , and the broken pair, y_2 . Model-0 has only one point state variable, x_1 , that occupies every lattice point. For the remainder of the discussion, state variables are identified by lower case letters and path variables are

Table 1. Model-0 state variables






State Variable	Degeneracy	Dual Representation
z1	1	
z2	3	
y1	1	
y2	1	
x1	1	

Table 2. Model-0 reduction relations

a)	$y1 = z1 + 2z2$
b)	$y2 = z2$
c)	$x1 = z1 + 3z2 = 1$

identified by upper case letters. Three-point clusters are represented by the letter z, 2-point clusters by the letter y, and point clusters by the letter x. Table 1 summarizes the state variables used in model-0. The name and the dual representation of the variables are shown along with the degeneracy of each variable. The degeneracy of the variable represents the number of ways of placing the cluster on the triangular lattice. For example, the z2 variable can be placed on the triangular lattice in three equivalent orientations and therefore has a degeneracy of 3.

The subcluster variables are related to the cluster variables through a set of reduction relations shown in Table 2 for Model-0. These relations connect the configuration of the cluster to its subclusters and ensure that the clusters and its subclusters maintain the normalization condition. These relations reduce the number of independent variables to the number of cluster variables. The normalization condition that the sum of the cluster probabilities equal 1 reduces the number of independent variables by 1. For Model-0, this results in only 1 independent variable which is arbitrarily chosen to be z1. These relations are used to eliminate the dependent variables in the entropy term in preparation for the maximizing step.

Although the reduction relations are used to describe the subcluster state variables in terms of the 3-point state variables, the state variables are defined following a procedure that starts with the 1-point state variables and generates the higher order (i.e. 2 and 3-point clusters) variables from the lower order variables by enumerating all possible combinations of the lower order variables. These configurations are checked for topological consistency and only clusters that are consistent are retained. For example, Model-0 has only 1 type of 1-point cluster since the model assumes a fully dense lattice with each point representing a cell. Two types of 2-point clusters (y1 and y2 in Table 1) are required to describe the neighbor

exchange process on the CVM lattice and these clusters represent interactions between the nearest and next-nearest neighbors on the CVM lattice. All possible combinations of the y_1 and y_2 clusters are enumerated to form the possible 3-point clusters but only the z_1 and z_2 clusters shown in Table 1 are topologically consistent.

3.3.2 Entropy

The kernel of both the CVM and PPM is the elucidation of the entropy of the system. For the systems considered in this work, the entropy represents the number of ways of arranging the clusters on a lattice such that the "equilibrium" distribution of the subclusters is also satisfied. The entropy for the 3-point approximation on a triangular lattice is given by Eq. (1) below:

$$e^{S/k} = \frac{\left\{ \prod (Nz_i)! \right\}^2 \left\{ \prod (Nx_i)! \right\}}{\left\{ \prod (Ny_i)! \right\}^3}, \quad (1)$$

where N is the number of lattice points, and the products are taken over all possible clusters. The entropy term depends on the order of approximation and on the type of CVM lattice used.⁶ The exponents in the entropy expression are derived by successively correcting the lower order expression for the correlations that arise from the higher order cluster.³⁵ For example, the 1-point entropy expression assumes all points are independent. The 2-point expression adjusts the 1-point expression by a correlation factor that includes information about nearest neighbor information.

3.3.3 Maximum Entropy

The reduction relations are used to express the entropy in terms of the independent variables and the entropy is then maximized with respect to the

independent variables. Model-0 has only one independent variable and the maximization of S in Eq. (1) leads to Eq. (2) below:

$$0 = 10z_1^2 + z_1 - 2. \quad (2)$$

The two solutions to the quadratic equation are 0.4 and 0.5, but the 0.4 root is chosen because the 0.5 root results in a negative value for the y_1 variable which is not allowed since all state variables must be in the interval of 0 to 1. The solution shown above is identical to Kikuchi's solution of the soap froth problem.

The solution method shown above is simple and concise for problems with a single independent variable but becomes very cumbersome for problems with more than one independent variable. The natural iteration method (NIM) developed by Kikuchi ³⁶ is used for more complicated problems. As the name implies, the solution is obtained by an iterative process between the cluster and subcluster variables. The process begins with an initial guess for each of the cluster variables. The reduction relations are used to calculate the values for the subcluster variables from the initial guess of the cluster variables. New values for the cluster variables are calculated from the subcluster variables using the set of CVM equations. These equations are derived by setting the derivative of the entropy expression with respect to the cluster variables to 0 and solving for the cluster variables in terms of the subcluster variables. The new set of cluster variables are compared to the cluster variables from the previous iteration to check for convergence. If the cluster variables have not converged to a specified level, the cluster variables are used as the initial guess for the next iteration and this procedure is repeated until the convergence criteria is satisfied. The NIM procedure is more amenable to computation and is used for Models -V and -VI.

3.3.4 Calculation of the CCD

The CCD is obtained from the state variables by enumerating all possible lattice point configurations and calculating the approximate probability for each of these configurations. Table 3 lists the 30 possible lattice point configurations that can be placed on the CVM lattice along with the degeneracy associated with each 7-point configuration. The configuration degeneracy is the number of equivalent configurations that can result from permutations of the six 3-point clusters in the configuration. The table is partitioned into 10 classes that correspond to the coordination of the central point (cell) in the 7-point configurations. The coordination of the central cell is obtained by counting the number of nearest neighbor (solid lines) and next nearest (dashed lines) bonds terminating at the central cell.

The probability of the configuration is approximated by a superposition of the six 3-point clusters in the configuration with an adjustment for the six 2-point clusters that are "counted" twice by the 3-point clusters. The equilibrium CCD calculated for Model-0 is shown in Section 3.3.5 describing the results of F-0.

3.3.5 F-0: Model-0 PPM

F-0 is the extension of E-0 (the CVM calculation of Model-0) and is the starting point for the original work presented in this dissertation. The PPM is very similar to the CVM and consists of the following steps: 1) identifying the cluster and subcluster path variables, 2) maximizing the path function to obtain the cluster path variables, and 3) integrating the path variables to obtain the state variables.

Table 4 lists the path variables and the path reduction relations for F-0 and are similar to the E-0 state variables and reduction relations. The notation for the

Table 3. Coordination configurations for Model-0

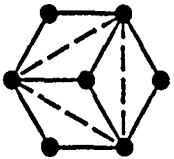
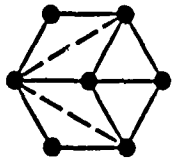
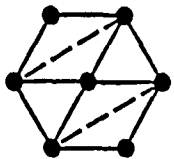
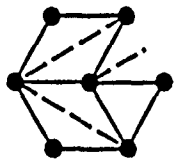
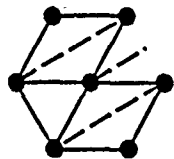
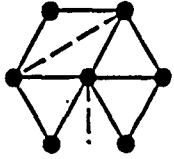
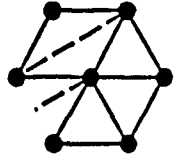
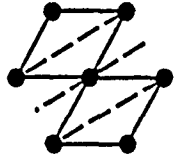
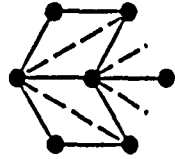
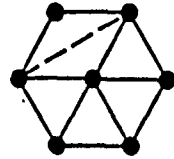
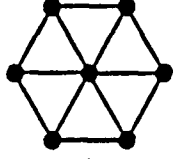
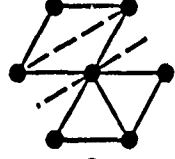
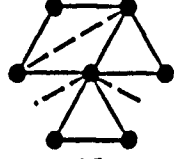
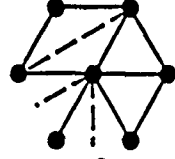
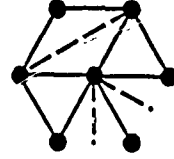
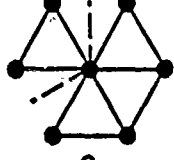
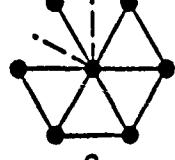
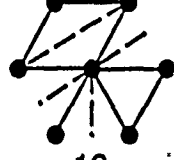
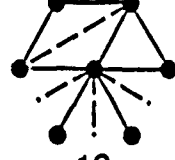
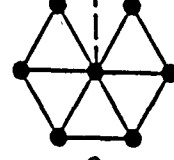
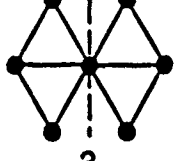
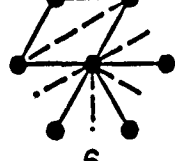
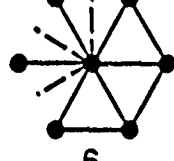
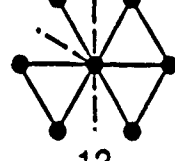
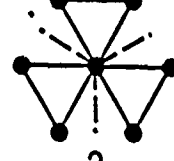
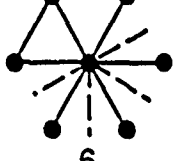
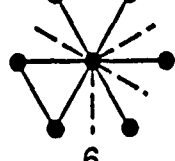
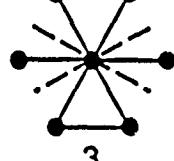
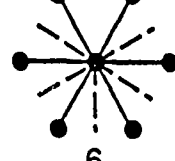
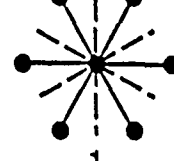
















 2	 6	 3	 12	 6
 12	 12	 3	 6	 6
 1	 6	 12	 12	 6
 6	 6	 12	 12	 6
 3	 6	 6	 12	 2
 6	 6	 3	 6	 1

Table 4. Model-0 path variables

Path Variable	Degeneracy	Dual Representation	
		t	$t+\Delta t$
Z11	1		
Z22	3		
Z12	3		
Z21	3		
Y11	1		
Y22	1		
Y12	1		
Y21	1		

path variables follows the notation used for the state variables and are of the form A_{ij} where A denotes the order of the cluster (i.e., 1, 2 or 3-point cluster). The indices i and j denote the specific state variables at time t and $t+\Delta t$, respectively. For example, Z_{12} is the path variable denoting the probability of finding a triangle which is the z_1 configuration at t and the configuration z_2 at $t+\Delta t$.

The path function is given below as Eq. (3) and is similar in form to the entropy expression of Eq. (1):

$$\phi = (\theta \Delta t) \frac{\sum_{NZ} \{ \Pi(NZ_{ij})! \}^2 \{ \Pi(NX_{ij})! \}}{\{ \Pi(NY_{ij})! \}^3} \quad (3)$$

The products over the path variables are taken over the number of possible path variables. The first term on the right side of Eq. (3) represents the probability of a T1 process occurring in time Δt . Theta is the T1 process rate so $\theta \Delta t$ is the probability that a T1 process occurs at each lattice site. The process rates, θ , must be supplied to the PPM calculation and contain the local physics that control the transitions of the specific cellular structure. We use the dimensionless time variable, θt , to keep the calculations general.

3.3.6 State-Path Equations

The path variables are related to the state variables through the state-path equations shown below for Model-0:

$$z_1(t+\Delta t) = Z_{11}(t) + 3Z_{21}(t), \quad (4)$$

$$z_2(t+\Delta t) = Z_{22}(t) + 3Z_{12}(t), \quad (5)$$

$$z_1(t) = Z_{11}(t) + 3Z_{12}(t), \quad (6)$$

$$z_2(t) = Z_{22}(t) + 3Z_{21}(t). \quad (7)$$

The time derivative of z_1 is obtained by subtracting Eq. (6) from Eq. (4) and taking the limit as Δt goes to zero resulting in Eq. (8) below:

$$dz_1/dt = 3(Z_{21}-Z_{12})/(\theta\Delta t) . \quad (8)$$

The path reduction relations are used to eliminate the subcluster path variables from Eq. (3) and we use the state-path equations to eliminate the T0 path variables (which represent the state variables that remain the same during Δt). We take the natural logarithm of Eq. (3) and maximize it with respect to the path variables Z_{12} and Z_{21} resulting in Eqs. (9) and (10) below:

$$Z_{12} = z_1^2 \theta \Delta t / y_1 , \quad (9)$$

$$Z_{21} = z_2 \theta \Delta t . \quad (10)$$

Substituting Eqs. (9) and (10) into Eq. (8), we obtain Eq. (11) which describes the evolution of the two-dimensional cellular structure that is due to a series of neighbor exchanges only:

$$dz_1/dt = 3(z_1^2/y_1 - z_2) . \quad (11)$$

Equation 11 is integrated to describe the behavior of the cellular structure. The result is shown in Fig. 6 which shows the state variable, z_1 , as a function of time. The cell coordination distribution is calculated from the state variables using a superposition approximation that was described previously. The cell coordination distributions (CCD) at several times are presented in Fig. 7.

3.3.7 F-0 Results and Discussion

There are two points of interest in Fig. 6. First, the long time behavior of z_1 calculated by the PPM is consistent with the CVM analysis presented above (shown as the dashed line in Fig. 6). Second, the state space of the dual network is partitioned into two regions, $z_1 < 0.4$ and $z_1 > 0.4$, and within each region, the evolution of the

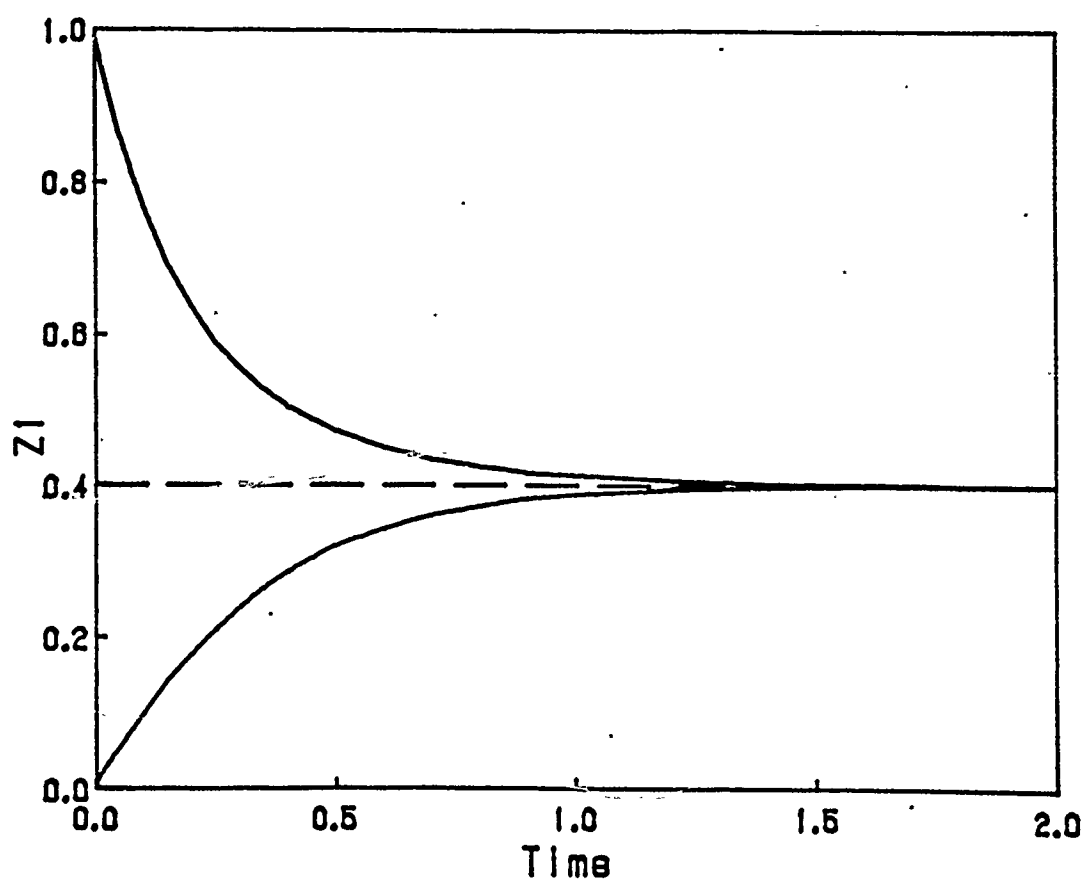


Figure 6. Evolution of the Model-0 state variable, z_1 , toward the CVM calculated stationary value of 0.4 (dashed line).

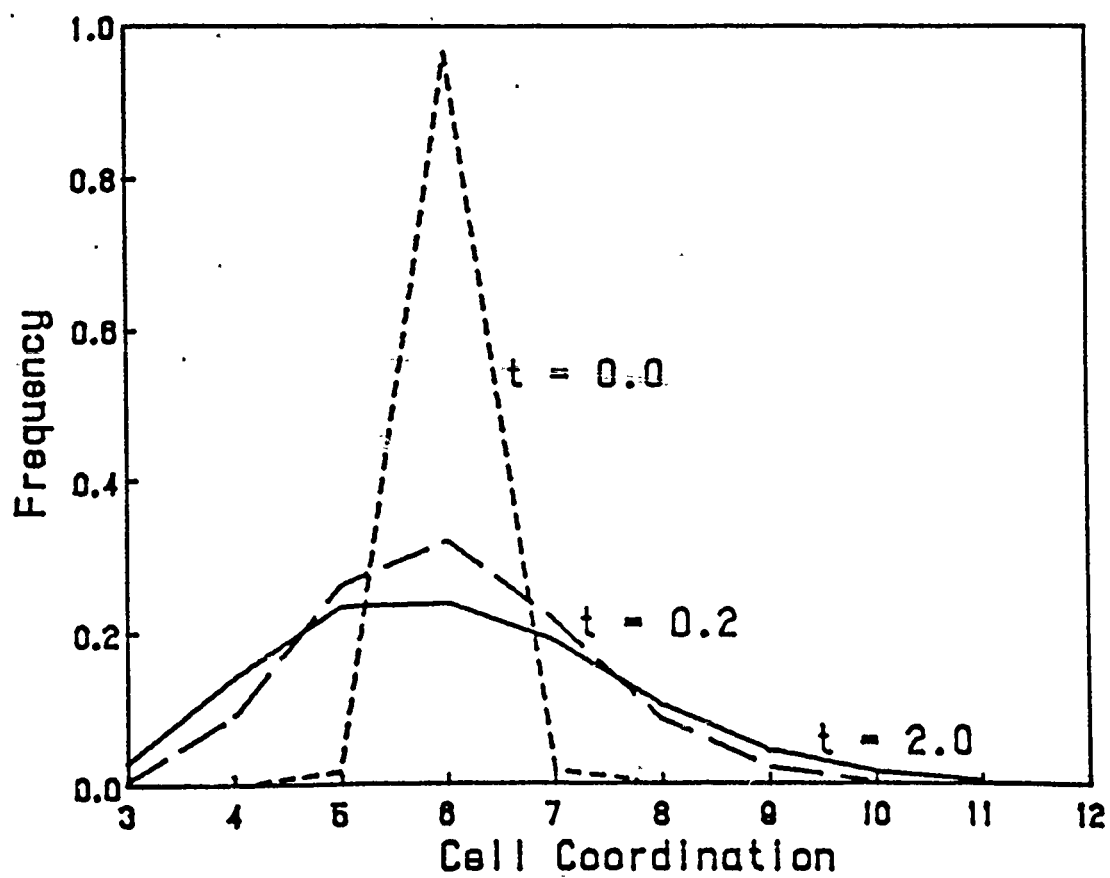


Figure 7. Development of the Model-0 CCD toward the stationary CCD (solid line).

structures is identical. This behavior is not surprising since the simplicity of Model-0 is such that a single state variable is sufficient to topologically describe the structure.

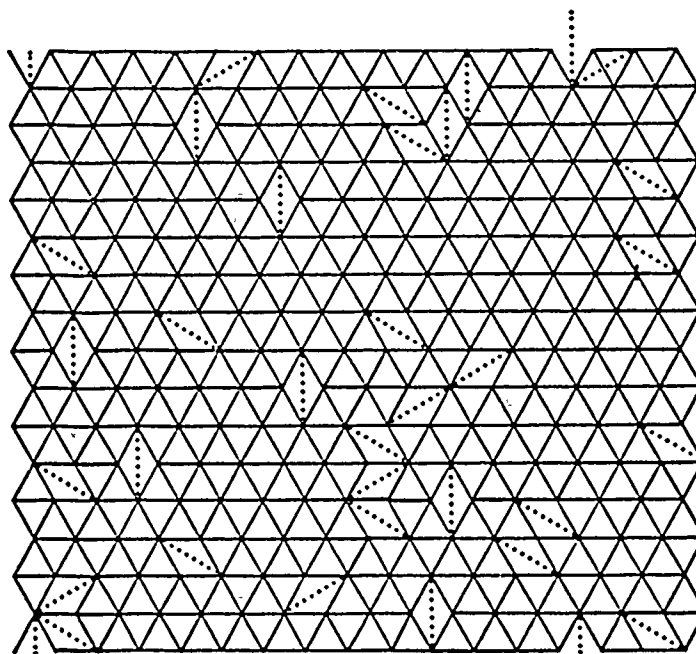
Figure 7 shows the calculated cell coordination distribution for three values of z_1 . The times indicated in Fig. 7 correspond to the time axis in Fig. 6. The initial distribution is very sharp with almost every cell adjacent to six other cells. The distribution broadens rapidly but slows as it approaches the equilibrium distribution. The distributions shown in Fig. 7 indicate that cellular structures always evolve toward the equilibrium (steady state) distribution of cell coordination and that structures with narrow distributions are in nonequilibrium states unless additional constraints are applied to the system.

We can render the evolution of a cellular structure from the state variables with the following procedure. The number of lattice points for the rendering, N , is chosen and the distributions of the various clusters are determined from the state variables calculated by the PPM as a function of time. A site on the CVM triangular lattice is chosen at random and a randomly chosen cluster (weighted by its probability of occurrence) is placed on the lattice at that site. This step is repeated until all the clusters have been placed on the dual lattice and all inconsistencies between neighboring clusters have been eliminated. Once the dual lattice has been generated, the real cellular structure is rendered by placing a triple point within the dual space triangle and connecting the triple points with real space boundaries such that each boundary intersects one dual space pair. The real structure renderings at different times are determined by the PPM generated state variables and represent a portion of the "typical" structure as calculated by the PPM. The successive renderings do not represent the same area of the real structure since the real structure is rendered independently from the previous rendering. However, we can link successive

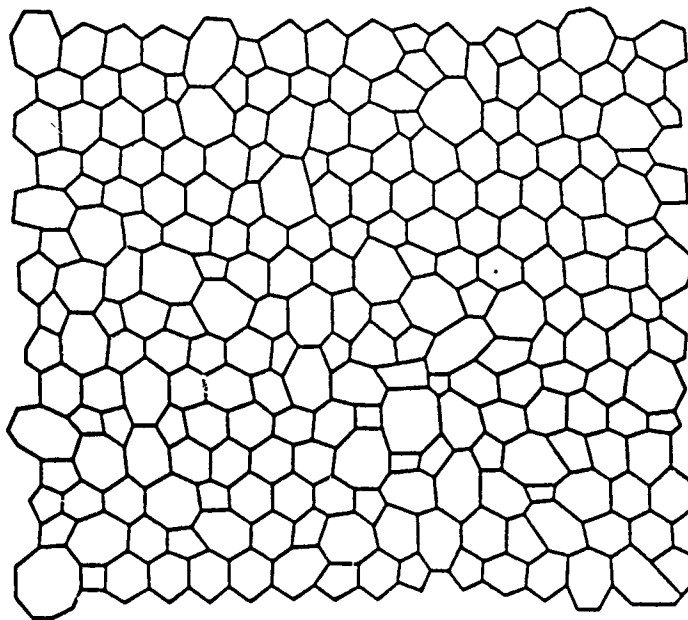
renderings by using the path variables generated by the PPM to weight the random picking of the state cluster. The advantage of using the path variables to determine the renderings is that the evolution of a specific area of the cellular structure can be followed through each topological transition. A second advantage of this method is that it attaches a scale to the temporal evolution of the structure via the specified process rates.

Model-0 allows a simpler procedure due to the small number of cluster types. In the Model-0 renderings, the dual lattice is initially occupied by only z_1 configurations and corresponds to a delta CCD at coordination 6. The y_2 pairs are placed on randomly chosen sites until the number of y_2 pairs satisfies the y_2 state probability calculated by the PPM for a particular time. Each placement of a y_2 pair represents a single T1 process occurring on the real structure. Figure 8 shows (a) the dual lattice and (b) the real structure rendering for $z_1=0.86$ ($t=0.05$) on a 16×16 lattice. Figure 9 shows the real structure renderings for $z_1=0.64$ ($t=0.2$) and 0.4 ($t=2.0$), respectively. The three renderings shown in Figs. 8-9 are correlated to each other and can be interpreted as the evolution of a specific area of a cellular structure. The renderings are correlated because the rendering procedure uses the previous rendering as the starting point for the next rendering. The series of renderings do not represent a true sequence since only the Z_{12} path variable is used to render the structure and therefore the structures do not exhibit the reverse T1 process that would be expected to occur in any structure. The renderings shown in the figures used only the Z_{12} information since this simplified the manual procedure used for the renderings.

The structures shown in Figs. 8 and 9 are similar in appearance to the cellular structures found in soap froths and polycrystalline planar sections. Figure 8a, in



a) Dual rendering



b) Cellular structure

Figure 8. Model-0 structural rendering at $t = 0.0$ showing a) the dual representation and b) cellular structure.

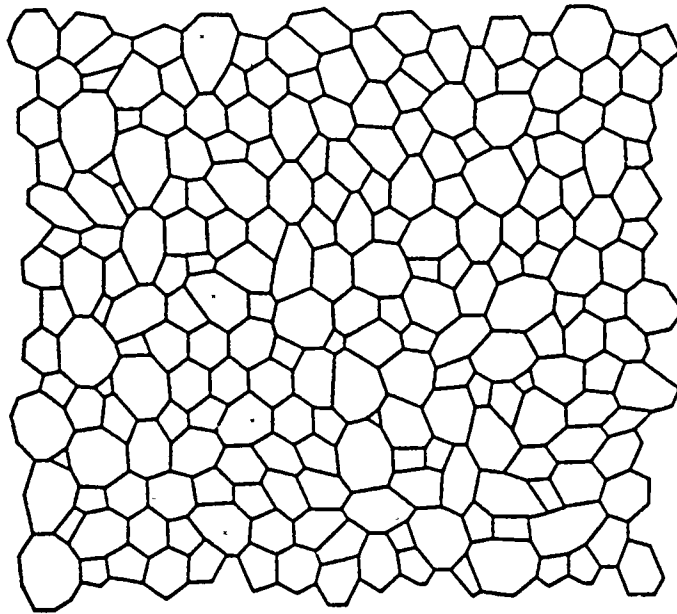
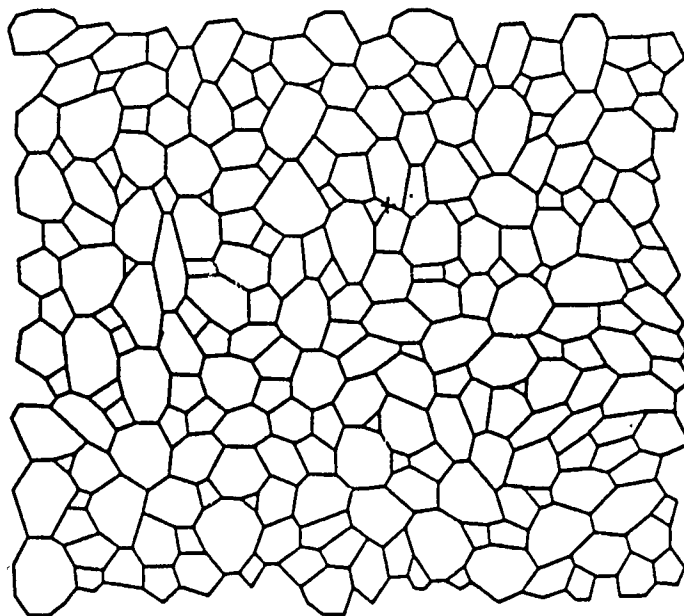
a) $t = 0.2$ b) $t = 2.0$

Figure 9. Model-0 Structural renderings at a) $t = 0.2$, and b) $t = 2.0$.

particular, appears to exhibit the trend that the size of the cell increases with coordination. Since our analysis is purely topological, this coordination-size correlation should be suspect. The suspect trend is due to the arbitrary placement of the triple point during the real space rendering. The triple point is placed within the dual triangle such that the cells remain as equiaxed as possible. The equiaxed criterion extends our purely topological approach to partially include the effects of geometry but since we do not know the cost function for nonequiaxed cells, we cannot include this directly into the CVM or PPM.

Tanemura used a similar approach to extend the CVM calculation of Model-0 to partially include geometry.³⁷ He assigned an "energy" to the two 2-point state clusters, minimized the free energy, and showed that the equilibrium distribution could be adjusted to produce a sharper distribution. The justification for this was the equivalence of the 2-point state cluster in dual space to the cell boundary in real space. Assuming that the 2-point clusters also represented different lengths of cell boundaries, Tanemura was able to include a grain boundary energy term along with the structural entropy term to form the free energy of the cellular structure. Although this resulted in a parametric model, it exhibited the expected behavior in that by increasing the ratio of the y_2 to y_1 bond energies (R_{12}), the CCD became sharper. In addition, for values of R_{12} between 1 and 2, the CCD calculation followed the perimeter law (see list of terms on p. vii) exactly. However, the slope of the perimeter correlation was much smaller than the slope obtained from experiments. The small slope in the correlation is in keeping with the assumption that the dual lattice does not require large deformations to produce the dual representation of the structure.

Incorporation of Tanemura's assumption in the PPM calculation would require different process rates for the Z12 and Z21 path variables. Since the process rates are left unspecified in this work, the PPM calculations using an adjustable parameter were not considered important.

3.4 Summary

The development of the CCD of a single phase structure undergoing only neighbor exchanges was described using the CVM and PPM. The results of the calculations show that cellular structures have an equilibrium CCD and will develop the equilibrium CCD along one of two possible evolutionary paths. The detailed description of the CVM and PPM presented in this chapter serves as a background to the next two chapters where more complex models are studied.

CHAPTER 4

DENSIFICATION: MODEL-V

Model-V is a three-point approximation of the two phase problem. Since the model allows two phases, we can study the densification process (sintering) by identifying the second phase as voids. Model-V allows the T1 (neighbor exchange) process and the elimination and creation of voids.

4.1 E-V Description

The equilibrium formulation of Model-V is named E-V and contains 7 3-point state variables, 6 2-point state variables, and 2 point state variables. The point state variables represent a cell (or grain) and a void. Table 5 lists the 7 triangle variables and the 6 2-point variables along with their degeneracies. Table 5 also shows the energies assigned to the 2-point variables and represent the grain boundary (ϵ_1, ϵ_3) and free surface (ϵ_2) energies. Table 6 lists the coefficients, α_{ij} , used in the reduction relations for the subcluster state variables. The reduction relations have the form given below:

$$y_i = \alpha_{ij} z_j . \quad (12)$$

The CVM calculation of Model-V requires two additional variables due to the addition of the second phase. One of these variables represents the "chemical potential" of the cell. This variable is provided for the calculation and sets the

Table 6. Ernie-V reduction relations for state variables

		z1	z2	z3	z4	z5	z6	z7
y1	(1)	1	2	1	1			
y2	(1)		1					
y3	(2)			1	1	1	1	
y4	(2)				1			
y5	(1)					1		1
y6	(1)						1	
x1	(1)	1	3	2	4	1	1	
x2	(1)			1	2	2	2	1

NOTE:

The coefficients shown in the table are used in Eq. (12) to obtain the state variable reduction relations. For example, the reduction relation for the y1 state variable is given below:

$$y1 = z1 + 2z2 + z3 + z4 .$$

equilibrium density of the structure. The second variable is used to distinguish the pairs that represent a free surface from the pairs that represent a cell (or grain) boundary.

The "bond energies" of the 2-point clusters are combined with the CVM entropy term to form a free energy of the system. The free energy is written in dimensionless form in Eq. (13) below:

$$\Phi = \frac{\beta F}{N} = 3\beta U \sum (\epsilon_i y_i) + 2 \sum \mathcal{L}(z_i) + \sum \mathcal{L}(x_i) - 3 \sum \mathcal{L}(y_i) , \quad (13)$$

where β has the usual meaning of $(kT)^{-1}$, N is the number of lattice points, and $\mathcal{L}(x) = x \ln(x) - x$, represents Stirling's approximation to the factorial function. The coefficient, U , in front of the energy summation has the dimension of energy and contains the geometric information of the system. The coefficients in the energy summation, ϵ_i , are dimensionless and represent the relative energies of the pair bonds with respect to the energy of the system. The first term represents the "internal energy" of the system and the sum is taken over all 2-point clusters. The second sum represents the topological entropy of mixing and is the log of the entropy term shown in Eq. (1).

Eq. (13) has the same structure as the Helmholtz free energy for thermodynamic systems when the first term is identified with the grain boundary and free surface energies of the system. We have written the internal energy summation in a slightly different form where the summation is over dimensionless variables. This is done in order to decouple the geometric behavior of the system from the topological behavior of the system. The decoupling is accomplished by assuming that the variable, U , in Eq. (13) represents the system-averaged energy per cell (or grain) boundary face and is a function of the average cell (or grain) size. The variable, U ,

contains most of the geometry of the system since it represents the absolute lengths (area) of both the free surface and cell boundaries. Since the cell boundary faces (edges in 2-dimensions) are much larger than atomic dimensions, U is very large compared to the entropy term in Eq. (13) and is identified as the driving force for densification. We set $U = 1$ in our calculations since we can not handle the interaction of geometry with topology in the PPM.

The pair bond coefficients in the energy summation describe the energies of the different types of pairs relative to the y_1 pair energy. The choice of the y_1 pair energy as the reference level is arbitrary but the ratios of the other pair energies to the y_1 pair energy is important in determining the probabilities of occurrence for each type of pair configuration. The most important coefficient is R_{31} which is the ratio of the y_3 pair energy to the y_1 pair energy. The y_3 configuration represents a free surface whereas the y_1 configuration represents a cell boundary. This ratio therefore affects the y_3 state variable in the partially dense system. A value of 1.5 for R_{31} was used in the base calculations for Model-V and corresponds to a dihedral angle of 140° . We can also crudely model the cell (grain) size distribution by assigning values to the other pair energy coefficients. This is accomplished by using Tanemura's assumption that the pair lengths in the dual lattice correspond to the lengths of the cell (grain) boundaries in the real network. The assumption is valid when the dual representation of the real cellular structure can be placed on the CVM lattice without excessive distortion of the dual representation. Although the topological description of the cellular structure remains invariant under distortion, the geometric (energy) description of the structure changes with distortion. Therefore, Tanemura's assumption is most applicable to structures with very narrow cell (grain) size distributions but as the size distribution broadens, larger distortions of the dual

representation will be required to fit the dual representation onto the CVM lattice and his assumption will not be applicable to these broadened structures.

The "chemical potential," CHM, of the Model-V system is identified as an undetermined multiplier that sets the number density of cells in the system. This is accomplished by adding to Eq. (13) the term, (CHM)(x1) to form the grand potential of the system. CHM is determined by the partial derivative of the grand potential with respect to the cell number density, x1, and is given in Eq. (14) below:

$$\text{CHM} = \frac{d\Phi}{dx_1} = \ln \left(\left(\frac{z_1}{z_7} \right)^2 \left(\frac{x_1}{x_2} \right) \left(\frac{y_5}{y_1 e^{-\beta \epsilon_1}} \right)^3 \right) . \quad (14)$$

4.2 E-V Results and Discussion

The equilibrium state variables are determined by the natural iteration method discussed in the previous chapter. The source listing of ERNIE-V that performs the NIM for Model-V is presented in Appendix A.

Figure 10 shows the equilibrium CCD at 3 different densities. The CCD for the fully dense network (x1=1.0) is the same as the CCD calculated in Model-0. The CCDs for partially dense networks show a shift in the most probable coordination from 6 in the fully dense case to 5 in the partially dense case. The shift is caused by voids that have a coordination of 4 or more. The 3 coordinated void does not reduce the coordination of the three adjacent grains but the 4 coordinated void reduces the coordination of 2 of the adjacent cells by 1. The second central moment of the CCD, μ , decreases in the partially dense systems.

Figure 11 shows the effect of R21 and R31 on the equilibrium CCD for the fully dense network (x1=1.0) and the partially dense network (x1=0.8). R21 is the

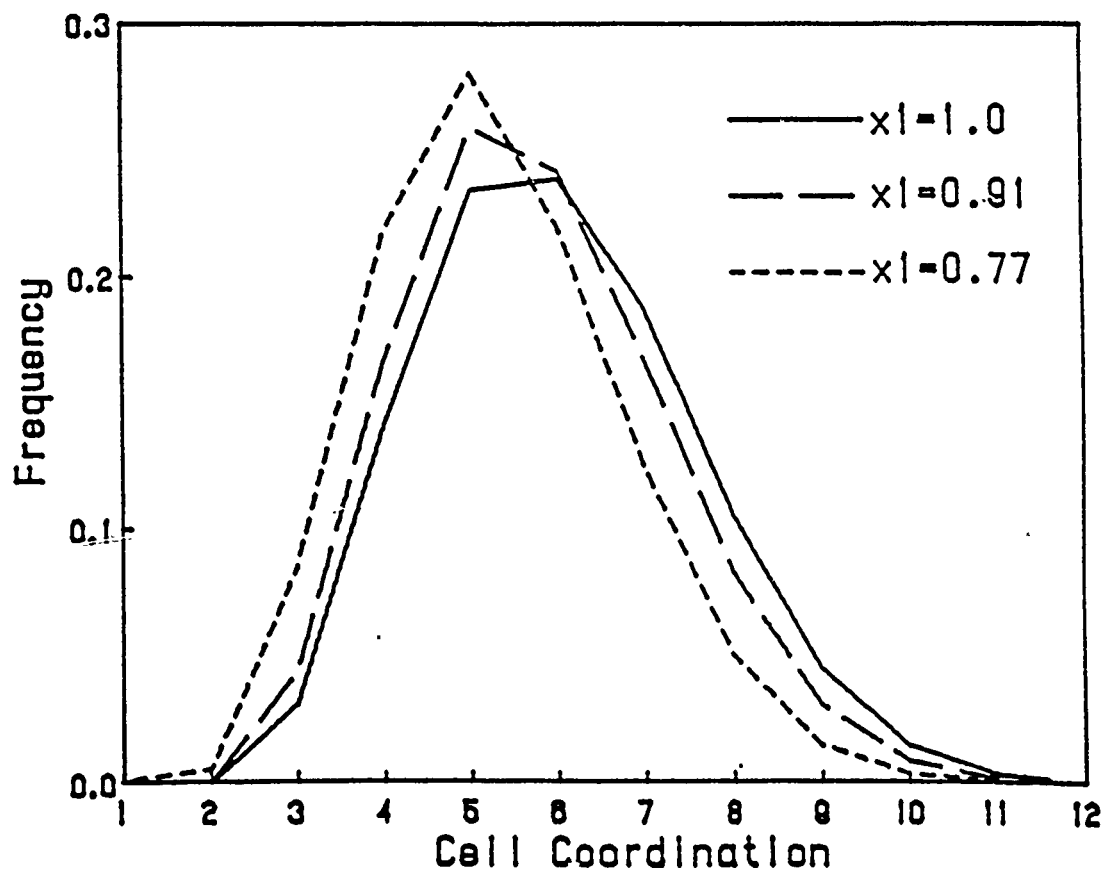


Figure 10. Effect of the input variable, CHM, on the Model-V calculated stationary CCD. The reference calculation used CHM = 100 which produced a stationary cell number density of 0.997 (solid line).

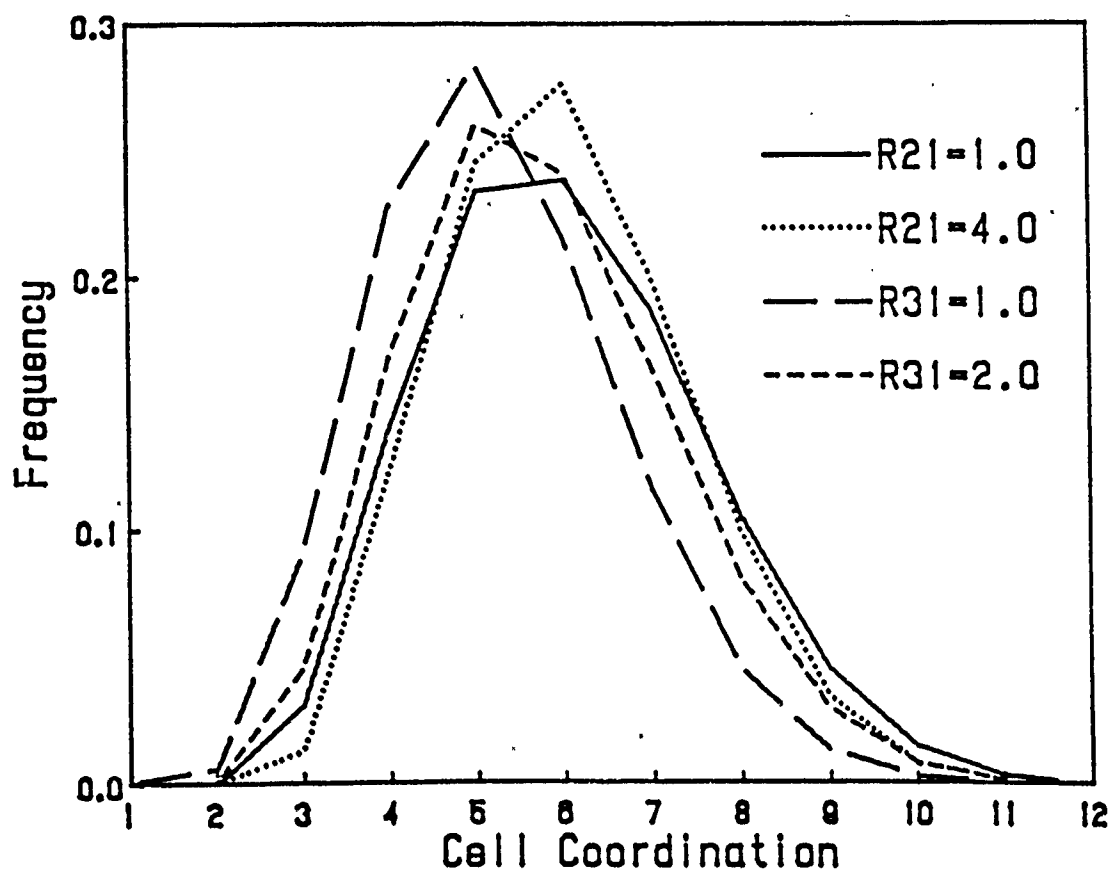


Figure 11. Effect of the input variables R_{21} and R_{31} on the Model-V calculated stationary CCD. R_{21} is the ratio of the second nearest neighbor interaction to the nearest neighbor interaction on the CVM lattice. R_{31} is the ratio of the free surface interaction to the cell boundary interaction on the CVM lattice.

















ratio of the y2 bond energy to the y1 bond energy and is identical to Tanemura's approach. As noted previously, the equilibrium CCD is sharper for values of R21 greater than 1.0; Fig. 11 shows this behavior. R31 is the ratio of the y3 bond energy (free surface) to the y1 bond energy (cell boundary). The R31 ratio has no effect on the CCD for the fully dense case since there is no free surface. In the partially dense systems, increasing the value of R31 shifts the CCD slightly toward the fully dense CCD. This behavior is reasonable since values of R31 greater than 1 give more weight to the x1 (cell or grain) and y2 (cell boundary) state variables than to the y3 (free surface) state variable. This moves the system in the direction of the fully dense case and therefore shifts the CCD toward the fully dense distribution.

4.3 F-V Description

The path variables for Model-V are shown in Table 7. There are 16 3-point path variables and 14 2-point path variables. Table 7 shows only the forward path variables since the reverse path variables change only the order of the state variables in time. Figure 12 shows the relation of the 7 state variables and 8 path variables. The state variables are enclosed in circles and the arrows linking the state variables represent the path variables. The horizontal links between the state variables represent the T1 path variables and the vertical links indicate the path variables that correspond to the densification step. The numbers in parentheses indicate the degeneracy of the path variable. Table 8 lists the coefficients for the subcluster reduction relations for the path variables and have the same form as the state variable reduction relations in Eq. (12). Table 9 lists the coefficients, σ_{ij} , for the state-path equations which have the form given below:

$$\Delta z_i = \sigma_{ij} S Z_j , \quad (15)$$

Table 7. Felix-V 3-point path variables

Path Variable	Degeneracy	Process	Dual Representation	
			t	$t+\Delta t$
Z12	3	N.E.		
Z34	6	F.S.E.		
Z56	3	F.S.E.		
Z13	3	V.F.		
Z24	6	V.F.		
Z35	6	V.F.		
Z46	6	V.F.		
Z57	3	V.F.		

NOTES:

N.E. Neighbor Exchange

F.S.E. Free Surface Elimination

V.F. Void Formation

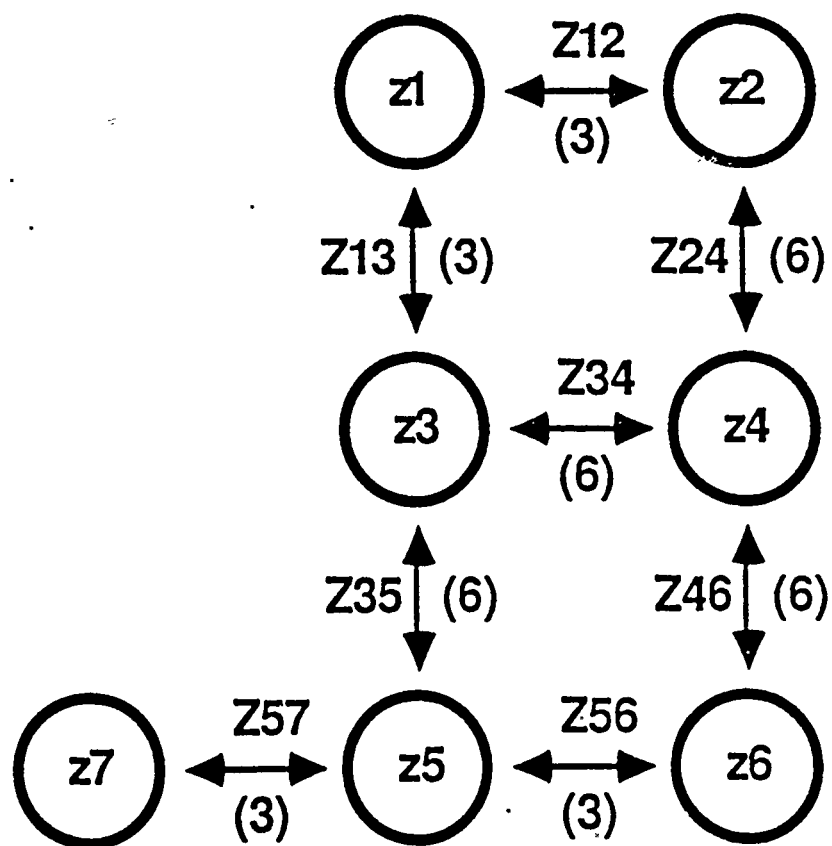


Figure 12. Relation of state variables to path variables

Table 8. Felix-V reduction relations for path variables

	z12	z34	z56	z13	z24	z35	z46	z57
y12 (1)	1							
y34 (2)		1						
y56 (1)			1					
y13 (2)				1	1	1	1	
y24 (2)					1			
y35 (2)						1		1
y46 (2)							1	
x12 (1)				1	2	2	2	1

NOTE:

The coefficients shown in the table are used in the same manner as the state variable reduction relations shown in Table 6 and Eq. (12). For example, the reduction relations for the Y35 and Y53 path variables are given below:

$$Y35 = Z35 + Z57 ,$$

$$Y53 = Z53 + Z75 .$$

Table 9. Felix-V state-path equations

	SZ12	SZ34	SZ56	SZ13	SZ24	SZ35	SZ46	SZ57
$\Delta z1$	-3			-3				
$\Delta z2$	1				-2			
$\Delta z3$		-2		1		-2		
$\Delta z4$		1			1		-1	
$\Delta z5$			-1			2		-1
$\Delta z6$			1				2	
$\Delta z7$								3

NOTE:

The coefficients shown in the table are used with Eq. (15) to obtain the state-path equations. For example, the state-path equation for the z2 state variable is given below:

$$\Delta z2 = z2(t+\Delta t) - z2(t) = SZ12 - 2SZ24 ,$$

where $SZ12 = Z12 - Z21$, etc.

where SZ_j is the difference between the forward and reverse path variable. Table 10 lists the T0 state-path reduction relations. The T0 process is the null process where the state variable remains unchanged during Δt .

The F-V calculations required two input variables to describe the process rates. The first rate variable, RT21 was the ratio of the neighbor exchange rate to the densification rate. This variable controlled the rate of densification with respect to neighbor exchanges. The calculations used a dimensionless time variable that was normalized to the T1 process rate. The second rate variable, CHM, was the ratio of the void elimination rate to the void production rate. This ratio is similar to the variable CHM in the CVM calculation since this ratio controls the final density of the system.

An additional complication of F-V over the F-0 calculation was that an inner iteration was required during the calculation of the path variables. The inner loop is typical of multi-variable PPM treatments and was required to simultaneously solve for the 3-point path variables and the subcluster path variables. It was used to maintain coherency between the cluster and subcluster path variables. The inner loop did not significantly add to the computational burden after the first few time steps since the small time steps used in the calculation kept the cluster and subcluster path variables coherent during the remainder of the calculation. The source listing of FELIX-V which performs the PPM calculation for Model-V is shown in Appendix A.

4.4 F-V Results and Discussion

Figure 13 shows the behavior of the point state variable, x_1 , for two different initial structures. The state variable, x_1 , is the probability of occurrence of a cell (grain) on the CVM lattice and represents the cell number density. If we assume that

Table 10. Felix-V Reduction relations for the T0 process

		z12	z34	z56	z13	z24	z35	z46	z57
z11	z1	-3			-3				
z22	z2	-1*				-2			
z33	z3		-2		-1*		-2*		
z44	z4		-1*			-1*		-1	
z55	z5			-1			-2*		-1
z66	z6			-1*				-2*	
z77	z7								-3*
y11	y1	-1			-2	-2	-2	-2	
y22	y2	-1*				-2			
y33	y3		-1		-1*	-1*	-1#	-1*	-1
y44	y4		-1*			-1*		-1	
y55	y5			-1			-2*		-2*
y66	y6			-1*				-2*	
x11	x1				-1	-2	-2	-2	-1
x22	x2				-1*	-2*	-2*	-2*	-1*

NOTES:

* Denotes coefficient for the reverse process, i.e. Z21 instead of Z12

Denotes coefficient for both the forward and reverse process.

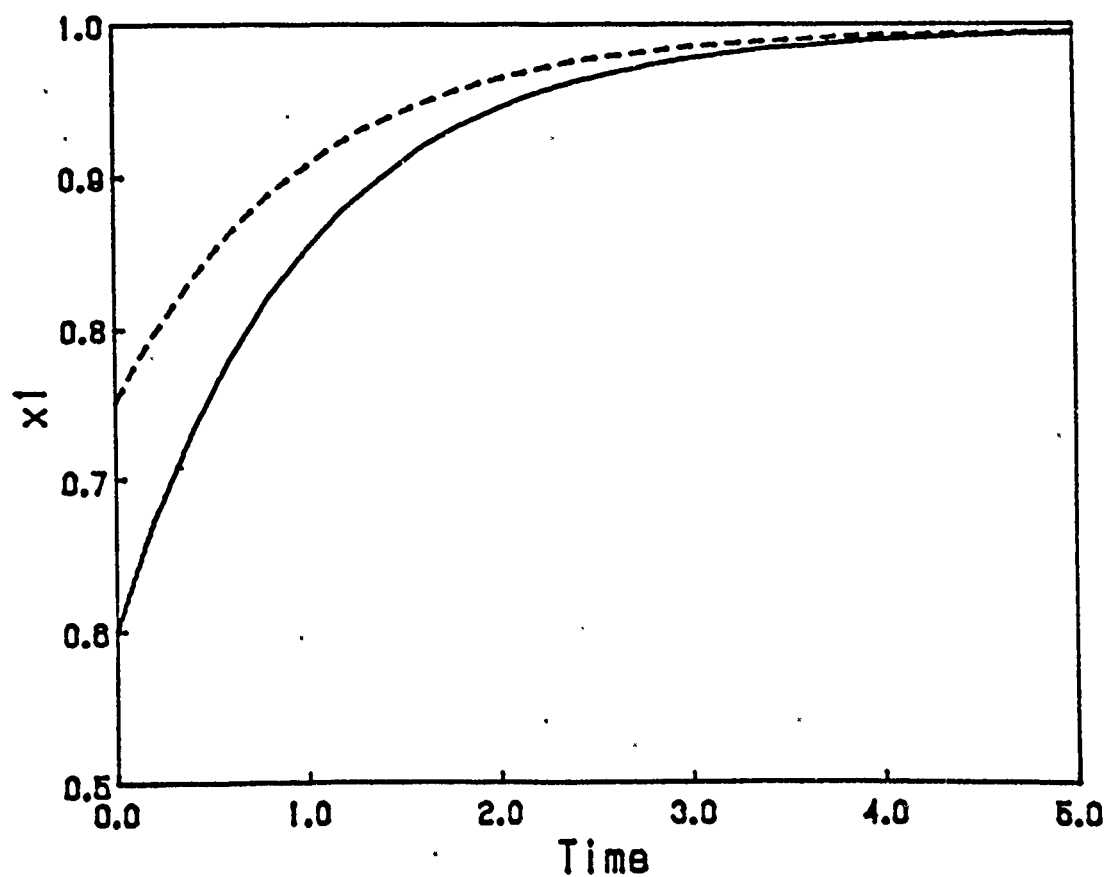


Figure 13. Model-V calculated cell number density, x_1 , as a function of time for two initially different structures. The reference calculation is shown by the solid line and the structure with an initial cell number density of 0.75 is shown by the dashed line.

the cells (grains) and voids have roughly the same size, then x_1 also represents the density of the structure. The time axis is in dimensionless units normalized to the T1 process rate. The ratio of the cell elimination to T1 process rate, RT_{21} , is set to 1.0 for both calculations. Both calculations used a $CHM=100$ resulting in a nearly fully dense system ($x_1=0.997$). Three-point state variables were specified such that initial structure densities of 0.6 and 0.75 were provided to the calculations. The base case is shown by the solid line and starts with an initial density of 0.6 while the dashed line shows the behavior of the structure that has an initial density of 0.75.

Figure 14 shows the CCD for the base case at three points along its evolution path. The initial CCD at $t=0.0$ and $x_1=0.6$ shows a peak at coordination 5 and has a CCD μ of 1.99. The CCD at $t=1.0$ and $x_1=0.84$ still exhibits a coordination peak at 5 but is very close to the equilibrium CCD shown at $t=5.0$ and $x_1=0.997$. The coordination peak at 5 was explained in a previous section and the broadening of the CCD is in keeping with the results obtained with the F-0 calculations. The significant feature in Fig. 14 is the very similar CCDs for the $t=1.0$ and $t=5.0$ structures. The CCDs are so close that the differences are completely swamped by the statistical uncertainties of available experimental data sets but these structures are characterized by number densities of 0.84 and 0.997 which can be easily determined.

Figure 15 shows the behavior of the CCD μ for the structures shown in Fig. 13. The CCD μ for both structures develop to their stationary values and are essentially indistinguishable by $t=2.0$.

Figure 16 shows the void coordination distribution (VCD) for the base calculation at $t=0.0$, 3.0, and 10.0. The VCD is calculated from the state variables in a manner similar to the calculation of the CCD described in the previous chapter. The VCD evolves to an equilibrium distribution indicated by the $t=10.0$ curve in Fig. 16.

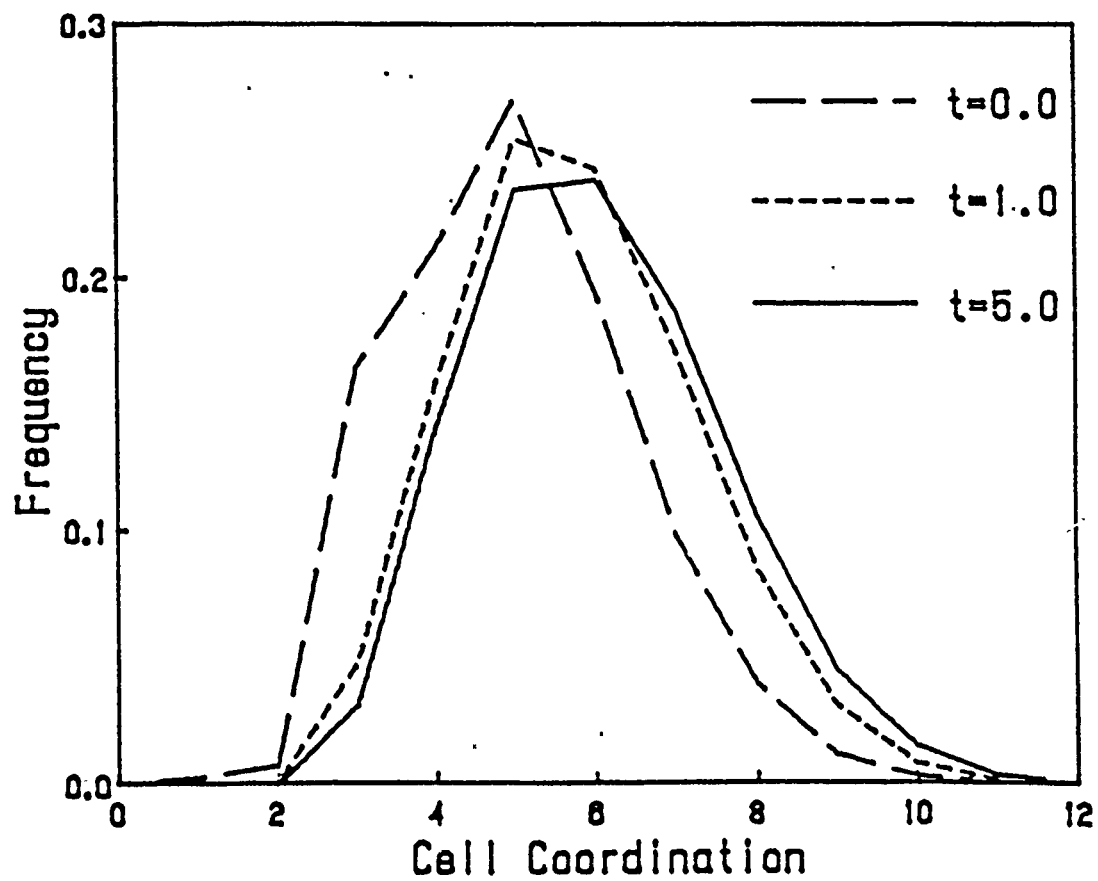


Figure 14. Model-V calculated development of the CCD toward the stationary CCD (solid line).

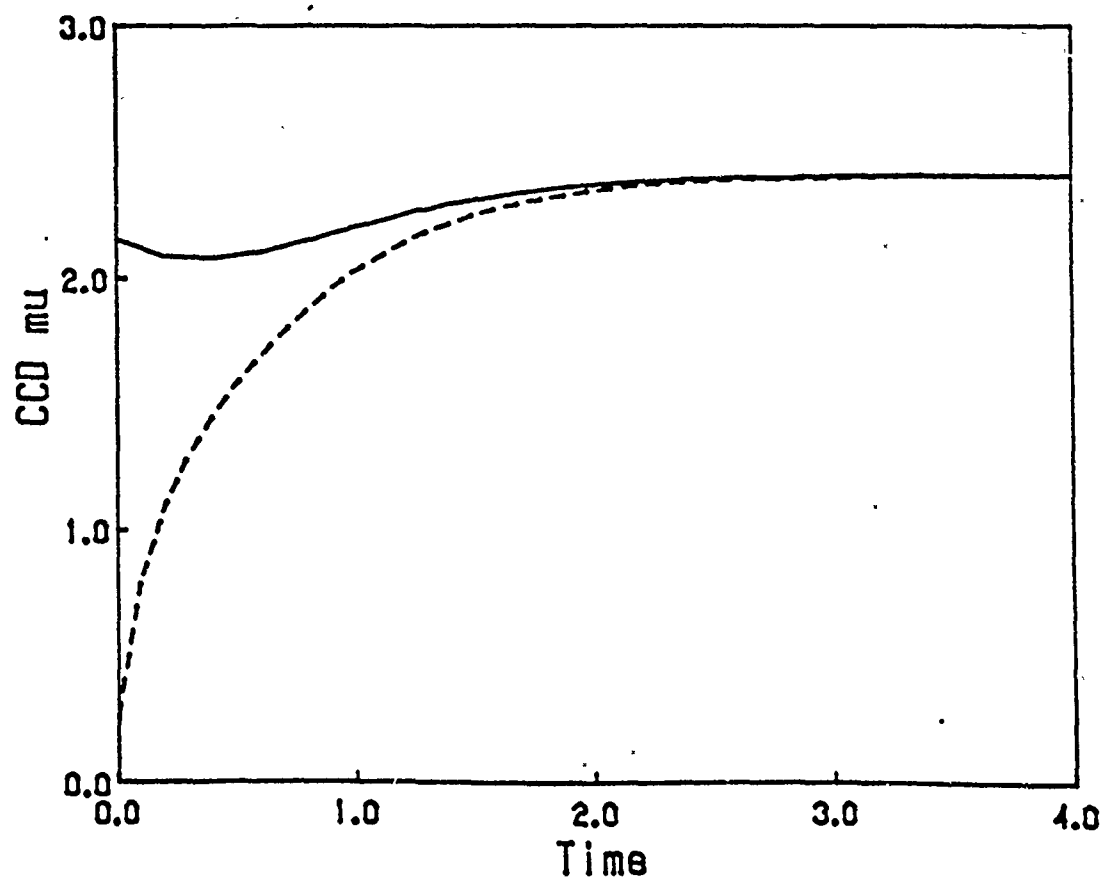


Figure 15. Behavior of the CCD μ for the structures shown in Figure 14.

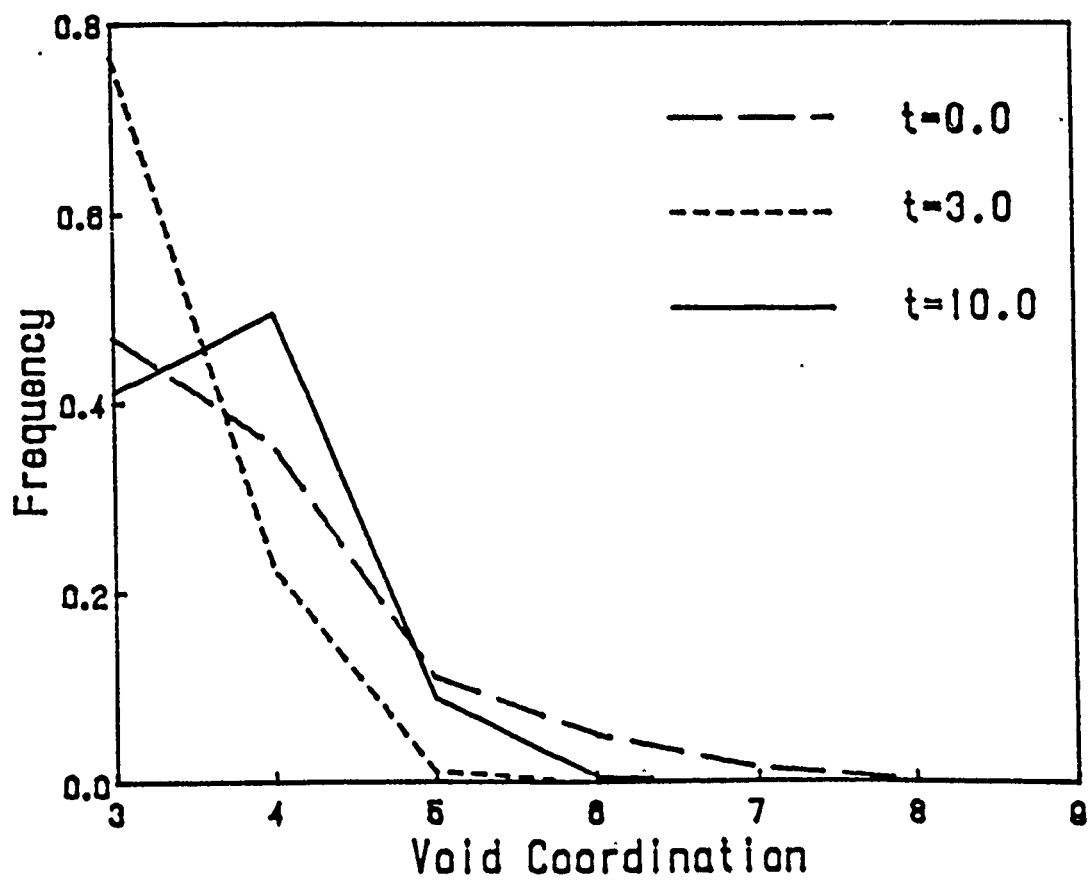


Figure 16. Development of the Void Coordination Distribution (VCD) toward a stationary distribution (solid line).

The initial VCD starts as a broad distribution peaked at coordination 3 but narrows its distribution at $t=1.0$ before developing the equilibrium distribution with a coordination peak at 4 and VCD μ of 3.69 at $t=10.0$. The VCDs shown in Fig. 16 are normalized to 1.0 and does not show the effect of densification on the density of the voids. Figure 17 shows the void density for the base case at $t=0.0$, 1.0 ($x_1=0.85$), and 2.0 ($x_1=0.95$). The void density distribution shown in Fig. 17 is obtained by multiplying the VCD by the void number density, x_2 . The void density distribution is the probability of finding an n -coordinated void in cellular structure whereas the VCD describes the relative frequency of an n -coordinated void with respect to the void population only. Figure 17 has 2 important implications. First, during the majority of the densification process, the VCD is peaked at 3 coordinated voids and does not reach a stationary distribution until well after the system has reached its stationary state. This indicates that different measures of structure such as density, the CCD, or the VCD develop to their respective stationary states with different characteristic times. Second, the decay of the void density distribution shown in Fig. 17 implies that the void distribution is a useful measure of partially dense structures but as the structure approaches full density, the void distribution becomes more difficult to experimentally determine due to the low probabilities of occurrence of the voids.

Figure 18 shows the behavior of the normalized system entropy (S_k), chemical potential (BMU), and grand potential (BGP) for the base calculation (initial density = 0.6, CHM=100). Figure 18 indicates that the entropy attains its stationary value early in the densification process and that the grand potential is dominated by the chemical potential as the structure approaches full density.

Figure 19 shows the state trajectories of several structures projected onto the z_1 - x_1 plane. The state space for Model-V has 7 dimensions (corresponding to the 7 3-

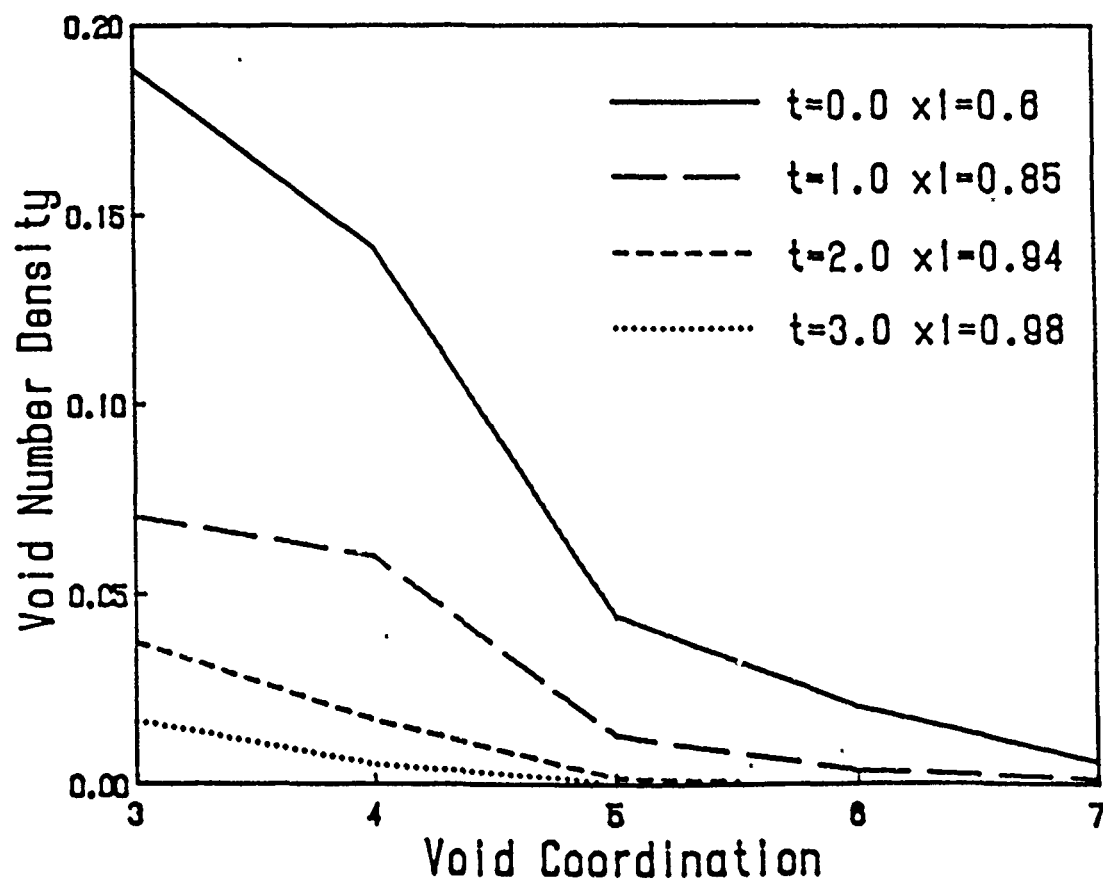


Figure 17. Model-V calculated Void Density Distribution (VDD) for the same times as in Figure 16. The decay of the VDD indicates increasing density of the structure.

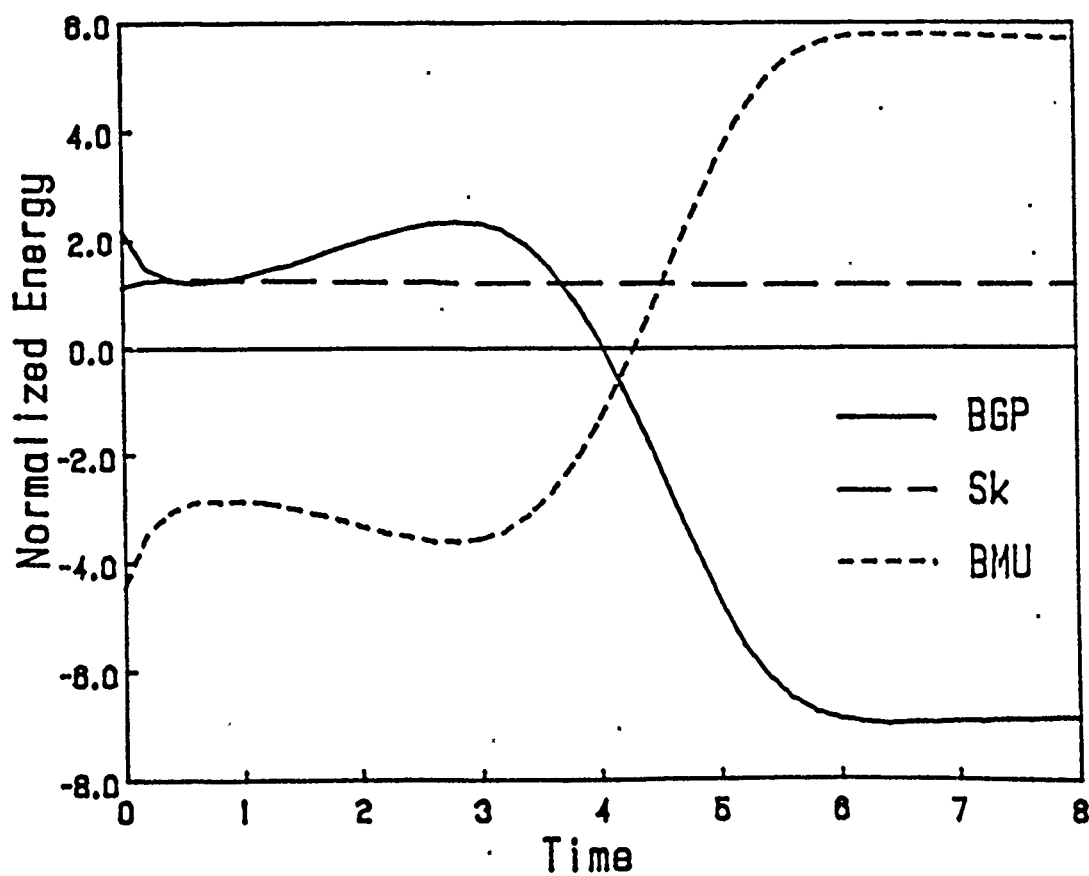


Figure 18. Behavior of the dimensionless structural entropy (S/k), "chemical potential" (BCHM), and "grand potential" (BGP). The entropy and chemical potential are given by Eqs. (1) and (14), respectively.

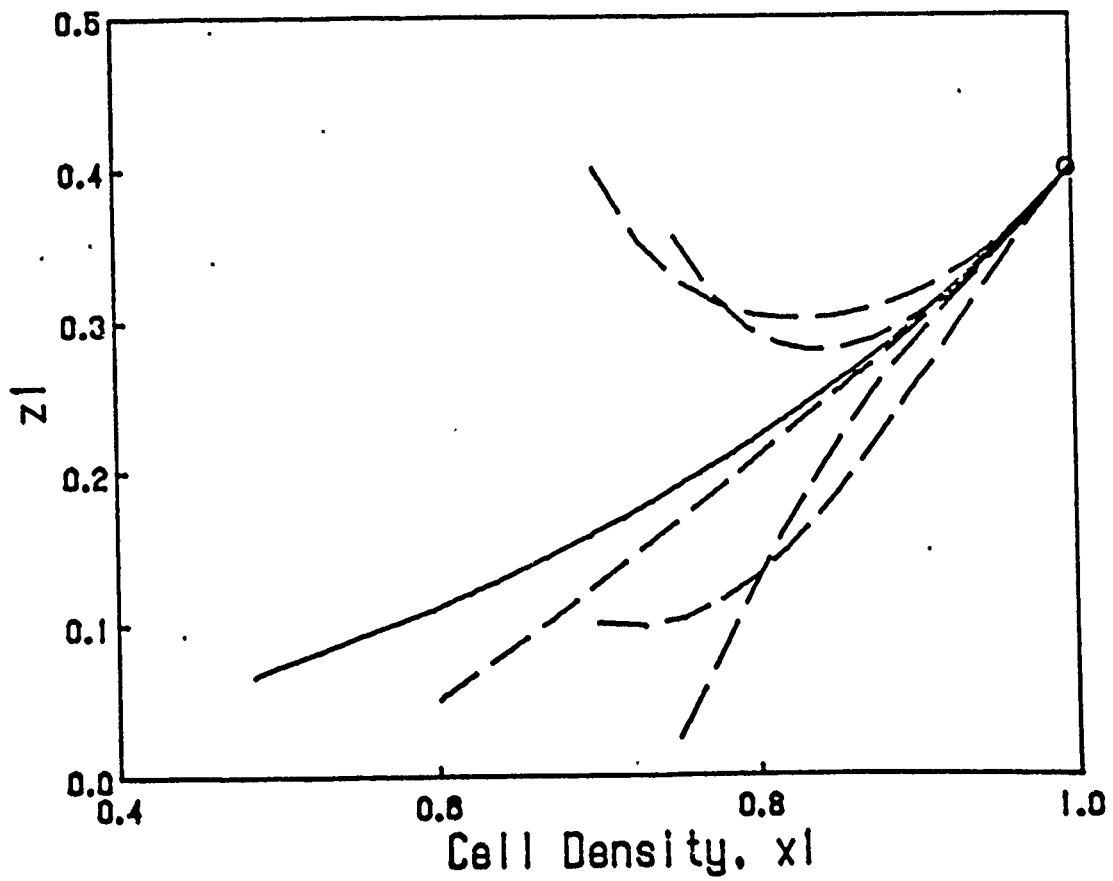


Figure 19. State trajectories of several structures with different initial conditions projected onto the z_1 - x_1 plane. Although initial structures may be different, all structures develop to the same stationary point (circle).

point cluster variables used in Model-V) so the projection of these trajectories onto the z_1 - x_1 plane results in a loss of information. The solid line in Fig. 19 indicates the stationary value of the z_1 state variable as a function of density (x_1). The 5 trajectories shown in Fig. 19 start at 3 different initial densities but approach a common stationary point at a density of 0.997 which is determined by the value of CHM provided to the calculation. This behavior is consistent with the E-V calculations and the results of the Model-0 calculations. The significant feature illustrated by Fig. 19 is that structures with the same initial density evolve along distinct paths. This also shows that the structure density is not sufficient in characterizing structure.

CHAPTER 5












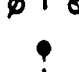
MODEL-VI

Model-VI is a three-point approximation of the single phase problem that incorporates both the T1 and T2 processes. The CVM analysis is essentially the same as the second model presented in Kikuchi's soap froth paper.³ The model represents a fully dense structure but allows for the elimination of a cell via the T2 process and can therefore be interpreted as following the initial stages of grain growth. As mentioned previously, the PPM calculations do not directly address the geometric evolution of the structure, so the experimental grain growth exponent presented in Chapter 2 cannot be verified by this calculation. The PPM calculations of Model-VI should be interpreted as the initial behavior of the structure prior to the onset of normal grain growth where the CCD is stable.

5.1 E-VI Description and Results

The model contains 13 triangle variables but topological restrictions in dual space reduce this set to 9 variables. The thirteenth variable (Kikuchi's model contained only 12 variables) was required to allow for all possible T1 processes on the dual network but this variable was found to be of second order in time in the PPM formulation and was therefore neglected in both the CVM and PPM calculations. Table 11 lists the 12 3-point state variables along with their degeneracies and indicate

Table 11. Ernie-VI 3-point state variables

State Variable	Degeneracy	Dual Representation
z1	1	
z2	3	
z3	6	
z4	6	
z5	12	
		
z7	3	
z8	12	
		
zA	12	
		
		

the variables that are equivalent. The first 2 3-point state variables are identical to the 3-point state variables used in Model-0 and the additional 3-point variables result from the incorporation of the 2 additional point state variables discussed below. Table 12 lists the subcluster state variables and Table 13 lists the reduction relations for the point and pair variables. Although the model is still single phase (i.e. fully dense), we now have three point variables because of the incorporation of the T2 process into our model.

The two additional point variables are required for the T2 process and represent a cell that was eliminated by a T2 process. Figure 20 presents the dual representation of a T2 process followed by a T1 process and show the three 1-point state variables. The two additional point variables should be interpreted as "not-cells" instead of voids as was done in Model-V since Model-VI is single phase. The not-cell represents an unoccupied lattice point in the dual lattice and represents the elimination of a cell via a T2 process. The not-cell is distinct from the void cell in Model-V in that the void cell represented a "hole" in the real structure while the not-cell represents a "vacancy" in the dual lattice. The densification process in Model-V was accomplished by replacing the void with a cell while the "growth" process in Model-VI represents a cell elimination.

Model-VI used the natural iteration method (NIM) described in Chapter 3 and essentially followed the Model-V calculational procedure. The source listing for ERNIE-VI is presented in Appendix B. The bond energies for the 2-point state variables were all set to the same small value for the calculations described below. This was done to keep the calculations purely topological in character since the Tanemura assumption underlying bond energy assignment was very restrictive.

Table 12. Ernie-VI subcluster state variables

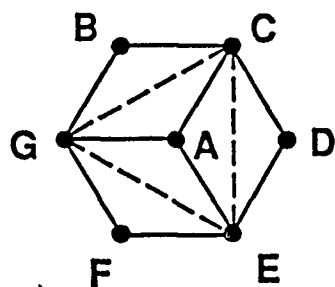
State Var.	Degeneracy	Dual Rep.	State Var.	Degeneracy	Dual Rep.
y1	1	●—●	y2	1	● ●
y3	2	● o	y4	2	● o
y5a	2	● ∅	y5b	2	● ∅
y6	4	● ∅	y7	2	●—○
y8	1	o o	y9	4	● ∅
yA	4	∅ ∅			
x1	1	●	x2	1	o
x3a	2	∅ ⊕	x3b	1	∅

Table 13. Reduction relations for Ernie-VI state variables

		z1	z2	z3	z4	z5	z7	z8	zA
y1	(1)	1	2	2	2	4			
y2	(1)		1						
y3	(2)			1			1	2	
y4	(2)			1					
y5a	(2)				2				
y5b	(2)					1		1	2
y6	(4)					1			
y7	(2)				1	1		1	2
y8	(1)						1		
y9	(4)							1	
yA	(4)								1
x1	(1)	1	3	4	4	8	1	4	4
x2	(1)			2			2	4	
x3a	(2)				1	1		1	2
x3b	(1)					2		2	4

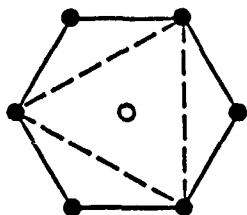
NOTE:

The coefficients shown in the table are used in the same manner as the Model-V coefficients shown in Table 6.



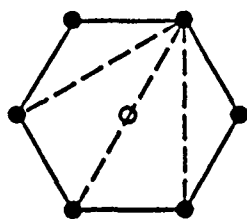
Cell A = x1

T2 Cell Elimination
(Cell A Eliminated)



Cell A = x2

T1 Neighbor Exchange
(Cells C & F become neighbors)



Cell A = x3

Figure 20. Illustration of the T1 and T2 process and the point state variables used in Model-VI

Model-VI also required a "chemical potential" to set the equilibrium cell number density. The "chemical potential" for Model-VI is shown without the bond energy adjustments in Eq. (16) below:

$$\text{CHM} = \ln \left(\left(\frac{z1}{z7} \right)^3 \left(\frac{x1}{x2} \right) \left(\frac{y1^3}{(y3^2 y8)} \right)^{1.5} \right) \quad (16)$$

The "grand potential" for the Model-VI system was formed and several calculations were performed with different CHM values in order to find the system with the maximum entropy. The maximum entropy system was identified as the equilibrium state for the Model-VI system. Figure 21 presents the entropy as a function of the cell number density (with respect to the CVM lattice), $x1$. The curve shown in Fig. 21 is the locus of points representing the maximum entropy given a value of $x1$. The maximum of these points is then taken as the stationary state of the system and is located at a cell number density of 0.86.

The CCD produced by the CVM calculation of Model-VI (solid line) is presented in Fig. 22 along with the Model-0 CCD (broken line). The CCDs from the two models are very similar and indicate that the T2 process does not greatly affect the CCD. This differs from the results of Kikuchi in which he found that the CCD of his model 2 was more sharply peaked at coordination 6. This difference is due to a counting error that Kikuchi made in the CCD generation from the state variables.

5.2 F-VI Description

The 3-point path variables are listed in Table 14. There are 30 3-point path variables but only 18 are distinct. The Z7D path variable (and its reverse variable, ZD7) is second order in time and was neglected reducing the number of distinct 3-

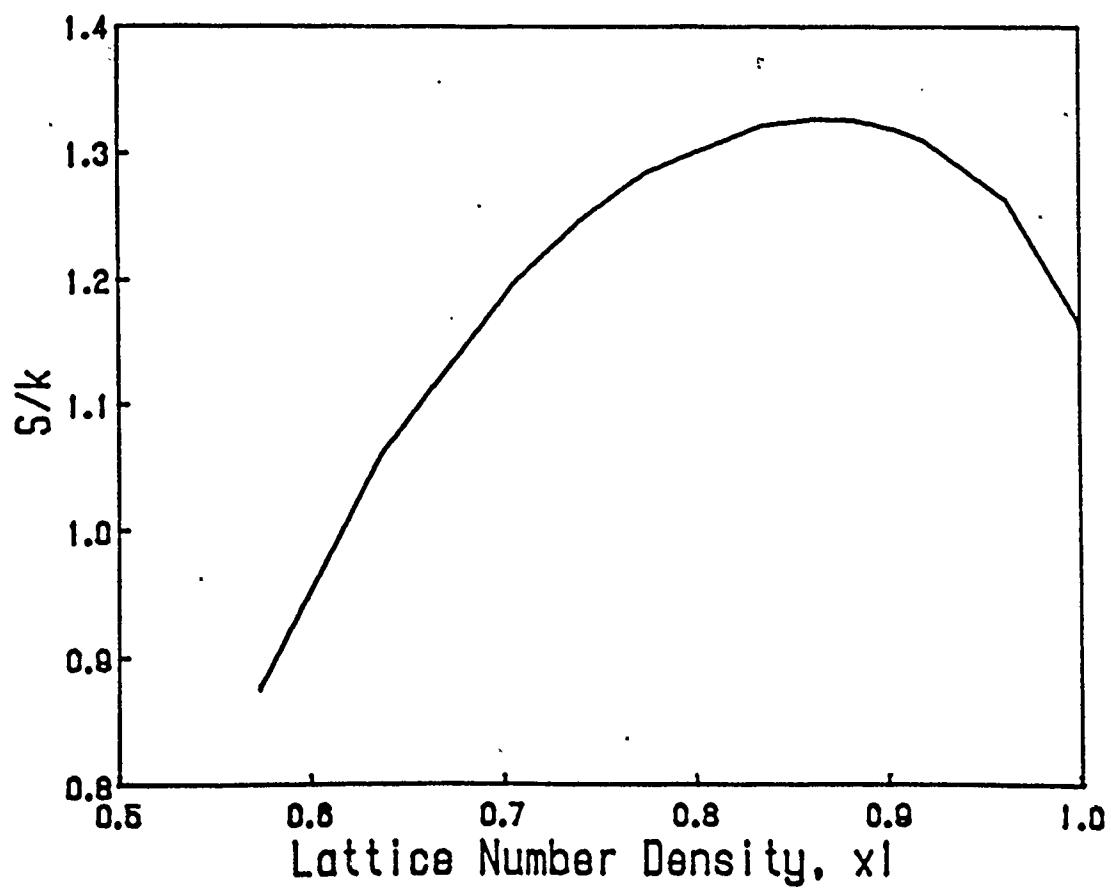


Figure 21. Model-VI CVM calculated (ERNIE-VI) entropy as a function of cell density, x_1 .

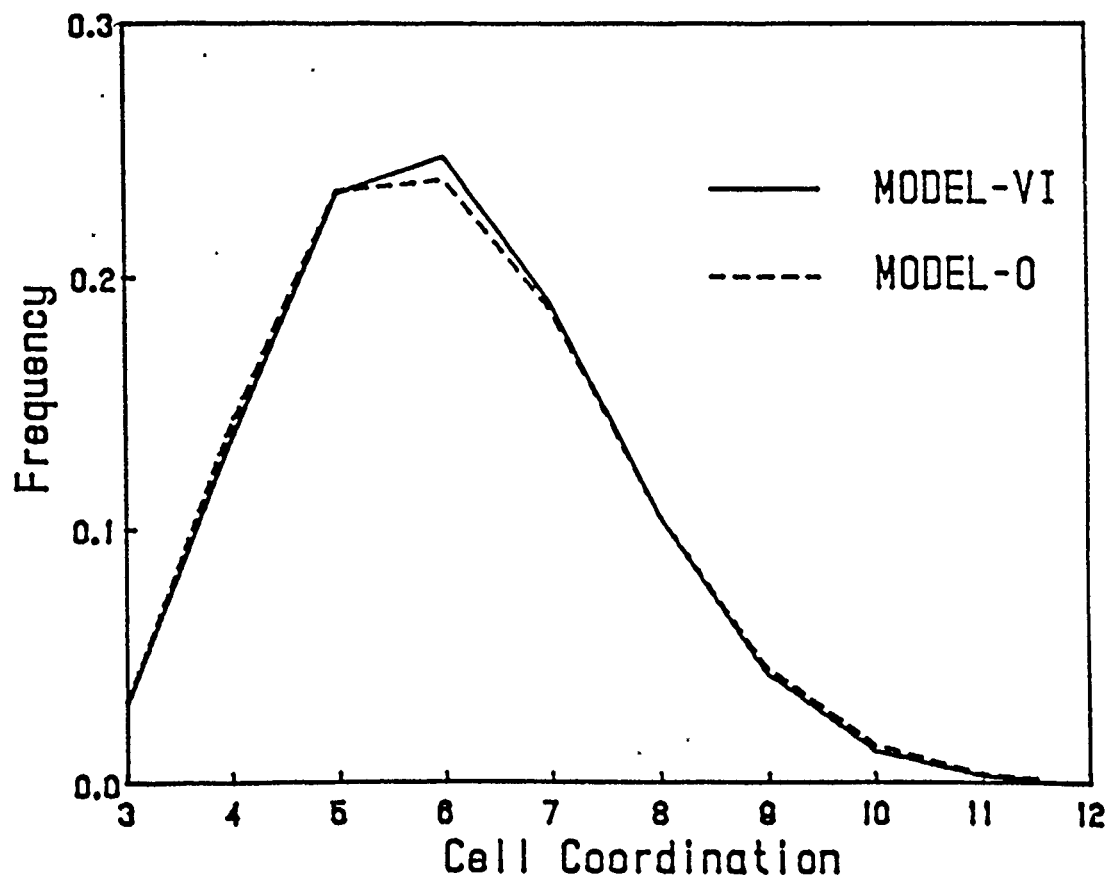











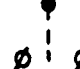








Figure 22. Comparison of the stationary CCDs calculated by Model-0 and Model-VI (ERNIE-VI).

Table 14. Felix-VI 3-point path variables

State Variable	Degeneracy	Dual Representation	
		t	$t+Dt$
z12	3		
z34	6		
z35	12		
z78	12		
z8A	24		
z23	6		
z37	6		
z58	12		
z7D	3		

point path variables to 16. Figure 23 shows the relation of the 9 state variables and 18 path variables. The horizontal links between the state variables enclosed by circles represent the T1 path variables and the vertical links represent the T2 path variables. The direction of the vertical links indicate cell elimination (downward direction) or cell creation (upward direction). The numbers in parentheses indicate the degeneracy of the path variable. Table 15 lists the subcluster reduction relations for the path variables and Table 16 lists the state-path equations. Table 17 list the T0 state-path reduction relations used to eliminate the T0 path variables.

The F-VI calculations used a dimensionless time variable that was normalized to the T1 rate process. The ratio of the forward T2 rate (cell elimination) to the T1 rate and the ratio of the reverse T2 rate (cell creation) to the forward T2 rate was provided as input to the calculations. The reverse T2 rate represents the creation of a three-sided cell and is included in the calculation since it is a valid process although unlikely in reality. As in Model-V, the first ratio behaved as a scaling factor for the dimensionless time variable and the second ratio set the equilibrium cell number density. The listing for FELIX-VI is presented in Appendix B.

5.3 F-VI Results

Figure 24 shows the behavior of the cell number density for several initial configurations and is similar to Figs. 6 and 13 for Models -0 and -V, respectively. The significant feature in Fig. 24 is that initially different structures develop to a common stationary state.

Figure 25 shows the evolution of the CCD at $t=0.0$, 0.1 , 0.3 , and 50.0 for the path depicted by the solid line in Fig. 24. The development of the CCD shown in the

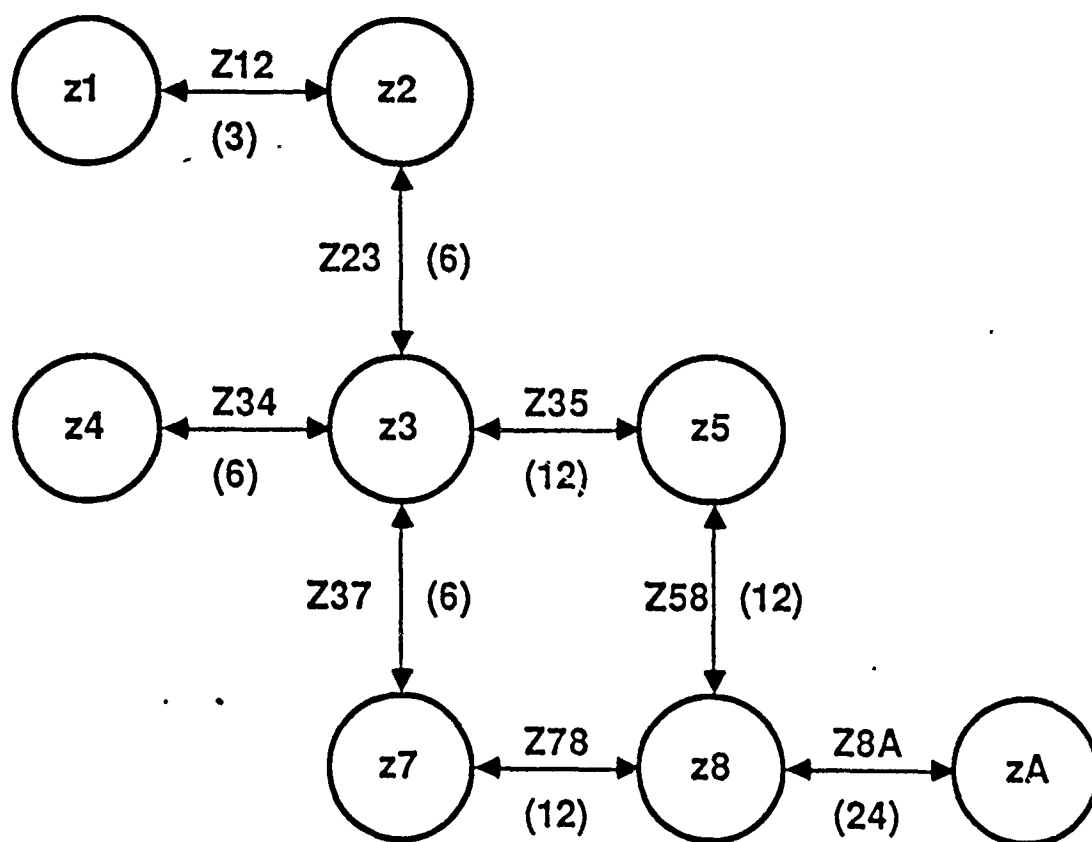


Figure 23. Relation of the state and path variables for Mode-VI

Table 15. Reduction relations for Felix-VI path variables.

	Z12	Z34	Z35	Z78	Z8A	Z23	Z37	Z58
Y12 (1)	1							
Y35a (2)		1						
Y35b (2)			1	1	2			
Y37 (2)			1	1	2			
Y46 (4)			1					
Y47 (2)		1						
Y89 (4)				1				
Y9A (8)					1			
Y13 (2)						1	1	2
Y24 (2)						1	1	2
Y13 (2)						1	1	2
Y24 (2)						1		
Y48 (2)							1	
Y69 (4)								1
X23a (2)		1	1	1	2			
X23b (1)			2	2	4			
X12 (1)						2	2	4

NOTE:

The coefficients shown in the table are used in the same manner as the Model-V path reduction coefficients shown in Table 8.

Table 16. Felix-VI State-Path Equations

	SZ12	SZ34	SZ35	SZ78	SZ8A	SZ23	SZ37	SZ58
$\Delta z1$	-3							
$\Delta z2$	1					-2		
$\Delta z3$		-1	-2			1	-1	
$\Delta z4$		1						
$\Delta z5$			1					-1
$\Delta z7$				-4			2	
$\Delta z8$				1	-2			1
ΔzA					2			

NOTE:

The coefficients shown in the table are used in the same manner as the Model-V state-path coefficients shown in Table 9.

Table 17. Felix-VI Reduction Relations for the T0 Process

		z12	z35	z78	z8A	z23	z37	z58
Z11	z1	-3						
Z22	z2	-1*				-2		
Z33	z3		-3	-1	-2	-1*	-1	
Z44	z4		-1*	-1*	-2			
Z55	z5		-1*					-1
Z77	z7			-4			-2*	
Z88	z8			-1*	-2			-1*
ZAA	zA				-2*			
Y11	y1	-1				-2	-2	-4
Y33	y3		-3	-3	-6	-1*	-1*	-2*
Y55	y5		-1*	-1*	-2*			
Y77	y7		-2*	-2*	-4*			
X11	x1					-2	-2	-4
X22	x2		-6	-6	-12	-2*	-2*	-2*
X33	x3		-2*	-2*	-4*			

NOTE:

An asterisk following the coefficient denotes the reverse path variable, i.e. Z21 instead of Z12. For example, the path reduction relation for the Z22 path variable is given below:

$$Z22 = z2 - Z21 - 2Z23 .$$

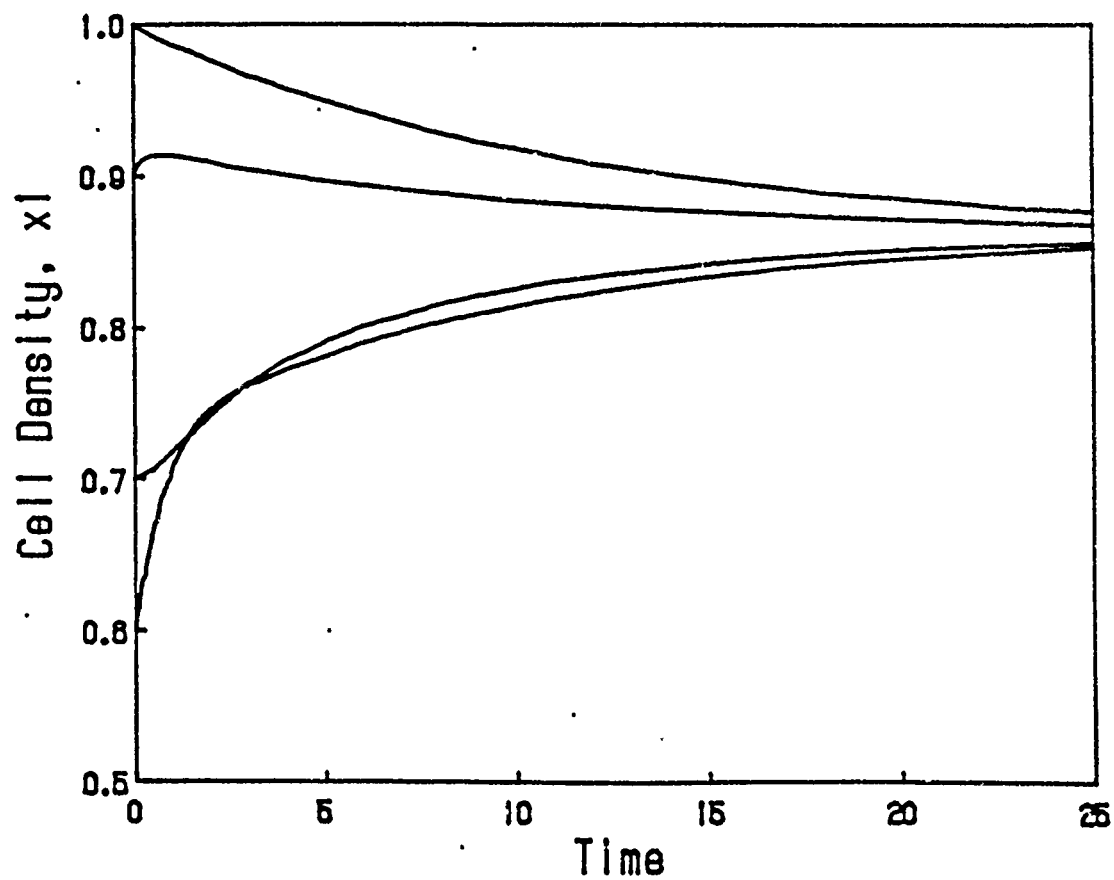


Figure 24. Model-VI calculated cell number density, x_1 , for several initially different structures.

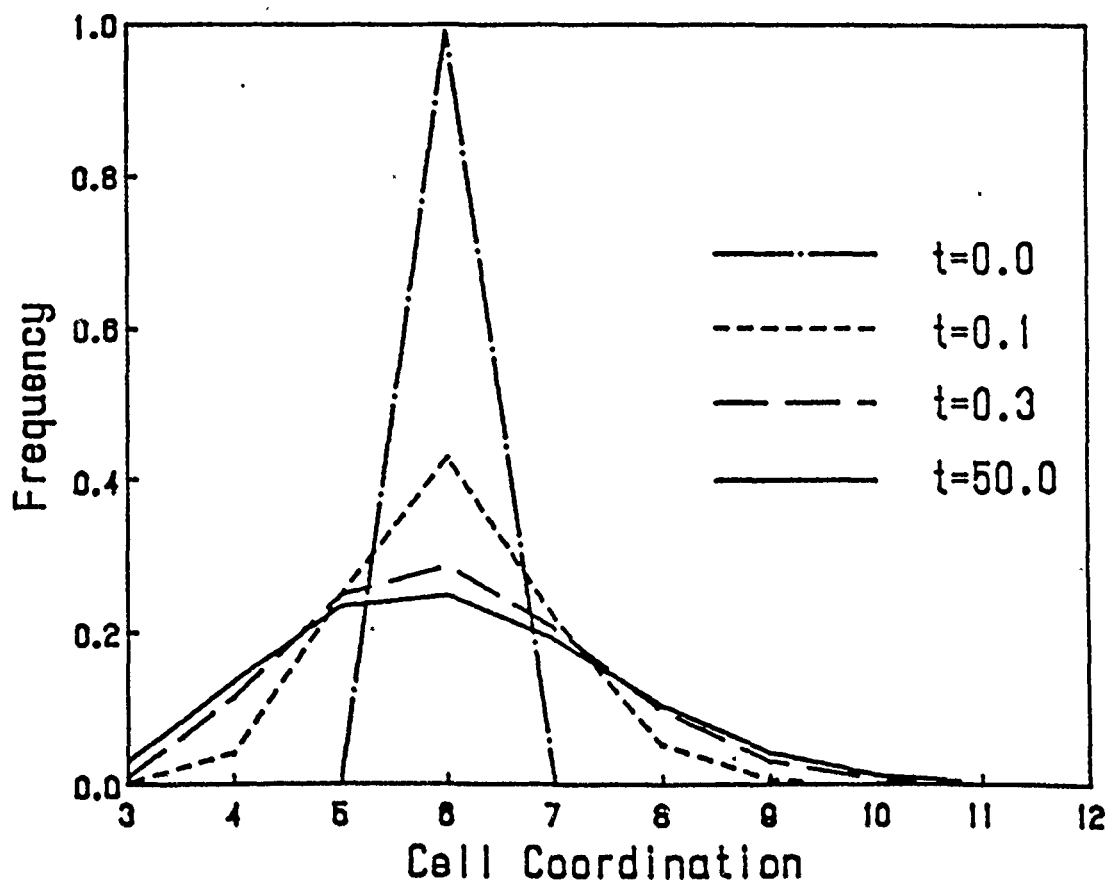


Figure 25. Development of the CCD for a structure with an initial cell number density of 0.6.

figure is similar to the behavior of Models -0 and -V shown in Figs. 7 and 14, respectively.

Figure 26 presents the state trajectories of several structures projected onto the x_2 - x_1 plane. Model-VI describes an 7-dimensional state space and projection onto a 2-dimensional space necessarily compresses some of the trajectory information. The important feature of Fig. 26 is the convergence of the different structures to a common stationary point indicated by the circle in the figure. Figure 26 is similar to Fig. 19 for Model-V. The difference between Fig. 26 and Fig. 19 is in the determination of the cell number density in both models. In Model-V, the cell (or grain) number density can be directly measured by counting the number of cells (grains) and the number of voids. In Model-VI however, the cell density, x_1 represents the occupation density of the dual representation on the CVM lattice and cannot be easily determined by experimental methods.

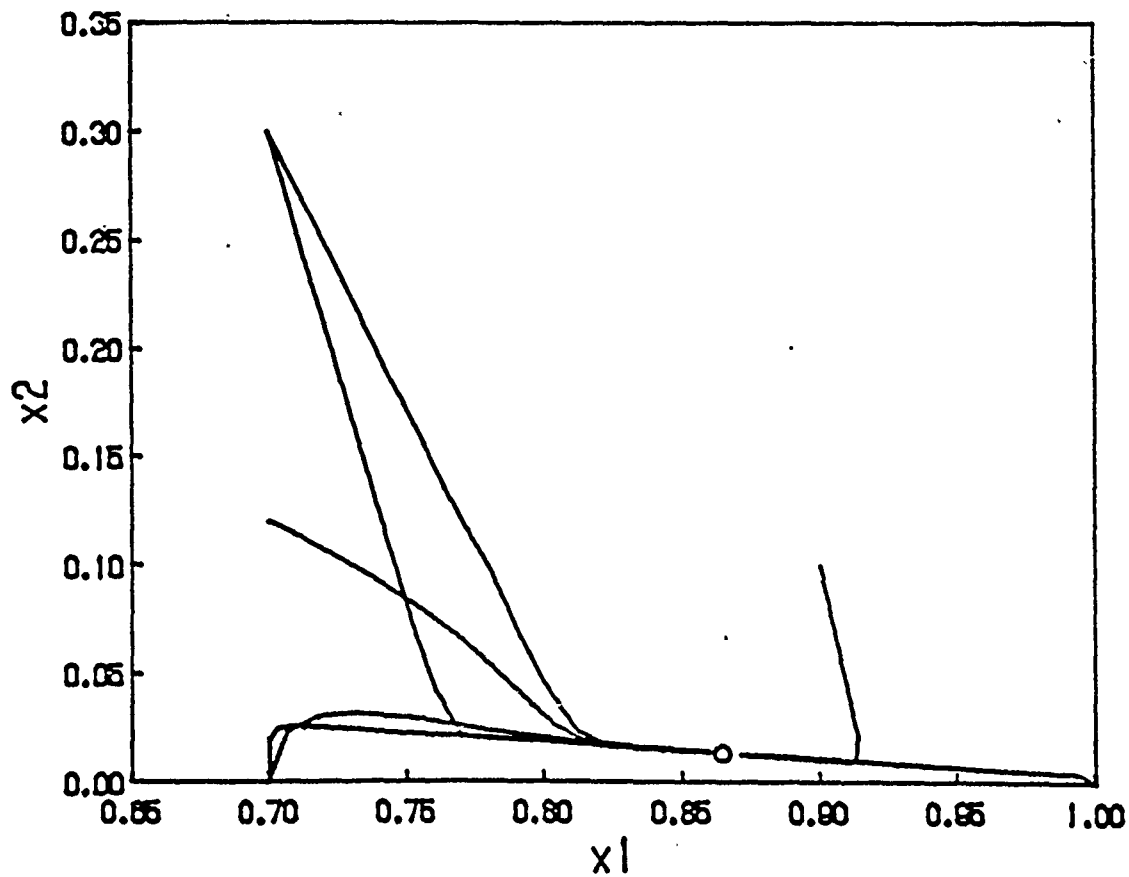


Figure 26. State trajectories of several structures with different initial conditions projected onto the x_2 - x_1 plane. The trajectories show that structures evolve along distinct paths but develop to a common stationary state (circle).

CHAPTER 6

SUMMARY

This chapter summarizes the results of the CVM and PPM calculations presented in this work. The results of the calculations are compared with available experimental data and the implications of these results to ceramic processing are briefly discussed.

Figure 27 presents the CCDs calculated by the CVM and the Monte Carlo simulations of the Exxon group. These distributions are compared to the experimental data set of Aboav on soap froths and to data gathered from an alumina microstructure. As discussed previously, both of the calculated CCDs are in reasonable agreement with the data. Both data sets have a sharper peak at coordination 6 than that exhibited by the calculations. In the case of the CVM calculations, the CCD can be sharpened by assigning different bond energies to the 2-point state variables but the CVM calculations do not produce CCDs with a maximum at coordination 5, as indicated by the Exxon simulations and the alumina data. The agreement between the Exxon and the CVM result is interesting since this agreement indicates that boundary energy may not be the determining factor in the shape of the stationary CCD. The Exxon simulations are performed on the real space structure and incorporate the effect of boundary energies on the structure. Since the simulation is on the real structure, the topological restrictions of space filling are automatically satisfied by the simulations.

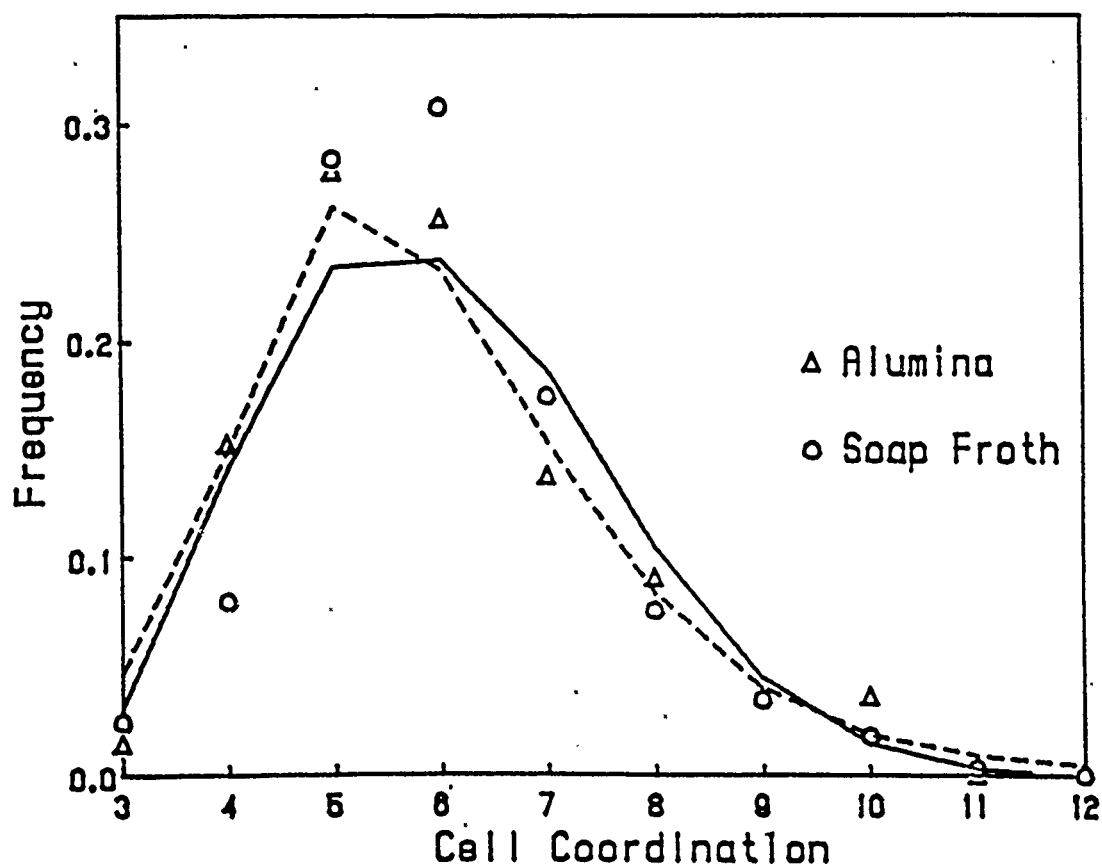


Figure 27. Comparison of the CVM calculated CCD (solid line) to computer simulations (dashed lines) and experimental data.

The CVM calculations use only topological information about the structure but predict a stationary CCD in good agreement with the simulations.

Figure 28 shows a comparison of the CVM calculated void coordination distribution to the VCD obtained from an alumina microstructure. The agreement shown in the figure may be misleading since the data sample is very small (less than 100 voids) and subject to large statistical uncertainties. Furthermore, the size of the voids are smaller than the grains which invalidates the assumption that void and grain sizes are roughly equal. This should result in a higher void to cell ratio which is exhibited by the alumina structure.

Since this work takes a novel approach to the evolution of cellular structures, the lack of existing direct experimental confirmation is not surprising. The comparison to real structures is further complicated by the inability of the present models to predict the grain size distribution which is the usual format for the description of cellular structures. In addition, it is extremely difficult to prepare an experiment that could directly show the broadening of the CCD prior to grain growth in a fully dense system. ³⁸ The difficulty is due the rapid development of the CCD which is usually completed before the system is fully dense. Experiments with soap froths can be initialized in the fully dense state and with a narrow CCD and Aboav's analysis of Smith's soap froths does show that the CCD broadens with time. ²³ The growth of the soap bubbles (and the reduction of the number of bubbles) terminated the experiment before a stationary CCD was attained. This result is not predicted by the PPM calculations since the calculations indicate that the development of the stationary CCD is very rapid. The reason for this discrepancy is due to the inability of the present models to handle the changing geometry of the cellular structure. Since the CVM and PPM calculations use only the topological information of the structure,

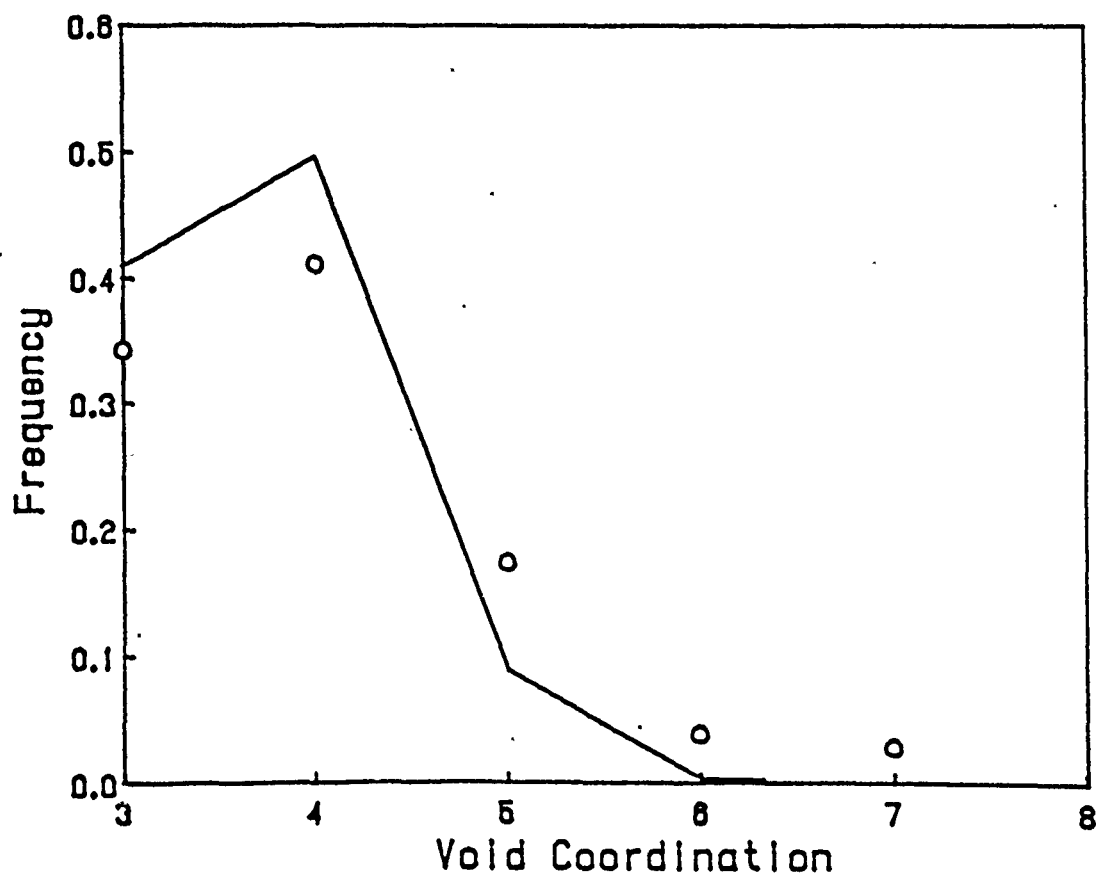


Figure 28. Comparison of the calculated VCD to data obtained from an alumina section.

the implicit assumption is that the geometry does not change. In the soap froth, the bubbles grow rapidly and therefor change the geometry of the system.

Ceramic particulate systems do not show rapid grain growth until the final stages of sintering so these systems may be more appropriate for comparison to the PPM calculations. Since Model-V models densification, we should be able to compare the PPM calculations to real systems. The most direct comparison would be the behavior of the CCD with time and the ratio of the void density to cell density. Both comparisons must make assumptions on the size of the voids and cells so the comparison with experiment is probably valid for only a narrow range of densities and is not justified in light of these assumptions.

The critical limitation of this work that prevents direct comparison to real systems is the inability of the CVM/PPM formulation to describe the geometric evolution of the cellular structure. As discussed previously, this is a result of describing a random cellular structure by a method that requires a lattice structure. The lattice structure required by the CVM/PPM imposes nonuniform deformations on the random cellular structure which results in the loss of information on the actual geometry of the system. Unfortunately, the continuum formulation of the CVM/PPM which would allow the direct description of a random cellular structure does not exist. In spite of this limitation, this work does have implications to ceramic processing and are summarized below.

First, the CVM/PPM calculations indicate a stationary CCD which is in agreement with the existing body of knowledge discussed in Chapter 2. In addition, the PPM calculations are consistent with the CVM results.

Second, the PPM calculations show that structures develop along unique paths and depend on the initial structure. All structures asymptotically approach the common stationary state described by the CVM results.

REFERENCES

- 1) I.A. Aksay, in Advances in Ceramics, Vol. 9, Amer. Ceram. Soc., 1984, p94.
- 2) E.A. Barringer, R. Brook, H.K. Bowen, in Sintering and Heterogeneous Catalysis, edited by G.C. Kuczynski et al., (Plenum Press, New York, 1984) pp. 1-21.
- 3) E. Barringer et al., in Ultrastructure Processing of Ceramics, Glasses, and Composites, edited by L.L. Hench and D.R. Ulrich (John Wiley & Sons, New York, 1984), pp. 315-333.
- 4) M.F. Yan, R.M. Cannon, H.K. Bowen, U. Chowdhry, "Effect of grain size distribution on sintered density" Mater. Sci. Engr. 60, 275-281, (1983).
- 5) M.A. Occhionero, J.W. Halloran, in Sintering and Heterogeneous Catalysis, edited by G.C. Kuczynski et al., (Plenum Press, New York, 1984) pp. 89-102.
- 6) R. Kikuchi, "A theory of cooperative phenomena," Phys. Rev. 81(6), 988-1003, March 15, 1951.
- 7) R. Kikuchi, "The path probability method," Progress of Theoretical Physics Supplement No. 35, (1966).
- 8) R. Kikuchi, "Shape distribution of two-dimensional soap froths," J.Chem.Phys. 24(4), 861-867 April, 1956.
- 9) D. Weaire, N. Rivier, "Soap, cells and statistics - random patterns in two dimensions," Contemp.Phys. 25(1), 59-99 (1984).
- 10) N. Rivier, A. Lissowski, "On the correlation between sizes and shapes of cells in epithelial mosaics," J. Phys. A15, L143 (1982).
- 11) P. Feltham, "Grain growth in metals," Acta Metall. 5, 97 (1957).
- 12) M. Hillert, "On the theory of normal and abnormal grain growth," Acta Metall. 13, 227 (1965).
- 13) N.P. Louat, "On the theory of normal grain growth," Acta Metall. 22, 721 (1974).
- 14) F.N. Rhines, K.R. Craig, "Mechanism of steady-state grain growth in aluminum," Metall. Trans. 5, 413 (1974).

- 15) P.S. Sahni, D.J. Srolovitz, G.S. Grest, M.P. Anderson, S.A. Safran, "Kinetics of ordering in two dimensions. II. quenched systems," *Phys. Rev.* B28, 2705 (1983).
- 16) M.P. Anderson, D.J. Srolovitz, G.S. Grest, P.S. Sahni, "Computer simulation of grain growth - I. kinetics," *Acta Metall.* 32(5), 783-791 (1984).
- 17) D.J. Srolovitz, M.P. Anderson, P.S. Sahni, G.S. Grest, "Computer simulation of grain growth - II. grain size distribution, topology, and local dynamics," *Acta Metall.* 32(5), 793-802 (1984).
- 18) M.P. Anderson, G.S. Grest, D.J. Srolovitz, "Grain growth in three dimensions: a lattice model," *Scripta Metall.* 19, 225 (1985).
- 19) D. Weaire, J.P. Kermode, "Computer simulation of a two-dimensional soap froth I. Method and motivation," *Phil. Mag.* B48(3), 245 (1983).
- 20) D. Weaire, J.P. Kermode, "Computer simulation of a two-dimensional soap froth II. Analysis of results," *Phil. Mag.* B50(3), 379 (1984).
- 21) D. Weaire, J.P. Kermode, "The evolution of the structure of a two dimensional soap froth," *Phil. Mag.* B47(3), L29 (1983).
- 22) C.S. Smith in *Metal Interfaces*, edited by C. Herring (American Society for Metals, Cleveland, Ohio, 1952), p. 65.
- 23) D.A. Aboav, "The arrangement of cells in a net," *Metallography* 13, 43 (1980).
- 24) J. Wejchert, D. Weaire, J.P. Kermode, "Monte Carlo simulation of the evolution of a two-dimensional soap froth," *Phil. Mag.* B53(1), 15 (1986).
- 25) J. von Neumann in *Metal Interfaces*, edited by C. Herring (American Society for Metals, Cleveland, Ohio, 1952), p. 108.
- 26) A. Soares, A.C. Ferro, M.A. Fortes, "Computer simulation of grain growth in a bidimensional polycrystal," *Scripta Metall.* 19, 1491 (1985).
- 27) C.W.J. Beenakker, "Evolution of two-dimensional soap-film networks," *Phys. Rev. Lett.* 57(19), 2454 (1986).
- 28) C.W.J. Beenakker, "Two-dimensional soap froths and polycrystalline networks: Why are large cells many-sided?," *Physica* 147A, 256 (1987).
- 29) C.W.J. Beenakker, "Numerical simulation of a coarsening two-dimensional network," *Phys. Rev.* A37(5), 1697 (1988).
- 30) M. Marder, "Soap-bubble growth," *Phys. Rev.* A36(1), 438 (1987).

- 31) N. Rivier, "Statistical crystallography structure of random cellular networks," *Phil. Mag* B52(3), 795 (1985).
- 32) M. Blanc, A. Mocellin, "Grain coordination in plane sections of polycrystals," *Acta Metall.* 27, 1231 (1979).
- 33) E. Carnal, A. Mocellin, "A topological model for plane sections of polycrystals," *Acta Metall.* 29, 135 (1981).
- 34) C.S. Pande, "On a stochastic theory of grain growth," *Acta Metall.* 35(11), 2671 (1987).
- 35) R. Kikuchi, "CVM entropy algebra and convergence of entropy hierarchy," *TPB*, (1988).
- 36) R. Kikuchi, "Superposition approximation and natural iteration calculation in cluster-variation method," *J. Chem. Phys.* 60(3), 1071-1080, 1 February 1974.
- 37) M. Tanemura, "Lattice model of the two-dimensional soap froth," Report of the Institute for Statistical Mathematics, 26(2), 107 (1979).
- 38) C.B. Martin, "Preparation and microstructure evolution of hierarchically clustered structures," M.S. Thesis, University of Washington, Seattle, WA, 1988.

APPENDIX A

MODEL-V SOURCE LISTINGS

This appendix contains the FORTRAN source code listings for the model-V calculations. Listing 1 shows the code for the model-V CVM calculation, ERNIE-V. Listing 2 shows the code for the model-V PPM calculation, FELIX-V. Both programs call GCN5F, shown in listing 3 to calculate the CCD from the state variables. Listing 4 shows subroutine where the VCD is calculated. The programs were compiled with the Microsoft FORTRAN v4.01 compiler using the /FPi87 option and the code was edited with Solution Systems' BRIEF v2.0 editor.

Listing 1. ERNIE-V

```

PROGRAM ERNIEV
C
C ERNIE-V IS THE 3 POINT CVM CALCULATION WITH SECOND PHASE
C
  IMPLICIT INTEGER*2 (I)
  IMPLICIT DOUBLE PRECISION (B,D,F,H,Q,T,X,Y,Z)
  CHARACTER*3 MTHS,MTHE
  COMMON /STATE/ Z1,Z2,Z3,Z4,Z5,Z6,Z7,Y1,Y2,Y3,Y4,Y5,Y6,X1,X2
  COMMON /COORD/ GCN(13),GNTOT,GCNAVE,GCNVAR,GCNCTOT
  COMMON /VCORD/ VCN(10),VCNTOT
  COMMON /THERM/ TEMP,SK,BE,BFN,BMU,BPV,BE1,BE2,BE3,XNPG,X1IN
  COMMON /TMARK/ ISH,ISM,ISS,ISF,ISY,ISN,ISD,MTHS,
+             IEH,IEM,IES,IEF,IEY,IEN,IED,MTHE,IDM,IDH,ELS
  CHARACTER*60 ATITLE
  CHARACTER*20 FIN,FOUT
  CHARACTER*2 FF /'\f'C/
  XSQ(X,Y) = (X-Y)*(X-Y)
  BOLTZK = 1.380662E-16
  PI      = 3.141592654
  A16     = 1.0/6.0
  A13     = 1.0/3.0
  XGROW   = 1.0
  ALAREA  = 1.0E-19
  XDELTA  = 9999.999
  IEND    = 0
  IPRT    = 0
  WRITE(*,2000)
  READ(*,2002) FIN
  WRITE(*,2001)
  READ(*,2002) FOUT
  OPEN(9,FILE=FIN)
  OPEN(10,FILE=FOUT,STATUS='NEW')
  CALL TIMARK(0)
  ICOUNT = 0
  READ(9,*) ATITLE
  READ(9,*) MAXSTERS,IPRINT,EPS
  READ(9,*) TEMP,E1,R31,R21,GSIZE,CHM
  READ(9,*) ZP1,ZP2,ZP3,ZP4,ZP5,ZP6,ZP7
  IF ((EPS .GT. 0.1) .OR. (EPS .LT. 1.0E-10)) EPS = 1.0E-7
  IF (CHM .EQ. 0.0) CHM = 1.0
  CHM2 = CHM*CHM
  ZNORM = ZP1 + 3.0*(ZP2 + ZP3 + 2.0*ZP4 + ZP5 + ZP6) + ZP7
  ZN = 1.0/ZNORM
  ZP1 = ZN*ZP1
  ZP2 = ZN*ZP2
  ZP3 = ZN*ZP3

```

```

ZP4 = ZN*ZP4
ZP5 = ZN*ZP5
ZP6 = ZN*ZP6
ZP7 = ZN*ZP7
YP1 = ZP1 + ZP3 + 2.0*(ZP2 + ZP4)
YP2 = ZP2
YP3 = ZP3 + ZP4 + ZP5 + ZP6
YP4 = ZP4
YP5 = ZP5 + ZP7
YP6 = ZP6
XP1 = ZP1 + 3.0*ZP2 + 2.0*ZP3 + 4.0*ZP4 + ZP5 + ZP6
XP2 = ZP3 + ZP7 + 2.0*(ZP4 + ZP5 + ZP6)
BETA = 1.0/(BOLTZK*TEMP)
BE1 = BETA*E1*0.5
BE2 = BETA*E1*0.5*R21
BE3 = BETA*E1*0.5*R31
XLIN = XP1
XNPG = PI*GSIZE*GSIZE/(3.0*ALAREA)
X1 = XP1
X2 = XP2
Y1 = YP1
Y2 = YP2
Y3 = YP3
Y4 = YP4
Y5 = YP5
Y6 = YP6
Z1 = ZP1
Z2 = ZP2
Z3 = ZP3
Z4 = ZP4
Z5 = ZP5
Z6 = ZP6
Z7 = ZP7
CALL CALCTH
CALL GCNVF
CALL VCNV
IPAGE = 1
WRITE(10,1000) FF,ATITLE
WRITE(10,1001) ISH,ISM,ISS,ISD,MTHS,ISY
WRITE(10,2010) FIN
WRITE(10,1002) MAXSTEPS,TEMP,BE1
WRITE(10,1003) IPRINT,CHM,E1
WRITE(10,1004) EPS,R21,GSIZE
WRITE(10,1005) R31,XNPG
WRITE(10,1010) ICOUNT,YP1,GCN(1),XDELTA,VCN(3),YP2,
+          GCN(2),BFN,VCN(4),YP3,GCN(3),SK,VCN(5),YP4,
+          GCN(4),BE,VCN(6),YP5,GCN(5),BMU,VCN(7),YP6,
+          GCN(6),BPV,VCN(8),GCN(7),GNTOT,VCN(9),ZP1,
+          GCN(8),GCNAVE,VCN(10),ZP2,GCN(9),GCNVAR,ZP3,

```



```

+          GCN(10),GCNCTOT,ZP4,GCN(11),VCN(1),ZP5,
+          GCN(12),VCN(2),XP1,ZP6,GCN(13),VCNCTOT,XP2,ZP7
  ICOUNT = 1
99 CONTINUE
  X16 = 0.0
  X26 = 0.0
  IF(XP1 .GT. 0.0) X16 = XP1**A16
  IF(XP2 .GT. 0.0) X26 = XP2**A16
  X13 = X16*X16
  IF(XP1 .GT. 0.0) THEN
    Z1 = YP1*DSQRT(YP1/XP1)
    Z2 = YP1*DSQRT(YP2/XP1)
  ELSE
    Z1 = 0.0
    Z2 = 0.0
  ENDIF
  IF(X26 .GT. 0.0) THEN
    Z3 = YP3*DSQRT(YP1)/(X13*X26)
    Z4 = DSQRT(YP1*YP3*YP4)/(X13*X26)
    Z5 = YP3*DSQRT(YP5)/(X16*X26*X26)
    Z6 = YP3*DSQRT(YP6)/(X16*X26*X26)
    Z7 = YP5*DSQRT(YP5/XP2)
  ELSE
    Z3 = 0.0
    Z4 = 0.0
    Z5 = 0.0
    Z6 = 0.0
    Z7 = 0.0
  ENDIF
  Z1 = Z1*EXP(-(1.5*BE1))*CHM2*CHM
  Z2 = Z2*EXP(-0.5*(2.0*BE1+BE2))*CHM2*CHM
  Z3 = Z3*EXP(-0.5*(BE1+2.0*BE3))*CHM2
  Z4 = Z4*EXP(-0.5*(BE1+BE2+BE3))*CHM2
  Z5 = Z5*EXP(-BE3)*CHM
  Z6 = Z6*EXP(-0.5*(BE2+2.0*BE3))*CHM
  ZNORM = Z1 + 3.0*(Z2+Z3+2.0*Z4+Z5+Z6) + Z7
  ZN = 1.0/ZNORM
  Z1 = ZN*Z1
  Z2 = ZN*Z2
  Z3 = ZN*Z3
  Z4 = ZN*Z4
  Z5 = ZN*Z5
  Z6 = ZN*Z6
  Z7 = ZN*Z7
  Y1 = Z1 + Z3 + 2.0*(Z2 + Z4)
  Y2 = Z2
  Y3 = Z3 + Z4 + Z5 + Z6
  Y4 = Z4
  Y5 = Z5 + Z7

```

```

Y6 = Z6
X1 = Z1 + 3.0*Z2 + 2.0*Z3 + 4.0*Z4 + Z5 + Z6
X2 = Z3 + Z7 + 2.0*(Z4 + Z5 + Z6)
XDELTA = XSQ(Z1,ZP1) + XSQ(Z2,ZP2) + XSQ(Z3,ZP3)
+       + XSQ(Z4,ZP4) + XSQ(Z5,ZP5) + XSQ(Z6,ZP6)
+       + XSQ(Z7,ZP7)
IF ( (XDELTA.LE.EPS) .OR. (ICOUNT.GE.MAXSTEPS) ) IEND =1
IPRT = MOD(ICOUNT,IPRINT)
IF ( (IEND .EQ. 1) .OR. (IPRT .EQ. 0) ) THEN
  CALL CALCTH
  CALL GCNVF
  CALL VCNV
  IPAGE = IPAGE + 1
  IF ( MOD(IPAGE,3) .EQ. 0 ) WRITE(10,1000) FF,ATITLE
  WRITE(10,1010) ICOUNT,Y1,GCN(1),XDELTA,VCN(3),Y2,
+       GCN(2),BFN,VCN(4),Y3,GCN(3),SK,VCN(5),Y4,
+       GCN(4),BE,VCN(6),Y5,GCN(5),BMU,VCN(7),Y6,
+       GCN(6),BPV,VCN(8),GCN(7),GNTOT,VCN(9),Z1,
+       GCN(8),GCNAVE,VCN(10),Z2,GCN(9),GCNVAR,Z3,
+       GCN(10),GCNCTOT,Z4,GCN(11),VCN(1),Z5,
+       GCN(12),VCN(2),X1,Z6,GCN(13),VCNTOT,X2,Z7
  IPAGE = IPAGE + 1
  IF (IEND .EQ. 1) THEN
    CALL TIMARK(1)
    WRITE(10,1099) IDH,IDM,ELS
    GO TO 9999
  ENDIF
ENDIF
ICOUNT = ICOUNT + 1
IF ( ICOUNT .LE. MAXSTEPS ) THEN
  XP1 = X1
  XP2 = X2
  YP1 = Y1
  YP2 = Y2
  YP3 = Y3
  YP4 = Y4
  YP5 = Y5
  YP6 = Y6
  ZP1 = Z1
  ZP2 = Z2
  ZP3 = Z3
  ZP4 = Z4
  ZP5 = Z5
  ZP6 = Z6
  ZP7 = Z7
  GO TO 99
ENDIF
1000 FORMAT(A,/,T10,A60,/)
1001 FORMAT(T20,'ESF RUN STARTED ON ',I2.2,':',I2.2,

```

```

+      ':',I2.2,2X,I2.2,A3,I4)
1002 FORMAT(T15,'MAXSTEPS =',I5,T35,'TEMP  =',0PF7.2,
+      T53,'E1/KT = ',1PE12.3)
1003 FORMAT(T15,'IPRINT  =',I5,T35,'CHM   =',0PF7.2,
+      T53,'E1      = ',1PE12.3)
1004 FORMAT(T15,'EPS      =',1PE7.1,T35,'R21   = ',
+      0PF6.2,T53,'GSIze = ',1PE12.3)
1005 FORMAT(T35,'R31     = ',0PF6.2,T53,'XNPG  = ',1PE12.3,/)
1010 FORMAT(T10,' N FREQUENCY',T25,'ICOUNT =',I5,
+T46,' N VOID FREQ',T61,1PE11.4,/,
+T10,' 0 ',0PF9.6,T25,'DELTA  =',1PE10.3,T46,
+ ' 3 ',0PF9.6,T61,1PE11.4,/,
+T10,' 1 ',0PF9.6,T25,'F/kTN   =',1PE10.3,T46,
+ ' 4 ',0PF9.6,T61,1PE11.4,/,
+T10,' 2 ',0PF9.6,T25,'S/k     =',1PE10.3,T46,
+ ' 5 ',0PF9.6,T61,1PE11.4,/,
+T10,' 3 ',0PF9.6,T25,'E/kTN   =',1PE10.3,T46,
+ ' 6 ',0PF9.6,T61,1PE11.4,/,
+T10,' 4 ',0PF9.6,T25,'mu/kT   =',1PE10.3,T46,
+ ' 7 ',0PF9.6,T61,1PE11.4,/,
+T10,' 5 ',0PF9.6,T25,'pV/kT   =',1PE10.3,T46,
+ ' 8 ',0PF9.6,T64,'Y^    Z',/,
+T10,' 6 ',0PF9.6,T25,'G TOTAL =',0PF9.6,T46,
+ ' 9 ',0PF9.6,T61,1PE11.4,/,
+T10,' 7 ',0PF9.6,T25,'GCN AVE =',0PF9.6,T46,
+ '10 ',0PF9.6,T61,1PE11.4,/,
+T10,' 8 ',0PF9.6,T25,'GCN VAR =',0PF9.6,
+T61,1PE11.4,/,
+T10,' 9 ',0PF9.6,T25,'DEF CON. =',0PF9.6,
+T61,1PE11.4,/,
+T10,'10 ',0PF9.6,T25,'VCN AVE =',0PF9.6,T52,'X ',
+T61,1PE11.4,/,
+T10,'11 ',0PF9.6,T25,'VCN VAR =',0PF9.6,T47,1PE11.4,
+T61,1PE11.4,/,
+T10,'12 ',0PF9.6,T25,'VCN TOT =',0PF9.6,T47,1PE11.4,
+T61,1PE11.4,/)
1099 FORMAT(T2,'***** Elapsed Time is ',I2.2,' Ho
+urs ',I2.2,' Minutes ',0PF5.2,' Seconds.  *****')
2000 FORMAT(T5,' INPUT FILE NAME: ',\ )
2001 FORMAT(T5,'OUTPUT FILE NAME: ',\ )
2002 FORMAT(A20)
2010 FORMAT(T30,'INPUT FILE: ',A20,/)
9999 STOP 'ERNIE V FINISHED OK'
      END

```

Listing 2. FELIX-V

```

PROGRAM F5F
C F5F IS VERSION F OF FELIXV
  IMPLICIT REAL*8 (S-Z)
  IMPLICIT INTEGER*2 (I)
  INTEGER*4 JCOUNT
  CHARACTER*3 MTHS,MTHE
  COMMON /STATE/ Z(7),Y(6),X(2)
  COMMON /PATH/ YP13,YP31,YP35,YP53,XP12,XP21,
+SZ(8),ZP(16)
  COMMON /RATES/ DT,RT1,RT2F,RT2R,RT4F,RT4R
  COMMON /RUNINF/ MAXTS,IPRINT,IPSW,IPGC,INMAX
  COMMON /PRTIN/ JCOUNT,ICTIN,ICTINM
  COMMON /STNORM/ IG(7)
  COMMON /THERM/ TEMP,SK,BE,BFN,BCP,BPV,BE1,BE2,
+BE3,XNPG,X1IN
  COMMON /GCORD/ GCN(13),GNTOT,GCNAVE,GCNVAR,GNCTOT
  COMMON /VCORD/ VCN(10),VCNTOT
  COMMON /TMARK/ ISH,ISM,ISS,ISF,ISY,ISN,ISD,MTHS,
+IEH,IEM,IES,IEF,IEY,IEN,IED,MTHE,IDM,IDH,ELS
  DIMENSION SDELTA(7),FRAZ(7)
  INMAX = 20
  EPS = 0.00001
  F16 =1.0/6.0
  CALL F5SET
  RT2F6 = RT2F**F16
  RT2R6 = RT2R**F16
  RT2F3 = RT2F6*RT2F6
  RT2R3 = RT2R6*RT2R6
  JCOUNT = 0
50 CONTINUE
  X16 = X(1)**F16
  X26 = X(2)**F16
  X13 = X16*X16
  X23 = X26*X26
  ZP(1) = 0.0
  ZP(2) = RT1 * Z(2)
  ZP(3) = 0.0
  ZP(4) = RT4R * Z(4)
  ZP(5) = 0.0
  ZP(6) = RT4R * Z(6)
  ZD7 = 0.0
  ZD8 = 0.0
  ZD9 = 0.0
  ZD10 = 0.0
  ZD11 = 0.0
  ZD12 = 0.0
  ZD13 = 0.0

```

```

ZD14 = 0.0
ZD15 = 0.0
ZD16 = 0.0
IF( Y(1) .GT. 0.0 ) THEN
  ZP(1) = RT1 * Z(1)*Z(1)/Y(1)
  ZD7 = RT2F6 * Z(1)*X16 /Y(1)
  ZD9 = RT2F3 * Z(2)*X13 /Y(1)
  IF( Y(3) .GT. 0.0 )
    ZD11 = RT2F6 * Z(3)*X16/DSQRT(Y(1)*Y(3))
  ZD13 = RT2F3 * Z(4)*X13 /Y(1)
ENDIF
IF( Y(3) .GT. 0.0 ) THEN
  ZP(3) = RT4F * Z(3)*Z(3)/Y(3)
  ZD8 = RT2R6 * Z(3)*X26 /Y(3)
  ZD10 = RT2R3 * Z(4)*X23 /Y(3)
  ZD14 = RT2R3 * Z(6)*X23 /Y(3)
  ZD15 = RT2F6 * Z(5)*X16 /Y(3)
ENDIF
IF( Y(5) .GT. 0.0 ) THEN
  ZP(5) = RT4F * Z(5)*Z(5)/Y(5)
  ZD16 = RT2R6 * Z(7)*X26 /Y(5)
  IF( Y(3) .GT. 0.0 )
    ZD12 = RT2R6 * Z(5)*X26/DSQRT(Y(3)*Y(5))
  ENDIF
ENDIF
ICTIN = 1
75 CONTINUE
XPF6 = 0.0
XPR6 = 0.0
IF( XP12 .NE. 0.0 ) XPF6 = 1.0/(XP12**F16)
IF( XP21 .NE. 0.0 ) XPR6 = 1.0/(XP21**F16)
TF136 = YP13*XPF6
TR316 = YP31*XPR6
TF133 = TF136*XPF6
TR313 = TR316*XPR6
TF356 = YP35*XPF6
TR536 = YP53*XPR6
ZP(7) = ZD7 * TF136
ZP(8) = ZD8 * TR316
ZP(9) = ZD9 * TF133
ZP(10) = ZD10 * TR313
ZP(11) = ZD11 * DSQRT(TF136*TF356)
ZP(12) = ZD12 * DSQRT(TR316*TR536)
ZP(13) = ZD13 * TF133
ZP(14) = ZD14 * TR313
ZP(15) = ZD15 * TF356
ZP(16) = ZD16 * TR536
YP13N = ZP(7) + ZP(9) + ZP(11) + ZP(13)
YP31N = ZP(8) + ZP(10) + ZP(12) + ZP(14)
YP35N = ZP(11) + ZP(15)

```

```

YP53N = ZP(12) + ZP(16)
XP12N = ZP(7)+2*(ZP(9)+ZP(11)+ZP(13))+ZP(15)
XP21N = ZP(8)+2*(ZP(10)+ZP(12)+ZP(14))+ZP(16)
XDELTA = XDIST(XP12N,XP12) + XDIST(XP21N,XP21)
YP13 = YP13N
YP31 = YP31N
YP35 = YP35N
YP53 = YP53N
XP12 = XP12N
XP21 = XP21N
IF (XDELTA.GT.EPS).AND.(ICTIN.LT.INMAX) THEN
    ICTIN = ICTIN + 1
    GO TO 75
ENDIF
ICTINM = MAX0(ICTINM, ICTIN)
DO 300 J=1,8
300    SZ(J) = ZP(2*J-1) - ZP(2*J)
    SDELTA(1) = 3.0*SZ(1) + 3.0*SZ(4)
    SDELTA(2) =      SZ(1) - 2.0*SZ(5)
    SDELTA(3) =      SZ(4) - 2.0*SZ(2) - 2.0*SZ(6)
    SDELTA(4) =      SZ(2) +      SZ(5) -      SZ(7)
    SDELTA(5) = 2.0*SZ(6) -      SZ(3) -      SZ(8)
    SDELTA(6) =      SZ(3) + 2.0*SZ(7)
    SDELTA(7) = 3.0*SZ(8)
    Z(1) = Z(1) - DT * SDELTA(1)
    Z(2) = Z(2) + DT * SDELTA(2)
    Z(3) = Z(3) + DT * SDELTA(3)
    Z(4) = Z(4) + DT * SDELTA(4)
    Z(5) = Z(5) + DT * SDELTA(5)
    Z(6) = Z(6) + DT * SDELTA(6)
    Z(7) = Z(7) + DT * SDELTA(7)
    ZTOT = 0.0
    DO 1 I=1,7
1      ZTOT = ZTOT + IG(I)*Z(I)
    ZNORM = 1.0/ZTOT
    DO 2 I=1,7
        Z(I) = ZNORM*Z(I)
2      IF ( Z(I) .LT. 0.0 ) WRITE(12,*) 'Z(',I,')
        += ',Z(I)
    Y(1) = Z(1) + 2*Z(2) + Z(3) + 2*Z(4)
    Y(2) = Z(2)
    Y(3) = Z(3) + Z(4) + Z(5) + Z(6)
    Y(4) = Z(4)
    Y(5) = Z(5) + Z(7)
    Y(6) = Z(6)
    X(1) = Y(1) + Y(2) + Y(3) + Y(4)
    X(2) = Y(3) + Y(4) + Y(5) + Y(6)
    JCOUNT = JCOUNT + 1
    ATIME = JCOUNT * DT

```

```

      IF ((MOD(JCOUNT,IPRINT) .EQ. 0) .OR.
+      (JCOUNT .EQ. MAXTS)) CALL F5PRINT(ETIME)
      IF ( JCOUNT .LT. MAXTS ) GO TO 50
      CALL TIMARK(1)
      WRITE(12,1099) IDH,IDM,ELS
1099 FORMAT(/,T2,'***** Elapsed Time is ',I2.2,
+ ' Hours ',I2.2,' Minutes ',0PF5.2,' Seconds.
+*****')
      STOP 'FELIX-V FINISHED OK'
      END
      BLOCK DATA ERNIE
      IMPLICIT REAL*8 (S-Z)
      IMPLICIT INTEGER*2 (I)
      COMMON /STNORM/ IG(7)
      DATA IG /1,3,3,6,3,3,1/
      END
      REAL*8 FUNCTION XDIST(A,B)
      REAL*8 A,B
      XDIST = A
      IF( B .NE. 0.0) XDIST = (A-B)*(A-B)/(B*B)
      RETURN
      END

```

```

      SUBROUTINE F5SET
C  RT1 : T1 TRANSITION RATE
C  RT2R : T2 REVERSE RATE   FREE SURFACE ELIMINATION
C  RT2F : T2 FORWARD RATE   FREE SURFACE FORMATION
C  RT4F : T4 FORWARD RATE   FREE SURF. ELIM. VIA T1
C  RT4R : T4 REVERSE RATE   FREE SURF. FORM. VIA T1
C  CHM : RT2R/RT2F          RATIO OF ELIM. TO FORM.
C  R42 = RT4R/RT2F
C  DT : INTEGRATION TIME STEP
C  IPSW : PRINT SWITCH = 0 ; SHORT PRINT EVERY IPRINT
C           > 0 ; SHORT PRINT EVERY IPRINT
C           STEPS AND FULL PRINT EVERY
C           IPSW*IPRINT STEPS
C           < 0 ; FULL PRINT EVERY
C           ABS(IPSW*IPRINT) STEPS .
C  IPGC : CHART SWITCH = 0 ; NO CHART FILE PRODUCED
C           != 0 ; CHART FILE PRODUCED EVERY
C           IPGC*IPRINT STEPS
C
      IMPLICIT REAL*8 (S-Z)
      IMPLICIT INTEGER*2 (I)
      COMMON /STATE/ Z(7),Y(6),X(2)
      COMMON /PATH/ YP13,YP31,YP35,YP53,XP12,XP21,
+SZ(8),ZP(16)
      COMMON /RATES/ DT,RT1,RT2F,RT2R,RT4F,RT4R
      COMMON /RUNINF/ MAXTS,IPRINT,IPSW,IPGC,INMAX
      COMMON /STNORM/ IG(7)

```

```

COMMON /THERM/ TEMP, SK, BE, BFN, BCP, BPV, BE1, BE2,
+BE3, XNPG, XIIN
CHARACTER*3 MTHS, MTHE
COMMON /TMARK/ ISH, ISM, ISS, ISF, ISY, ISN, ISD, MTHS,
+IEH, IEM, IES, IEF, IEY, IEN, IED, MTHE, IDM, IDH, ELS
CHARACTER*60 RUNAME
CHARACTER*20 FIN, FOUT, FCHT1, FCHT2
CHARACTER*2 FF /'\f'C/
BOLTZK = 1.380662E-16
PI = 3.141592654
ALAREA = 1.0E-19
ICTIN = 0
WRITE(*,2000)
READ(*,2005) FIN
WRITE(*,2001)
READ(*,2005) FOUT
OPEN(11, FILE=FIN)
OPEN(12, FILE=FOUT, STATUS='NEW')
READ(11, *) RUNAME
READ(11, *) MAXTS, IPRINT, IPSW, IPGC, INMAX
READ(11, *) TEMP, E1, R31, R21, GSIZE
READ(11, *) DT, RT1, CHM, RT2R, F42
READ(11, *) (Z(J), J=1,7)
CLOSE(11)
IF( IPGC .NE. 0 ) THEN
    WRITE(*,2002)
    READ(*,2005) FCHT1
    WRITE(*,2003)
    READ(*,2005) FCHT2
    OPEN(13, FILE=FCHT1, STATUS='NEW')
    OPEN(14, FILE=FCHT2, STATUS='NEW')
ENDIF
CALL TIMARK(0)
IF( INMAX .LT. 25 ) INMAX = 75
IF( DT .GT. 1.0 ) DT = 1.0
IF( DT .LT. 1.0E-6 ) DT = 1.0E-6
BETA = 1.0/(BOLTZK*TEMP)
BE1 = BETA*E1*0.5
BE2 = BE1*R21
BE3 = BE1*R31
XNPG = PI*GSIZE*GSIZE/(3.0*ALAREA)
RT2F = RT2R / CHM
RT4R = F42 * RT2F
RT4F = F42 * RT2R
ZTOT = 0.0
DO 1 I=1,7
1    ZTOT = ZTOT + IG(I)*Z(I)
    ZNORM = 1.0/ZTOT
DO 2 I=1,7

```



```

2      Z(I) = ZNORM*Z(I)
      XP12 = AMIN1(DT*RT2R,RT1)
      XP21 = XP12 / CHM
      YP13 = 0.5*XP12
      YP35 = 0.5*XP12
      YP31 = 0.5*XP21
      YP53 = 0.5*XP21
      Y(1) = Z(1) + 2*Z(2) + Z(3) + 2*Z(4)
      Y(2) = Z(2)
      Y(3) = Z(3) + Z(4) + Z(5) + Z(6)
      Y(4) = Z(4)
      Y(5) = Z(5) + Z(7)
      Y(6) = Z(6)
      X(1) = Y(1) + Y(2) + Y(3) + Y(4)
      X(2) = Y(3) + Y(4) + Y(5) + Y(6)
      XLIN = X(1)
      WRITE(12,1000) FF,RUNAME
      WRITE(12,1001) ISH,ISM,ISS,ISD,MTHS,ISY
      WRITE(12,1002) MAXTS, TEMP, DT
      WRITE(12,1003) IPRINT, R21, RT1
      WRITE(12,1004) IPSW, R31, CHM
      WRITE(12,1005) IPGC, E1, RT2R
      WRITE(12,1006) GSIZE, F42
      WRITE(12,1007) (Z(J),J=1,7)
      IF ( IPSW .EQ. 0 ) WRITE(12,1020)
      IF( IPGC .GT. 0 ) THEN
        WRITE(13,1030) FIN,RUNAME
        WRITE(13,1001) ISH,ISM,ISS,ISD,MTHS,ISY
        WRITE(13,1031)
        WRITE(14,1030) FIN,RUNAME
        WRITE(14,1001) ISH,ISM,ISS,ISD,MTHS,ISY
        WRITE(14,1032)
      ENDIF
      CALL F5PRINT(0.0)
      IF( IPSW .GT. 0 ) WRITE(12,1020)
1000 FORMAT(A,/,T15,A60,/)
1001 FORMAT(T20,'F5F RUN STARTED ON ',I2.2,':',J2.2,
+':',I2.2,2X,I2.2,A3,I4,/)
1002 FORMAT(T15,'MAXTS =',I5,T30,'TEMP = ',0PF7.2,
+T49,'DT =',1PE10.3)
1003 FORMAT(T15,'IPRINT =',I5,T30,'R21 = ',0PF8.3,
+T49,'RT1 =',1PE10.3)
1004 FORMAT(T15,'IPSW =',I5,T30,'R31 = ',0PF8.3,
+T49,'CHM =',1PE10.3)
1005 FORMAT(T15,'IPGC =',I5,T30,'E1 = ',1PE8.2,
+T49,'RT2R =',1PE10.3)
1006 FORMAT(T30,'GSIZE = ',1PE8.2,T49,'F42 =',1PE10.3)
1007 FORMAT(T10,7(0PF8.6,1X)/)
1020 FORMAT(T17,'TIME',T26,'S/k',T35,'X1',T43,'Z1',T50,

```

```
      +'AVE',T58,'VAR',T65,'MXIT')
1030 FORMAT(A,1X,A)
1031 FORMAT(1X,'TIME',T11,'X(1)',T19,'Z(1)',T28,'S/k',
      +T36,'AVE',T44,'VAR',T52,'DCN',T61,'DEN',T70,'VAVE'
      +,T79,'VMU',T86,'VTOT')
1032 FORMAT(2X,'TIME',T13,'0',T21,'1',T29,'2',T37,'3',
      +T45,'4',T53,'5',T61,'6',T69,'7',T77,'8',T85,'9',
      +T93,'10',T101,'11',T109,'12',T117,'Z1',T128,'Z2',
      +T139,'Z3',T150,'Z4',T161,'Z5',T172,'Z6',T183,'Z7')
2000 FORMAT(T3,'INPUT FILE NAME: ',\ )
2001 FORMAT(T2,'OUTPUT FILE NAME: ',\ )
2002 FORMAT(T3,'1st CHART FILE NAME: ',\ )
2003 FORMAT(T3,'2nd CHART FILE NAME: ',\ )
2005 FORMAT(A20)
      RETURN
      END
```

Listing 3. CCD Calculation

```

SUBROUTINE GCN5F
C GCN5F CALCULATES THE GRAIN COORDINATION FOR F5F
IMPLICIT DOUBLE PRECISION (B,D,F,H,Q,T,X,Y,Z)
COMMON /STATE/ Z(7),Y(6),X(2)
COMMON /GCORD/ GCN(13),GNTOT,GCNAVE,GCNVAR,GNCTOT
IF( Y(1) .NE. 0.0 ) THEN
    T0 = Z(1)/Y(1)
    T1 = Z(2)/Y(1)
    T3 = Z(3)/Y(1)
    T4 = Z(4)/Y(1)
ELSE
    T0 = 0.0
    T1 = 0.0
    T3 = 0.0
    T4 = 0.0
ENDIF
IF ( Y(3) .EQ. 0.0 ) THEN
    T33 = 0.0
    T43 = 0.0
    T5 = 0.0
    T6 = 0.0
ELSE
    T33 = Z(3)/Y(3)
    T43 = Z(4)/Y(3)
    T5 = Z(5)/Y(3)
    T6 = Z(6)/Y(3)
ENDIF
BS1 = T0*T0
BS2 = 2*T0*T1
BS3 = T1*T1
HS2 = BS1*T0
HS3 = 3*BS1*T1
HS4 = 3*BS3*T0
HS5 = BS3*T1
QS3 = BS1*BS1
QS4 = 2*BS1*BS2
QS5 = 6*BS1*BS3
QS6 = 2*BS2*BS3
QS7 = BS3*BS3
D3 = T3*T33
D4 = T4*T43
D34 = T3*T43
D5 = T5*T5
D6 = T6*T6
D56 = T5*T6
B0 = T1 + D3 + T4

```

$B1 = 2 \cdot D34$
 $B2 = D4$
 $H0 = D3 \cdot T5$
 $H1 = D3 \cdot T6 + 2 \cdot D34 \cdot T5$
 $H2 = D4 \cdot T5 + 2 \cdot D34 \cdot T6$
 $H3 = D4 \cdot T6$
 $Q0 = D3 \cdot D5$
 $Q1 = 2 \cdot (D34 \cdot D5 + D3 \cdot D56)$
 $Q2 = D4 \cdot D5 + D3 \cdot D6 + 2 \cdot D34 \cdot D56$
 $Q3 = 2 \cdot (D34 \cdot D6 + D4 \cdot D56)$
 $Q4 = D4 \cdot D6$
 $F0 = D3 \cdot D5 \cdot T5$
 $F1 = 2 \cdot D34 \cdot D5 \cdot T5 + 3 \cdot D3 \cdot D5 \cdot T6$
 $F2 = D4 \cdot D5 \cdot T5 + 6 \cdot D34 \cdot D5 \cdot T6 + 3 \cdot D3 \cdot D6 \cdot T5$
 $F3 = D3 \cdot D6 \cdot T6 + 6 \cdot D34 \cdot D6 \cdot T5 + 3 \cdot D4 \cdot D5 \cdot T6$
 $F4 = 2 \cdot D34 \cdot D6 \cdot T6 + 3 \cdot D4 \cdot D6 \cdot T5$
 $F5 = D4 \cdot D6 \cdot T6$
 $GCN(1) = D5 \cdot D5 \cdot D5$
 $GCN(2) = 6 \cdot (D5 \cdot D5 \cdot D56 + F0 \cdot T5)$
 $GCN(3) = 3 \cdot H0 \cdot H0 + 6 \cdot (F0 \cdot T0 + Q0 \cdot B0) + 15 \cdot D5 \cdot D5 \cdot D6$
 $+ 12 \cdot D5 \cdot (D5 \cdot D34 + 2 \cdot D56 \cdot D3)$
 $GCN(4) = 20 \cdot D5 \cdot D56 \cdot D6 + 6 \cdot D5 \cdot (D5 \cdot D4 + 8 \cdot D56 \cdot D34 +$
 $+ 5 \cdot D5 \cdot D3) + 6 \cdot (F0 \cdot T1 + F1 \cdot T0 + Q0 \cdot B1 + Q1 \cdot B0 + H0 \cdot H1)$
 $+ 6 \cdot Q0 \cdot BS1 + 12 \cdot H0 \cdot B0 \cdot T0 + 2 \cdot B0 \cdot B0 \cdot B0$
 $GCN(5) = 15 \cdot D5 \cdot D6 \cdot D6 + 24 \cdot D56 \cdot (D5 \cdot D4 + 3 \cdot D56 \cdot D34 + D6 \cdot D3)$
 $+ 6 \cdot (F1 \cdot T1 + F2 \cdot T0 + Q2 \cdot B0 + Q1 \cdot B1 + Q0 \cdot B2 + H0 \cdot H2)$
 $+ 3 \cdot H1 \cdot H1 + 12 \cdot (H0 \cdot B0 \cdot T1 + H0 \cdot B1 \cdot T0 + H1 \cdot B0 \cdot T0)$
 $+ 6 \cdot (Q1 \cdot BS1 + Q0 \cdot BS2 + B0 \cdot B0 \cdot B1 + H0 \cdot HS2) + 9 \cdot B0 \cdot B0 \cdot BS1$
 $GCN(6) = 6 \cdot (D56 \cdot D6 \cdot D6 + D6 \cdot (D6 \cdot D3 + 8 \cdot D56 \cdot D34 + 5 \cdot D5 \cdot D4))$
 $+ 6 \cdot (F2 \cdot T1 + F3 \cdot T0 + Q3 \cdot B0 + Q2 \cdot B1 + Q1 \cdot B2 + H0 \cdot H3 + H1 \cdot H2)$
 $+ 6 \cdot (Q2 \cdot BS1 + Q1 \cdot BS2 + Q0 \cdot BS3 + B0 \cdot B0 \cdot B2 + B0 \cdot B1 \cdot B1)$
 $+ 12 \cdot (H0 \cdot (B2 \cdot T0 + B1 \cdot T1) + H1 \cdot (B1 \cdot T0 + B0 \cdot T1) + H2 \cdot B0 \cdot T0)$
 $+ 6 \cdot (H0 \cdot HS3 + H1 \cdot HS2) + 9 \cdot (B0 \cdot B0 \cdot BS2 + 2 \cdot B0 \cdot B1 \cdot BS1)$
 $+ 6 \cdot B0 \cdot QS3$
 $GCN(7) = D6 \cdot D6 \cdot D6 + 12 \cdot D6 \cdot (D6 \cdot D34 + 2 \cdot D56 \cdot D4)$
 $+ 6 \cdot (F3 \cdot T1 + F4 \cdot T0 + Q4 \cdot B0 + Q3 \cdot B1 + Q2 \cdot B2 + H1 \cdot H3) + 3 \cdot H2 \cdot H2$
 $+ 6 \cdot (Q3 \cdot BS1 + Q2 \cdot BS2 + Q1 \cdot BS3) + 2 \cdot B1 \cdot B1 \cdot B1$
 $+ 12 \cdot (H0 \cdot B2 \cdot T1 + H1 \cdot (B2 \cdot T0 + B1 \cdot T1) + H2 \cdot (B1 \cdot T0 + B0 \cdot T1))$
 $+ 12 \cdot (H3 \cdot B0 \cdot T0 + B0 \cdot B1 \cdot B2) + 6 \cdot (H0 \cdot HS4 + H1 \cdot HS3 + H2 \cdot HS2)$
 $+ 9 \cdot (B0 \cdot B0 \cdot BS3 + B1 \cdot B1 \cdot BS1 + 2 \cdot B0 \cdot B2 \cdot BS1 + 2 \cdot B0 \cdot B1 \cdot BS2)$
 $+ 6 \cdot (B0 \cdot QS4 + B1 \cdot QS3) + BS1 \cdot BS1 \cdot BS1$
 $GCN(8) = 6 \cdot (F5 \cdot T6 + F4 \cdot T1 + F5 \cdot T0 + Q4 \cdot B1 + Q3 \cdot B2 + H2 \cdot H3)$
 $+ 6 \cdot (Q4 \cdot BS1 + Q3 \cdot BS2 + Q2 \cdot BS3 + B1 \cdot B1 \cdot B2 + B0 \cdot B2 \cdot B2)$
 $+ 12 \cdot (H1 \cdot B2 \cdot T1 + H2 \cdot (B2 \cdot T0 + B1 \cdot T1) + H3 \cdot (B1 \cdot T0 + B0 \cdot T1))$
 $+ 6 \cdot (H0 \cdot HS5 + H1 \cdot HS4 + H2 \cdot HS3 + H3 \cdot HS2)$
 $+ 9 \cdot (B1 \cdot B1 \cdot BS2 + 2 \cdot (B0 \cdot B1 \cdot BS3 + B0 \cdot B2 \cdot BS2 + B1 \cdot B2 \cdot BS1))$
 $+ 6 \cdot (B0 \cdot QS5 + B1 \cdot QS4 + B2 \cdot QS3) + 3 \cdot BS2 \cdot BS1 \cdot BS1$
 $GCN(9) = 3 \cdot H3 \cdot H3 + 6 \cdot (F5 \cdot T1 + Q4 \cdot B2 + Q4 \cdot BS2 + Q3 \cdot BS3 + B1 \cdot B2 \cdot L2)$
 $+ 12 \cdot (H2 \cdot B2 \cdot T1 + H3 \cdot (B2 \cdot T0 + B1 \cdot T1))$

```

++ 6*(H1*HS5 +H2*HS4 +H3*HS3)
++ 9*(B1*B1*BS3+B2*B2*BS1+2*(B0*B2*BS3+B1*B2*BS2))
++ 6*(B0*QS6 +B1*QS5 +B2*QS4) + 15*BS1*BS1*BS3
  GCN(10) = 6*Q4*BS3 + 12*H3*B2*T1 + 2*B2*B2*B2
++ 6*(H2*HS5 +H3*HS4) + 9*B2*B2*BS2 + 18*B1*B2*BS3
++ 6*(B0*QS7 + B1*QS6 + B2*QS5) + 10*BS1*BS2*BS3
  GCN(11) = 6*H3*HS5 + 9*B2*B2*BS3+6*B1*QS7+6*B2*QS6
+      + 15*BS1*BS3*BS3
  GCN(12) = 6*B2*QS7 + 3*BS2*BS3*BS3
  GCN(13) = BS3*BS3*BS3
  GNTOT = 0.0
  GN1TOT = 0.0
  GN2TOT = 0.0
  GNCTOT = 0.0
  DO 10 J=1,13
    GNTOT = GNTOT + GCN(J)
    GNCTOT = GNCTOT + ABS(J-7)*GCN(J)
10  GN1TOT = GN1TOT + (J-1)*GCN(J)
    IF( GNTOT .NE. 0.0) THEN
      GCNAVE = GN1TOT/GNTOT
      GNCTOT = 0.5*GNCTOT/GNTOT
      ANORM = 1.0/GNTOT
    ELSE
      GCNAVE = -1.0
      GNCTOT = -1.0
      ANORM = -1.0
    ENDIF
    DO 11 J=1,13
11  GN2TOT = GN2TOT+(J-1-GCNAVE)*(J-1-GCNAVE)*GCN(J)
      IF( GNTOT .NE. 0.0) GCNVAR = GN2TOT/GNTOT
      DO 20 J=1,13
20  GCN(J) = ANORM*GCN(J)
    RETURN
  END

```

Listing 4. VCD Calculation

```

SUBROUTINE VCN5F
IMPLICIT REAL*8 (B,H,Q,S-Z)
COMMON /STATE/ Z(7),Y(6),X(2)
COMMON /VCORD/ VCN(10),VCNTOT
IF ( Y(3) .EQ. 0.0 ) THEN
    T3 = 0.0
    T4 = 0.0
    T5 = 0.0
    T6 = 0.0
ELSE
    T3 = Z(3)/Y(3)
    T4 = Z(4)/Y(3)
    T5 = Z(5)/Y(3)
    T6 = Z(6)/Y(3)
ENDIF
T44 = 1.0
IF( Y(4) .EQ. 0.0) T44 = 0.0
IF( Y(5) .EQ. 0.0) THEN
    T55 = 0.0
    T7 = 0.0
    TX = 0.0
ELSE
    T55 = Z(5)/Y(5)
    T7 = Z(7)/Y(5)
    TX = X(2)/Y(5)
ENDIF
T66 = 1.0
IF( Y(6) .EQ. 0.0) T66 = 0.0
Q1 = T4*T44 + T6*T66
Q2 = T3*T3
Q3 = T5*T5
QX = TX*TX
H11 = Q1*Q1
H12 = Q1*Q2
H22 = Q2*Q2
B2 = Q3*TX
B3 = T7*T5*Q3*QX
B3L = B2*B2
B4 = B3L*T7*T7*TX
B4L = B3L*Q3*TX
B4M = B3L*T7*T5*TX
VCN(3) = 2*H11*Q1
VCN(4) = 9*H11*Q2
VCN(5) = 6*Q1*H22
VCN(6) = H22*Q2
VCN(4) = VCN(4) + 3*B2*H11*H11
VCN(5) = VCN(5) + 18*B2*H11*H12

```

```

VCN(6) = VCN(6) + 33*B2*H11*H22
VCN(7) =          18*B2*H12*H22
VCN(8) =          3*B2*H22*H22
VCN(5) = VCN(5) + 6*B3L*H11*H11*Q1
VCN(6) = VCN(6) + 45*B3L*H11*H11*Q2+12*B3*H11*H12*T3
VCN(7) = VCN(7) +114*B3L*H11*H12*Q2+30*B3*H11*H22*T3
VCN(8) = VCN(8) +129*B3L*H11*H22*Q2+12*B3*H12*H22*T3
VCN(9) =          60*B3L*H12*H22*Q2+ 2*B3*H22*H22*T3
VCN(10)=          9*B3L*H22*H22*Q2
VCN(6)=VCN(6)+ 9*B4*H11*H11*Q2+ 9*B4L*H11*H11*H11
VCN(7)=VCN(7)+36*B4*H11*H22*Q1+48*B4M*H11*H11*Q2*T3
VCNTOT = 0.0
VCN(1) = 0.0
VCN(2) = 0.0
DO 100 I=3,10
    VCNTOT = VCNTOT + VCN(I)
100  VCN(1) = VCN(1) + I*VCN(I)
    IF(VCNTOT .GT. 0.0) THEN
        VCN(1) = VCN(1)/VCNTOT
        VNORM = 1.0/VCNTOT
    ENDIF
    DO 110 I=3,10
110  VCN(2) = VCN(2) + (I-VCN(1))*(I-VCN(1))*VCN(I)
        IF(VCNTOT .GT. 0.0) VCN(2) = VCN(2)/VCNTOT
        DO 120 I=3,10
120  VCN(I) = VCN(I)*VNORM
    RETURN
END

```

APPENDIX B

MODEL-VI SOURCE LISTINGS

This appendix contains the FORTRAN source code listings for model-VI. Listing 1 shows the main program listing for the CVM calculation of model-VI, ERNIE-VI. Listing 2 shows the main program listing for the PPM calculation of model-VI, FELIX-VI. Listing 2 also contains the input subroutine for FELIX-VI and contains the documentation for running FELIX-VI. Listing 3 is the subroutine (GCN6F) that calculates the CCD from the state variables provided by ERNIE-VI and FELIX-VI.

The programs were edited with Solution Systems' BRIEF v2.0 editor and compiled with the Microsoft FORTRAN v4.01 compiler using the /FPI87 option.

Listing 1. ERNIE-VI

```

      PROGRAM ERNIE6
C ERNIE-VI IS THE 3-PT CVM CALCULATION OF MODEL 1
C   I.E. CELL AND NOT-CELL PTS WITH Z13 INCLUDED
C   ZD SET TO ZERO SINCE ZD7 IS SECOND ORDER
      IMPLICIT REAL*8 (S-Z)
      IMPLICIT INTEGER*2 (I)
      CHARACTER*3 MTHS,MTHE
      COMMON /STATE/ X(3),Y(12),Z(10)
      COMMON /GCORD/ GCN(10),AVE,AMU,ADC,ATOT
      COMMON /RUNIN/ E1,R12,R13,R14,GSIZE,ATAR,
+TEMP,CHM,EPSE,EPSI
      COMMON /RUNIF/ MAXTS,JCOUNT,IPRINT,TLM,DELTA,EXLAM
      COMMON /IDEGN/ IG(10)
      COMMON /THSYS/ BFN,SK,BMU,BPV,BETA,BE1,BE2,
+BE3,BE4,GBF,X1IN
      COMMON /TMARK/ ISH,ISM,ISS,ISF,ISY,ISN,ISD,MTHS,
+IEH,IEM,IES,IEF,IEY,IEN,IED,MTHE,IDM,IDH,ELS
      DIMENSION XP(3), YP(12)
      F13      = 1.0/3.0
      JCOUNT = 0
      CALL E6SET
      CHM2 = CHM*CHM
      DQ 30 J=1,12
30      YP(J) = Y(J)
      DO 40 J=1,3
40      XP(J) = X(J)
100 CONTINUE
      JCOUNT = JCOUNT + 1
      SX13 = 0.0
      SX23 = 0.0
      SX33 = 0.0
      IF( XP(1) .NE. 0.0 ) SX13 = 1.0/(XP(1)**F13)
      IF( XP(2) .NE. 0.0 ) SX23 = 1.0/(XP(2)**F13)
      IF( XP(3) .NE. 0.0 ) SX33 = 1.0/(XP(3)**F13)
      S11 = YP(1)*SX13
      S57S = DSQRT(YP(5)*YP(7))
      S57 = YP(5)*SX13*YP(7)*SX33
      Z(1) = S11**1.5
      Z(2) = S11*DSQRT(YP(2)*SX13)
      Z(3) = DSQRT(S11*YP(3)*SX13*YP(4)*SX23)
      Z(4) = DSQRT(S11*S57)
      Z(5) = DSQRT(S11*YP(6)*SX33*S57S*SX13)
      Z(6) = DSQRT(YP(3)*SX13*YP(3)*SX23*YP(8)*SX23)
      Z(7) = DSQRT(YP(3)*SX13*YP(9)*SX23*S57S*SX33)
      Z(8) = DSQRT(S57*YP(10)*SX33)
      Z(9) = DSQRT(S57*YP(11)*SX33)

```

```

Z(10) = 0.0
Z(1) = Z(1)*CHM2*CHM*DEXP(-3*BE1)
Z(2) = Z(2)*CHM2*CHM*DEXP(-(2*BE1 + BE2))
Z(3) = Z(3)*CHM2*DEXP(-(BE1 + BE2))
Z(4) = Z(4)*CHM2*DEXP(-(BE1 + BE3))
Z(5) = Z(5)*CHM2*DEXP(-(BE1 + BE2 + 0.5*BE3))
Z(6) = Z(6)*CHM*DEXP(-(BE2))
Z(7) = Z(7)*CHM*DEXP(-(BE2 + 0.5*BE3))
Z(8) = Z(8)*CHM*DEXP(-(BE2 + BE3))
Z(9) = Z(9)*CHM*DEXP(-(BE2 + BE3))
Z(10) = 0.0
TLM = TOPNR((Z(8)+Z(9)), (Z(5)+Z(7)), Z(4), Z(10))
IF( TLM .LE. 0.0 ) TLM = 1.0
TLM2 = TLM*TLM
Z(4) = Z(4)/TLM2
Z(5) = Z(5)*TLM
Z(7) = Z(7)*TLM
Z(8) = Z(8)*TLM2
Z(9) = Z(9)*TLM2
Z(10) = Z(10)/(TLM2*TLM2)
EXLAM = 0.0
DO 200 J=1,10
200   EXLAM = EXLAM + IG(J)*Z(J)
EXNORM = 1.0/EXLAM
DO 300 J=1,10
300   Z(J) = Z(J)*EXNORM
Y(1) = Z(1) + 2*( Z(2) + Z(3) + Z(4) + 2*Z(5) )
Y(2) = Z(2)
Y(3) = Z(3) + Z(6) + 2*Z(7)
Y(4) = Z(3)
Y(5) = Z(5) + Z(7) + Z(8) + Z(9)
Y(6) = Z(5)
Y(7) = Z(4) + Z(5) + Z(7) + Z(8) + Z(9)
Y(8) = Z(6)
Y(9) = Z(7)
Y(10) = Z(8)
Y(11) = Z(9)
Y(12) = Z(10)
X(2) = 2*Y(3)
X(3) = 2*Y(5)
X(1) = 1.0 - X(2) - 3*X(3)
DELTA = XSQ(Y(1), YP(1)) + XSQ(Y(2), YP(2)) +
+XSQ(Y(3), YP(3)) + XSQ(Y(4), YP(4)) + XSQ(Y(5), YP(5)) +
+XSQ(Y(6), YP(6)) + XSQ(Y(7), YP(7)) + XSQ(Y(8), YP(8)) +
+XSQ(Y(9), YP(9)) + XSQ(Y(10), YP(10)) + XSQ(Y(11), YP(11))
DO 400 J=1,12
400   YP(J) = Y(J)
DO 500 J=1,3
500   XP(J) = X(J)

```

```

      IF( MOD(JCOUNT,IPRINT) .EQ. 0) CALL E6PRINT(JCOUNT)
      IF((JCOUNT.LI.MAXTS).AND.(DELTA.GE.EPSE)) GOTO 100
      CALL E6PRINT(JCOUNT)
      CALL TIMARK(1)
      WRITE(17,1099) IDH,IDM,ELS
1099 FORMAT(T2,'***** Elapsed Time is ',I2.2,'
+Hours ',I2.2,' Minutes ',0PF5.2,' Seconds.
+ *****')
      STOP 'ERNIE-VI FINISHED OK'
      END
      FUNCTION TOPNR(SA,SB,SC,SD)
C TOPNR SOLVES THE 6TH ORDER TOPOLOGICAL CONSTRAINT BY
C THE NEWTON RALPHSON METHOD
      IMPLICIT REAL*8      (S-Z)
      IMPLICIT INTEGER*2 (I)
      COMMON /RUNIN/ E1,R12,R13,R14,GSIZE,ATAR,
+TEMP,CHM,EPSE,EPSI
      COMMON /RUNIF/ MAXTS,JCOUNT,IPRINT,TLM,DELTA,EXLAM
      IM = 100
      IC = 0
      XP = 1.0
10 IC = IC + 1
      XP2 = XP*XP
      FX = XP2*(-SC + XP2*XP*(SB + XP*SA)) - SD
      FPX = XP*(-2*SC + XP2*XP*(5*SB + XP*6*SA))
      IF( FPX .EQ. 0.0) THEN
          TOPNR = 1.0
          RETURN
      ENDIF
      HX = FX/FPX
      X = XP - HX
      DEL = (X-XP)/X
      XP = X
      IF((ABS(DEL).GT.EPSI).AND.(IC.LT.IM)) GOTO 10
      IF ( IC .GE. IM ) WRITE(*,111) JCOUNT,IC,DEL,X
      TOPNR = X
111 FORMAT(T2,'*** WARNING: AT ITERATION',I4,
+' ,TOPNR DID NOT CONVERGE AFTER',I4,' ITERATIONS.',/,
+T10,'DEL,X: ',1PE10.3,2X,1PE10.3,/)
      RETURN
      END
      FUNCTION XSQ(X,Y)
      IMPLICIT REAL*8 (S-Z)
      XSQ = (X-Y)*(X-Y)
      IF( Y .NE. 0.0 ) XSQ = XSQ/(Y*Y)
      RETURN
      END
      BLOCK DATA ERNIE
      IMPLICIT REAL*8      (S-Z)

```

```
IMPLICIT INTEGER*2 (I)
COMMON /IDEGN/ IG(10)
DATA IG/1,3,6,6,12,3,12,6,6,3/
END
```

Listing 2. FELIX-VI

```

PROGRAM F6RB
C F6RB IS RESTRUCTURED F6R WITH THE 08MAY CORRECTIONS
C     INPUT FILE ON 016
C     OUTPUT FILE ON 017
C     CHART1 FILE ON 018 (SYSTEM INFO)
C     CHART2 FILE ON 019 (GCN INFO)
C     DEBUG FILE ON 020
C FELIX2-VI IS THE 3-PT PPM MODEL 1 CALCULATION.
C VERSION A CALCULATES THE PATH VARIABLES SIMULTANEOUSLY
C IN AN INNER ITERATION LOOP
C ARRAYS ARE DIFFERENT FROM MODEL ERNIE-VI TO REFLECT THE
C ELIMINATION OF THE STATE VARIABLE ZD SINCE THE Z7D
C PATH VARIABLE IS SECOND ORDER IN TIME. ALSO, THE ZA
C AND ZC HAVE BEEN COMBINED (SEE NOTES) INTO THE Z(8)
C VARIABLE
C THE ARRAYS ARE DEFINED AS FOLLOWS:
C Z(8)      : 3-PT SV; 1,2,3,4,5,7,8,A
C Y(10)     : 2-PT SV
C X(3)      : 1-PT SV
C IG(8)     : WEIGHT FACTORS FOR Z(8)
C SDELTA(8) : PV DIFF 12-21;34;35;78;8A;23;37;58
C IPRINT = TIME STEPS PER PRINTOUT CALL
C IPGC  = CHART FILE SWITCH; WRITES PER PRINTOUT CALL
C IPSW  = SUMMARY PRINT SWITCH; WRITES PER PRINTOUT CALL
      IMPLICIT REAL*8   (S-Z)
      IMPLICIT INTEGER*2 (I)
      INTEGER*4 JCOUNT
      CHARACTER*3 MTHS,MTHE
      COMMON /STATE/ X(3),Y(10),Z(8)
      COMMON /GCORD/ GCN(10),AVE,AMU,ADC,ATOT
      COMMON /RUNIN/ E1,R12,R13,GSIZE,ATAR,EPS
      COMMON /RUNIF/ MAXTS,IPRINT,IPSW,IPGC,INMAX
      COMMON /THSYS/ BFN,SK,BMU,BPV,BETA,BE1,BE2,
+BE3,BE4,GBF,X1IN
      COMMON /PATH/ YP13,YP31,YP35,YP53,XP23,XP32,
+SZ(8),ZP(16)
      COMMON /RATES/ DT,RT1,RT2F,RT2R,TEMP
      COMMON /STNORM/ IG(8),IGY(10),IGX(3)
      COMMON /PRTIN/ JCOUNT,ICTIN,ICTINM,SX1,XDELTA
      COMMON /TMARK/ ISH,ISM,ISS,ISF,ISY,ISN,ISD,MTHS,
+IEH,IEM,IES,IEF,IEY,IEN,IED,MTHE,IDM,IDH,ELS
      DIMENSION SDELTA(8),FRAZ(8)
      XDELTA = 9.999E+10
      SX1    = 0.0
      F13    = 1.0/3.0
      F23    = 2.0/3.0

```

```

CALL F6SET
JCOUNT = 0
50 CONTINUE
XT1F = 0.0
XT1R = 0.0
XT2F = 0.0
XT2R = RT2R
IF( Y(1) .NE. 0.0 ) THEN
    XT2F = 0.5*RT2F*(X(1)/Y(1))*((Z(2)+Z(3)+2*Z(5))
+    /Y(1))**2.0)
    ENDIF
IF( Y(3) .NE. 0.0 ) THEN
    XT1F = Z(3)*RT1/Y(3)
    ENDIF
IF( Y(5) .NE. 0.0 ) THEN
    XT1R = 0.25*RT1*Z(4)/Y(5)
    ENDIF
ZP(1) = 0.0
IF( Y(1) .NE. 0.0 ) ZP(1) = RT1 * Z(1)*Z(1)/Y(1)
ZP(2) = RT1 * Z(2)
ZP(5) = Z(3) * XT1F
ZP(6) = Z(5) * XT1R
ZP(7) = Z(6) * XT1F
ZP(8) = Z(7) * XT1R
ZP(9) = Z(7) * XT1F
ZP(10) = Z(8) * XT1R
ZP(11) = Z(2) * XT2F
ZP(12) = Z(3) * XT2R
ZP(13) = Z(3) * XT2F
ZP(14) = Z(6) * XT2R
ZP(15) = Z(5) * XT2F
ZP(16) = Z(7) * XT2R
XP12 = 2.0*(ZP(11) + ZP(13) + 2*ZP(15))
XP21 = 2.0*(ZP(12) + ZP(14) + 2*ZP(16))
XP23 = 2.0*(ZP(5) + ZP(7) + 2*ZP(9))
XP32 = 2.0*(ZP(6) + ZP(8) + 2*ZP(10))
YP13 = 0.5*XP12
YP31 = 0.5*XP21
YP35 = 0.5*XP23
YP53 = 0.5*XP32
ZP(3) = ZP(5) + ZP(7) + 2*ZP(9)
ZP(4) = ZP(6) + ZP(8) + 2*ZP(10)
DO 300 J=1,8
300    SZ(J) = ZP(2*J-1) - ZP(2*J)
    SX1 = SZ(6) + SZ(7) + 2*SZ(8)
    SDELTA(1) = -3.0*SZ(1)
    SDELTA(2) = SZ(1) - 2.0*SZ(6)
    SDELTA(3) = SZ(6) - SZ(2) - 2.0*SZ(3) - SZ(7)
    SDELTA(4) = SZ(2)

```

```

SDELTA(5) =      SZ(3) -      SZ(8)
SDELTA(6) = 2.0*SZ(7) - 4.0*SZ(4)
SDELTA(7) =      SZ(4) - 2.0*SZ(5) +      SZ(8)
SDELTA(8) = 2.0*SZ(5)
DO 350 J=1,8
350   Z(J) = Z(J) + DT * SDELTA(J)
      ZTOT = 0.0
      DO 1 I=1,8
        ZTOT = ZTOT + IG(I)*Z(I)
        IF( Z(I) .LT. 0.0 ) THEN
          WRITE(17,5000) JCOUNT,I,Z(I)
          WRITE(17,5001) (Z(J),J=1,8)
          WRITE(17,5001) (SDELTA(J),J=1,8)
          WRITE(17,5001) (SZ(J),J=1,8)
          WRITE(17,5001) (ZP(J),J=1,16,2)
          WRITE(17,5001) (ZP(J),J=2,16,2)
          STOP 'FELIX-VI ERROR: NEGATIVE STATE VARIABLE'
        ENDIF
1      CONTINUE
      ZNORM = 1.0/ZTOT
      DO 2 I=1,8
2      Z(I) = ZNORM*Z(I)
      Y(1) = Z(1) + 2*( Z(2) + Z(3) + Z(4) + 2*Z(5) )
      Y(2) = Z(2)
      Y(3) = Z(3) + Z(6) + 2*Z(7)
      Y(4) = Z(3)
      Y(5) = Z(5) + Z(7) + 2*Z(8)
      Y(6) = Z(5)
      Y(7) = Z(4) + Z(5) + Z(7) + 2*Z(8)
      Y(8) = Z(6)
      Y(9) = Z(7)
      Y(10) = Z(8)
      X(2) = 2*Y(3)
      X(3) = 2*Y(5)
      X(1) = 1.0 - X(2) - 3*X(3)
      JCOUNT = JCOUNT + 1
      ATIME = JCOUNT * DT
      IF((MOD(JCOUNT,IPRINT).EQ.0)) CALL F6PRINT(ATIME)
      IF ( JCOUNT .LT. MAXTS ) GO TO 50
      CALL TIMARK(1)
      WRITE(17,1099) IDH,IDM,ELS
1099  FORMAT(/,T2,'***** Elapsed Time is ',I2.2,'
+Hours ',I2.2,' Minutes ',0PF5.2,' Seconds.
+ *****')
5000  FORMAT(T5,'AT STEP',I5,' Z('',I1,'') =',1PE10.3,
+      ' Z,SDELTA,SZ,ZP ARRAYS FOLLOWS')
5001  FORMAT(8(1PE10.3))
      STOP 'PROGRAM FINISHED OK'
      END

```

```

SDELTA(5) =      SZ(3) -      SZ(8)
SDELTA(6) = 2.0*SZ(7) - 4.0*SZ(4)
SDELTA(7) =      SZ(4) - 2.0*SZ(5) +      SZ(8)
SDELTA(8) = 2.0*SZ(5)
DO 350 J=1,8
350.  Z(J) = Z(J) + DT * SDELTA(J)
ZTOT = 0.0
DO 1 I=1,8
  ZTOT = ZTOT + IG(I)*Z(I)
  IF( Z(I) .LT. 0.0 ) THEN
    WRITE(17,5000) JCOUNT,I,Z(I)
    WRITE(17,5001) (Z(J),J=1,8)
    WRITE(17,5001) (SDELTA(J),J=1,8)
    WRITE(17,5001) (SZ(J),J=1,8)
    WRITE(17,5001) (ZP(J),J=1,16,2)
    WRITE(17,5001) (ZP(J),J=2,16,2)
    STOP 'FELIX-VI ERROR: NEGATIVE STATE VARIABLE'
  ENDIF
1  CONTINUE
  ZNORM = 1.0/ZTOT
  DO 2 I=1,8
2    Z(I) = ZNORM*Z(I)
  Y(1) = Z(1) + 2*( Z(2) + Z(3) + Z(4) + 2*Z(5) )
  Y(2) = Z(2)
  Y(3) = Z(3) + Z(6) + 2*Z(7)
  Y(4) = Z(3)
  Y(5) = Z(5) + Z(7) + 2*Z(8)
  Y(6) = Z(5)
  Y(7) = Z(4) + Z(5) + Z(7) + 2*Z(8)
  Y(8) = Z(6)
  Y(9) = Z(7)
  Y(10) = Z(8)
  X(2) = 2*Y(3)
  X(3) = 2*Y(5)
  X(1) = 1.0 - X(2) - 3*X(3)
  JCOUNT = JCOUNT + 1
  ATIME = JCOUNT * DT
  IF((MOD(JCOUNT,IPRINT).EQ.0)) CALL F6PRINT(ATIME)
  IF ( JCOUNT .LT. MAXTS ) GO TO 50
  CALL TIMARK(1)
  WRITE(17,1099) IDH,IDM,ELS
1099 FORMAT(/,T2,'***** Elapsed Time is ',I2.2,'
+Hours ',I2.2,' Minutes ',0PF5.2,' Seconds.
+ *****')
5000 FORMAT(T5,'AT STEP',I5,' Z(',I1,') =',1PE10.3,
+      ' Z,SDELTA,SZ,ZP ARRAYS FOLLOWS')
5001 FORMAT(8(1PE10.3))
  STOP 'PROGRAM FINISHED OK'
END

```



```

READ(16,*) RUNAME
READ(16,*) MAXTS, IPRINT, IPSW, IPGC, INMAX
READ(16,*) E1, R12, R13, GSIZE, ATAR
READ(16,*) RT1, RT2F, CHM
READ(16,*) TEMP, DT, EPS
READ(16,*) (Z(J), J=1, 8)
IF( IPGC .NE. 0 ) THEN
    WRITE(*,2002)
    READ(*,2005) FCHT1
    WRITE(*,2003)
    READ(*,2005) FCHT2
    OPEN(18, FILE=FCHT1, STATUS='NEW')
    OPEN(19, FILE=FCHT2, STATUS='NEW')
ENDIF
CALL TIMARK(0)
IF( INMAX .LT. 25 ) INMAX = 75
IF( DT .GT. 1.0 ) DT = 1.0
IF( DT .LT. 1.0E-6 ) DT = 1.0E-6
RT2R = RT2F/CHM
BETA = 1.0/(BOLTZK*TEMP)
BE1 = 0.5*BETA*E1
BE2 = BE1*R12
BE3 = BE1*R13
BE4 = BE1*R14
GBF = (PI/6.0)*GSIZE*GSIZE/ATAR
IF( (Z(5)+Z(7)+Z(8)) .EQ. 0.0 ) THEN
    Z(5) = 0.25*Z(4)
    Z(7) = Z(5)
    Z(8) = 2*Z(5)
ELSE
    Z(4) = Z(5) + Z(7) + 2*Z(8)
ENDIF
ZTOT = 0.0
DO 1 I=1,8
1   ZTOT = ZTOT + IG(I)*Z(I)
    ZNORM = 1.0/ZTOT
    DO 2 I=1,8
2   Z(I) = ZNORM*Z(I)
    Y(1) = Z(1) + 2*( Z(2) + Z(3) + Z(4) + 2*Z(5) )
    Y(2) = Z(2)
    Y(3) = Z(3) + Z(6) + 2*Z(7)
    Y(4) = Z(3)
    Y(5) = Z(5) + Z(7) + 2*Z(8)
    Y(6) = Z(5)
    Y(7) = Z(4) + Z(5) + Z(7) + 2*Z(8)
    Y(8) = Z(6)
    Y(9) = Z(7)
    Y(10) = Z(8)
    X(2) = 2*Y(3)

```

```

X(3) = 2*Y(5)
X(1) = 1.0 - X(2) - 3*X(3)
XP23 = RT1*X(2)
XP32 = RT1*X(3)
YP35 = 0.5*XP23
YP53 = 0.5*XP32
YP13 = RT2F*Y(1)
YP31 = RT2R*Y(3)
WRITE(17,1000) FF
WRITE(17,1001) RUNAME
WRITE(17,1002) ISH,ISM,ISS,ISD,MTHS,ISY
WRITE(17,2010) FIN
WRITE(17,1003) MAXTS,    TEMP,    E1
WRITE(17,1004) IPRINT,  DT,      R12
WRITE(17,1005) IPSW,    RT1,     R13
WRITE(17,1006) IPGC,    RT2F,    GSIZE
WRITE(17,1007) INMAX,   CHM,     ATAR
WRITE(17,1008)                EPS
WRITE(17,1009) (Z(J),J=1,8)
IF ( IPSW .EQ. 0 ) WRITE(17,1020)
IF( IPGC .GT. 0 ) THEN
    WRITE(18,1030) FIN,RUNAME
    WRITE(18,1002) ISH,ISM,ISS,ISD,MTHS,ISY
    WRITE(18,1031)
    WRITE(19,1030) FIN,RUNAME
    WRITE(19,1002) ISH,ISM,ISS,ISD,MTHS,ISY
    WRITE(19,1032)
ENDIF
CALL F6PRINT(0.0)
IF( IPSW .GT. 0 ) WRITE(17,1020)
1000 FORMAT(A)
1001 FORMAT(T10,A60,/)
1002 FORMAT(T20,'F6F RUN STARTED ON ',I2.2,':',I2.2,
+':',I2.2,2X,I2.2,A3,I4)
1003 FORMAT(T15,'MAXTS =',I5,T35,'TEMP = ',0PF7.2,T54,
+'E1 = ',1PE8.2)
1004 FORMAT(T15,'IPRINT =',I5,T35,'DT = ',1PE8.2,T54,
+'R12 = ',0PF8.3)
1005 FORMAT(T15,'IPSW =',I5,T35,'RT1 = ',1PE8.2,T54,
+'R13 = ',0PF8.3)
1006 FORMAT(T15,'IPGC =',I5,T35,'RT2F = ',1PE8.2,T54,
+'GSIZE = ',1PE8.2)
1007 FORMAT(T15,'INMAX =',I5,T35,'CHM = ',1PE8.2,T54,
+'ATAR = ',1PE8.2)
1008 FORMAT(T35,'EPS = ',1PE8.2)
1009 FORMAT(T15,'Z(I): ',T25,4(0PF10.6),/,
+T25,4(0PF10.6),/)
1020 FORMAT(T12,'TIME',T21,'S/k',T30,'X1',T38,'Z1',
+T45,'AVE',T53,'VAR',T63,'BFN',T70'MXIT')

```

```
1030 FORMAT(A,1X,A)
1031 FORMAT(1X,'TIME',T11,'X(1)',T20,'Z(1)',T28,
+ 'S/k',T36,'AVE',T44,'VAR',T52,'DCN',T61,'BFN',
+ T71,'BMU')
1032 FORMAT(2X,'TIME',T13,'3',T21,'4',T29,'5',T37,'6',
+ T45,'7',T53,'8',T61,'9',T69,'10',T77,'11',
+ T85,'12',T93,'Z1',T104,'Z2',T115,'Z3',T126,
+ 'Z4',T137,'Z5',T148,'Z6',T159,'Z7',T170,'Z8')
2000 FORMAT(T5,'      INPUT FILE NAME: ',\ )
2001 FORMAT(T5,'      OUTPUT FILE NAME: ',\ )
2002 FORMAT(T5,' FIRST CHART FILE NAME: ',\ )
2003 FORMAT(T5,' SECOND CHART FILE NAME: ',\ )
2005 FORMAT(A20)
2010 FORMAT(T30,'INPUT FILE: ',A20,/)
      RETURN
      END
```

Listing 3. CCD Calculation

```

SUBROUTINE GCN6F
C GCN6F CALCULATES THE GRAIN COORDINATION FOR MODEL
C FELIX-VI

```

```

  IMPLICIT REAL*8 (S-Z)
  COMMON /STATE/ X(3),Y(10),Z(8)
  COMMON /GCORD/ GCN(10),AVE,AMU,ADC,ATOT
  REAL*8 B0(10),B1(10),B2(10),B3(10),
+ B4(10),B5(10),B6(10)

```

```

  YIN1 = 1.0/Y(1)
  T1 = Z(1) * YIN1
  T2 = Z(2) * YIN1
  T3 = Z(3) * YIN1
  T4 = Z(4) * YIN1
  T5 = Z(5) * YIN1
  IF ( Y(3) .EQ. 0.0 ) THEN
    T33 = 0.0
    T7 = 0.0
    T8 = 0.0

```

```

  ELSE
    YIN3 = 1.0/Y(3)
    T33 = Z(3) * YIN3
    T7 = Z(6) * YIN3
    T8 = Z(7) * YIN3

```

```

  ENDIF
  IF ( Y(5) .EQ. 0.0 ) THEN
    T45 = 0.0
    T55 = 0.0
    T85 = 0.0
    TA5 = 0.0

```

```

  ELSE
    YIN5 = 1.0/Y(5)
    T45 = Z(4) * YIN5
    T55 = Z(5) * YIN5
    T85 = Z(7) * YIN5
    TA5 = Z(8) * YIN5

```

```

  ENDIF
  IF ( Y(7) .EQ. 0.0 ) THEN
    T47 = 0.0
    T57 = 0.0
    T87 = 0.0
    TA7 = 0.0

```

```

  ELSE
    YIN7 = 1.0/Y(7)
    T47 = Z(4) * YIN7
    T57 = Z(5) * YIN7
    T87 = Z(7) * YIN7

```

```

      TA7 = Z(8) * YIN7
ENDIF
T56 = 0.0
IF ( Y(6) .NE. 0.0 ) T56 = Z(5)/Y(6)
Q1  = T1*T1
Q12 = 2*T1*T2
Q2  = T2*T2
Q3  = T3*T33
Q34 = T3*T47
Q35 = T3*T57
Q38 = T33*T85
Q22 = T33*T87
Q43 = T4*T33
Q4  = T4*T47
Q4I = T4*T45
Q45 = T5*T45
Q46 = T5*T47
Q5  = T5*T55
Q6  = T5*T57
Q7  = T7*T7
Q78 = T7*T85
Q835= T8*T85
Q84 = T8*T47
Q87 = T7*T87
Q9  = T8*T87
QA  = TA5*TA7
QB  = TA7*TA7
R0  = T2 + T3 + 2*T5*T56
R1  = 2*Q45 + Q4
R2  = Q3 + 2*Q46
R3  = Q6
H1  = Q4I*TA5
H2  = 2*T4*Q38 + 2*Q4*TA5
H3  = Q3*T7 + Q4*TA7 + 2*(T4*Q22 + Q46*TA5)
H4  = 2*(Q46*TA7 + T5*Q22)
H5  = Q6*TA7
G2  = Q835*Q4I
G3  = QA*Q4I + 2*(Q38*T4*T7 + Q835*Q4)
G4  = Q7*Q3 + Q9*Q4 + 2*Q22*T4*(TA5 + T7)
+   + 2*(A4*QA + Q46*Q8)
G5  = 2*(Q46*QA + Q35*T7*T8 + Q22*TA7*T4 + Q9*Q46)
+   + Q9*Q3 + QB*Q4
G6  = Q9*Q6 + 2*TA7*( TA7*Q46 + Q22*T5 )
G7  = TA7*TA*Q6
F3  = Q835*Q4I*T7
F4  = 2*Q38*Q7*T4
+   + 2*Q835*(Q4I*TA7 + Q4*T7)
+   + Q9*Q4*T7
F5  = Q9*Q4*T7 + Q3*Q7*T7 + QA*Q4I*TA7 + 2*Q34*Q7*T8

```

```

+ + 2*(Q9*Q4*TA5 + Q835*Q4*TA7 + Q22*T4*TA5*T7)
+ + 2*(Q38*Q9*T4 + Q835*Q46*T7)
+ + 2*Q9*Q46*T7
F6 = 2*( Q835*Q46*TA7 + Q9*Q46*TA5 + QB*Q4*TA5)
+ + 2*(Q22*QA*T4 + Q7*Q35*T8 + Q3*Q9*T7)
+ + 2*(Q34*T8*(TA7*T7 + Q9) + Q46*Q9*T7 + Q9*Q4*TA7)
+ + Q9*Q6*T7
F7 = QB*Q4*TA7+Q9*Q6*T7+Q3*Q9*TA7+4*Q9*Q46*TA7
+ + 2*(QB*Q22*T4+Q9*Q35*T8+Q35*T7*TA7*T8+QB*Q46*TA5)
F8 = 2*(QB*Q22*T5 + Q9*Q6*TA7 + QB*Q46*TA7)
F9 = QB*Q6*TA7
A3 = Q1*Q1
A4 = 2*Q1*Q12
A5 = 6*Q1*Q2
A6 = 2*Q2*Q12
A7 = Q2*Q2
C2 = Q1*T1
C3 = 3*Q1*T2
C4 = 3*Q2*T1
C5 = Q2*T2
B6(1) = 0.0
B6(2) = 0.0
B6(3) = 0.0
B6(4) = Q1*Q1*Q1
B6(5) = 3*Q1*Q1*Q12
B6(6) = 15*Q1*Q1*Q2
B6(7) = 10*Q1*Q12*Q2
B6(8) = 15*Q1*Q2*Q2
B6(9) = 3*Q12*Q2*Q2
B6(10) = Q2*Q2*Q2
B5(1) = 0.0
B5(2) = 0.0
B5(3) = 6*R0*A3
B5(4) = 6*(R1*A3 + R0*A4)
B5(5) = 6*(R2*A3 +R1*A4 + R0*A5)
B5(6) = 6*(R3*A3 + R2*A4 + R1*A5 + R0*A6)
B5(7) = 6*(R3*A4 + R2*A5 + R1*A6 + R0*A7)
B5(8) = 6*(R3*A5 + R2*A6 + R1*A7)
B5(9) = 6*(R3*A6 + R2*A7)
B5(10) = 6*R3*A7
B4(1) = 0.0
B4(2) = 9*R0*R0*Q1
B4(3) = 6*H1*C2 + 18*R1*R0*Q1 + 9*R0*R0*Q12
B4(4) = 6*(H2*C2+H1*C3)+9*(R0*R0*Q2+R1*R1*Q1)
+ + 18*R0*(R2*Q1 + R1*Q12)
B4(5) = 6*(H3*C2 + H2*C3 + H1*C4) + 9*R1*R1*Q12
+ + 18*(Q1*(R3*R0+R2*R1)+R0*(Q2*R1+Q12*R2))
B4(6) = 6*(H4*C2 + H3*C3 + H2*C4 + H1*C5)
+ + 9*(Q1*R2*R2 + Q2*R1*R1)

```

```

+ + 18*(Q1*R1*R3 + Q2*R0*R2 + Q12*(R0*R3 + R1*R2))
B4(7) = 6*(H5*C2 + H4*C3 + H3*C4 + H2*C5)
+ + 9*Q12*(R1*R3 + R2*R2)
+ + 18*(Q1*R2*R3 + Q2*(R0*R3 + R1*R2))
B4(8) = 6*(H5*C3 + H4*C4 + H3*C5) + 18*Q12*R2*R3
+ + 9*(Q1*R3*R3 + Q2*(R1*R3 + R2*R2))
B4(9) = 6*(H5*C4+H4*C5)+9*Q12*R3*R3+18*Q2*R2*R3
B4(10) = 6*H5*C5 + 9*Q2*R3*R3
B3(1) = 2*R0*R0*R0
B3(2) = 6*R0*R0*R1 + 12*H1*R0*T1
B3(3) = 6*(R0*R0*R2 + R0*R1*R1 + G2*Q1)
+ + 12*(T1*(R0*H2 + R1*H1) + T2*R0*H1)
B3(4) = 2*R1*R1*R1 + 6*(R0*R0*R3 +G3*Q1 + G2*Q12)
+ + 12*(R0*R1*R2 +T1*(H3*R0+H2*R1+H1*R2)
+ + T2*(H2*R0+H1*R1))
B3(5) = 6*(R0*R2*R2 + R1*R1*R2 + 2*R0*R1*R3)
+ + 6*(G4*Q1 + G3*Q12 + G2*Q2)
+ + 12*T1*(H4*R0 + H3*R1 + H2*R2 + H1*R3)
+ + 12*T2*(H3*R0 + H2*R1 + H1*R2)
B3(6) = 6*(R1*R2*R2 + R1*R1*R3 + 2*R0*R2*R3)
+ + 6*(G5*Q1 + G4*Q12 + G3*Q2)
+ + 12*T1*(H5*R0 + H4*R1 + H3*R2 + H2*R3)
+ + 12*T2*(H4*R0 + H3*R1 + H2*R2 + H1*R3)
B3(7) = 6*R0*R3*R3 + 2*R2*R2*R2 + 12*R1*R2*R3
+ + 6*(G6*Q1 + G5*Q12 + G4*Q2)
+ + 12*T1*(H5*R1 + H4*R2 + H3*R3)
+ + 12*T2*(H5*R0 + H4*R1 + H3*R2 + H2*R3)
B3(8) = 6*(R1*R3*R3+R2*R2*R3+G7*Q1+G6*Q12+G5*Q2)
+ + 12*(T1*(H5*R2+H4*R3)+T2*(H5*R1+H4*R2+H3*R3))
B3(9) = 6*(R2*R3*R3 + G7*Q12 + G6*Q2)
+ + 12*(T1*H5*R3 + T2*(H5*R2 + H4*R3))
B3(10) = 2*R3*R3*R3 + 6*G7*Q2 + 12*T2*H5*R3
B2(1) = 0.0
B2(2) = 3*H1*H1 + 6*G2*R0
B2(3) = 6*( F3*T1 + G2*R1 + G3*R0 + H1*H2)
B2(4) = 6*(F3*T2+F4*T1+G2*R2+G3*R1+G4*R0+H1*H3)
+ + 3*H2*H2
B2(5) = 6*(F4*T2+F5*T1+G2*R3+G3*R2+G4*R1+G5*R0)
+ + 6*(H2*H3 + H1*H4)
B2(6) = 6*(F5*T2+F6*T1+G3*R3+G4*R2+G5*R1+G6*R0)
+ + 6*(H2*H4 + H1*H5) + 3*H3*H3
B2(7) = 6*(F6*T2+F7*T1+G4*R3+G5*R2+G6*R1+G7*R0)
+ + 6*(H3*H4 + H2*H5)
B2(8) = 6*(F7*T2+F8*T1+G5*R3+G6*R2+G7*R1+H3*H5)
+ + 3*H4*H4
B2(9) = 6*(F8*T2 + F9*T1 + G6*R3 + G7*R2 + H4*H5)
B2(10) = 3*H5*H5 + 6*(F9*T2 + G7*R3)
B1(1) = 0.0
B1(2) = 0.0

```

```

B1(3) = 6*Q835*Q7*Q4I
B1(4) = 12*Q7*(Q78*Q43 + Q4I*Q835)
B1(5) = 6*(Q7*Q7*Q3 + Q9*(QA*Q4I + Q7*Q4))
+ + 24*Q9*Q43*T85*T7
+ + 12*Q7*(Q84*T7*T3 + Q835*Q46 + Q43*TA5*T87)
+ + 12*Q9*(Q4*(Q835 + TA5*T7))
+ + 12*Q835*(Q4*TA7*T7 + Q4I*QB)
B1(6) = 6*(Q9*Q9*Q4 + QA*QB*Q4I + 3*Q3*Q7*Q9)
+ + 24*Q9*(Q34*T7*T8 + Q4*QA)
+ + 12*Q7*(Q35*T7*T8 + Q34*TA7*T8 + Q9*Q46)
+ + 12*Q43*(Q9*(TA7*T85 + TA5*T87) + QA*T87*T7)
+ + 12*Q835*Q46*(TA7*T7 + Q9)
+ + 12*Q9*T7*(Q46*TA5 + Q4*TA7)
+ + 12*QB*Q835*Q4
B1(7) = 6*Q9*(Q9*Q3 + Q7*Q6 + 3*Q4*QB)
+ + 24*Q9*(Q46*TA7*(TA5+T7)+T8*(Q35*T7+Q34*TA7))
+ + 12*QB*(Q34*T7*T8+Q835*Q46+Q4*QA+Q43*TA5*T87)
+ + 12*Q9*Q9*Q46
+ + 12*TA7*(Q3*Q9*T7 + Q7*Q35*T8)
B1(8) = 6*(QB*(QB*Q4 + Q9*Q3) + Q9*Q9*Q6)
+ + 24*Q9*Q35*TA7*T85 + 36*QB*Q9*Q46 + 12*Q9*Q6*Q3
+ + 12*QB*(TA7*(Q46*TA5 + Q22*T4) + Q87*T33*T5)
B1(9) = 18*QB*Q9*Q6 + 12*QB*(QB*Q46 + Q22*TA7*T5)
B1(10) = 6*QB*QB*Q6
B0(1) = 0.0
B0(2) = 0.0
B0(3) = 0.0
B0(4) = Q7*Q7*Q7
B0(5) = 6*Q7*Q7*Q9
B0(6) = 3*Q9*Q9*Q7 + 6*Q7*Q9*(Q9 + TA7*T7)
+ + 12*Q9*QB*QA
B0(7) = 2*Q9*Q9*Q9 + 6*QB*Q7*Q9
+ + 12*Q9*Q9*T7*TA7
B0(8) = 9*Q9*Q9*QB + 6*QB*Q9*T7*TA7
B0(9) = 6*QB*QB*Q9
B0(10) = QB*QB*QB
DO 50 J=1,10
50 GCN(J)=B6(J)+B5(J)+B4(J)+B3(J)+B2(J)+B1(J)+B0(J)
ATOT = 0.0
AVE = 0.0
AMU = 0.0
ADC = 0.0
DO 500 J=1,10
ATOT = ATOT + GCN(J)
AVE = AVE + (J+2)*GCN(J)
ADC = ADC + ABS(J-4)*GCN(J)
500 AMU = AMU + (J+2)*(J+2)*GCN(J)
AVE = AVE/ATOT
ADC = 0.5*ADC

```



```
AMU = AMU/ATOT - AVE*AVE  
ANM = 1.0/ATOT  
DO 600 J=1,10  
600   GCN(J) = GCN(J) * ANM  
RETURN  
END
```

VITA

Steven K. Fukuda was born on 14 September 1952 in Honolulu, Hawaii (before it was destroyed by tourists). He graduated from Kalani High School in 1970, received a B.S. in engineering from Case Western Reserve University in 1974, a M.S. in nuclear engineering from the University of Maryland in 1976, and received a third piece of paper (Ph.D.) from the University of Washington in 1988. More importantly, the author has been searching for a balance between Feynman's "pleasure of finding things out" and the reality of Firesign Theatre's "I Think We're All Bozo's on this Bus". The search continues.

APPENDIX III

Seong Il Kim*

*The Destruction of Hierarchical Structures
and Rheological Behavior of
Aqueous, Ceramic Particle Systems*
Ph.D. Dissertation

Department of Materials Science and Engineering,
University of Washington,
Seattle, Washington

1988

* Currently Research Scientist at Sherritt Technologies, Sherritt Gordon Ltd., Fort Saskatchewan, Alberta, Canada T8L 2P2.

10 December, 1989

In presenting this dissertation in partial fulfillment of the requirements for the Doctoral degree at the University of Washington, I agree that the Library shall make its copies freely available for inspection. I further agree that extensive copying of this dissertation is allowable only for scholarly purposes, consistent with "fair use" as prescribed in the U.S. Copyright Law. Requests for copying or reproduction of this dissertation may be referred to University Microfilms, 300 North Zeeb Road, Ann Arbor, Michigan 48106, to whom the author has granted "the right to reproduce and sell (a) copies of the manuscript in microform and/or (b) printed copies of the manuscript made from microform."

Signature _____

Date _____

University of Washington

Abstract

Structure-Property Relationships of Aqueous Ceramic Particulate Systems

by Seong Il Kim

Chairperson of the Supervisory Committee: Professor Ilhan A. Aksay

Department of Materials Science and Engineering

The structure-property relationships of aqueous ceramic particulate systems including nanometer- and micrometer-sized particles were studied in order to understand how to increase particle concentration of nanometer-sized particle suspensions with low viscosity. Packing density as a function of filtration pressure was studied at different particle interaction energy states using different particle sizes and was discovered to be related to storage modulus, yield strain, and particle structure.

Pressure-sensitive and -insensitive packing density was related to the barrier for compaction due to particle interaction energy. The difference in packing behavior of nanometer- and micrometer-sized particle systems was explained by using SEM photos of microstructures and by measuring the storage modulus. The nanometer-sized particle system showed an elastic property at a lower concentration (≥ 3 volume %), than the micrometer-sized particle system (≥ 35 volume %), because the nanometer-sized particle system showed higher energy per unit volume of sample. The yield strain decreased with increasing particle concentration in a power-law fashion (slope is -2.1) for a nanometer-sized particle system. This observation was unique and was ex-

plained by scaling theory. Structural information, fractal dimension $D=2$, was obtained for the boehmite system from the scaling theory and the experimental results on the storage modulus and yield strain.

Contents

LIST OF FIGURES	iv
LIST OF TABLES	ix
1. INTRODUCTION	1
2. LITERATURE REVIEW	6
2.1 Particle Interactions in Colloidal Suspensions	6
2.2 Powder Consolidation through Colloidal Processing	12
2.3 Pressure Filtration	18
2.4 Rheology	26
2.4.1 Theory of Viscoelasticity	27
2.4.2 Viscoelasticity of Colloidal Systems	35
3. EXPERIMENTAL PROCEDURES	39
3.1 Material	39
3.2 Suspension Preparation	39
3.3 Pressure Filtration	44
3.4 Sedimentation and Centrifugation	47
3.5 Freeze Drying	47
3.6 Dynamic Oscillatory Strain Sweep	48
3.7 Stress Relaxation	50
3.8 Structure by Scanning Electron Microscopy	50
4. RESULTS AND DISCUSSION	52
4.1 Effects of Filtration Pressure	52
Effect of Pressure on Dispersed Alumina Suspensions	52
Effect of Pressure on Flocculated Alumina Suspensions	57
Effects of Pressure on Micrometer- and Nanometer-Sized Particle Systems	62

4.2 Quantitative Characterization of Rheological Behavior	69
4.3 Elastic Constant and Yield Strain of Colloidal Particulate Systems ...	80
5. CONCLUSIONS	96
Relationship Between Packing Density and Filtration Pressure	96
Rheological Behavior of Nanometer- and Micrometer-Sized Particle Sys- tems	97
Relationship of Pressure Filtration and Rheological Behavior	98
REFERENCES	99
APPENDIX: Energy Calculation in Particle Systems	106

LIST OF FIGURES

Number		Page
1	Particle size versus maximum allowable particle concentration in aqueous medium.	2
2	Strength versus flaw size in the sintered product.	3
3	Total interaction energy curves, $V_{(1)}$ and $V_{(2)}$, obtained by the summation of an attraction curve, V_A , with different repulsion curves, $V_{R(1)}$ and $V_{R(2)}$.	8
4	Schematic representation of the structure of the electric double layer according to Stern's Theory.	10
5	Diagrammatic representation of the origin of electrostatic stabilization for negatively charged particles.	11
6	Schematic cross-sectional view of the filtration system.	14
7	Hydraulic pressure profiles across the consolidated layer and the mold.	16
8	Phase diagram (outlined with thin solid lines) for a colloidal system of only one type of particle. In electrostatically interacting systems, the reduced temperature scale is approximately proportional to $(\zeta/\zeta_0)^2$, where ζ is the surface potential and ζ_0 is a normalization constant. The maximum packing density is predicted to be $\sim 74\%$. (b) Sedimentation (thick solid line with unfilled circles) and slip cast (thick broken line with unfilled triangles) densities are lower than the predicted dense packing value. ³⁰	17

9	Microstructure of freeze-dried 5 volume % α -alumina (AKP-30) suspension at $pH=8.5$. At 5 volume %, particles form a loose network structure which has third and higher generation voids.	19
10	Pore fraction of cakes cast at 400 psi as a function of electrophoretic mobility of slip.	20
11	Relative density of different bodies produced from the same Al_2O_3 powder by filtration at different applied pressures.	22
12	Increasing the degree of flocculation increased the slope of the consolidation curve.	23
13	Fractal dimension, D versus interparticle attraction at different times.	25
14	Model for ideal elastic material and purely viscous material.	28
15	Keivin/Voigt and Maxwell model for viscoelastic material.	30
16	Relationship between stress and strain of an elastic material under the sinusoidally oscillating mode.	31
17	Relationship between stress and strain of a pure viscous material under the sinusoidally oscillating mode.	33
18	Example of Lissajou Figure at (a) linear viscoelastic, (b) plastic, and (c) viscous region for polymeric material.	34
19	Vectorial resolution of components of complex modulus in sinusoidal deformation.	36
20	Particle size distribution of AKP-30	40

21	Particle size distribution of AKP-50.	41
22	Zeta potential versus pI relationship of Sumitomo alumina (AKP-30).	42
23	Schematic diagram of pressure filtration cylinder.	45
24	Difference in settling behavior of flocculated and dispersed suspensions.	46
25	Schematic diagram of dynamic oscillatory fluid spectrometer.	49
26	Time profile of a simple shear stress relaxation experiment following sudden strain.	51
27	Consolidation time versus thickness of consolidated layer at different pressure levels.	53
28	Effect of pressure on filtration time.	55
29	Effect of pressure on the permeability of consolidated powder compacts.	58
30	Structure relaxation with time at different pI's at fixed pressure.	60
31	Structure relaxation with time at different pressure levels at fixed binding energy.	61
32	Packing density as a function of applied filtration pressure at different particle interaction energy states for micrometer-sized alumina (AKP-30) and nanometer-sized boehmite systems.	63
33	Effect of increasing amplitude of sinusoidally oscillatory strain on the storage modulus (G') and the loss modulus (G'') on the sample with 7 volume % of particle concentration at pI = 3.5.	65

34	The hierarchy of voids decays with increasing powder concentration at the most flocculated state (pH=8.5).	67
35	SEM micrographs of freeze-dried (a) alumina suspension (5 volume % particle) at pH=8.5 and (b) boehmite (6 volume %) at pH=6.5.	68
36	Storage modulus versus particle concentration for boehmite suspension at pH=5.5, alumina (AKP-30 and 50) suspensions at pH=8.5.	70
37	Effect of increasing amplitude of sinusoidally oscillatory strain on the storage modulus (G') and the loss modulus (G'') of the sample prepared at pH=5.6.	72
38	Microstructure of freeze-dried boehmite gel (3 volume % particle and pH=5.5).	73
39	Sine wave of applied strain and torque response at strain 5.25 % of the sample prepared at pH=5.6.	75
40	Lissajou Figure at strain 3.75 %.	77
41	Lissajou Figure at strain 5.25 %.	78
42	Stress relaxation (shear stress versus time) of the sample prepared at pH=5.6.	79
43	Effect of increasing amplitude of sinusoidally oscillatory strain on the storage modulus (G') and the loss modulus (G'') of the sample prepared at pH=3.5.	81
44	Effect of increasing amplitude of sinusoidal strain of the torque response of the sample prepared at pH=3.5.	82
45	Stress relaxation (shear stress versus time) of the sample prepared at pH=3.5.	83

46	Difference in rheological behavior between nanometer- and micrometer-sized particle/water mixtures at highly flocculated state.	84
47	Effect of increasing amplitude of sinusoidally oscillatory strain on the storage modulus (G') and the loss modulus (G'') of the sample prepared at pI = 7.5.	86
48	Effect of pI on the settling rate and turbidity of boehmite suspensions. Initial concentration of particles is 0.05 volume %.	88
49	Relationship between the storage modulus in linear viscoelastic region and particle concentration for the flocculated boehmite system.	90
50	Relationship between the yield strain and particle concentration for the flocculated boehmite system.	92
51	Relationship between cluster size and particle concentration.	93

LIST OF TABLES

Number		Page
1	Filtration Pressure vs. Packing Density of Consolidated Layer from the Suspensions of $pH = 3.0$	56
2	Brief Summary of Difference in Rheological Behavior between Nanometer- and Micrometer-Sized Particle Systems	85

ACKNOWLEDGMENTS

The author would like to thank Dr. Ilhan A. Aksay for his guidance throughout the research for this dissertation. He would also like to thank fellow workers in the Advanced Materials Technology Program for helpful discussions and all their help.

The author would also like to thank: Dr. Wei H. Shih for helpful discussions on scaling theory and pressure filtration; Dr. James C. Seferis, Dr. Jan Manson, and Dr. Hiroshi Watanabe for helpful discussions concerning viscoelasticity; and Mr. Larry Chick for his guidance on presentation and writing techniques.

Finally, the author wishes to acknowledge his family members for constant encouragement, and the Army Research Office for financial support for this work.

1. INTRODUCTION

In the processing of ceramic powder, the colloidal processing technique has proved to be the best way to control the interaction energy between particles and the microstructures of consolidated powder compacts. However, there are still problems to be solved.

First, the difference in rheological behavior between micrometer- and nanometer-sized particle suspensions is not understood (Figure 1).¹ A micrometer-sized particle is defined as larger than $0.1\text{ }\mu\text{m}$ in diameter; a nanometer-sized particle is defined as smaller than $0.1\text{ }\mu\text{m}$ in diameter. By using micrometer-sized particles, it is possible to make suspensions with a high concentration of particles (> 55 volume %) with low viscosity ($< 1\text{ pa}\cdot\text{sec}$). However, in order to control the structure of the final product on a smaller scale, and in order to have better mechanical properties due to finer-grained microstructures and decreased defect sizes (Figure 2),² it is preferable to use nanometer-sized particles. In suspensions with nanometer-sized particles, the maximum particle concentration that can be added is less than 30 volume %, at which point the suspension becomes a gel. In this study a gel is defined as having a linear viscoelastic region in dynamic rheological measurement. So far, no study has been reported which gives an understanding of the difference in rheological behavior between micrometer- and nanometer-sized particle suspensions.

Second, behavior of packing density as a function of filtration pressure at different particle interaction energy states is not well understood, and study so far has been limited to micrometer-sized particle systems. Previous studies have shown that the packing density of the micrometer-sized particle system is pressure-sensitive when the suspension is prepared in the flocculated state, and pressure-insensitive when the suspension is prepared in the highly dispersed state,³⁻⁸ but no explanations were given.

Rheological behavior and packing density of colloidal particulate systems are related to the structure formed by particles in suspension. Therefore, the objective of this work is to investigate the structure-property relationship of the aqueous

2. LITERATURE REVIEW

2.1 Particle Interactions in Colloidal Suspensions

A colloidal suspension consists of a dispersion medium (the continuous phase) and the colloidal particles (dispersed phase). Dispersion of particles in colloidal suspension can be achieved by the steric or electrostatic mechanism. The steric mechanism relies on sufficient adsorption of polymer on the particles to provide a barrier that will control the interaction of particles.⁹ Electrostatic stabilization is based on establishing a diffuse double layer of ions at the particle-liquid interface. There are two main forces in electrostatic dispersion between the colloidal particles, the van der Waals attraction and the Coulombic repulsive force. In a colloidal suspension, particles encounter each other frequently due to Brownian movement, convection, and gravitational forces. Depending on the magnitude of these forces, particles form a permanent contact (i.e., flocculate) and lose stability, or remain free after they encounter each other. The London-van der Waals forces are large enough to cause long-range attraction for particle separation distances of greater than 5 nm for many colloidal systems.^{10,11}

In 1937, Hamaker derived the expression for the attractive potential in the case of two spherical particles with equal radii a , separated *in vacuo* by a distance l between particle surfaces.¹²

$$V_A = -\frac{A}{12} \left[\frac{1}{x(x+2)} + \frac{1}{(x+1)^2} + 2 \ln \frac{x(x+2)}{(x+1)^2} \right] \quad (1)$$

where $x = l/2a$ and A = Hamaker constant.

If a small interparticle separation is assumed, such that $l \ll a$ (i.e., $x \gg 1$), this equation simplifies to

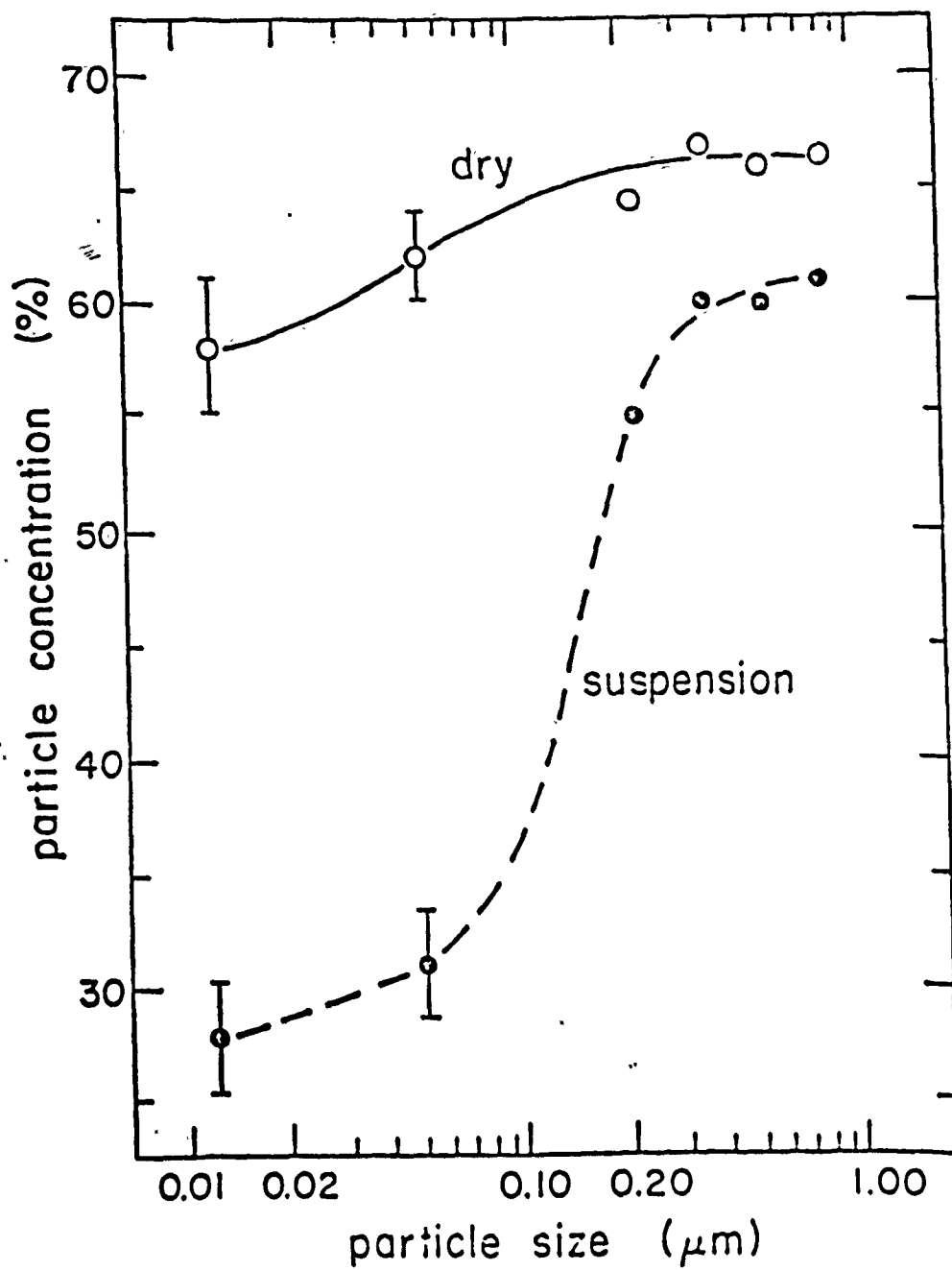
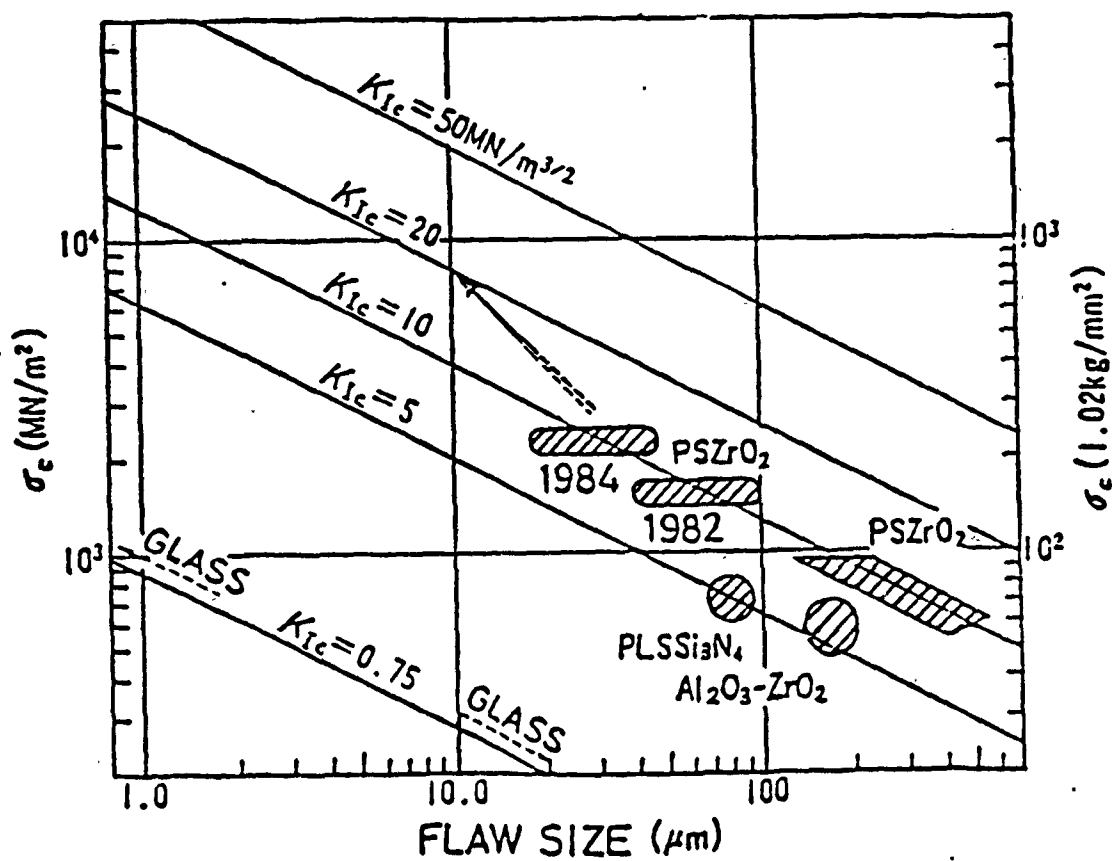


Figure 1. Particle size versus maximum allowable particle concentration in aqueous medium.¹



Strength of present and future ceramics.

Figure 2. Strength versus flaw size in the sintered product.²

ceramic particulate system. The results may contribute to an understanding of how to increase particle concentrations in nanometer-sized particle suspensions. We will then be able to prepare concentrated suspensions and gels with nanometer-sized particles, and the processing of a monolithic component will be possible through the elimination of excessive shrinkage and cracking during the drying and sintering stages.¹

In order to achieve the objective, the following approach was taken. First, the effect of filtration pressure on the packing behavior of colloidal suspensions was studied at different particle interaction energy states for micrometer- and nanometer-sized particle systems. The results of this approach showed that (i) for micrometer-sized particle systems, packing density is pressure-sensitive for the flocculated system (at pH 7.0, 7.5, and 8.5) and pressure-insensitive for the highly dispersed system (at pH 3.0)--when there are pores larger than first-generation void, packing density becomes pressure-sensitive; (ii) for the nanometer-sized particle system, even in the dispersed state packing density is pressure-sensitive as particle concentration increases which is due to the formation of a gel with a finite value of the storage (i.e., elastic) modulus; (iii) the slope of the packing density vs. applied pressure changes for different density ranges--slopes with larger gradients mean more compaction due to elimination of higher hierarchical voids, and slopes with smaller gradients mean less compaction due to elimination of lower hierarchical voids; (iv) similar slopes exist in different pressure ranges for micrometer- and nanometer-sized particle systems due to elimination of the same type of voids; (v) starting from the same structure, yield stress is higher for the nanometer-sized particle system than for the micrometer-sized particle system--the elastic modulus at fixed particle concentration is three orders higher for the nanometer-sized particle system than for the micrometer-sized particle system.

Second, the rheological behavior of nanometer- and micrometer-sized particle systems was studied by measuring the storage modulus and yield strain as a function of particle concentration at different particle interaction energy states. The results of this approach showed that (i) the yield strain decreases as a function of particle

concentration in a power-law fashion; (ii) structural information was obtained by scaling theory and experimentally measured storage modulus and yield strain as a function of particle concentration; (iii) the difference in rheological behavior between micrometer- and nanometer-sized particle systems was understood.

3. EXPERIMENTAL PROCEDURES

3.1 Material

The alumina particle/water system was chosen for this study because it is an important ceramic material and its suspension characteristics have been extensively studied by many researchers.^{3,61-63}

Powders used in this study were of two types: micrometer-size α -alumina and nanometer-size boehmite. The α -alumina (AKP-30 and 50) was supplied by Sumitomo Chemical Company in Osaka, Japan, and boehmite (γ -AlOOH, Catapal-D) was supplied by Vista Chemical Company in Houston, Texas. Particle size distribution of α -alumina was measured by sedigraph (Micrometrics, Norcross, GA 30093). Median diameters of AKP-30 and 50 are 0.4 μm and 0.2 μm , respectively (Figures 20 and 21).

As a nanometer-size particle system, boehmite (AlOOH) was chosen. The boehmite used was Catapal D. Its chemical composition is $\text{Al}_2\text{O}_3 \cdot 1.25 \text{H}_2\text{O}$, which has a slightly higher water content than stoichiometric boehmite ($\text{Al}_2\text{O}_3 \cdot \text{H}_2\text{O}$). These powders are agglomerated plate-like boehmite crystallites. Average size of the agglomerates is 65 μm . They can be dispersed in acidic solution and broken up into single crystallites or smaller aggregates. The size of the crystallites determined by x-ray line broadening by Vista Chemical Company is 40 \AA in the 020 direction and 64 \AA in the 021 direction. Particle size measurement by TEM⁶³ was approximately 50-100 \AA in diameter and 10-20 \AA in thickness.

3.2 Suspension Preparation

Alumina powder suspensions were prepared by electrostatic stabilization. Measurement of electrophoretic mobility (Particle Micro-Electrophoresis Apparatus Mark II, Rank Brothers, Bottisham, Cambridge, England) of alumina powder (Figure 22),⁶⁵ showed it has high zeta potential (80 mV) at pH = 3.0 and an isoelectric point (IEP)

$$V_A = - \frac{A}{12} \frac{1}{2d} = - \frac{Aa}{12H} \quad (2)$$

In 1936, De Boer¹³ obtained the expression for the attractive potential in the case of two infinitely large blocks with parallel plane surfaces facing each other. The attractive potential for two plates of thickness δ , at a distance $2d$ from each other, is found to be

$$V_A = - \frac{A}{48} \frac{1}{\pi} \left[\frac{1}{d^2} + \frac{1}{(d + \delta)^2} - \frac{2}{(d + \frac{\delta}{2})^2} \right] \quad (3)$$

The major problem in calculating the van der Waals interaction between colloidal particles is evaluating the Hamaker constant, A . Two methods are available. The first of these methods is the London-Hamaker microscopic approach, and the second is the macroscopic approach, of which detailed explanations are available elsewhere.^{11,14-17} These Hamaker constants for single materials usually vary between about 10^{-20} J and 10^{-19} J. For example, the Hamaker constant for alumina is 4.2×10^{-20} ; more examples are given in reference 18.

In order to obtain a stable colloidal suspension, it is necessary to provide repulsive forces between particles. These repulsive forces must be greater than the attraction forces (Figure 3).¹⁴

The surface of most materials becomes electrically charged when brought into contact with polar (i.e., aqueous) medium. Ionization, ion adsorption and ion dissolution are attributed to the charging mechanisms. This surface charge influences the distribution of nearby ions in the polar medium. Ions of opposite charge (counter-ions) are attracted towards the surface and ions of like charge (co-ions) are repelled away from the surface. The principle of electroneutrality demands that the net charge in the dispersion medium be equal, but of opposite sign to that of the particle surface. This leads to the formation of an electric double layer made up of the charged surface and a neutralizing excess of counter-ions over co-ions distributed in a diffused manner

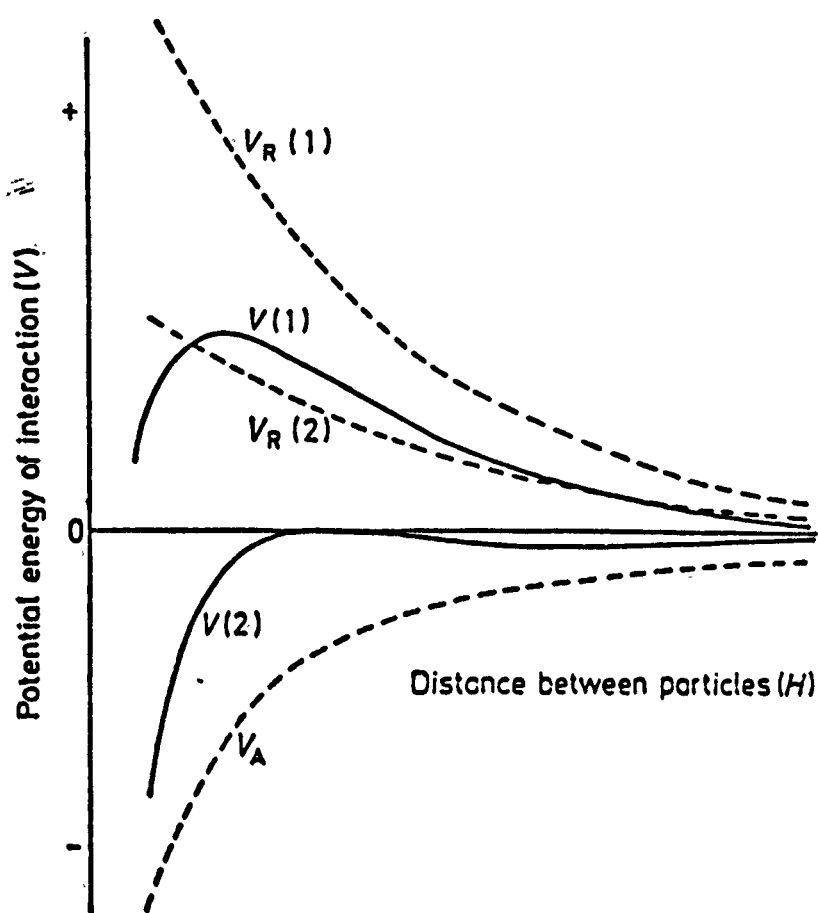


Figure 3. Total interaction energy curves. $V_{(1)}$ and $V_{(2)}$ are obtained by the summation of an attraction curve, V_A , with different repulsion curves, $V_R(1)$ and $V_R(2)$.¹⁴

in the polar medium. In electrostatic stabilization, the Coulombic repulsion between the colloidal particles is of long-range character, comparable to that of the attraction (5-10 nm), and can impart stability. These double layers provide stability by mutual repulsion when the double layer overlaps in electrostatic stabilization (Figures 4 and 5).^{11,19}

The magnitude of the energy of repulsion in the case of spherical particles can be expressed by what is known as the DLVO theory (Derjagin and Landau²⁰ and Verwey and Overbeek²¹). For large κa , symmetrical electrolytes (only one electrolyte with ions of charge number $+z$ and $-z$), and relatively large distances (H large),

$$V_R = 32 \pi \epsilon \epsilon_0 a (RT\gamma / zF)^2 \ln [1 + \exp(-\kappa H)] \quad (4)$$

$$\gamma = \tanh(zF\phi_0 / 4RT)$$

$$1/\kappa = (\epsilon \epsilon_0 RT / F^2 \sum C_i z_i^2)^{1/2}$$

where

ϵ = relative permittivity (or dielectric constant) of the dispersion medium

ϵ_0 = permittivity of the vacuum

a = radius of spherical particle

R = gas constant

T = absolute temperature

z = charge number of ions

F = Faraday constant

$1/\kappa$ = thickness of the electrical double layer (κ = Debye-Hückle length)

H = distance between particles surfaces

C_i = concentration of ions of type i in the dispersion medium

ϕ_0 = surface potential

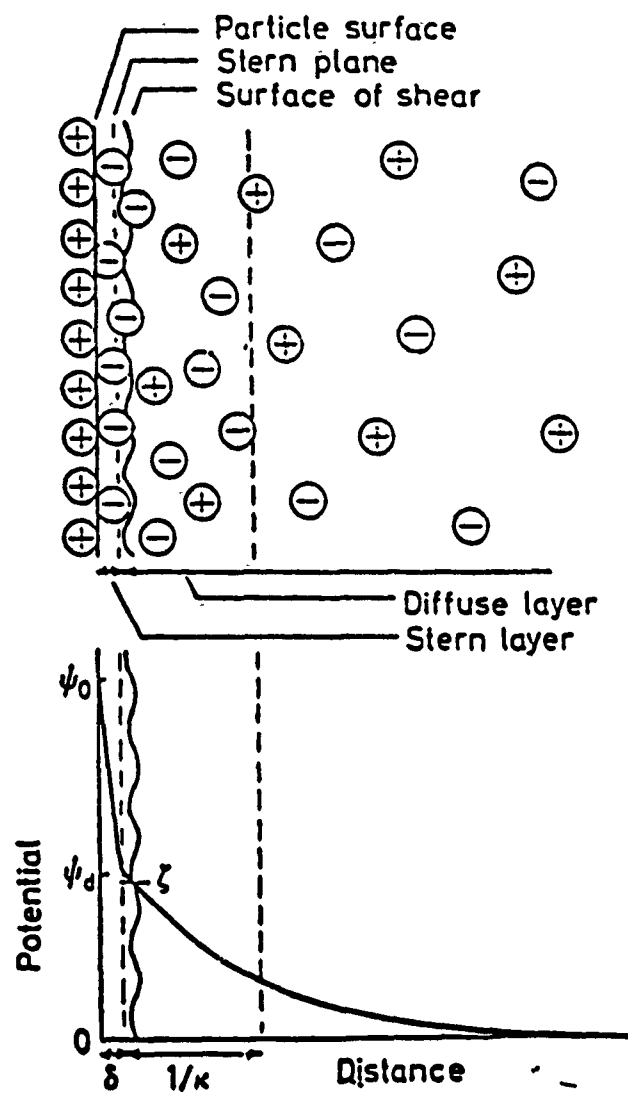


Figure 4. Schematic representation of the structure of the electric double layer according to Stern's theory.¹⁴

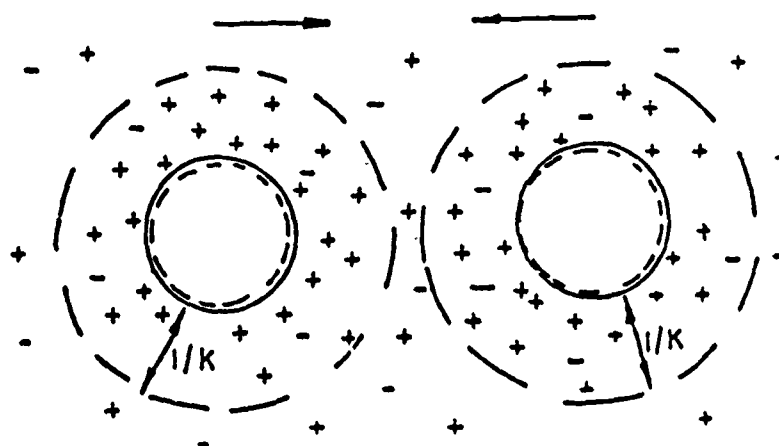


Figure 5. Diagrammatic representation of the origin of electrostatic stabilization for negatively charged particles.¹¹

With plate-like particles, a repulsive potential can be approximated by DLVO theory.²²

$$V_R = \frac{64nkT}{\kappa} \gamma^2 e^{-2\kappa d} \quad (5)$$

$$\gamma = \frac{\{\exp(e\psi_n/2kT) - 1\}}{\{\exp(e\psi_o/2kT) + 1\}}$$

where

n = the ion density

d = half of the interparticle distance

κ = Debye's reciprocal length

ψ_o = the surface potential, in place of which the ζ -potential is used in practice

From the above equations we can specify the methods for increasing repulsive energy as follows: (1) use a liquid medium with high dielectric constant; when $\epsilon = 0$, dispersion of particles is impossible, (2) increase γ by increasing the zeta potential, (3) increase the double layer thickness by decreasing the concentration of ions and charge number of ions in the dispersion medium,^{14,23} (4) decrease the distance between particles by increasing the particle concentration. Of these methods, (1) and (3) can be done fairly easily.

2.2 Powder Consolidation through Colloidal Processing

Colloidal filtration (also known as slip casting) has been used in ceramics to make complex shaped articles. In order to understand the process one must have an appreciation of the mechanism of the filtration process itself and the nature of the colloidal suspension and its role in microstructure development during the consolidation process²⁴

The filtration mechanism has been studied for different ceramic materials by many researchers.²⁵⁻²⁹ In 1953, Deeg²⁵ found out that the consolidation layer grows proportionally with the square root of the time. He treated the filtration process as a diffusion process. Several years later, Dietzel and Mosterzky^{26,27} also found the same relationship between filtration time and growth rate, and that the filtration process is due to capillary suction by the plaster mold.

Adcock and McDowall²⁸ improved the model which treated the filtration process as a viscous flow of liquid medium through the pores of consolidated layer. However, they failed to include the resistance of the mold to liquid flow.

In 1985, Aksay²⁴ derived the filtration equation by treatment of Darcy's law in a rigorous way.

$$\left(\frac{\xi_c^2}{t}\right) = \left(\frac{P_t - P_o}{\frac{\eta m_c}{2} + \frac{\eta m_m}{2\epsilon_m}}\right) \quad (6)$$

where

- ξ_c = thickness of the consolidated layer
- t = filtration time
- $P_t - P_o$ = pressure drop
- η = viscosity of liquid medium
- m_c = specific porous medium resistance of consolidated layer
- m_m = specific porous medium resistance of the mold
- ϵ_m = porosity of mold
- n = system parameter, $n = 1 - X_p = \epsilon_c / X_p$
- X_p = volume concentration of particles in the suspension
- ϵ_c = porosity of consolidated layer

This equation indicates that the filtration rate, $\left(\frac{\xi_c^2}{t}\right)$, can be enhanced by (i) in-

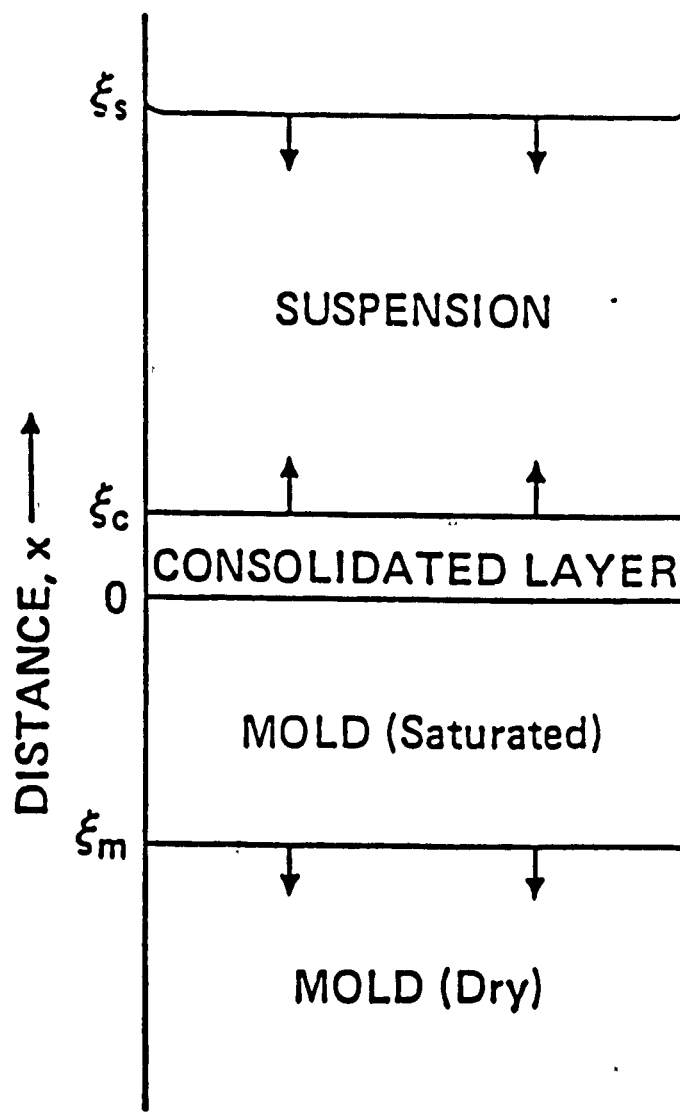


Figure 6. Schematic cross-sectional view of the filtration system.²⁴

creasing total pressure drop (Figure 7), (ii) decreasing viscosity of the liquid medium, (iii) increasing particle concentration in the suspension, (iv) increasing porosity of the consolidated layer with the use of larger size particles, (v) decreasing resistance of the mold. Since submicron-size powders are preferred for use in ceramic processing and colloidal processing is done at room temperature, it is more practical for the processor to use either a high-pressure drop or a highly concentrated suspension.

In colloidal processing the nature of the colloidal suspension directly affects the microstructure of the consolidated compact. Even though colloidal processing has been used by ceramists for many years, there are no guidelines for tailoring the suspension property as well as the microstructure of consolidated powder compacts.

Aksay and Kikuchi²³ pioneered the establishment of a fundamental understanding of the relationship between particle interaction energy and particle number density, ranging from dilute suspensions to highly concentrated suspensions (> 60 v/o). They constructed a phase diagram (Figure 8) for a one-component ceramic particulate/aqueous system. With the use of the phase diagram, one can prepare dispersed suspensions of high solids loadings (≥ 50 volume %) above a critical interaction potential, and flocculated suspensions of low solids loadings below a critical point. After consolidation, it is predicted that regardless of the interaction potential, high packing density, i.e., 74 volume % ((a) in Figure 8) is expected if the colloidal system can attain its equilibrium (i.e., the lowest free energy) state.¹ However, these equilibrium packing densities are never obtained experimentally ((b) in Figure 8)^{30,31} because the metastable hierarchically-clustered particle compacts form during the consolidation stage.^{30,32} The formation of the particle clusters resembles the nucleation and growth mechanism of crystals in an atomic system: during the consolidation of colloidal suspensions, particle concentration increases at the consolidation front; when it reaches critical concentration, multiple nucleation takes place; with further increment of particle concentration, more particles come together and form densely packed particle clusters. Finally, a polycrystalline-like material is obtained which contains different types of voids: first-generation voids, which are the voids within

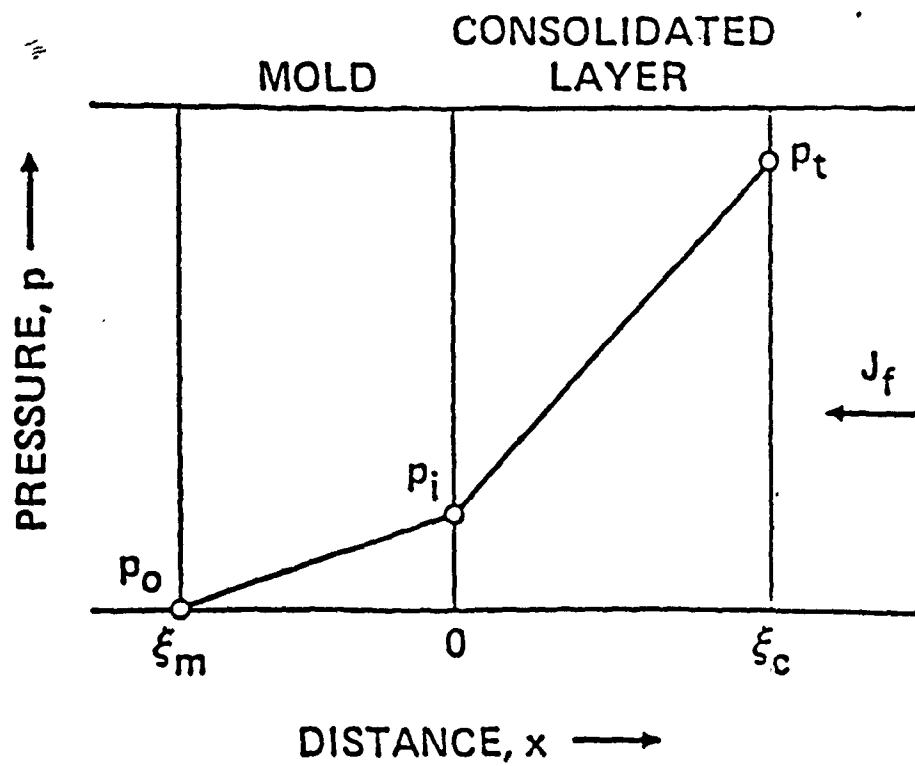


Figure 7. Hydraulic pressure profiles across the consolidated layer and the mold.²⁴

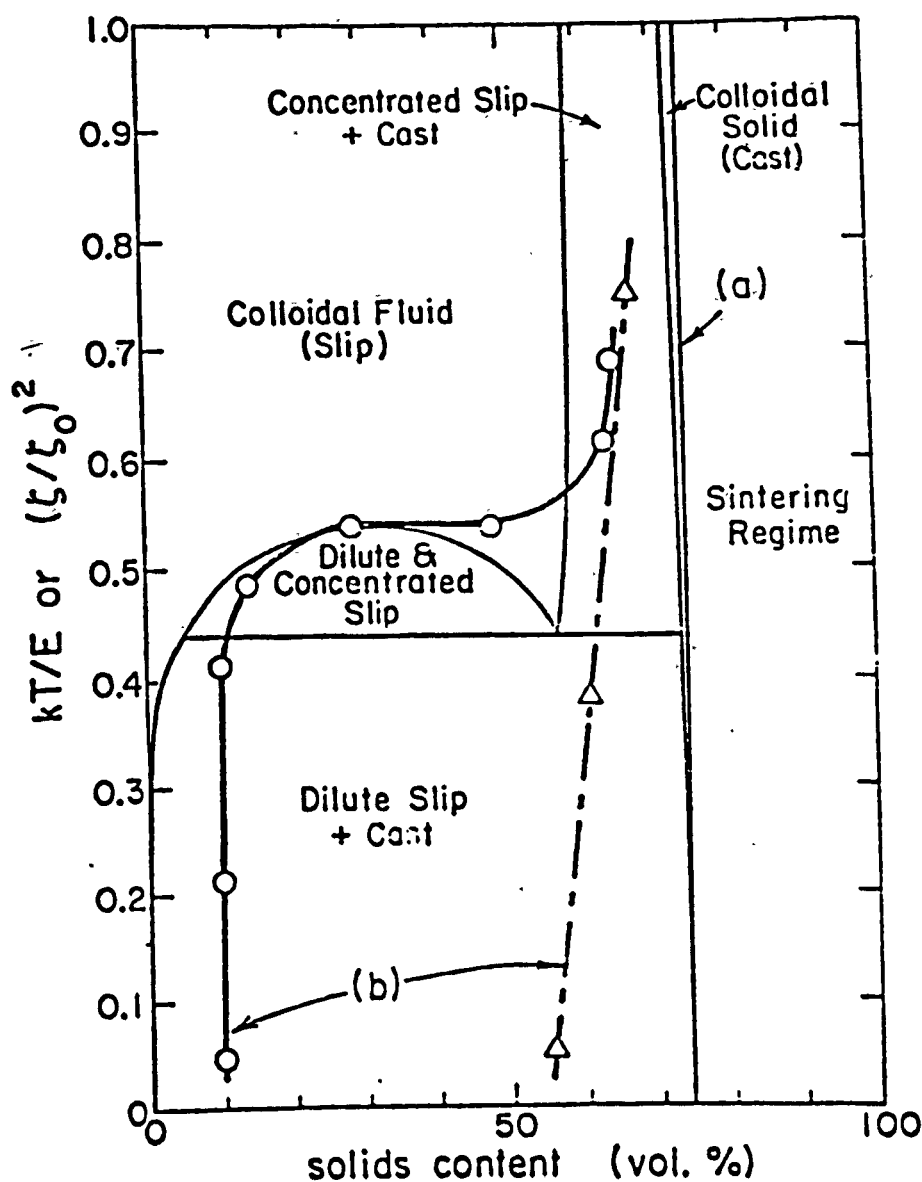


Figure 8. (a) Phase diagram (outlined with thin solid lines) for a colloidal system of only one type of particle. In electrostatically interacting systems, the reduced temperature scale is approximately proportional to $(\zeta/\zeta_0)^2$, where ζ is the surface potential and ζ_0 is a normalization constant. The maximum packing density is predicted to be $\sim 74\%$. (b) Sedimentation (thick solid line with unfilled circles) and slip cast (thick broken line with unfilled triangles) densities are lower than the predicted dense packing value.³⁰

the first-generation clusters of primary particles, second-generation voids, which are the voids between the first-generation clusters of particles, and third-generation voids, which are the voids between second-generation clusters of particles. When consolidation by free settling is conducted in a highly dispersed state, the binding energy between particles is low and mobility of particles is high. As a result, particles can move around the clusters, find dimples, and pack densely. Average packing densities of 64 volume % are obtained with monosized particles containing the hierarchy of voids up to the second generation. When the consolidation by free settling is done in a highly flocculated state, the binding energy between particles is high and mobility of particles is low, so that when the particles encounter each other in the suspension state, they form permanent clusters at low particle concentrations (< 10 volume %) and low-density clustered networks at higher particle concentration (~ 15 volume %). As a result, particles form a loosely-packed compact (Figure 9) containing third- and higher-generation voids.

2.3 Pressure Filtration

As discussed earlier, the colloidal processing technique provides a control on the particle interaction energy of the microstructure of the consolidated powder compact. Usually powder suspensions are prepared at the minimum interparticle attractive energy states. However, when the suspension contains two or more powder phases, it is necessary to induce flocculation to prevent phase separation during consolidation. Many researchers^{3,7} have studied the packing behavior of colloidal solids at different interparticle energies under pressure, but no clear explanations were given.

Fennelly and Reed^{3,7} studied the pressure filtration of 50 volume % Al_2O_3 aqueous suspensions in which the repulsive interparticle forces were systematically increased with the addition of a polyelectrolyte. They showed that the packing density of the consolidated layer (Figure 10) and thus its permeability was strongly dependent on the degree of dispersion. The cast layer from the highest electrophoretic



Figure 9. Microstructure of freeze-dried 5 volume % α -alumina (AKP-30) suspension at pH = 8.5. At 5 volume %, particles form a loose network structure which has third and higher generation voids.

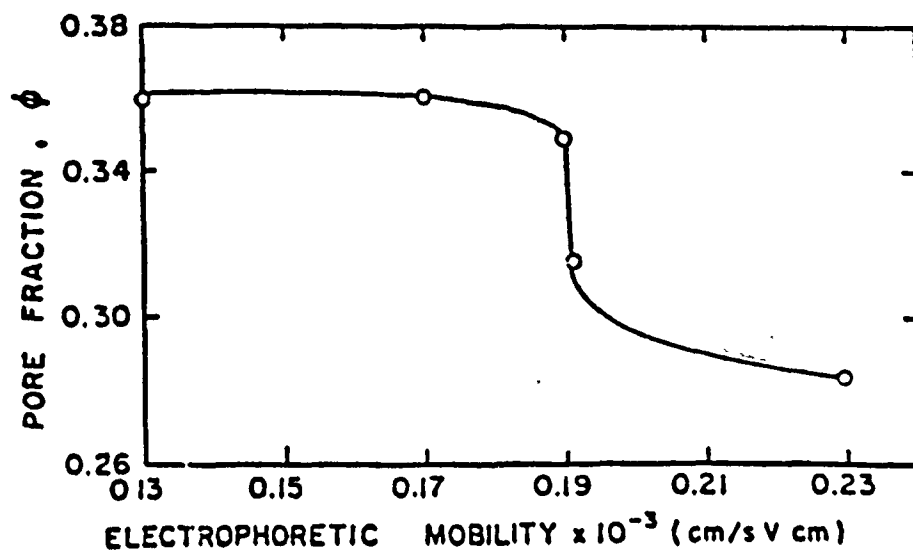


Figure 10. Pore fraction of cakes cast at 2.758 MPa (≈ 400 psi) as a function of electrophoretic mobility of slip.³

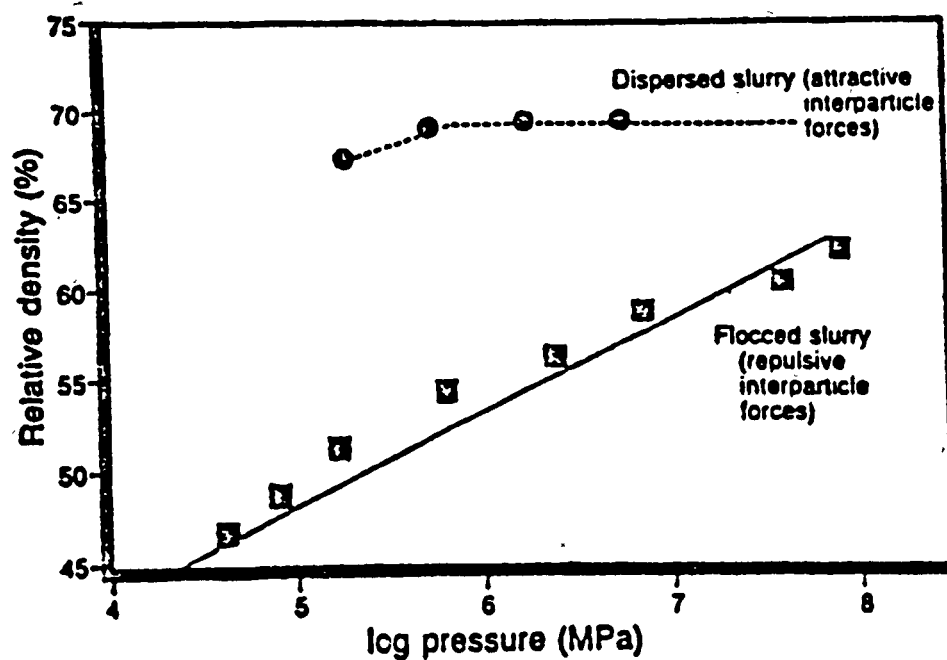


Figure 11. Relative density of different bodies produced from the same Al_2O_3 powder by filtration at different applied pressures. Bodies were consolidated from either dispersed ($\text{pH} = 2$) or flocced ($\text{pH} = 8$) aqueous slurries containing 20 volume % solids.⁵

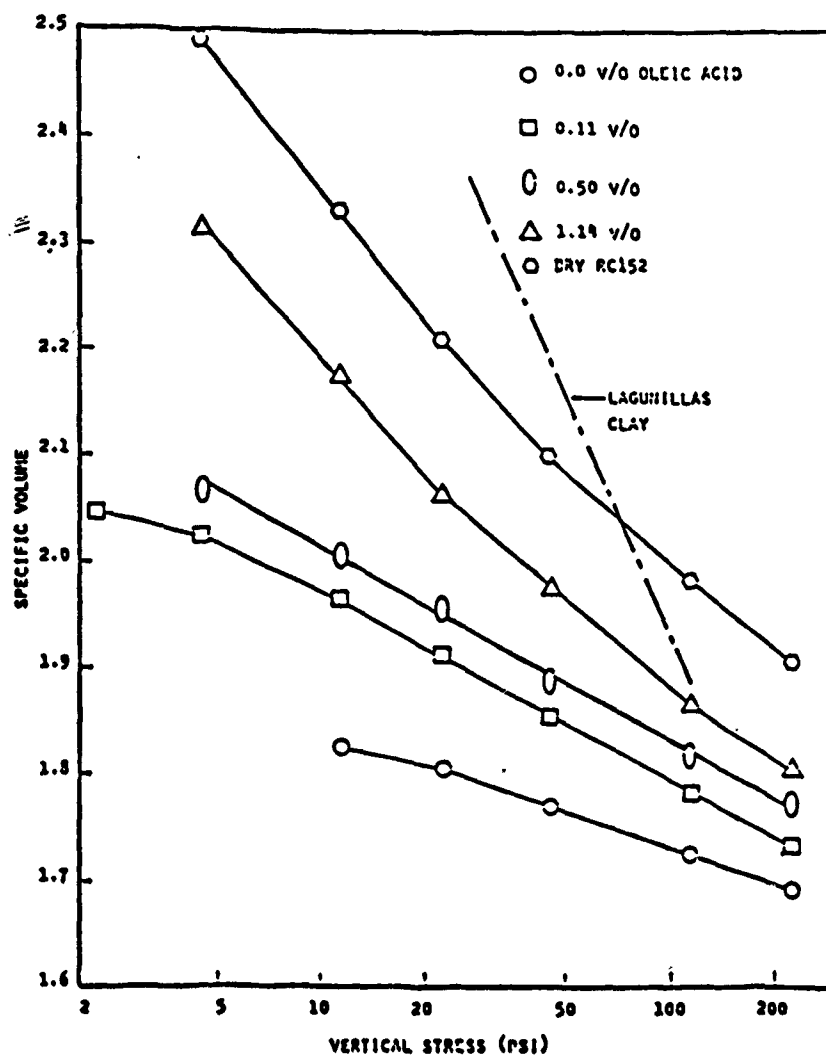


Figure 12. Increasing the concentration of oleic acid increased the degree of flocculation and the slope of the consolidation curves.⁷ The specific volume is defined as total volume at system divided by volume of solid. 2 psi = 1.379×10^{-2} MPa, 5 psi = 3.447×10^{-2} MPa, 10 psi = 6.895×10^{-2} MPa, 20 psi = 1.379×10^{-1} MPa, 50 psi = 3.447×10^{-1} MPa, 100 psi = 6.895×10^{-1} MPa, and 200 psi = 1.379 MPa.⁸

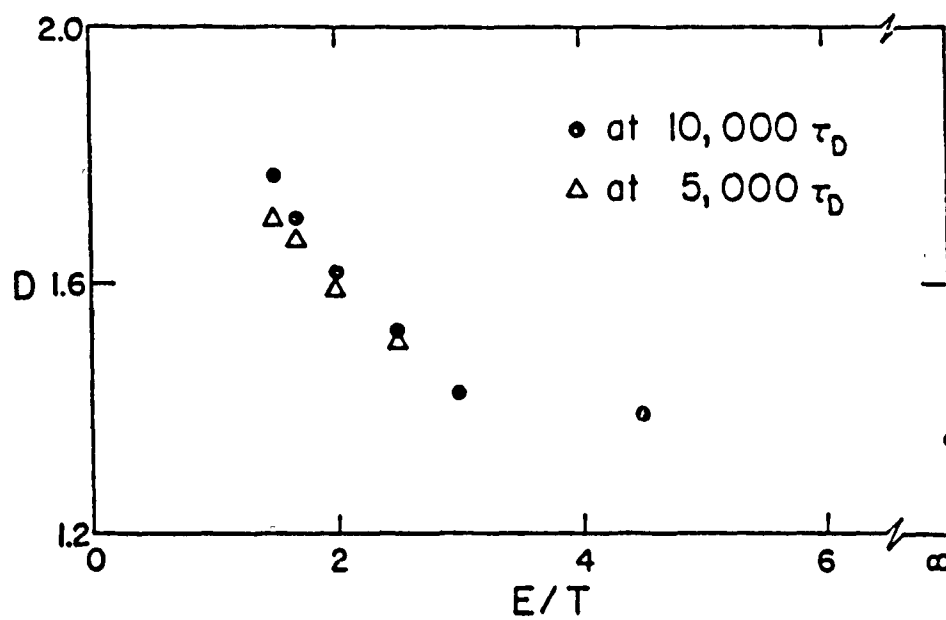


Figure 13. Fractal dimension, D , versus interparticle attraction at different times.³⁴

2.4 Rheology

Rheology is the science of the deformation and flow of materials and its study has contributed much towards clarifying ideas concerning the nature of colloidal systems. It is a subject of tremendous and increasing technological importance in many industries, such as rubber, plastics, food, paint, ceramics and textiles, where the stability of the products involved is to a large extent judged in terms of their mechanical properties.⁴³

In ceramics, flow behavior is important in slip casting, tape casting, extrusion, injection molding, etc. For many simple fluids, the study of rheology involves the measurement of viscosity. For such fluids, the viscosity depends primarily upon temperature and hydrostatic pressure. However, the rheology of colloidal particle systems is much more complex because particle systems show nonideal behavior.

The classical theory of hydrodynamics deals with properties of viscous liquids, for which, in accordance with Newton's law, the stress is always directly proportional to the rate of strain but independent of the strain itself, i.e., it deals with Newtonian viscous fluids. The classical theory of elasticity deals with mechanical properties of elastic solids, for which, in accordance with Hooke's law, stress is directly proportional to strain in case of small deformation but independent of the rate of strain, i.e., it deals with Hookean elastic solids.⁴⁴ These categories are idealizations. Most materials, particularly those of a colloidal nature, show mechanical behavior which is intermediate between these two extremes, with both viscous and elastic characteristics. Such materials are called viscoelastic.

The rheological behavior of colloidal systems depends mainly on the following factors:

- 1) viscosity of the dispersion medium
- 2) particle concentration
- 3) particle shape
- 4) particle-particle and particle-dispersion medium interaction

Because of the complications involved, this aspect of rheology is still in many respects a mainly descriptive science. However, since the 1950's considerable advances have been made towards understanding rheological behavior and putting it on to a quantitative basis.⁴⁵

2.4.1 *Theory of Viscoelasticity*

Measuring the viscosity of a material is done by a standard method which characterizes the rheological behavior of material that flows. Usually liquids or particle/water mixtures do not show a purely viscous behavior. In most cases, they exhibit a viscoelastic behavior, having properties of both solids and liquids. If we use a mechanical analogy, a viscoelastic material can be explained by elastic elements (springs) and viscous elements (dashpots imagined as pistons moving in oil). Therefore, measuring only the viscosity is often an insufficient method for the characterization of rheological behavior. The elastic component of the viscoelastic material can cause problems in the process or, in special cases, can be desirable in particular processes. To understand viscoelastic material,^{44,46,47} we consider two extreme cases: ideal elastic behavior and purely viscous behavior. The behavior of most of the materials we are dealing with is somewhere between these two extremes: therefore, they are called viscoelastic materials.

To characterize and quantify viscoelastic behavior, two models have been created for both extreme cases, ideal elastic behavior and purely viscous behavior. The model for an ideal elastic material is a spring (Figure 14a). To pull the end of a spring from point a to b, a measured force F is required. The classical theory of elasticity deals with mechanical properties of elastic solids, for which, in accordance with Hooke's law, force is always directly proportional to the strain of the spring, which is denoted by symbol γ , but independent of the rate of strain. In addition, when a spring is released after it is deformed to point b, it will immediately return to its

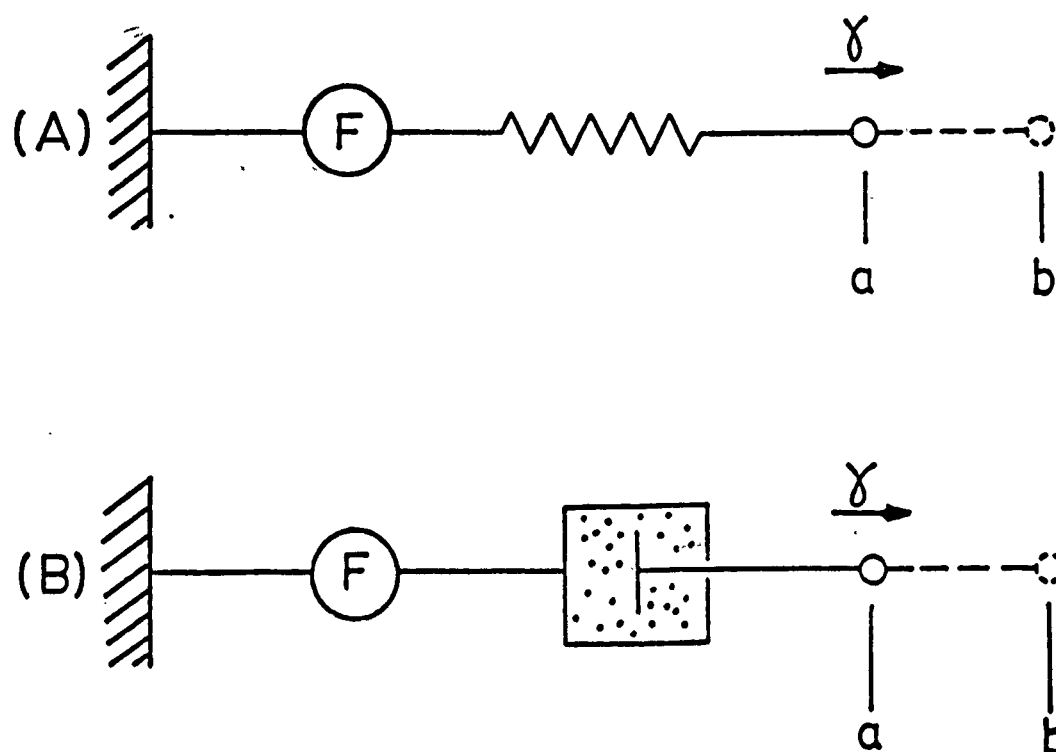


Figure 14. Model for ideal elastic (a), and purely viscous material (b).

original position a. This is because the spring (ideal elastic material) has fully stored the applied energy during deformation.

The model for purely viscous material is a dashpot (Figure 14b). A measured force F is required to pull the dashpot from point a to b. The classical theory of hydrodynamics deals with properties of viscous liquids, for which, in accordance to Newton's law, the force is always directly proportional to the rate of strain but independent of the strain amplitude. If we release the dashpot in position b, it will not return to its original position a. This is due to the fact that in a dashpot (purely viscous material) the applied energy is fully lost as heat during deformation.

The above two extreme models can be incorporated to illustrate the rheological behavior of all materials (Figure 15). Details of the Maxwell and Voigt model are in Reference 43. When viscoelastic materials are subjected to sinusoidally oscillating strain, the stress response is neither exactly in phase with the strain (as it is for a perfectly elastic solid), nor 90 degrees out of phase (as it is for a perfectly viscous liquid), but is somewhere in between. Thus if we write

$$\text{strain } \gamma = \gamma_0 \sin \omega t \quad (7)$$

$$\text{stress } \sigma = \sigma_0 \sin(\omega t + \delta) \quad (8)$$

where ω is angular frequency and δ is the phase lag, equation (8) can be expanded as

$$\sigma = \sigma_0 \sin \omega t \cos \delta + \sigma_0 \cos \omega t \sin \delta \quad (9)$$

The stress can then be considered to consist of two components: (i) stress of magnitude $(\sigma_0 \cos \delta)$ in phase with the strain. The stress of an elastic material under the sinusoidally oscillating mode is dependent on the degree of deformation (Figure 16). Therefore we find that stress and strain are in phase. There is no phase shift ($\delta = 0$). (ii) Stress of magnitude $(\sigma_0 \sin \delta)$ 90 degrees out of phase with the strain.

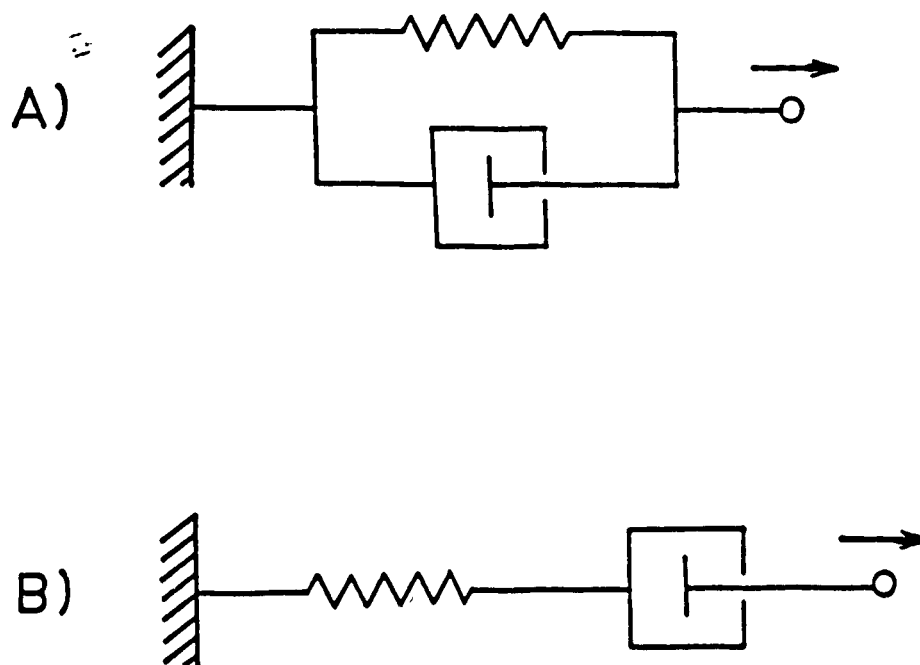


Figure 15. (a) Kelvin-Voigt model and (b) Maxwell model for viscoelastic material.

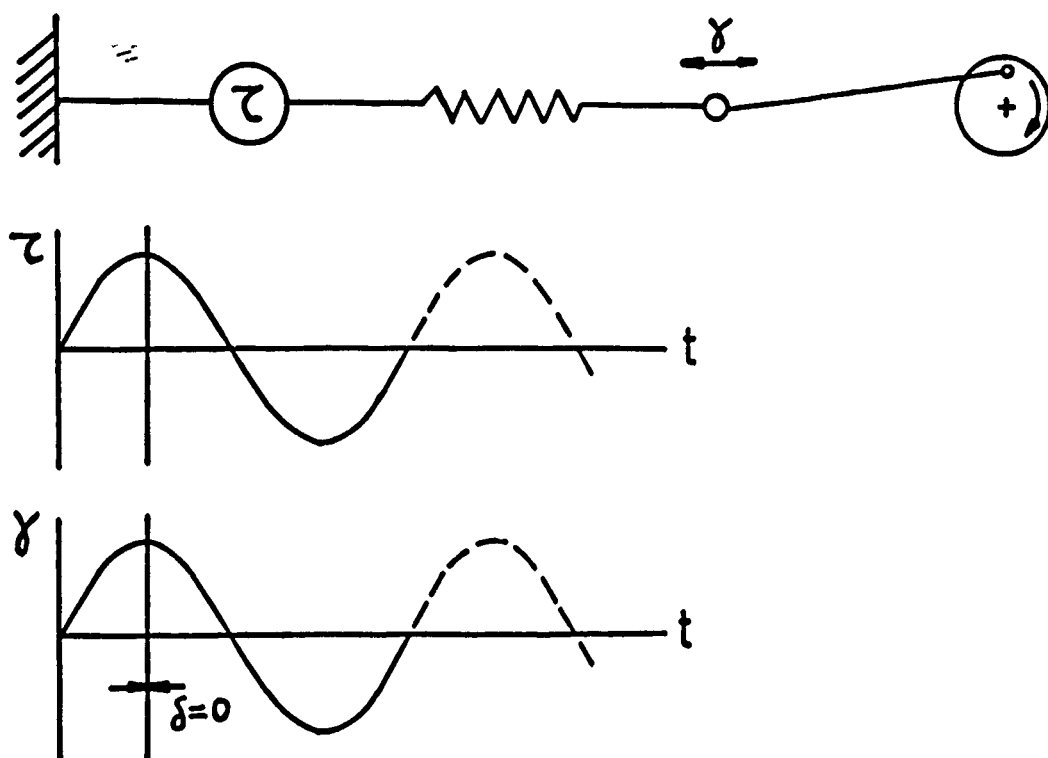


Figure 16. Relationship between stress and strain of a pure elastic material under the sinusoidally oscillating mode.

The stress of a pure viscous material under the sinusoidally oscillating mode is dependent on the rate of strain. At the two maximum amplitudes of strain values, the rate of strain is zero because the system changes direction of strain application. Therefore, we find that stress and strain are 90 degrees out of phase ($\delta = 90^\circ$) (Figure 17). Now, if the sine waves of stress and strain are combined together, the Lissajou pattern can be made. The Lissajou pattern clarifies the stress-strain relationship, and the amount of energy dissipated during sinusoidal deformation. Figure 18⁴⁸ shows examples of the Lissajou figure at linear viscoelastic, plastic, and viscous regions for polymeric material.

When the stress in phase with the strain ($\sigma_o \cos \delta$) and the stress 90° out of phase with the strain ($\sigma_o \sin \delta$) are divided by the strain, we can separate the modulus into an in-phase (real) and out-of-phase (imaginary) component. These relationships are:

$$\sigma = \gamma_o G' \sin \omega t + \gamma_o G'' \cos \omega t \quad (10)$$

where

$$G' = \frac{\sigma_o}{\gamma_o} \cos \delta$$

$$G'' = \frac{\sigma_o}{\gamma_o} \sin \delta$$

G' is the real part of the modulus, and G'' is the imaginary part. The storage modulus is a measure of the energy stored and recovered per cycle, and the loss modulus is a measure of energy dissipation or loss as heat per cycle of sinusoidal deformation.

Stress (τ) and strain (γ) are related by the complex modulus (G^*). The complex modulus includes complete information on the viscoelastic properties: the elastic component, the viscous component, and the phase shift between the stress and strain. The complex modulus is defined as:

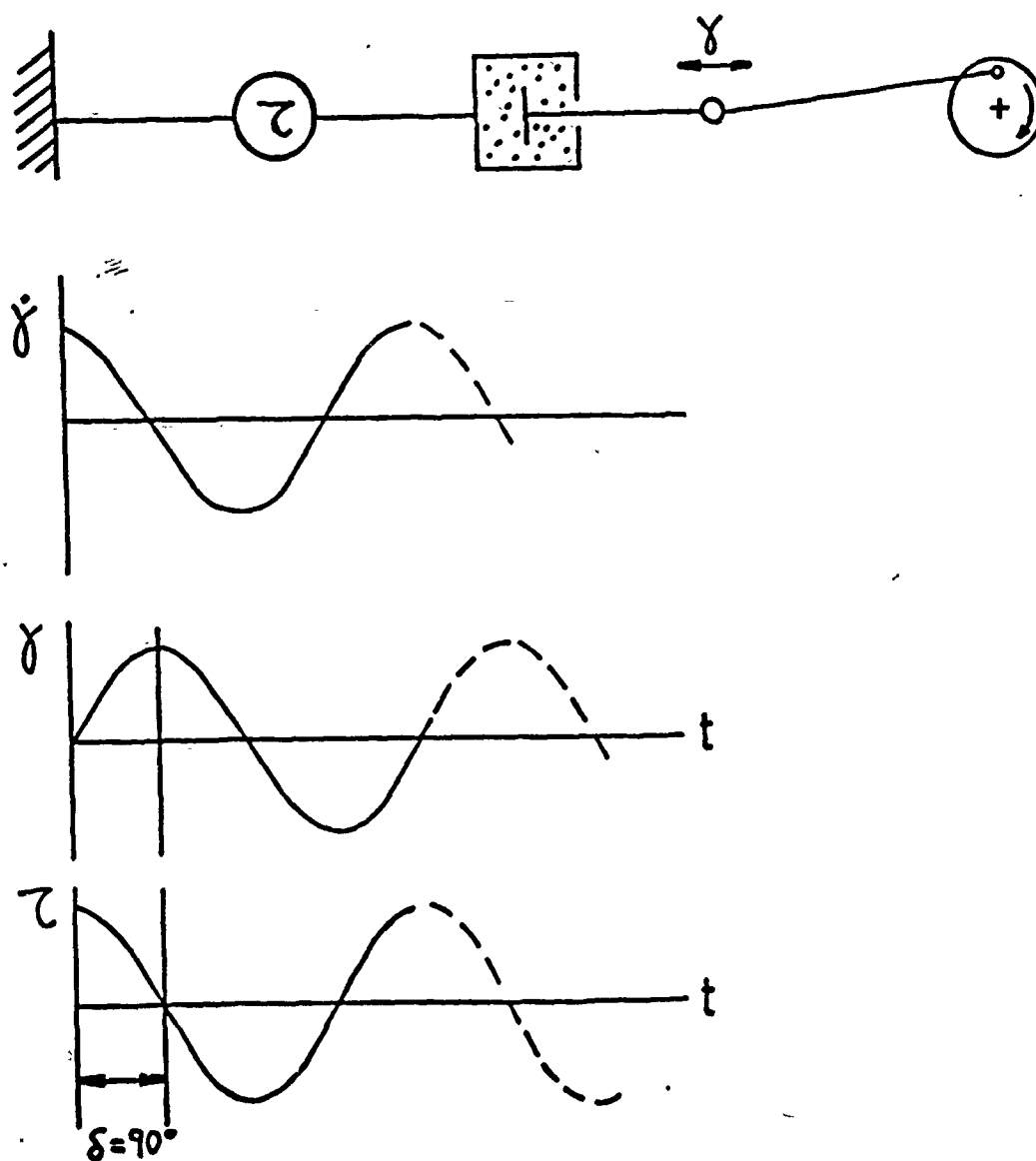


Figure 17. Relationship between stress and strain of purely viscous material under the sinusoidally oscillating mode.

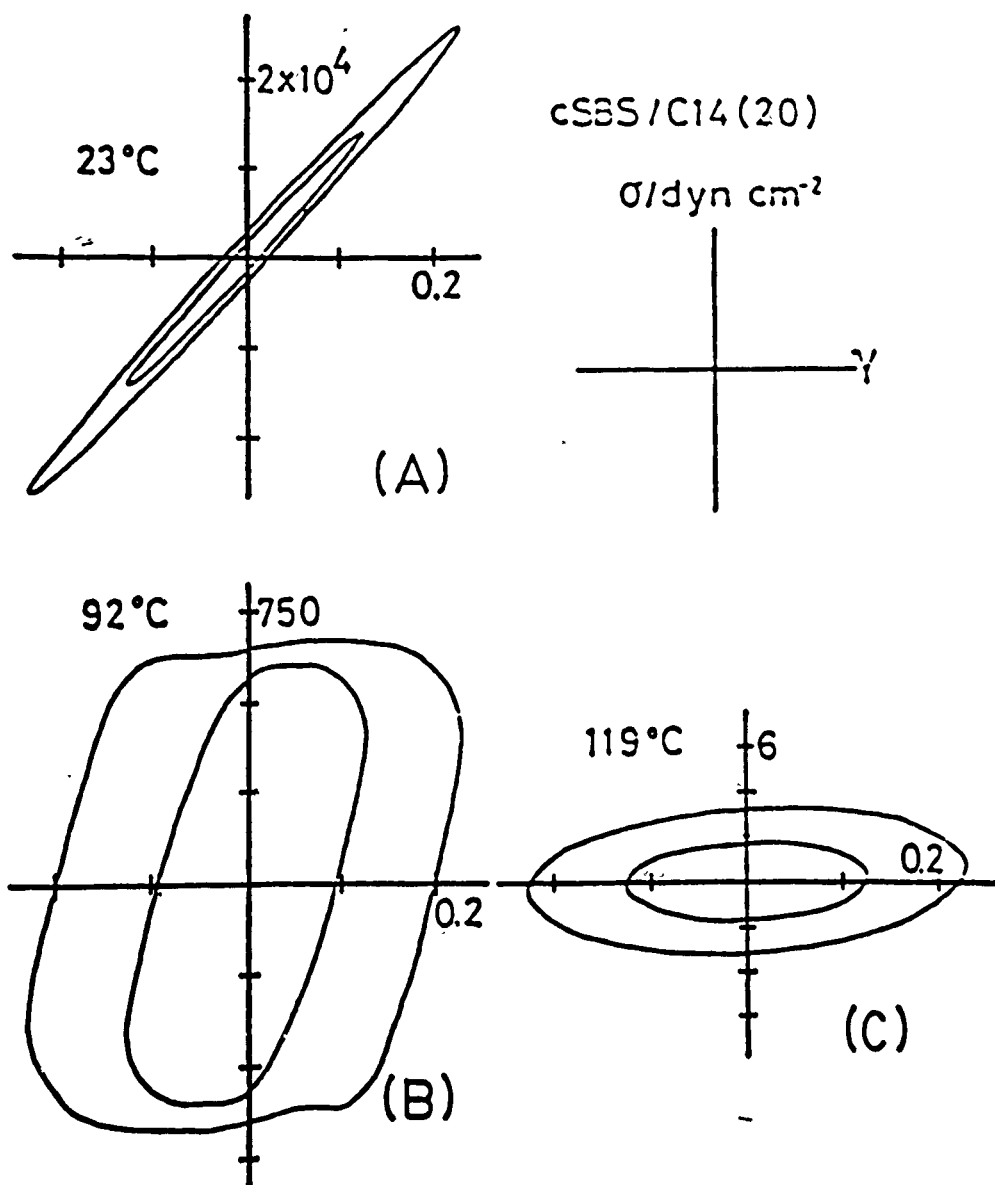


Figure 18. Example of Lissajou figure at: (a) linear viscoelastic; (b) plastic; (c) viscous region for polymeric material.⁴⁸

$$G^* = G' + iG'' \quad (11)$$

The storage and loss modulus can be calculated using the following trigonometric identities:

$$G' = G^* \cos \delta \quad (11)$$

$$G'' = G^* \sin \delta \quad (13)$$

A useful parameter which is a measurement of the ratio of energy loss to energy stored is called the loss tangent:

$$\tan \delta = G'' / G' \quad (14)$$

When the storage modulus and the loss modulus are independent of strain, the condition is defined as the linear viscoelastic region. When the storage modulus is larger than the loss modulus, the overall property of the material is more elastic. When the storage modulus is smaller than the loss modulus, the material behaves like a viscous material.

2.4.2 *Viscoelasticity of Colloidal Systems*

There are many papers⁴⁸⁻⁵² on the viscoelastic properties of polymer systems, but work on the viscoelasticity of colloidal systems⁵³⁻⁵⁹ is not as extensive as that on the polymer system.

The viscoelastic properties of dispersions of microcrystalline boehmite (AlOOH) particles, covering a range of high concentrations (> 35 volume %) and containing different electrolytes, have been studied by Ramsay et al.⁵³ For stable dispersions, sols in the lower range of concentration (13.5 volume %) have viscoelastic properties with predominantly viscous fluid behavior. When the particle concentration increases

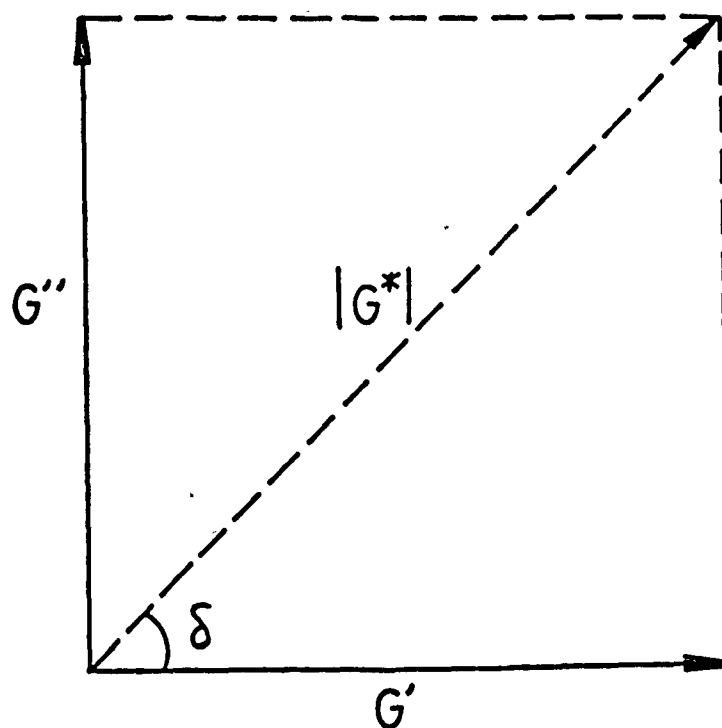


Figure 19. Vectorial resolution of components of complex modulus in sinusoidal shear deformation.

from 14.5 to 24.2 volume %, the response at low strains was almost entirely elastic ($G' \gg G''$) until a particular value of strain was exceeded. The value of $G'_{\gamma \rightarrow 0}$ increases with particle concentration, and the linear viscoelastic region, γ_c , is insensitive to the particle concentration.

The behavior of the storage moduli, $G'_{\gamma \rightarrow 0}$, combined with the particle concentration, showed a power-law relationship, but there was no explanation as to why. When destabilized by the addition of certain counter ions, this elasticity was lost and a plastic property developed. Eventually ($[\text{anion}] > 10^{-1} \text{ mole dm}^{-3}$) sedimentation occurred due to coagulation of the sol particles. At fixed particle concentration, $G'_{\gamma \rightarrow 0}$ is higher for the system with higher ionic concentration. The value of r_c doesn't change with particle concentration.

The study on the viscoelastic properties of clay suspensions⁵⁴ showed similar rheological behavior, such that the addition of electrolyte resulted in an increase in $G'_{\gamma \rightarrow 0}$ by a factor of ~ 3 at $0.01 \text{ mole dm}^{-3}$, but a decrease in the value of the critical strain, r_c , from $\sim 7 \times 10^{-2}$ to $\sim 1 \times 10^{-2}$.

Sontag and Russel⁵⁵ reported the dependence of the storage modulus on the volume fraction of polystyrene lattices, which ranged from 0.03 to 0.25. The linear viscoelastic region was observed up to strains as large as 5%. Sontag and Russel found that the storage modulus in the linear viscoelastic region, G' , scales like $G' \sim \phi^n$, with $n=2.5$ for freshly flocculated samples and $n=4.4$ for aged samples. For a particle volume fraction of 0.07, the G' value for aged samples is higher than that for fresh samples. Their explanation is that aging should produce stronger samples, due either to chain ends becoming connected to the network, or to the strengthening of contacts between particles. The power-law behavior between G' and ϕ was not explained.

The scaling behavior of the rheological property of colloidal particle systems was studied by Buscall et al.⁵⁸ In their study, the instantaneous shear modulus G and compressive strength P_j of aggregate networks formed with a mean diameter of 26 nm have been measured as a function of particle concentration. Above the critical

volume fraction ϕ_g of 0.05, particles form a network and G scales like $G \sim \phi^n$, with $n = 4 \pm 0.5$. This value for the exponent is in good agreement with the results by Ball and Brown⁵⁹ on the assumption that the clusters forming the network are fractal objects.

In an attempt to explain the power-law behavior of the storage modulus, G' , with colloidal particle concentrations, Shih et al.⁶⁰ recently developed a scaling theory for the elastic constant as well as the yield strain of colloidal gels. In their theory, the structure of the colloidal gel network is considered to be a collection of flocs, which are fractal objects and are closely packed throughout the sample. Depending on the relative value of the elastic constant of the inter-floc links compared to that of the floc itself, two regimes are found. In the strong-link (inter-floc) regime, the elastic modulus of the gels increases but yield strain decreases with increasing particle concentration. However, in the weak-link regime both the elastic constant and the yield strain increase with increasing particle concentration.

3. EXPERIMENTAL PROCEDURES

3.1 Material

The alumina particle/water system was chosen for this study because it is an important ceramic material and its suspension characteristics have been extensively studied by many researchers.^{3,61-63}

Powders used in this study were of two types: micrometer-size α -alumina and nanometer-size boehmite. The α -alumina (AKP-30 and 50) was supplied by Sumitomo Chemical Company in Osaka, Japan, and boehmite (γ -AlOOH, Catapal-D) was supplied by Vista Chemical Company in Houston, Texas. Particle size distribution of α -alumina was measured by sedigraph (Micrometrics, Norcross, GA 30093). Median diameters of AKP-30 and 50 are 0.4 μm and 0.2 μm , respectively (Figures 20 and 21).

As a nanometer-size particle system, boehmite (AlOOH) was chosen. The boehmite used was Catapal D. Its chemical composition is $\text{Al}_2\text{O}_3 \cdot 1.25 \text{H}_2\text{O}$, which has a slightly higher water content than stoichiometric boehmite ($\text{Al}_2\text{O}_3 \cdot \text{H}_2\text{O}$). These powders are agglomerated plate-like boehmite crystallites. Average size of the agglomerates is 65 μm . They can be dispersed in acidic solution and broken up into single crystallites or smaller aggregates. The size of the crystallites determined by x-ray line broadening by Vista Chemical Company is 40 \AA in the 020 direction and 64 \AA in the 021 direction. Particle size measurement by TEM⁶³ was approximately 50-100 \AA in diameter and 10-20 \AA in thickness.

3.2 Suspension Preparation

Alumina powder suspensions were prepared by electrostatic stabilization. Measurement of electrophoretic mobility (Particle Micro-Electrophoresis Apparatus Mark II, Rank Brothers, Bottisham, Cambridge, England) of alumina powder (Figure 22),⁶⁵ showed it has high zeta potential (80 mV) at $\text{pH} = 3.0$ and an isoelectric point (IEP)

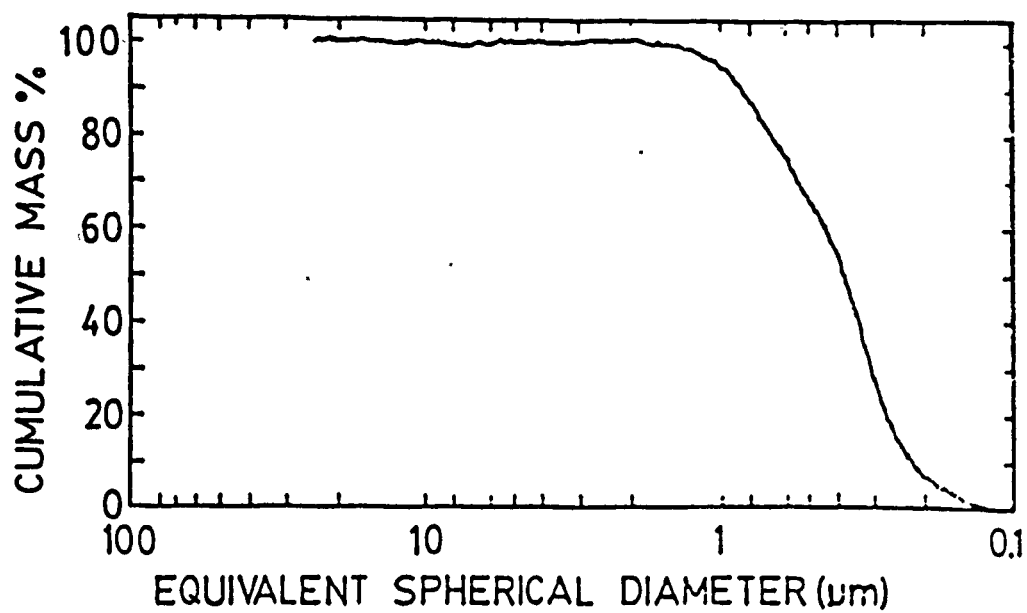


Figure 20. Particle size distribution of AKP-30 α -alumina.

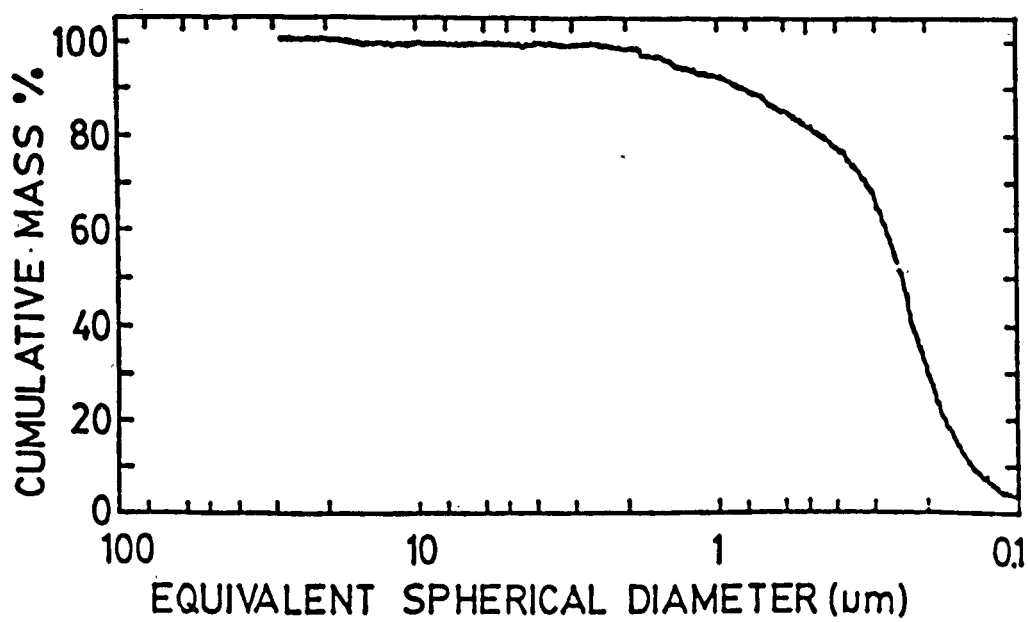


Figure 21. Particle size distribution of AKP-50 α - Al_2O_3 .

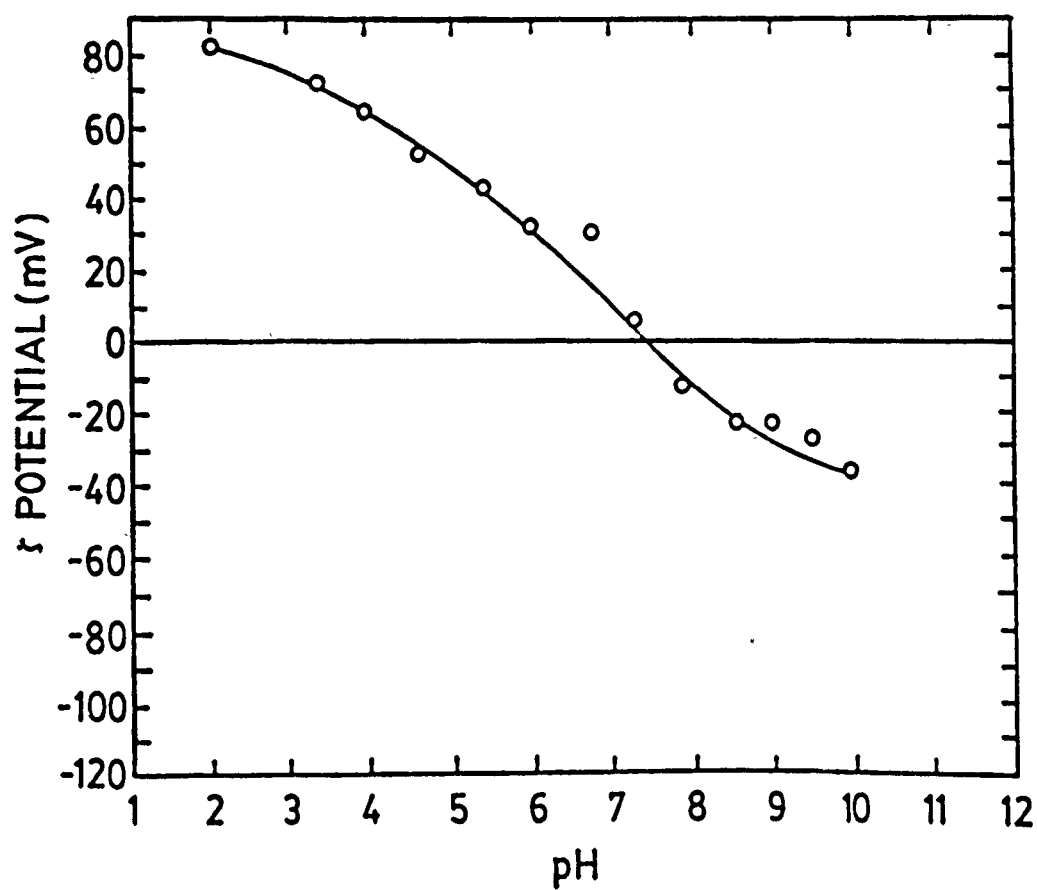


Figure 22. ζ -potential versus pH relationship of Sumitomo Al₂O₃ (AKP-30). When the particles in the suspension have a larger zeta potential, particles have a high repulsive energy. The suspension with higher particle concentration can be made.

at $pH = 7.5$ (0 mV). However, the sedimentation experiments showed that the sedimentation height of the suspensions at $pH = 8.5$ was higher than that of any other pH suspensions. The real IEP seems to be $pH = 8.5$, probably due to the increase of particle concentration from extremely dilute, when measuring electrophoretic mobility to 15 volume % of the particle concentration. Therefore, highly dispersed suspensions at $pH = 3.0$ and flocculated suspensions at $pH = 8.5$ could be obtained. The degree of flocculation increases when approaching $pH = 8.5$.

Boehmite powder suspensions were prepared by electrostatic stabilization. Boehmite powder was mixed with distilled water and 0.03 mole of nitric acid was then added to 1 mole of boehmite. The mixture was shaken in a wrist-action shaker for 48 hours to break up the agglomerates. To eliminate the hard agglomerates, the suspensions were left for 48 hours, resulting in a sediment in the bottom of the suspension. The top portion of the suspensions were decanted and used for the experiments. The pH was then adjusted to the desired value by adding 1 M NaOH solution. A well-dispersed suspension of 5 volume % was obtained at $pH = 3.5$, and a highly flocculated state at $pH = 7.5$. The degree of flocculation was increased by adding NaOH solution when $pH = 7.5$ was approached.

For the pressure filtration experiment on the alumina powder suspension, the particle concentration of the starting suspension was 25 volume % at $pH = 3.0$. For the flocculated system, the particle concentration of the starting suspension was 15 volume % at $pH = 7.0$, 7.5, and 8.5. When the particle concentration is lower than 15 volume % in flocculated suspension, particles tend to settle down and leave a clean supernatant on the top of the suspension. In order to prevent sedimentation during filtration, 15 volume % of suspension was chosen.

For pressure filtration of the boehmite suspension, the starting particle concentration was 5 volume %. In order to illustrate the rheological behavior of a particle/water mixture, various mixtures of boehmite powder suspensions from 1 to 10 volume % were prepared. Powder concentrations of alumina in suspensions ranged from 20 to 35 volume %.

3.3 Pressure Filtration

Figure 23 shows the schematic diagram of the pressure filtration cylinder. Since this is made of translucent Lexan (high impact-resistant polycarbonate made by General Electric Co.), it was possible to perform *in-situ* measurements of the suspension height for flocculated suspensions or for the consolidated layer for dispersed suspensions (Figure 24).

The Lexan cylinder and bottom cap are held together by a hand-tightened screw and top port for pressurizing with nitrogen gas. The cylinder body is recessed and grooved to accept the filter (Catalogue No. VCWP 04700, pore size 0.1 μm , Millipore Corporation, Bedford, MA 01730), and has a rubber O-ring and perforated plug. A pressure manifold containing two gauges with different ranges was connected to the pressure line.

After a gas-tight plug was put in the top portion of the cylinder, 15 ml of suspension was introduced while the cylinder was in inverted position. The reason for using the plug is to prevent the pressurized gas from dissolving in the aqueous medium and forming the decompression bubbles in the consolidated compact after the pressure is released.⁸³ Filter paper, rubber O-ring, perforated plug, and bottom cap were then put on.

In filtration rate determinations, the cylinder was filled with suspension and a timer was started as soon as the pressure was applied. For the dispersed suspension, consolidated layer thickness was measured in five-hundredths of a centimeter, as observed through the Lexan cylinder using a cathetometer (Gaertner Scientific Corporation, Chicago, IL). But in the case of the flocculated suspension, the interface between suspension and consolidated layer was not clear enough to observe, so the height of the suspension was measured with time.

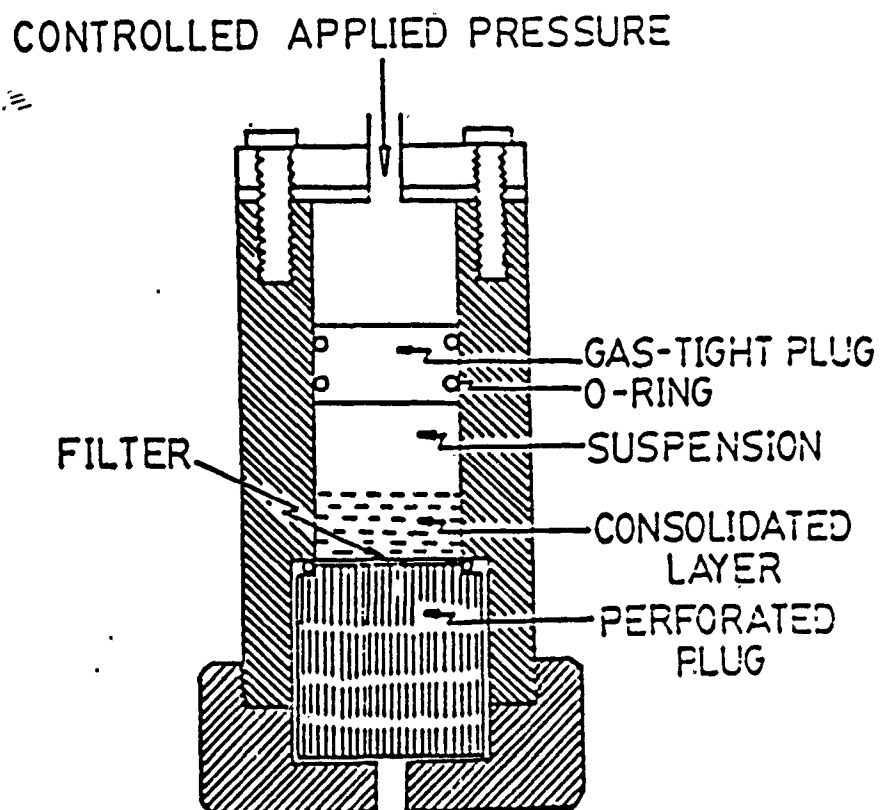


Figure 23. Schematic diagram of pressure filtration cylinder.

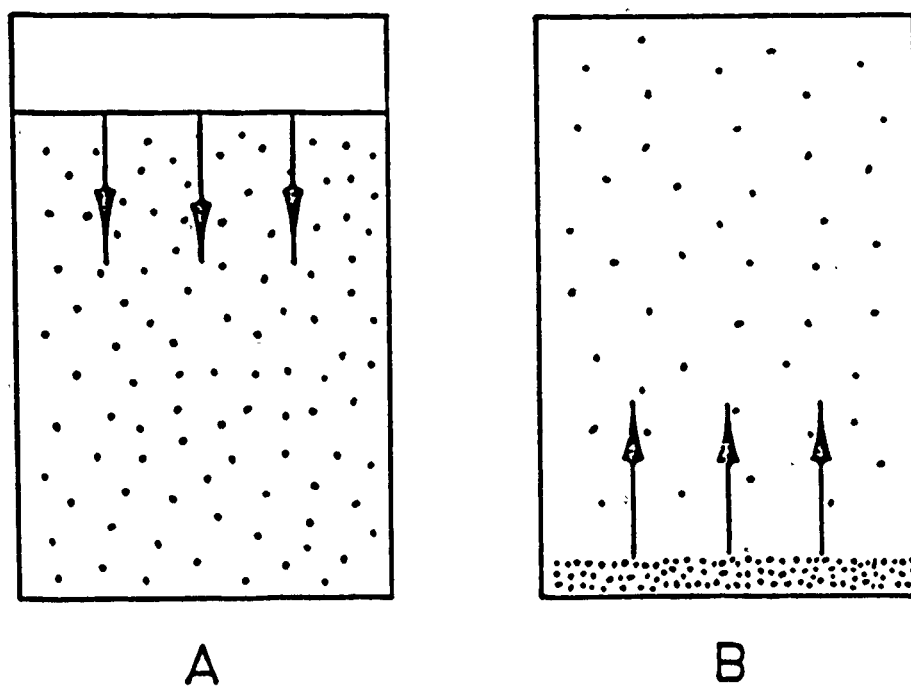


Figure 24. Difference in settling behavior of flocculated (A) and dispersed (B) suspensions.

3.4 Sedimentation and Centrifugation

Our pressure filtration apparatus is capable of studying pressures above 20 psi. Below 20 psi, the friction between the piston and the wall becomes important and the data is not reliable. In order to study the packing behavior in the low pressure range, sedimentation and centrifugation are used. Sedimentation and pressure filtration are similar in that both involve filtration and compaction processes. Therefore, sedimentation and centrifugation are good approximations to low-pressure filtration.

The centrifugation was done on the IEC Model CL Centrifuge (DAMON/IEC Division, Needham Heights, MA 02194). The corresponding gravitational force for each setting has been determined previously. The smallest force corresponds to 38.5 G and the highest setting to 1955 G. Although it was desirable to use a high enough solid loading to form a measurable volume of sediment and to reduce the error in measuring the sediment volume, it was necessary to use minimum solid loading in the suspension to minimize the gradient in the gravitational force within the sample. Suspensions of 3 volume % particles were prepared at various pI's.

3.5 Freeze Drying

Measuring the porosity of the powder compacts at different times during pressure filtration provides only a macroscopic view of porosity changes during compaction stages. In order to obtain detailed information on the decay of voids in the powder compact, it was necessary to simulate the compaction stages at different times of pressure filtration by preparing freeze-dried flocculated suspensions at different powder concentrations from 5 to 45 volume %. After this was done, SEM observation was conducted. The freeze-dried samples were prepared as follows: first, an alumina suspension was prepared at pI = 3.0 with ultrasonication to break up the particle agglomerates; second, the pI was adjusted to 8.5 to obtain flocculated states; and

third, a glass slide was dipped into the suspension and transferred to a liquid nitrogen bath. Then the ice in the sample was removed by sublimation in a vacuum jar.

3.6 Dynamic Oscillatory Strain Sweep

The test station of the dynamic oscillatory rheometer (Rheometrics Fluid Spectrometer, Model 8400, Rheometrics, Inc., Piscataway, NJ 08854) consists of a transducer, a sample holder and a motor (12, 16, and 15, respectively, in Figure 25). The test fixture used was a parallel plate (50 mm in diameter). The sample sits between these two parallel plates. Gap settings for parallel plate measurements were between 1 and 1.5 mm. The bottom plate is connected to the motor which applies strain in the oscillatory mode to the sample. The top plate is connected to the transducer, which measures the torque response from the sample. To minimize the evaporation of water from the sample during measurement, the fiberglass pad in the top cover was soaked with water.

In a dynamic oscillatory strain sweep mode the motor applies strain to the sample in an oscillatory manner at a fixed shear frequency, and the amount of strain can be increased stepwise during the measurement.

With this dynamic oscillatory test method, information was obtained on the modulus of the material, the torque value, and the sine wave of the torque response as a function of strain. By studying these data, an understanding of the changes to the internal structure of the sample during the application of strain can be obtained.

The Lissajou pattern, which is a combination of the sine waves of applied strain and the torque response, can then be constructed. This pattern clarifies the stress-strain relationship and the amount of energy dissipated during deformation.

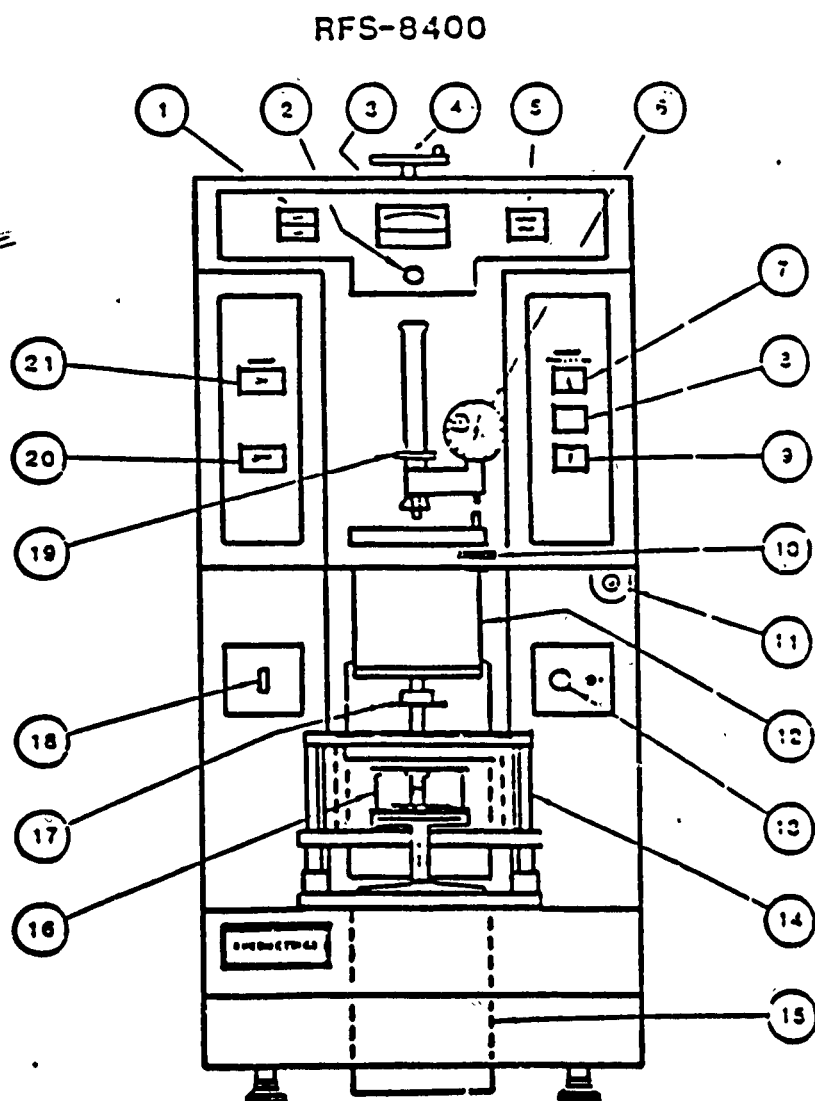


Figure 25. Schematic diagram at dynamic oscillatory fluid spectrometer.

3.7 Stress Relaxation

Stress relaxation is a rather neglected technique which can give much useful information about viscoelastic materials. In this type of experiment, material is subjected to a rapidly applied small strain, which is held constant for the remainder of the experiment, and the time-dependent decrease in the stress required to maintain a sample at constant deformation is monitored as a function of time (Figure 26).

If the material is a solid-like material with strong internal structure, it will maintain the stress for a long time; that is, it will have a long relaxation time. If the material is liquid-like, it will dissipate the stress as heat very quickly, because it has no internal structure with which to store the stress.

3.8 Structure by Scanning Electron Microscopy

In order to relate the rheological behavior to the microstructure formed by particles in the aqueous medium, the freeze-drying technique was used. SEM observation was then conducted.

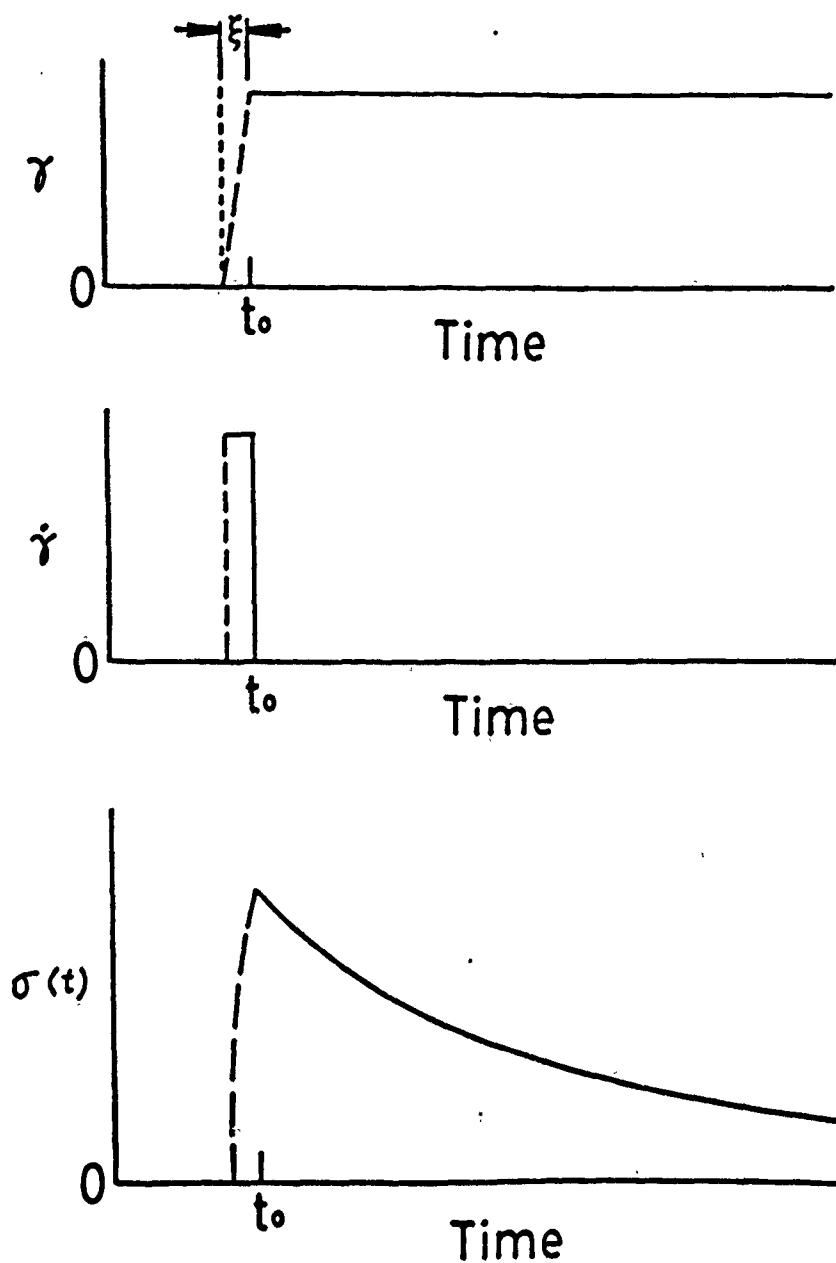


Figure 26. Time profile of a simple shear stress relaxation experiment following sudden strain. Shear strain is imposed within a brief period of time, ξ , by a constant rate of strain, $\dot{\gamma} = \frac{\gamma}{\xi}$.

4. RESULTS AND DISCUSSION

4.1 Effects of Filtration Pressure

This section is divided into three subsections. The first subsection discusses the effects of filtration pressures up to 3.447 MPa (= 500 psi) on dispersed alumina suspensions (AKP-30).

The second discusses the effect of pressure on flocculated suspensions of alumina (pH = 7.0, 7.5, and 8.5).

The third subsection deals with the effect of pressure on packing density at different particle interaction energy states of nanometer-sized boehmite and micrometer-sized alumina (AKP-30) systems.

Effect of Pressure on Dispersed Alumina Suspensions

First, effects on filtration rate and packing density are discussed. Figure 27 shows the result of filtration kinetics measurements. The filtration rate, which is the slope of the square of the consolidated layer thickness versus filtration time, increases with an increase of the applied pressure. This result is expected, based on Aksay and Schilling's derivation²⁴ of the filtration equation,

$$\frac{\xi_c^2}{t} = \frac{2P}{\eta n a_c} \quad (15)$$

where

ξ_c = thickness of the consolidated layer

t = filtration time

P = pressure drop

η = viscosity of the liquid medium

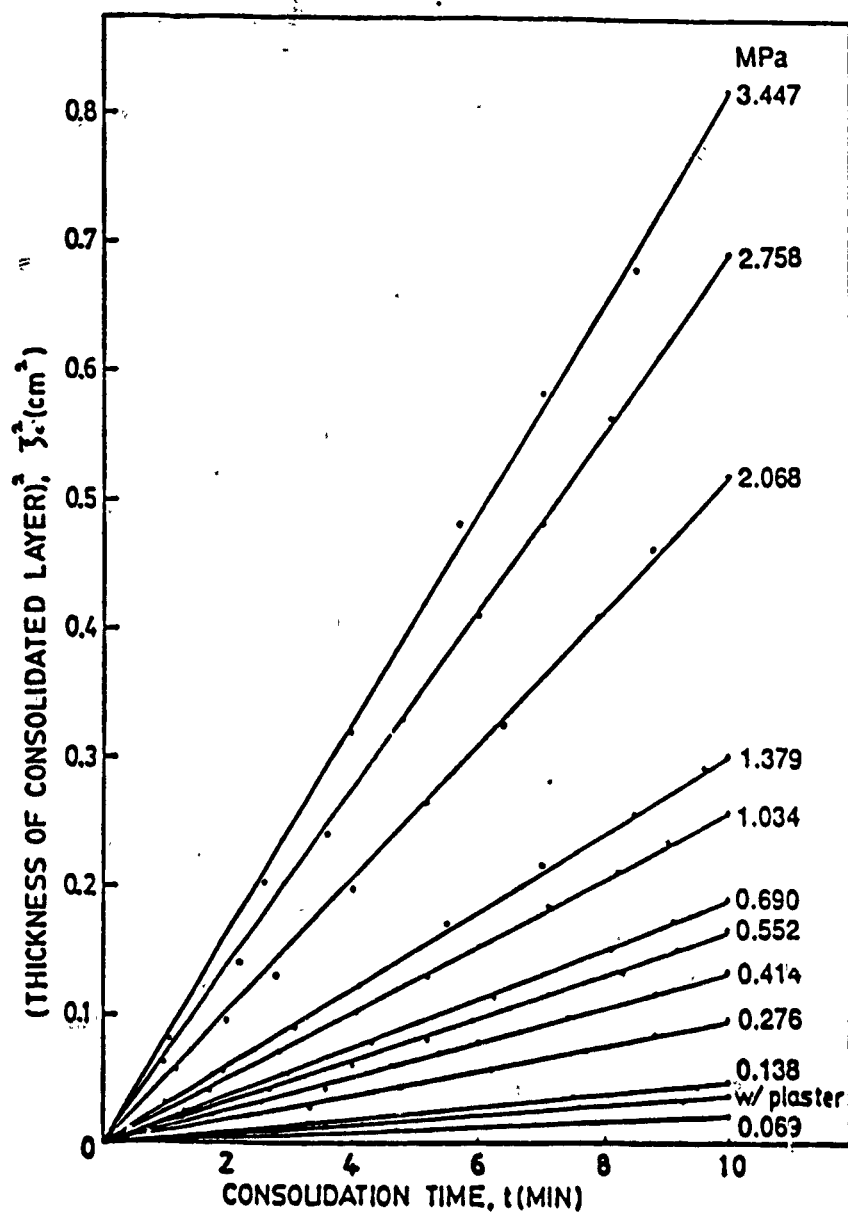


Figure 27. Consolidation time versus thickness of consolidated layer at different pressure levels. The greater the slope, the faster the consolidation rate.

α_c = specific porous medium resistance of the consolidated layer

n = system parameter, $n = 1 - X_p - \epsilon_c / X_p$

X_p = volume concentration of particles in the suspension

ϵ_c = porosity of the consolidated layer

Figure 28 shows the effect of pressure on the filtration time. Up to 6.895×10^{-1} MPa (= 100 psi), the filtration rate increases by a factor of 6 compared to using a plaster mold alone. Adcock and McDowall²⁸ also observed a 4.5 times increase in the filtration rate by applying pressure of 60 psi compared to a plaster mold alone. Further increases in pressure above 6.895×10^{-1} MPa do not affect the filtration rate significantly. The reason can be explained as follows. By manipulating the filtration equation (Equation 15), one can obtain the relationship between filtration time, applied pressure and specific resistance of the consolidated layer:

$$t = \frac{\eta n \alpha_c \xi_c^2}{P} \quad (16)$$

The viscosity of a liquid medium (distilled water) is the same for all the suspensions. Since the concentration of powders in the starting suspensions and the final densities of the consolidated layers (Table I) are the same, the system parameter, n , becomes constant. Lange⁵ also observed that the packing density of the consolidated layer from the dispersed slurry is independent of applied filtration pressure. The simplified form for a fixed consolidated layer thickness is:

$$t = \frac{\alpha_c}{P} \text{ (constant) at fixed } \xi_c^2. \quad (17)$$

Since the specific resistance of the consolidated layer, α_c , is constant (which will be explained in Figure 29), Equation (17) becomes:

$$t = (1/P) \text{ (constant) at fixed } \xi_c^2. \quad (18)$$

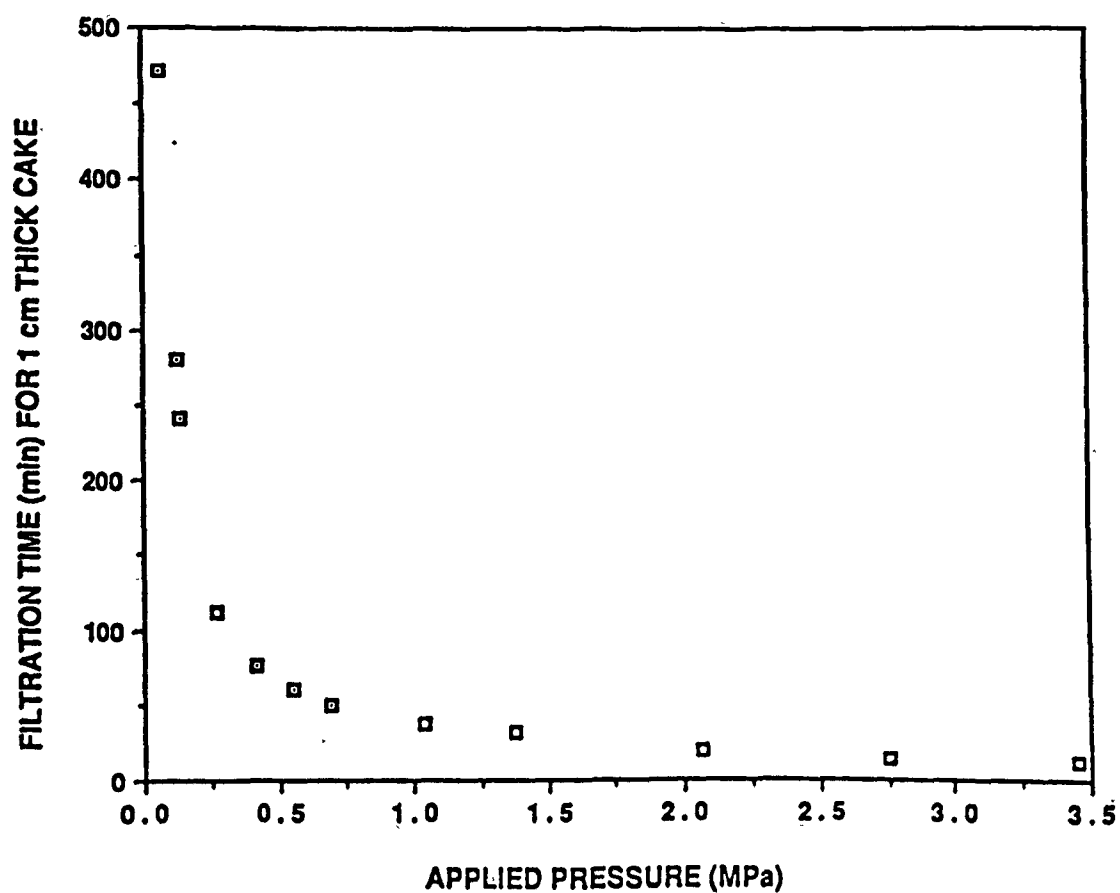


Figure 28. Effect of pressure on filtration time. Filtration rate increases about 6 times at 6.895×10^{-1} MPa than using the plaster mold alone (suction pressure of plaster mold is about 1.24×10^{-1} MPa).

**TABLE I. Filtration Pressure versus Packing Density of Consolidated Layer
from the Suspensions of pH = 3.0**

Pressure (MPa)	1.379×10^{-1}	6.895×10^{-1}	1.379	3.447
Density (%)	64.54	64.76	65.00	64.87

This equation clearly shows why the filtration time to obtain a certain thickness of consolidated layer does not decrease much above 6.895×10^{-1} MPa. One can conclude that there is no one-to-one relationship between applied filtration pressure and filtration rate.

Second, the effect on pore morphology is discussed. Figure 29 shows the square of the thickness of the consolidated layer at 10 min plotted as a function of the applied pressure. The slope is constant. The meaning of constant slope can be understood as follows. One can get a simplified form of Equation 16 by fixing the consolidation time, the viscosity of the liquid medium, and the system parameter as constant (because packing density (Table I), and particle concentrations of the suspensions are the same):

$$\alpha_c = \frac{P}{\xi_c^2} \text{ (constant) at fixed } t. \quad (19)$$

Then, the slope is the specific resistance of the liquid flow through the pores of the consolidated layer. This indicates that the pore morphology of the consolidated layer that is formed from highly dispersed systems is not affected by filtration pressure up to 3.447 MPa. Therefore, one can conclude that there is no structure relaxation of the consolidated layer from highly dispersed alumina suspensions.

Effect of Pressure on Flocculated Alumina Suspensions

Particles in flocculated suspensions form a loosely packed structure that does not collapse by its own weight when the volume fraction of the particles is greater than critical concentration, the so-called percolation threshold. In this section, we discuss the relationship between the structure relaxation behavior and the interparticle energy with the application of pressure.

First, the effects of different degrees of flocculation on filtration rate and packing density at fixed applied pressure are discussed.

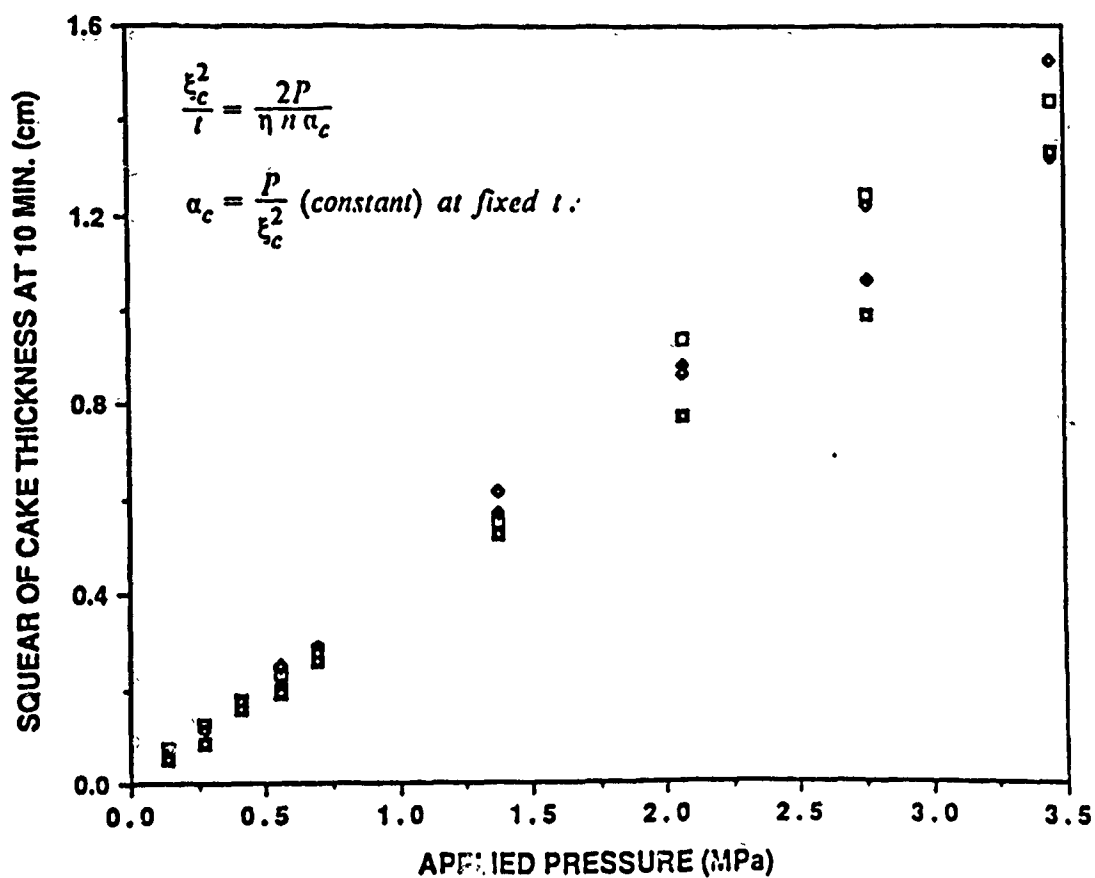


Figure 29. Effect of pressure on the permeability of consolidated powder compacts. The slope indicates an inverse of the specific resistance of liquid flow through the consolidated layer.

Figure 30 shows the suspension height versus filtration time of colloidal solids of alumina powder prepared at different particle interaction energy states under fixed pressure (i.e., at $pH=8.5$, 7.5 , and 7.0 under 1.379×10^{-1} MPa ($=20$ psi)). The magnitude of repulsive energy between particles increases for decreasing pH , that is $E(8.5) < E(7.5) < E(7.0)$; where E is the repulsive energy as a function of the pH . The degree of flocculation is maximum at $pH=8.5$. One can see that as the degree of flocculation increases, the slope of the plot (at a given time) becomes steeper and compaction stops at an earlier stage. These slopes indicate the structure relaxation and filtration rate. The end point of compaction indicates final packing density and is reached when there is a balance between the externally applied pressure and the strength of the colloidal solid structure.

When the repulsive energy between particles in the suspension is reduced by adding excess ions, the attractive energy between particles increases. Then, particles in the suspension lose their freedom of mobility and form permanent particle clusters. The size of the particle cluster is larger when the attractive energy between particles is higher. Larger cluster size contributes to lower resistance for liquid flow through the consolidated layer. Therefore, the filtration rate is highest for the most flocculated system at $pH=8.5$.

However, packing density is lowest at $pH=8.5$. When the attractive energy between particles is increased, such as in the case of $pH=8.5$, sticking probability between particles becomes higher, and particles tend to form stronger ramified network structures.³⁴ As a result, the relaxation behavior of the $pH=8.5$ sample stops at an earlier stage than the $pH=7.0$ sample does. Therefore, packing density is lowest at $pH=8.5$.

Second, the effects of different levels of pressure on filtration rate and packing density at fixed particle interaction energy state are discussed.

Figure 31 shows the suspension height versus filtration time of highly flocculated colloidal solids at fixed particle interaction energy states under different pressure (i.e., at $pH=8.5$ under 1.379×10^{-1} MPa ($=20$ psi), 3.447×10^{-1} MPa ($=50$ psi), 1.379 MPa

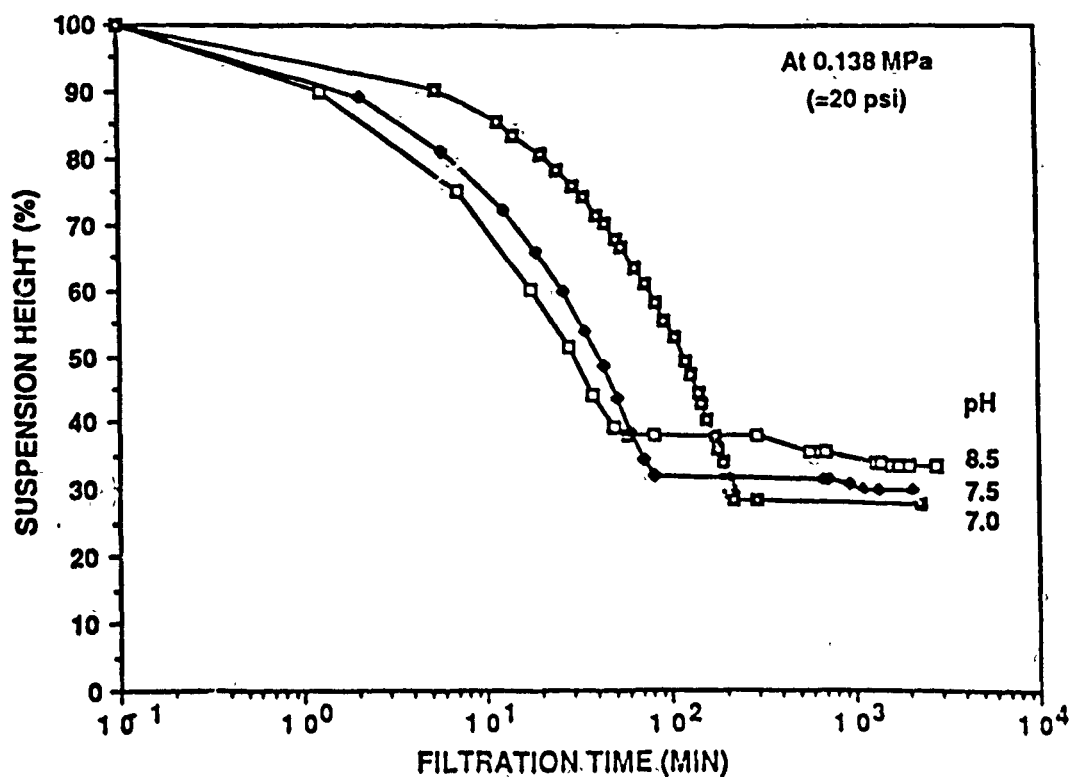


Figure 30. Structure relaxation behavior with time at different binding energies. Sample at higher binding energy state (pH = 8.5) has a stronger particle network structure in the suspension. This forms a more open consolidated layer upon pressure. So the relaxation rate is faster. But, the relaxation stops earlier because it has a stronger structure.

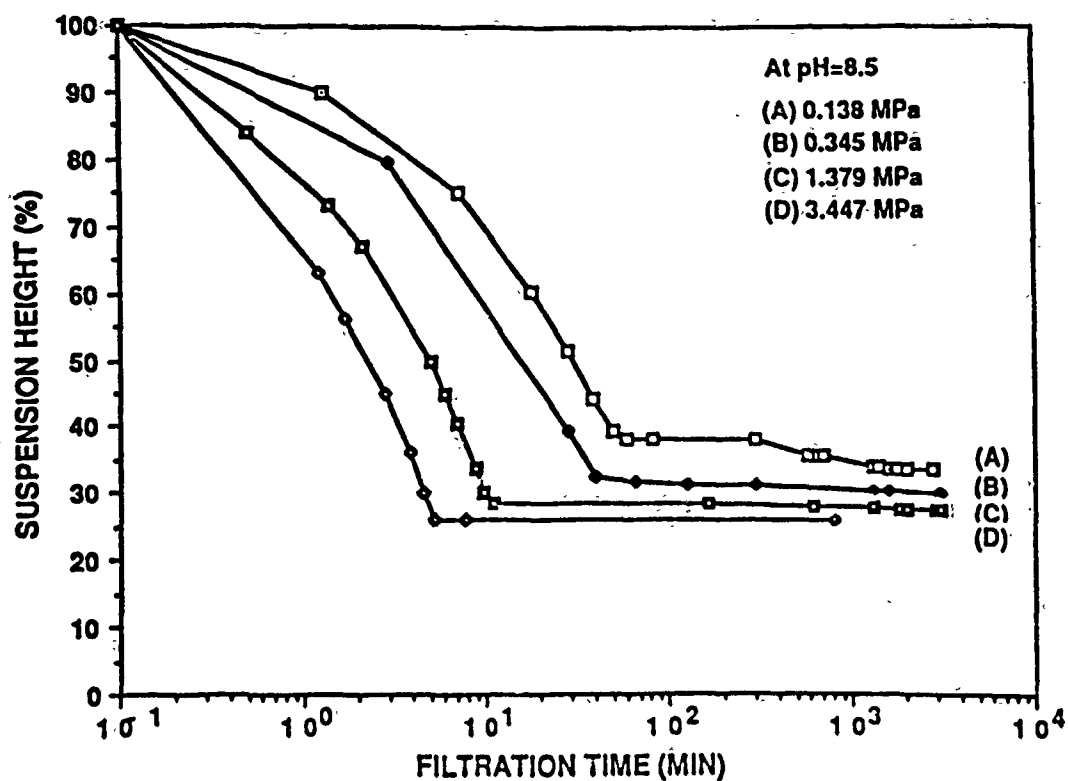


Figure 31. Structure relaxation behavior with time at different pressure levels at fixed binding energy.

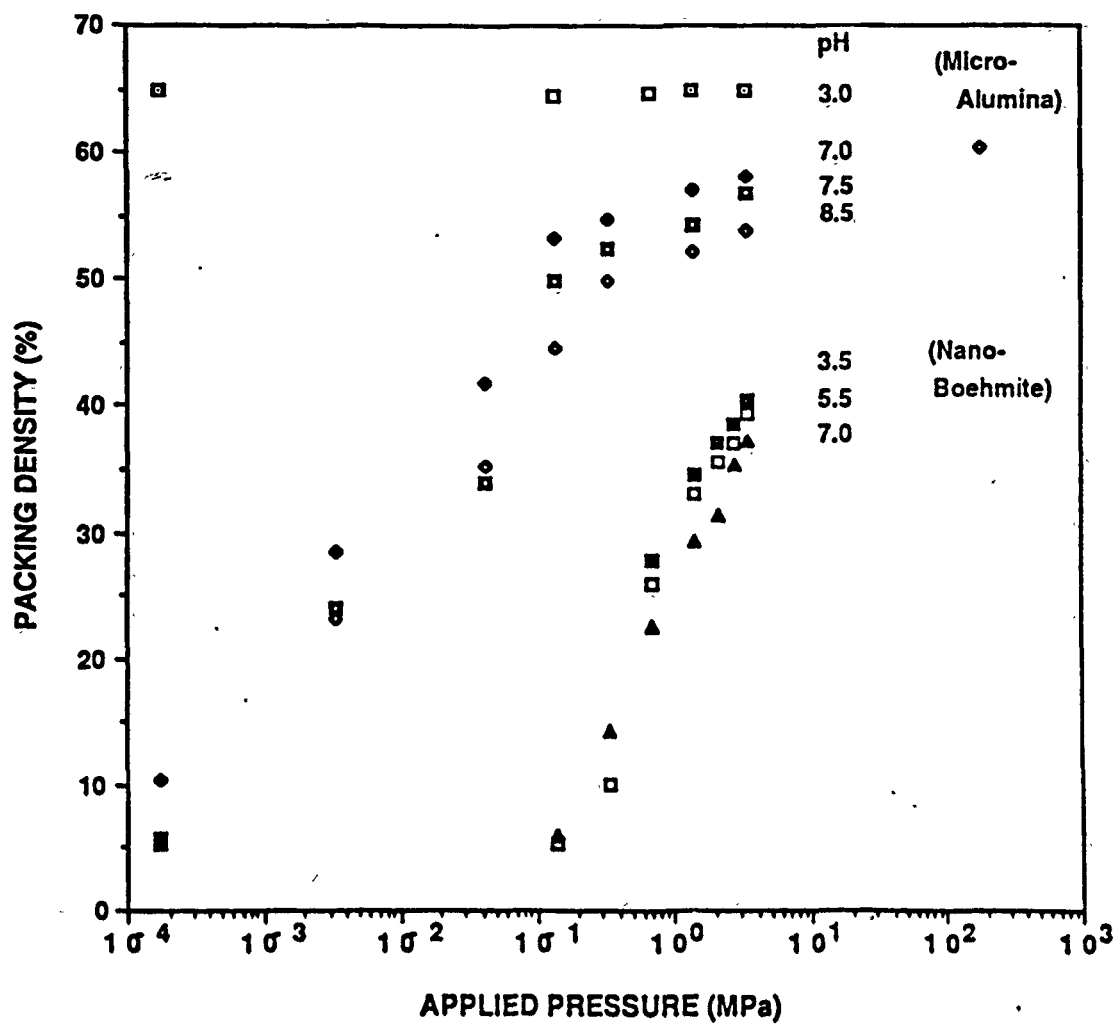


Figure 32. Packing density as a function of applied filtration pressure at different particle interaction energy states for micrometer-sized alumina (AKP-30) and nanometer-sized boehmite systems.

attractive energy between particles. When the barrier is high, particles tend to form loosely packed structures. These loosely packed structures can be easily collapsed when externally applied stress exceeds the strength of the structures. Therefore, colloidal solids prepared at highly attractive energy states show a large amount of compaction and pressure-sensitive packing density. However, when the barrier is at the minimum, particles are free to move around and do not form permanent clusters. As a result, particles form a densely packed structure even with gravity-induced sedimentation. This packing density is pressure-insensitive up to a filtration pressure of 3.447 MPa. Gallagher⁶⁶ also observed that the packing density becomes pressure-insensitive when the barrier for compaction was adjusted to the minimum by adsorption of a "lubricating" polymer onto particle surface.

Second, the nanometer-sized particle system shows pressure-sensitive packing density even at the minimum attractive energy state ($pH=3.5$). Pressure-sensitive packing density indicates that this system has a finite value for the barrier for compaction. This can be understood by analyzing Figure 33. Figure 33 shows that the mixture of boehmite and water has a finite value for the storage modulus, G' , when the particle concentration is 7 vol % at $pH=3.5$. This finite value of the elastic modulus results in a finite value for the barrier of compaction, causing the pressure-sensitive packing density. The fact that the suspension of boehmite at 5 volume % at $pH=3.5$ is dispersed sol and the suspensions of boehmite at 7 volume % at 3.5 is flocculated gel, indicates that there is a transition from the dispersed to flocculated state as particle concentration is increased.⁶⁷ A similar transition from the dispersed state to the flocculated state as concentration is increased is also seen in silica suspensions.⁶⁸ The transition from a dispersed to a flocculated state by increasing particle concentration is due to the increase in counter-ion concentration as the particle concentration is increased. This effect is more pronounced for nanometer-sized particles. As particle size becomes smaller at fixed volume concentration, the number of counter-ions increases dramatically, resulting in a smaller double layer. Furthermore, the thickness of the double layer is comparable to the particle size and a slight

STRAIN SWEEP, BOEHMITE, 7 V/O, pH=3.5

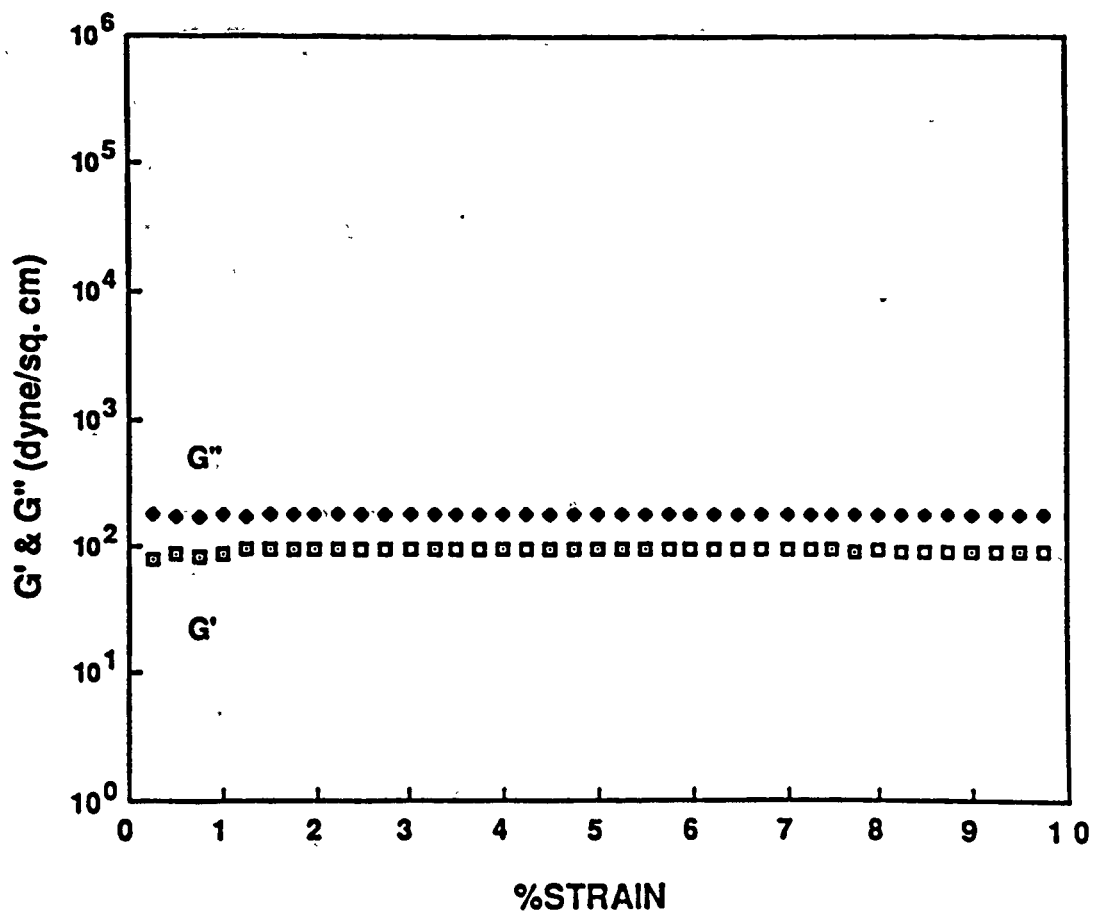
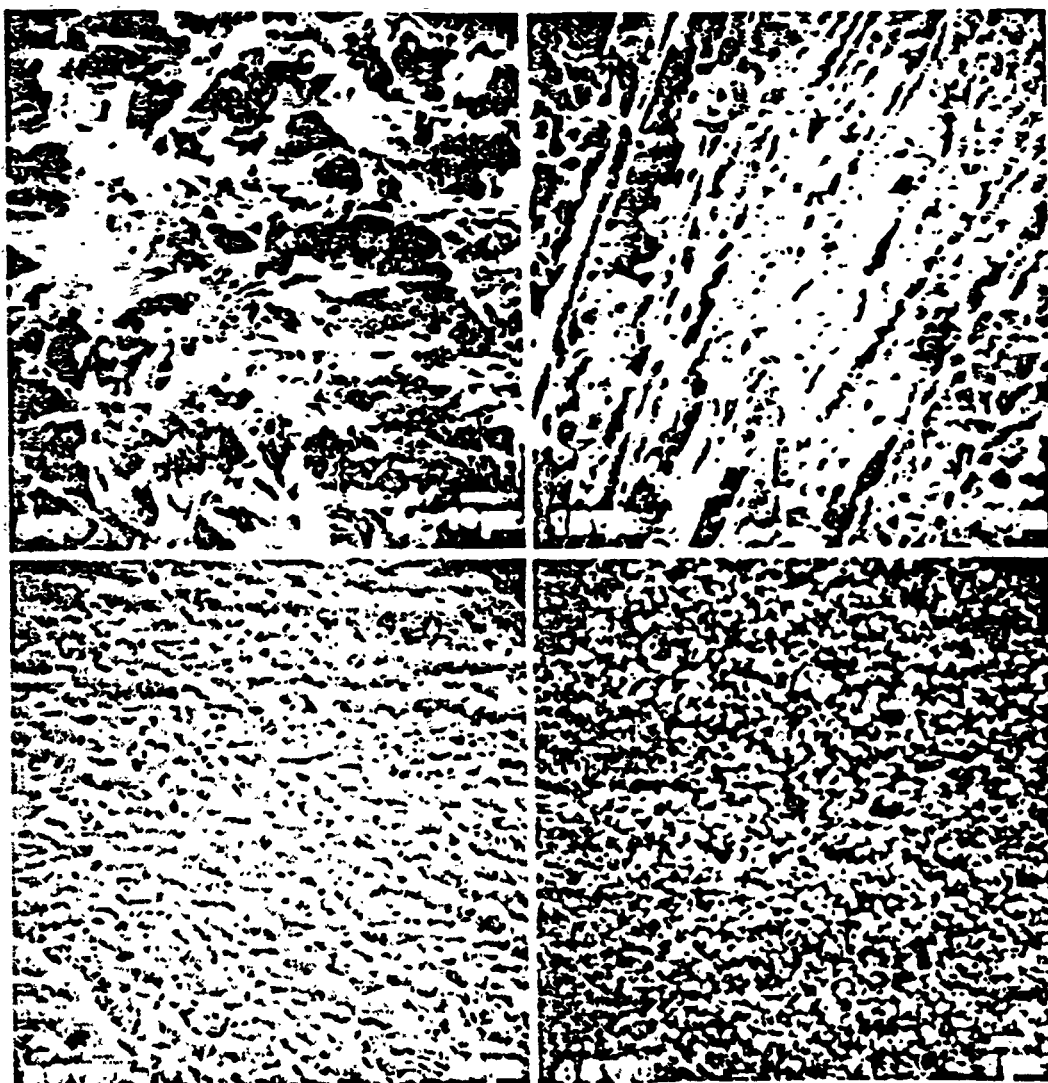


Figure 33. Effect of increasing amplitude of sinusoidally oscillatory strain on the storage modulus (G') and the loss modulus (G'') on the sample with 7 volume % of particle concentration at pH = 3.5.

change in the double layer thickness has a drastic effect on the interaction between particles. Therefore, the effect due to the counter-ion screening is more pronounced for small particles than large ones. In addition, the crowding effect due to the increasing particle concentration also enhances the frequency of collision between clusters, resulting in faster gelation.

Third, the experiments done by sedimentation and centrifugation showed a higher slope (i.e., more compaction) for the low pressure range (up to 1.379×10^{-1} MPa) and lower (i.e., less compaction) for the high pressure range (from 1.379×10^{-1} to 3.447 MPa). This can be explained by considering the hierarchical structure of colloidal solids. Figure 34 shows the SEM photos of the freeze-dried samples at different particle concentrations at pI = 8.5. At 5 volume % of powder concentration, particles form an open network-like structure which has a large amount of porosity, including third- and higher-generation voids (voids between the second-generation particle clusters). These third- and higher-generation voids are eliminated by increased concentration of particles (corresponding to 30 volume %) or by increased pressure level. At 45 volume % packing density (corresponding to 1.379×10^{-1} MPa), most of the third-generation voids are eliminated, and most of the existing voids are first-generation voids (voids between the primary particles, i.e., first-generation particle clusters) and second-generation voids (voids between the first-generation particle clusters). Above 1.379×10^{-1} MPa, second-generation voids are eliminated. Therefore, different slopes indicate the existence of different microstructures containing different generations of voids and different amounts of compaction. This also indicates that colloidal solids with higher-generation void(s) are weaker in strength than those with lower-generation void(s) when the particle size is fixed.

Fourth, the slopes of the micrometer-sized alumina system between 1.71×10^{-4} and 1.379×10^{-1} MPa are similar to those of the nanometer-sized boehmite system between 1.379×10^{-1} and 3.447 MPa. From the previous argument, similar slopes indicate similar microstructures. In fact, SEM photos (Figure 35) of microstructures of alumina (5 volume %) and boehmite (6 volume %) are almost identical. As a



ALUMINA, pH=8.5

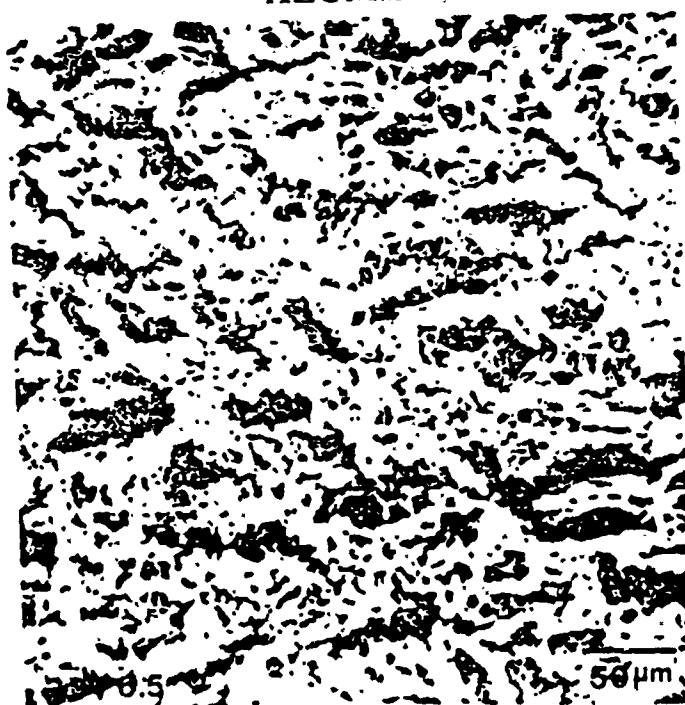
Figure 34. The hierarchy of voids decays with increasing powder concentration at the most flocculated state (pH=8.5) of alumina suspension. At 5 volume %, particles form a loose network structure which has third- and higher generation voids. When the particle concentration increases, the third generation voids are eliminated at 45 volume %.

A



ALUMINA

B



BOEHMITE

Figure 35. SEM micrographs of freeze-dried (a) alumina suspension (5 volume % particle) at pH = 8.5, and (b) boehmite (6 volume % particle) at pH = 6.5.

result, one can say that third- and higher-generation voids are eliminated between 1.71×10^{-4} and 1.379×10^{-1} MPa for the micrometer-sized particle system and between 1.379×10^{-1} and 3.447 MPa for the nanometer-sized particle system.

Fifth, in the pressure range between 1.379×10^{-1} and 3.447 MPa the nanometer-sized particle system shows a higher slope than the micrometer-sized particle system. The higher slope indicates that a larger amount of the voids are eliminated by restructuring. Between 1.379×10^{-1} and 3.447 MPa, third and higher generation voids are eliminated for the nanometer-sized particle system, and the second-generation voids are eliminated for the micrometer-sized particle system. This indicates that elimination of higher-generation voids results in more compaction (i.e., higher slope).

Sixth, starting from the same type of microstructure (Figure 35) with the same type of voids (third- and higher-generation voids), the applied pressure required to start compaction for the nanometer-sized boehmite system is three orders higher in magnitude than that for the micrometer-sized alumina system. That is, 1.379×10^{-1} MPa for the boehmite system, and 1.71×10^{-4} MPa for the alumina system. In order to start compaction, barrier for compaction (i.e., yield stress) must be overcome. The yield stress is strongly related to the storage modulus of the system. Figure 36 show the relationship between the storage modulus and particle concentration for different particle size systems. When one compares the value of the storage modulus between boehmite and alumina (AKP-30) at fixed particle concentration, the nanometer-sized boehmite system is three orders higher in magnitude than the micrometer-sized alumina system. Therefore, starting from the same type of microstructure, boehmite requires higher pressure to start compaction.

4.2 Quantitative Characterization of Rheological Behavior

In order to quantitatively characterize the rheological behavior, two types of tests were conducted: (i) a dynamic strain sweep, which shows the different rheological behaviors such as linear viscoelastic, plastic, viscous deformation region, yield strain, and thixotropic behavior, etc., as a function of applied strain; (ii) a stress relaxation

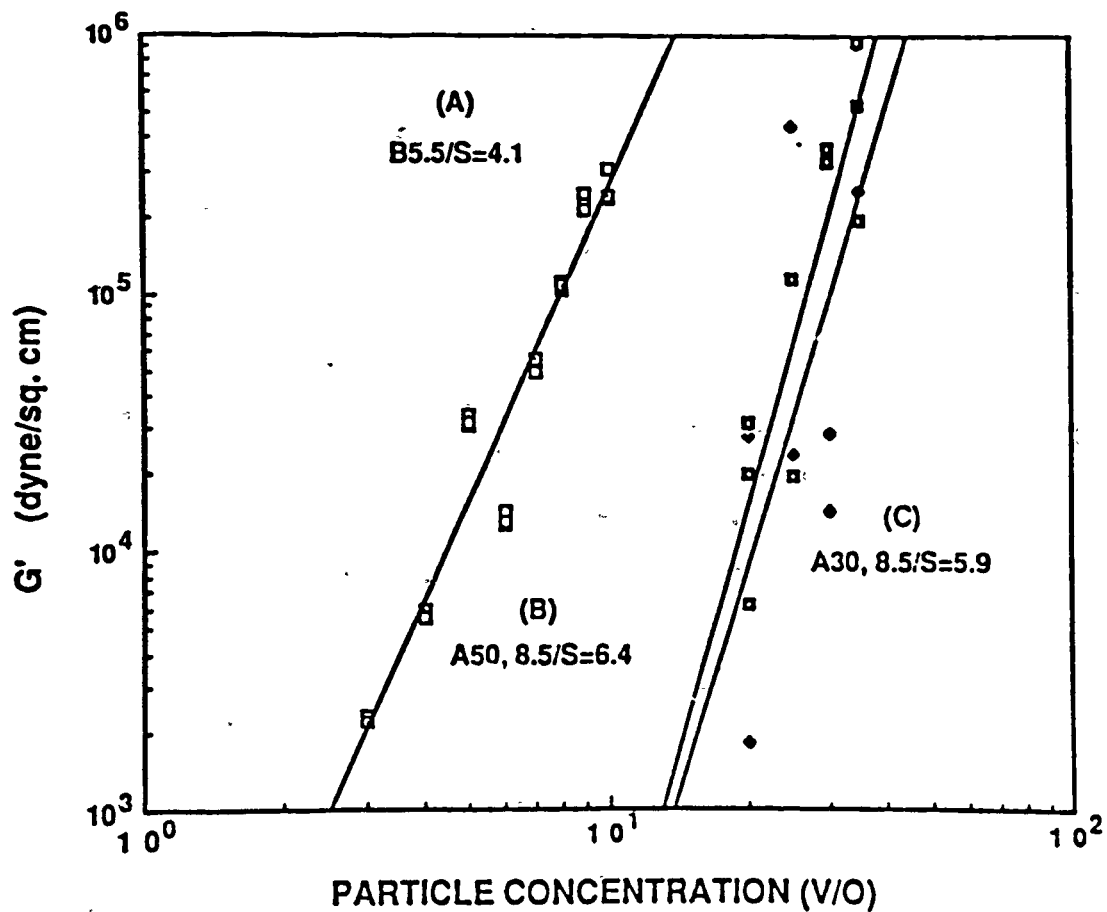


Figure 36. Storage modulus versus particle concentration for (A) boehmite suspension at $pH = 5.5$, slope is 4.1, (B) alumina (AKP-50) suspension at $pH = 8.5$, slope is 6.4 and (C) alumina (AKP-30) suspension at $pH = 8.5$.

experiment, which measures the stress relaxation behavior upon applying a fixed amount of strain instantaneously to the sample. Generally, solid-like materials have an infinite relaxation time, whereas the relaxation of liquid-like materials takes place instantaneously (i.e., relaxation time is zero) and viscoelastic materials have a finite relaxation time. First, the results from the flocculated gel-like sample are given, and then the results from the well-dispersed fluid-like sample will be presented.

Figure 37 shows the behavior of the storage and loss moduli as a function of applied strain amplitude at a fixed shear frequency of 0.7 rad/sec for the mixture of 5 volume % boehmite particles and water at $pH=5.6$. At this level of particle concentration and pH , the appearance of the sample is gel-like.

Figure 38 shows the microstructure of the freeze-dried boehmite sample (3 volume %, $pH=5.6$). The particles are interconnected and form a three-dimensional network structure. This particle network structure may be considered to be an elastic element and the matrix liquid medium as a viscous element.

In Figure 37, the storage and loss moduli are almost constant up to 3.75% strain. At 3.75% strain the loss modulus increases by a small amount but the storage modulus remains almost the same. The magnitude of the loss modulus is only 1.75% of the storage modulus. The constant storage modulus means that a constant amount of energy is stored and recovered during the application and release of oscillatory strain. Also, the constant loss modulus means that a constant amount of energy is dissipated as heat during the test. Therefore, this indicates that there is neither noticeable change in the elastic element (i.e., no disruption in the particle network structure) nor in the viscous element (i.e., liquid medium). There may be only a bond stretching between particles or between clusters. Since the definition of linear viscoelasticity is that the storage and loss moduli are independent of the strain,⁴⁴ this material may be classified as an almost linear viscoelastic material up to 3.75% strain.

When the amount of strain is increased above 3.75%, the storage modulus starts decreasing and the loss modulus increases greatly up to 5.25% strain. This indicates

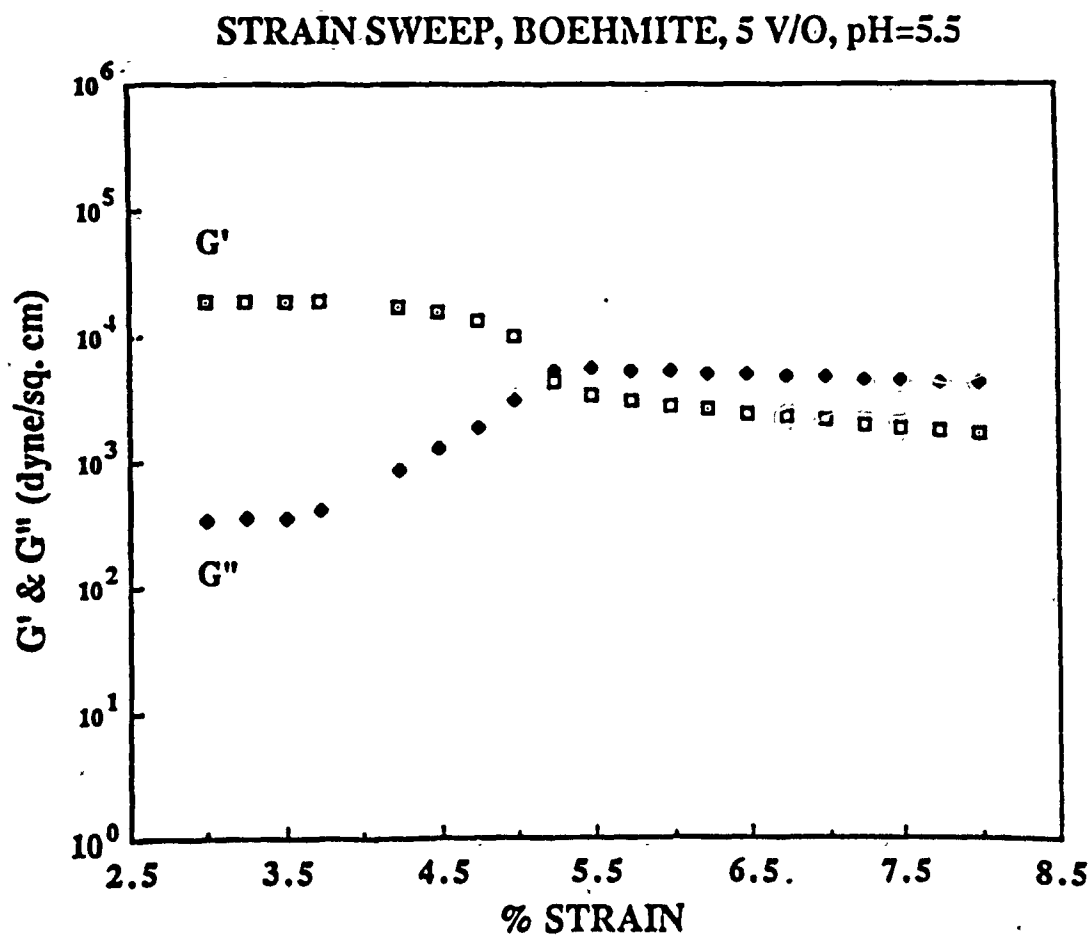


Figure 37. Effect of increasing the amplitude of the sinusoidally oscillatory strain on the storage modulus (G') and the loss modulus (G''). The linear viscoelastic region is up to 3.75% strain. At a strain of 4.25%, yielding occurs. Above 5.25% strain the overall behavior is viscous-like.



Figure 38. Microstructure of freeze-dried boehmite gel (3 volume % particle and pH = 5.5).

that above 3.75% strain the properties of the material change drastically. The decrease of the storage modulus means that a breakdown of the particle network structure occurs.⁵³⁻⁵⁵ This breakdown is caused when the magnitude of the externally applied stress exceeds the strength of the particle network structure and the structure starts to yield and produces smaller structures. At the same time, increasing the loss modulus means that these smaller structures become a dispersed phase in the liquid medium and contribute to increased energy dissipation. The transition of the modulus from strain-independent to strain-dependent corresponds to the onset of plastic flow.

For further increments of strain greater than 5.25%, the value of the loss modulus becomes larger than that of the storage modulus, with the storage modulus decreasing to an almost constant value. This means that the macroscopic character of this material becomes more viscous-like.

A further understanding of viscoelasticity can be obtained by examining the sine waves of applied strain and torque response. When the particles form a continuous network structure throughout the sample, the structure responds to the sinusoidally-applied strain within the linear viscoelastic region by taking the form of a sine wave with a characteristic wave length and amplitude. However, when a large amount of strain is applied to the sample, the continuous network structure starts breaking apart and produces smaller structures. Upon application of sinusoidal strain, these smaller structures show sine waves with different wave lengths and amplitudes due to the different strengths and sizes of the structures. Therefore, when the sine wave of torque response from the sample has a perfect sine wave shape, we know that there is no breakdown of the internal network structures, and the material is in the linear viscoelastic region. When the sine wave of torque response from the sample loses its perfect sine wave shape, we know that there is a breakdown of the internal network structure because the sine wave of torque response from the sample is a superposition of sine waves from variously-sized structures in the sample.

Figure 39 is an example of sine waves of applied strain and torque response at the strain level of 5.25%, at which the loss modulus becomes greater than the storage

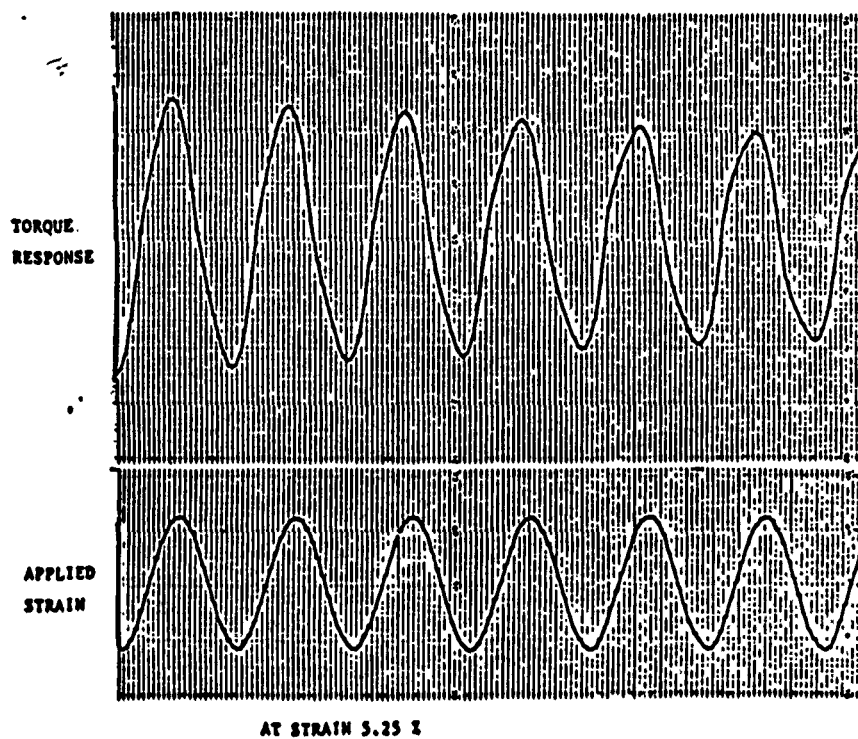


Figure 39. Sine wave of applied strain and torque response at the crossover point of storage and loss modulus. The distortion of the torque response is an indication of particle network structure breakdown. The decreasing magnitude of torque response shows that this material is thixotropic.

modulus. This plot shows a significant amount of distortion of sine wave, due to destruction of the network structure, resulting in a time delay between the application of strain and the torque response. This plot also shows that the decreasing amplitude of the sine wave of torque response with the increasing number of cycles of applied strain (i.e., increasing time at fixed shear frequency) is an indication of thixotropy.

If we combine the sine waves of applied strain and torque response, and construct the Lissajou pattern, we can visualize the direct relationship between applied strain and torque response. Figure 40 shows the Lissajou pattern at a strain level of 3.75%. The torque increment is proportional to the applied strain and the trace of torque and applied strains is a straight line. There is no hysteresis behavior. One can thus say that this material behaves like a linear viscoelastic material⁵⁵ without losing energy during the application of sinusoidal deformation.

Figure 41 shows the Lissajou pattern after the yield point. The Lissajou pattern becomes a highly distorted lozenge shape. The torque is not proportional to the strain and the area of the pattern is large, which shows a large amount of hysteresis behavior. This indicates that the material has lost its characteristic yield point and has become a plastic-like material consuming large amounts of energy during deformation.

Figure 42 shows the shear stress relaxation behavior (shear stress versus time) of the flocculated gel-like boehmite sample. When the fixed amount of strain (0.1%) is applied to the sample instantaneously, the shear stress increases very rapidly to the maximum value of 2×10^2 dyne/cm² and decreases very slowly with time. The internal structure of the sample can withstand the strain when the strain applied to the sample initially, so there is a rapid increment of shear stress. When the applied strain to the sample is maintained, the shear stress decreases very slowly with time, which is probably due to the slow motion of fluid in the sample and/or a gradual breakdown of internal structure. This implies that there is a strong internal structure formed by particles in a gel-like sample, and the slow motion of fluid in the sample and/or a breakdown of structure occurs slowly with time.

LISSAJOU FIGURE AT STRAIN 3.75 %

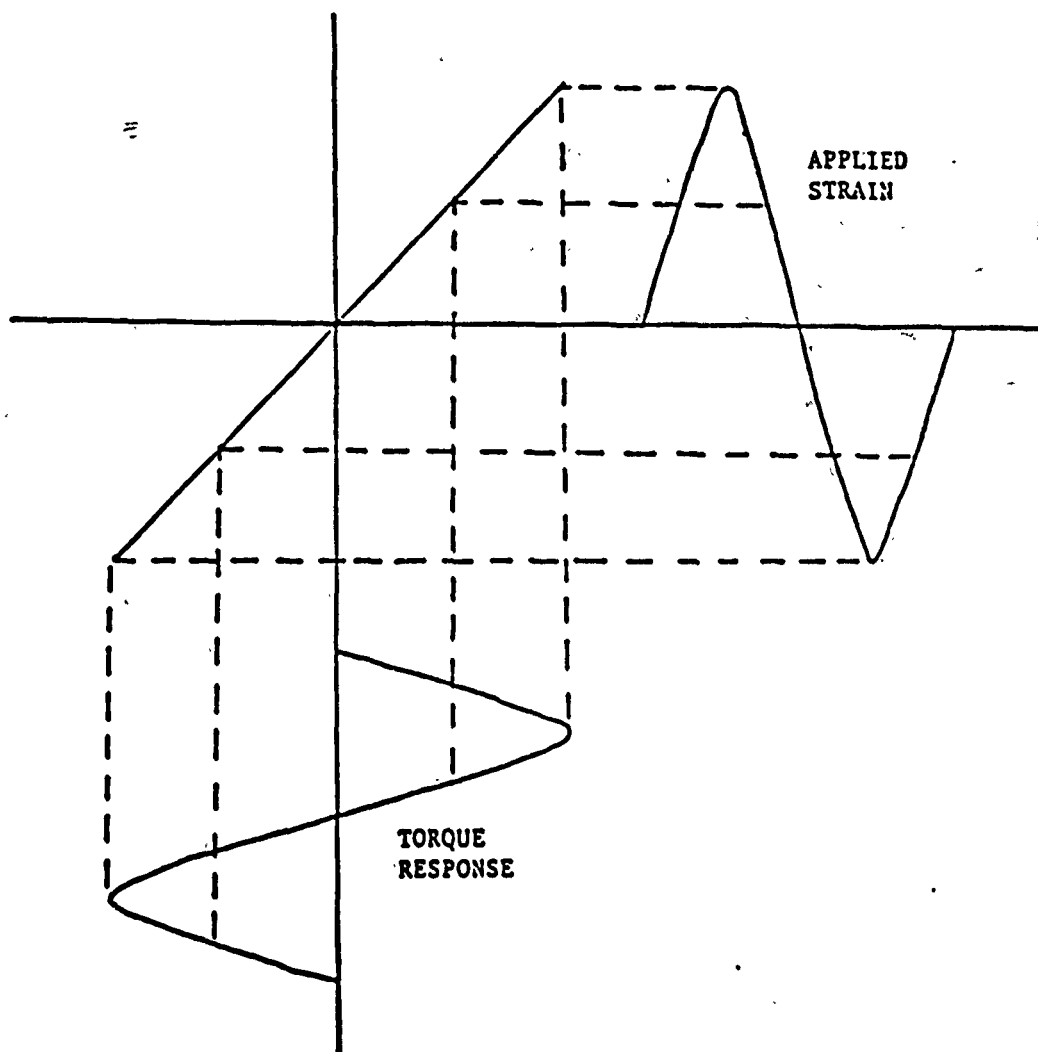


Figure 40. Lissajou figure, a combination of the sine waves for applied strain and torque response, shows that there is a linear relationship between applied strain and torque response. This indicates there is no energy dissipation in the linear viscoelastic region.

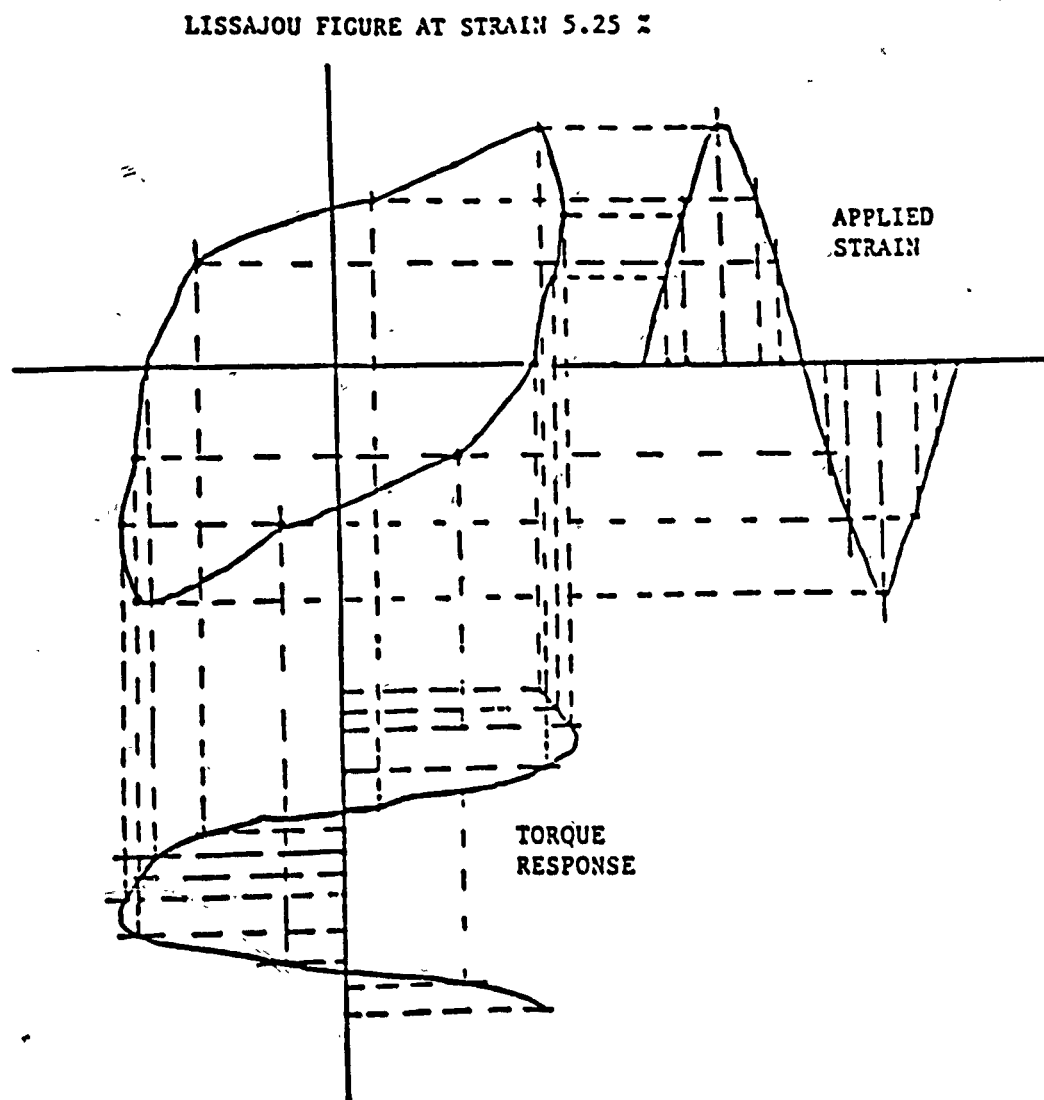


Figure 41. Lissajou figure after yield point shows a large amount of hysteresis. The area is proportional to the amount of energy dissipated during the sinusoidally oscillatory deformation.

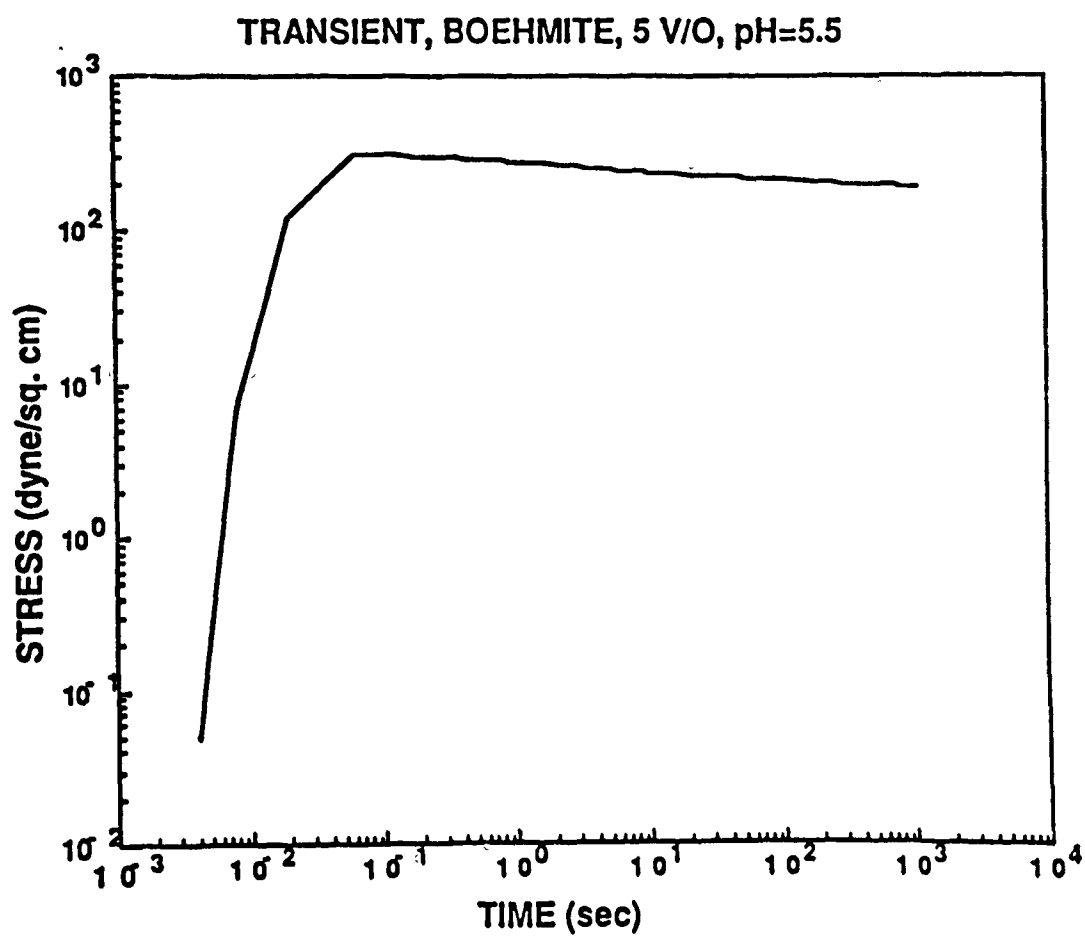


Figure 42. Shear stress versus time after the strain is applied instantaneously for the gel-like sample. The sample holds the stress for a long time due to the elasticity of the internal particle network structure.

Thus far, the results from a highly flocculated gel-like boehmite sample have been studied. Next, the well-dispersed boehmite samples were studied.

When the boehmite particles are dispersed in water, the rheological behavior of the sample is very different from that of the gel-like sample. Figure 43 shows the storage and loss moduli as a function of applied strain at a fixed frequency of 0.7 rad/sec with 5 volume % boehmite particles in water at $pH=3.5$. There is much scattering of the data points. The values of the torque response (Figure 44) are smaller than 10^{-3} gr-cm. Since the transducer's limit of measuring capability is 10^{-2} gr-cm respectively, these data points are not valid. When the strain is applied to the well-dispersed sample by the motor located at the bottom of the sample and the energy is not transmitted to the transducer located at the top of the sample, the value of torque response is too small to measure. Because there is no continuous network structure throughout the sample, the energy cannot be transmitted through the sample and is simply dissipated as heat. This is characteristic rheological behavior of well-dispersed samples.

The stress relaxation behavior (Figure 45) of the well-dispersed sample shows that when the strain is applied to the sample instantaneously, the shear stress increases and reaches a maximum value of 2×10^{-2} dyne/cm² and disappears so rapidly that the transducer could not measure it; that is, stress relaxation time is zero. This is another indication that the sample lacks a continuous internal structure. This can be classified as a viscous material.

4.3 Elastic Constant and Yield Strain of Colloidal Particulate Systems

The comparison of rheological behavior between nanometer-sized boehmite/water and micrometer-sized alumina powder/water mixtures in the highly flocculated state is shown in Figure 46.

First, when the system is highly flocculated, the nanometer-sized boehmite system shows elastic property at a low concentration of particles (≈ 3 volume %) at $pH=5.5$, while the micrometer-sized alumina system shows it at a high concentration of

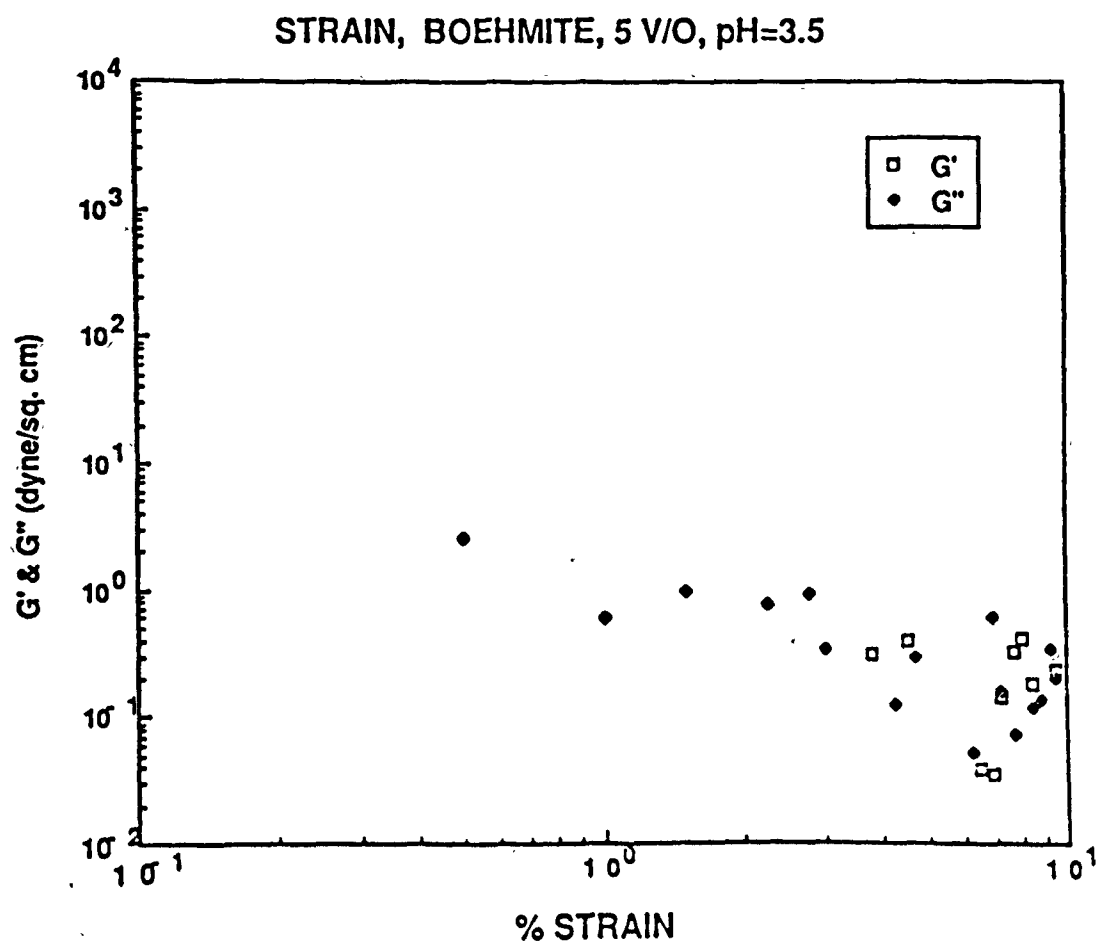


Figure 43. Effect of increasing the amplitude of the sinusoidally oscillatory strain on the storage modulus (G') and the loss modulus (G'') of the sample prepared at pH = 3.5.

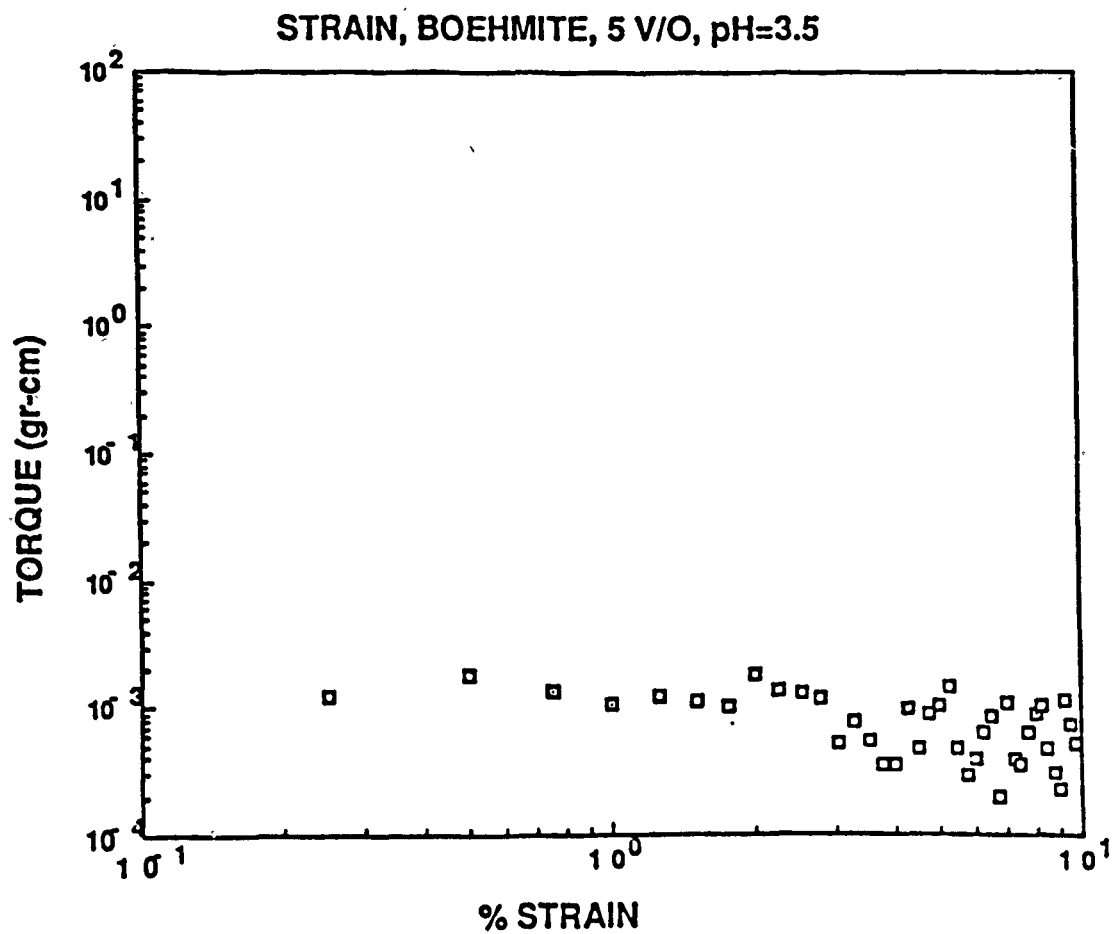


Figure 44. Effect of increasing the amplitude of the sinusoidally oscillatory strain of the torque response of the sample prepared at pH = 3.5.

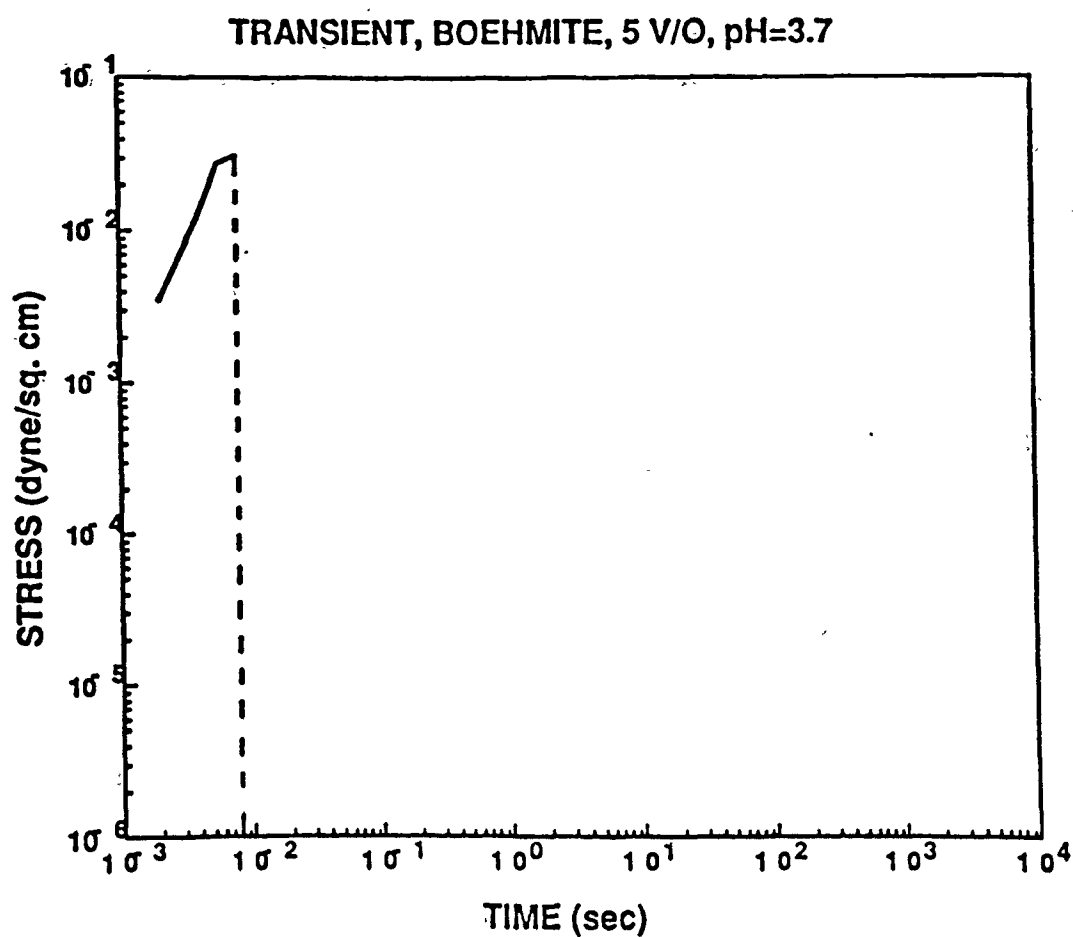
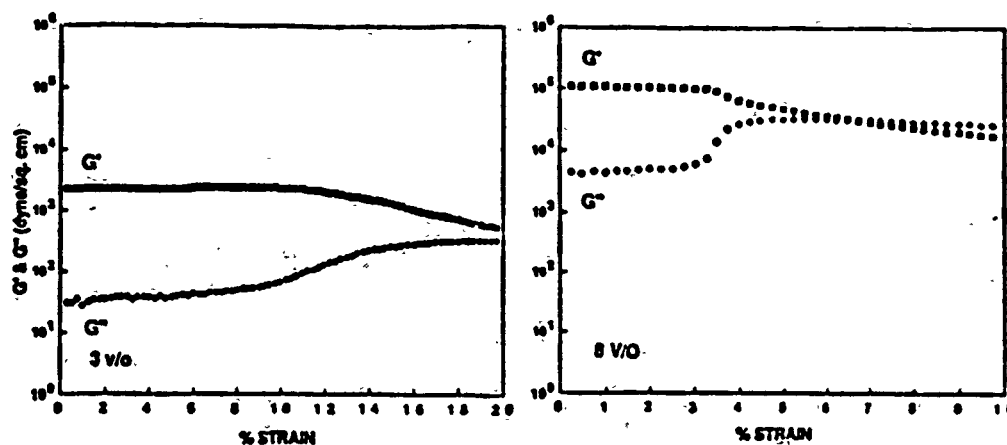


Figure 45. Shear stress versus time after the strain is applied instantaneously for the fluid-like sample. The sample does not hold the stress because there is no elastic internal particle network structure.

NANOMETER BOEHMITE AT pH 5.5



MICROMETER ALUMINA AT pH 8.5

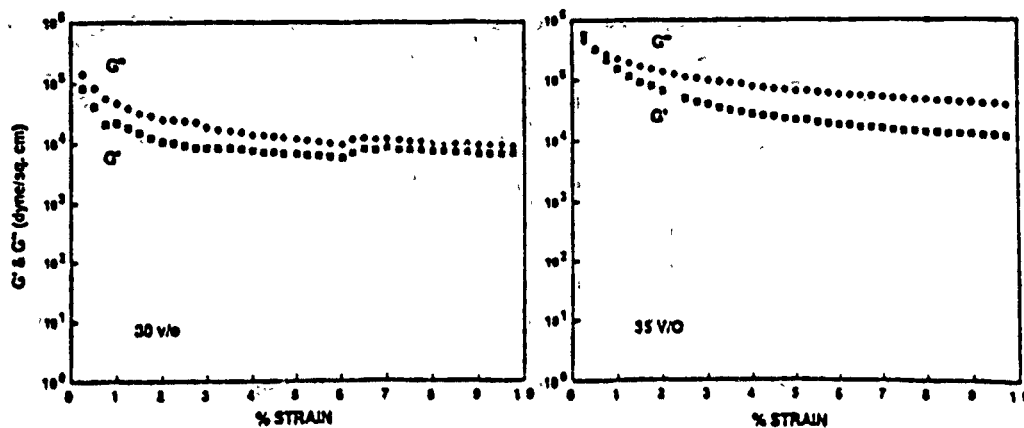


Figure 46. Difference in rheological behavior between nanometer- and micrometer-sized particle/water mixtures at highly flocculated states.

particles (≥ 35 volume %) at $\text{pH} = 8.5$. Second, no linear viscoelastic region is observed in the micrometer-sized alumina system. Third, the linear viscoelastic region of the boehmite system disappears at $\text{pH} = 7.5$ (Figure 47), which is a more flocculated state and closer to the isoelectric point than $\text{pH} = 5.6$.⁶⁴ Fourth, the linear viscoelastic region of the boehmite system is dependent on the particle concentration: the linear viscoelastic region shrinks, and the storage modulus increases with increasing particle concentration. Table II is a brief summary of Figures 46 and 47.

Table II. Brief Summary of Difference in Rheological Behavior Between Nanometer- and Micrometer-Sized Particle Systems

	NANOMETER BOEHMITE	MICROMETER ALUMINA
ELASTIC PROPERTY	> 3 v/o ($\text{pH} = 5.5$)	> 35 v/o ($\text{pH} = 8.5$)
LINEAR VISCOELASTIC REGION	Yes ($\text{pH} < 6.5$) <hr/> NO ($\text{pH} = 7.5$)	Could not observe

We want to discuss, first, why the elastic property appears at different particle concentrations for different particle size systems.

This can be understood by considering the particle interaction energy and the total number of particles per unit volume of sample. We calculate the attractive energy between particles by assuming the Hamaker constants of the two systems to be the same, and that particles are not clustered. Attractive energy between a pair of particles when they are separated at 50 \AA is $-9.23 \times 10^{-26} \text{ (J}\cdot\text{\AA}^2)$ for boehmite and $-6.4 \times 10^{-20} \text{ (J)}$ for alumina. Attractive energy between a pair of micrometer-sized

STRAIN SWEEP, BOEHMITE, 5 V/O, pH=7.5

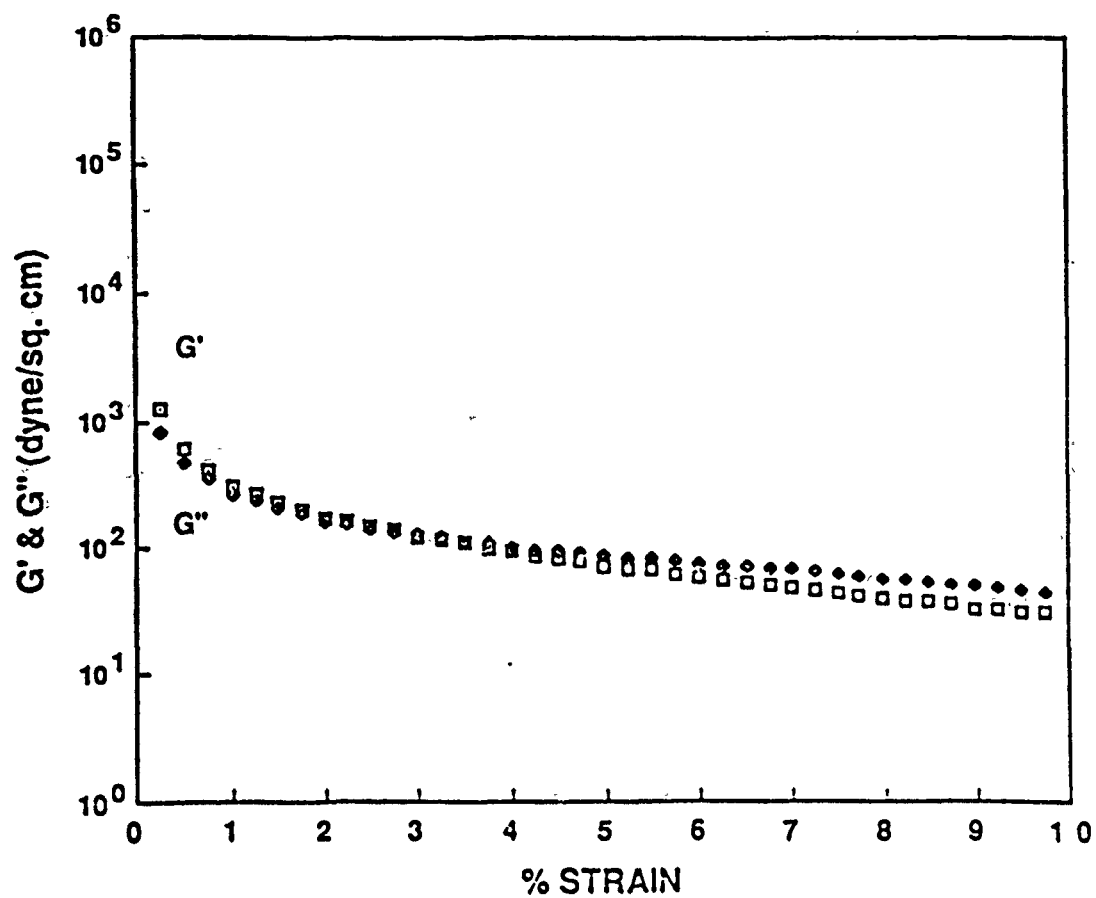


Figure 47. Effect of increasing the amplitude of the sinusoidally oscillatory strain on the storage modulus (G') and the loss modulus (G'') of the sample prepared at pH = 7.5.

alumina is six orders of magnitude higher than that of nanometer-sized boehmite. However, if we consider the total number of particles in the system, the boehmite system has 7.545×10^{17} particles in 5 volume % of suspension and the alumina system has 4.835×10^{13} particles in 35 volume % of suspension. Since one is dealing with a sample as a whole rather than a pair of particles, one should consider the total energy of the system per unit volume. The total attractive energy of the 5 volume % nanometer-sized boehmite system (-3.07×10^{-4} J) is about 100 times greater than 35 volume % of the micrometer-sized alumina system (-3.09×10^{-6} J) (see Appendix for calculation). Therefore, the nanometer-sized boehmite system shows an elastic property at a much lower concentration than the micrometer-sized alumina system.

Second, why does the nanometer-sized particle/water system show a linear viscoelastic region while the micrometer-sized particle/water system does not? The nanometer-sized particle/water system has about 100 times greater attractive energy than the micrometer-sized particle/water system. Because of the higher binding energy of the system, the nanometer-sized particle/water system can withstand a larger amount of strain without having a permanent deformation. However, the total binding energy of the micrometer-sized particle system per unit volume is so small that the yield strain of the system per unit volume is too small to measure. Therefore, the nanometer-sized particle system shows a linear viscoelastic region, but the micrometer-sized particle system does not.

Third, we want to discuss why the linear viscoelastic region of the boehmite system disappears at $pH=7.5$, which is a more flocculated state and closer to the isoelectric point than at $pH=5.6$. This can be explained by considering the size of the smallest forming unit for network structures.

Figure 48 shows the settling rate of a boehmite particle agglomerate, and the thickness and opaqueness of the sedimentation layer at a certain time after the suspensions were left for free settling. Initially, 0.05 volume % boehmite suspensions

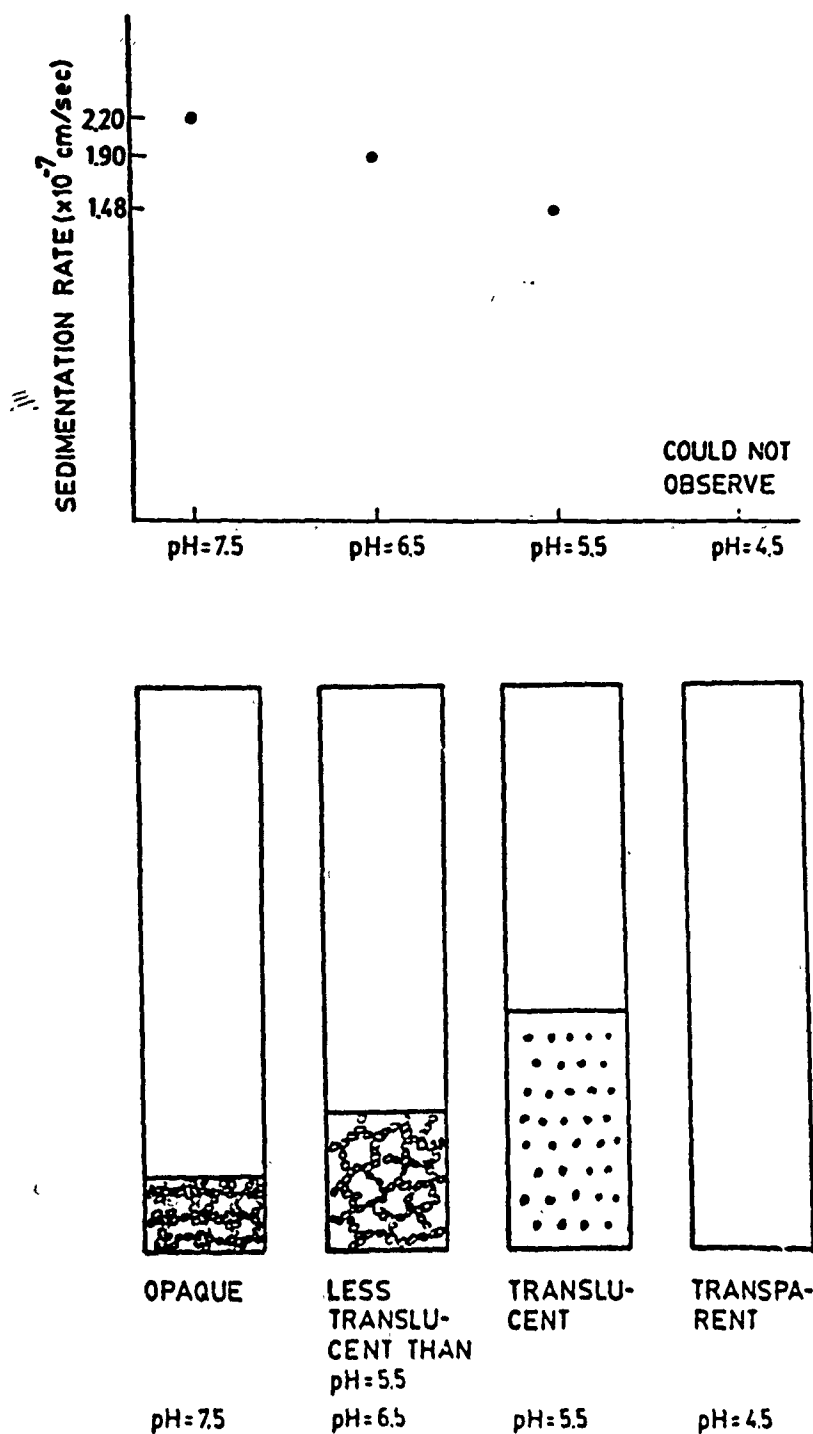


Figure 48. Effect of pH on the settling rate and turbidity of boehmite suspensions. Initial concentration of particles is 0.05 volume %.

were prepared at pII = 4.5, 5.5, 6.5, and 7.5. With increasing pII, the sedimentation rate becomes higher, and the opaqueness of the sediment layer increases.

The magnitude of the attractive energy between particles increases with increasing pII, that is, $E(7.5) > E(6.5) > E(5.5) > E(4.5)$, where E is the attractive energy as a function of the pII. The degree of flocculation is maximum at pII = 7.5.

At pII = 4.5, there is no sediment observed, and the suspension looks transparent. This indicates that the attractive energy between particles is not great enough to form larger agglomerates, and the nanometer-sized particles or their agglomerates are too small to settle. Therefore, particles or agglomerates stay in the dispersed phase and do not cause scattering of light. However, at pII = 7.5, the sedimentation rate is highest, and the sediment layer is completely opaque. At this pII, the attractive energy between particles is strong enough to form larger agglomerates. Ramsey⁵³ also observed that sedimentation occurred due to a coagulation of the sol particles when anion concentration is greater than 10^{-1} mole dm^{-3} . As a result, these larger agglomerates settle quickly and form a densely-packed compact which does not transmit light. Therefore, if the large agglomerates formed at pII = 7.5 become a basic building unit for the network structure, the effective number of particles or number of bonds in the structure decreases. The total attractive energy of the system with a larger building unit for the network structure then becomes smaller than that of the system with a smaller building unit; the structure in the system can therefore be destroyed at a small amount of strain, which leads to the disappearance of the linear viscoelastic region at pII = 7.5.

Fourth, the behavior of elastic constant and yield strain as a function of particle concentration will be discussed.

Figure 49 shows the relationship between the storage modulus in the linear viscoelastic region and the particle concentration for the flocculated (at pII = 5.6) nanometer-sized boehmite system. When the particle concentration increases from 3 to 10 volume %, the storage modulus increases very rapidly in a power-law fashion. The slope is approximately 4.1. This power-law exponent is in good agreement with

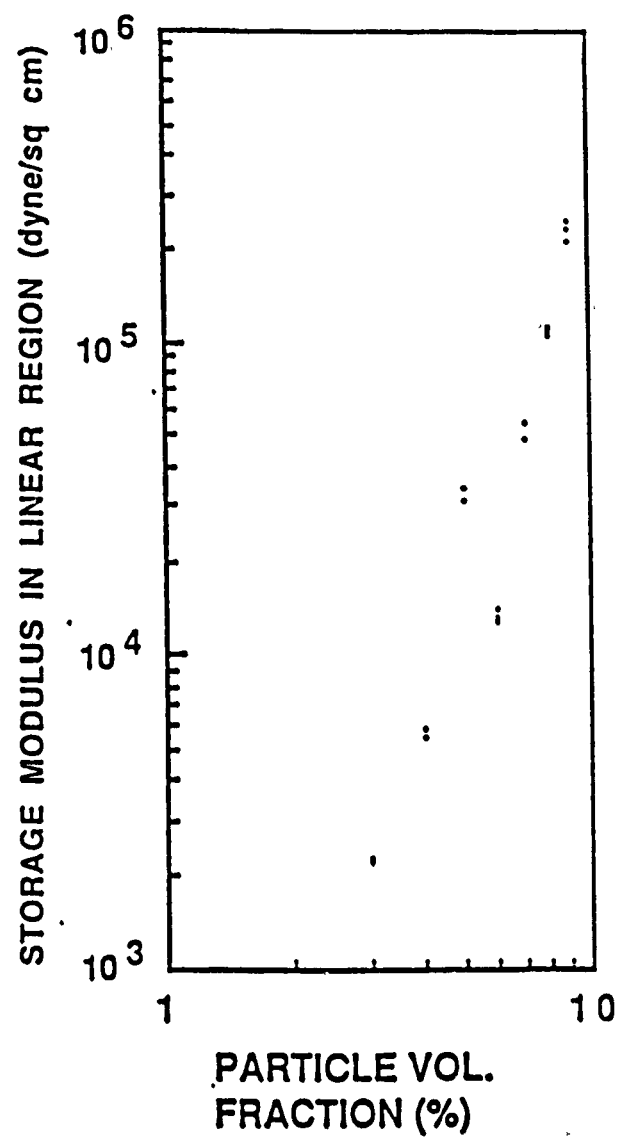


Figure 49. Relationship between the storage modulus in linear viscoelastic region and particle concentration for the flocculated boehmite system.

the exponent of compactive yield stress and concentration for spherical particles to be 4 ± 0.5 , provided $0.075 < \text{particle concentration} < 0.4$.⁵⁸ Russel⁵⁵ also reported the power-law behavior of the polystyrene latex particle system. The exponent of the storage modulus and particle concentration ($0.03 < \phi < 0.23$) is 4.4 for an aged sample. Our number is a reasonable number when compared to Buscall's and Russel's.

The relationship between the yield strain, where the linear viscoelastic region ends, and the particle concentration for the same system (as in Figure 47) is shown in Figure 50. The yield strain decreases very rapidly in a power-law fashion with increasing particle concentration. The slope is about -2.1.

These behaviors of increasing storage modulus and decreasing yield strain with increasing particle concentration can be explained by using the scaling theory for a colloidal particle system by Shih.⁶⁰ Refer to Reference 60 for a detailed discussion of scaling theory. In that theory, the whole sample consisted of clusters of particles (Figure 51). The small cluster is a fractal object. The property of the whole sample depends on the property of the small cluster. There is a scaling relationship between the size of the cluster and particle concentration (Equation 20).

$$\xi \sim \phi^{\frac{1}{D-d}} \quad (20)$$

where

ξ : cluster size

ϕ : particle concentration

D : fractal dimension

d : Euclidian dimension.

This relationship shows that the size of the cluster decreases with increasing particle concentration. This was confirmed by Dietler et al.⁶⁹

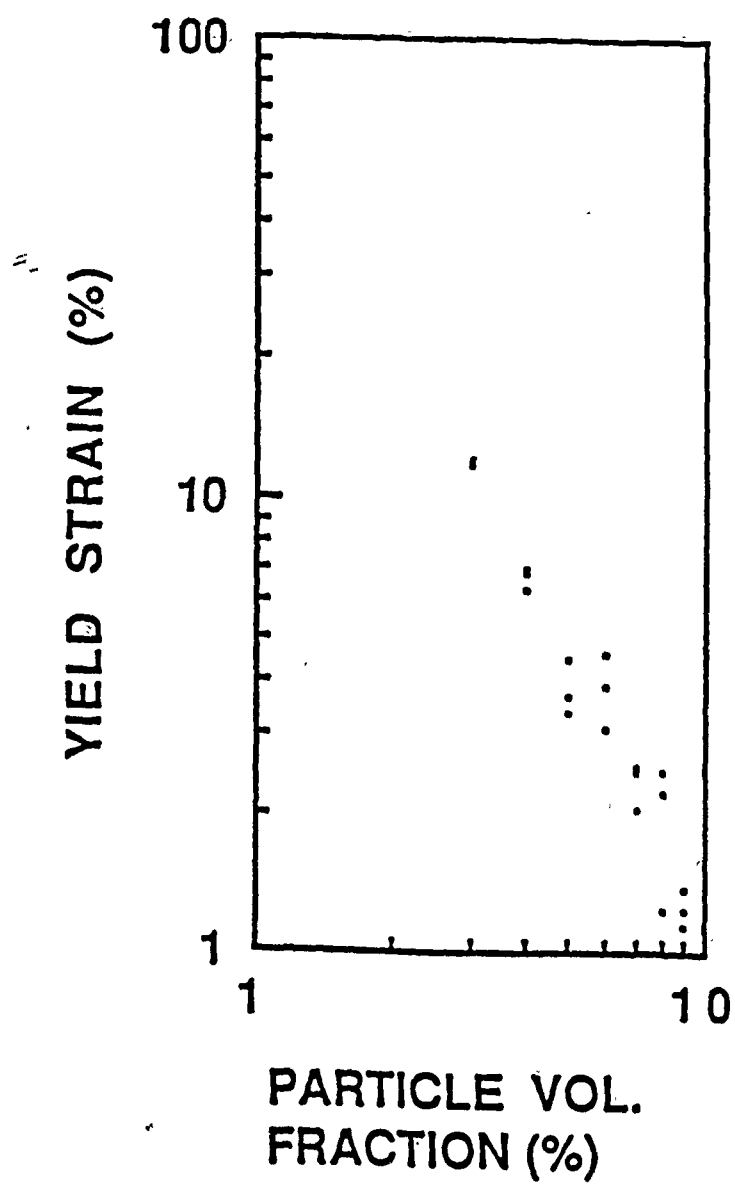
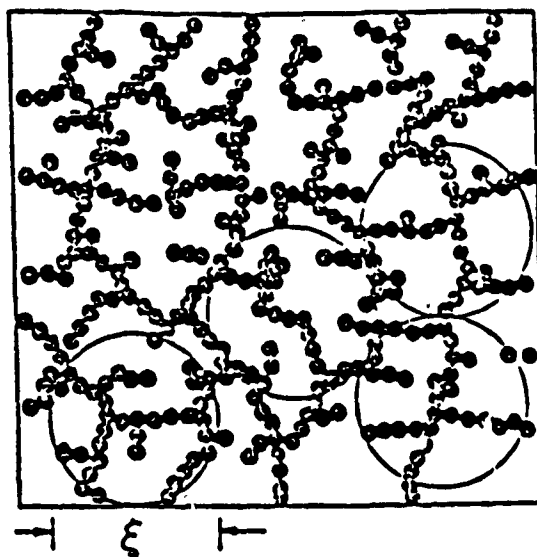


Figure 50. Relationship between the yield strain and particle concentration for the flocculated boehmite system.

<SCALING THEORY>



$$\xi = \varphi^{-1/(D-d)}$$

ξ : average size of cluster

φ : particle concentration

Figure 51. Relationship between cluster size and particle concentration.

The scaling theory predicts the relationship (Equation 21) between the modulus of the cluster in the sample and the size of the cluster ξ , and the relationship (Equation 22) between the yield strain γ_y and the size of the cluster.

$$k_\xi \sim \frac{k_o}{\xi^{d+x}} \sim \varphi^{\frac{d+x}{d-\varphi}} \quad (21)$$

$$\gamma_y \sim \xi^{1+x} \sim \varphi^{-\frac{1+x}{d-\varphi}} \quad (22)$$

where k_o = bending constant between two adjoining particles, and x = tortuosity of the backbone of the cluster.

When the particle concentration increases, the size of the cluster becomes smaller. As a result, the modulus of the sample increases (Equation 21), and the yield strain of the sample decreases (Equation 22). The prediction of the scaling theory is in good agreement with the experimental result obtained.

Furthermore, the scaling theory can extract the structural information, such as the fractal dimension, D , and the tortuosity of the backbone of the cluster, x , by using the experimental result of dynamic strain sweep. From the measurement of dynamic strain sweep, we find the relationship between the storage modulus and particle concentration as well as the relationship between the yield strain and particle concentration to be

$$G' = \varphi^{4.1} \quad (23)$$

$$\gamma_y = \varphi^{-2.1} \quad (24)$$

By substituting the exponent of Equation 23 for one of Equation 25, and the exponent of Equation 24 for one of Equation 26, we can calculate the fractal dimension number and the tortuosity of the backbone of cluster.

$$(d + x)/(d - D) = 4.1 \quad (25)$$

$$(1 + x)/(d - D) = 2.1 \quad (26)$$

where $d=3$ in three dimensions.

We obtain the fractal dimension $D=2$, which is in good agreement with the result of the numerical simulation of cluster-cluster aggregation^{70,71} and other colloidal aggregates.⁷²⁻⁷⁴ The tortuosity of the backbone of the cluster $x=1.1$ is a reasonable number in comparison to the $x=1$ to 1.3 obtained in a numerical simulation of a two-dimensional cluster-cluster aggregation.⁷⁶

5. CONCLUSIONS

From this work, the structure-property relationship of the aqueous ceramic particulate system can be understood by studying packing density versus filtration pressure, elastic constant, and yield strain. There are three broad conclusions which can be drawn from this work: the first concerns the relationship between packing density and applied filtration pressure; the second concerns the rheological behavior of the micrometer- and nanometer-sized particle systems; the third relates pressure filtration to rheological behavior.

Relationship Between Packing Density and Filtration Pressure

(i) When the micrometer-sized particle system suspension is prepared in the highly attractive energy state, packing density is pressure-sensitive because the barrier for compaction is high, making restructuring very difficult and resulting in a loosely-packed structure containing third-generation and higher voids. When there are pores which can be eliminated by restructuring, and when the strength of the structure is exceeded by externally applied stress, compaction occurs. Packing density then becomes pressure-sensitive. When the suspension is prepared in the minimum attractive energy state, the barrier for compaction is negligible. Therefore, the packing density of a gravity-induced sedimentation layer is the same as that of the pressure-filtered sample at 3.45 MPa, resulting in a pressure-insensitive packing density. Packing density can be pressure-sensitive, depending on the availability of open pores and restructuring. Gallagher's results⁶⁶ showed that the flocculated polymer reduces the binding energy between particles enough to allow restructuring of flocs to a higher density during consolidation, and packing density becomes pressure-insensitive up to the pressure of 3.447 MPa.

(ii) For the nanometer-sized particle system, even in the highly dispersed state the packing density is pressure-sensitive as particle concentration increases. This is because the particle and water mixture forms a gel and shows a finite value of storage

modulus at 7 volume % of particle concentration and in the minimum attractive energy states. This results in a loosely packed structure which becomes pressure-sensitive.

(iii) The slopes of packing density versus applied pressure change for different pressure ranges: slopes with higher gradients appear in the lower pressure range and slopes with smaller gradients appear in the higher pressure range. This was explained by observing SEM photos of freeze-dried suspensions with different particle concentrations. Different slopes are due to different microstructures with a different hierarchy of voids: (a) slopes with larger gradients mean more compaction due to elimination of higher hierarchical voids; (b) slopes with smaller gradients mean less compaction due to elimination of lower hierarchical voids.

(iv) Between 1.379×10^{-1} and 3.447 MPa, the slope of the packing density versus applied pressure is higher for the nanometer-sized and lower for the micrometer-sized particle system. This is because third-generation and larger voids are eliminated from the nanometer-sized particle system, while the second-generation void is eliminated from the micrometer-sized particle system. Third- and higher-generation voids occupy more space than a second-generation void does. Therefore, elimination of the higher hierarchical void results in more compaction (i.e., higher slope).

(v) Slopes of the micrometer-sized alumina system between 1.71×10^{-4} and 1.379×10^{-1} MPa are similar to those of the nanometer-sized boehmite system between 1.379×10^{-1} and 3.447 MPa. The similar slope is due to elimination of the same type of voids.

Rheological Behavior of Nanometer- and Micrometer-Sized Particle Systems

(i) The nanometer-sized particle system shows an elastic property at a lower particle concentration (≥ 3 volume %) than the micrometer-sized particle system (≥ 35 volume %). This is due to the difference in particle number density, resulting in higher energy per unit volume for the nanometer-sized boehmite system.

(ii) For the nanometer-sized particle system, yield strain decreases with increasing particle concentration. The slope is -2.1. This is due to shrinkage of the average cluster size with increasing particle concentration.

(iii) The structural information was obtained by the scaling theory and the experimentally measured of storage modulus and yield strain. The fractal dimension $D=2$ for the boehmite system is in good agreement with the numerical simulation of the cluster-cluster aggregation system and other colloidal aggregates.

Relationship of Pressure Filtration and Rheological Behavior

The applied pressure required to start compaction of the same type of structure for the nanometer-sized boehmite system compared to the micrometer-sized alumina system is three orders of magnitude higher. This is because the elastic modulus at fixed particle concentration is three orders of magnitude higher for the boehmite system than for the alumina system, which is attributed to higher particle number density in the nanometer-sized particle system.

Given the above discussions, it is now possible to understand how to prepare highly concentrated nanometer-sized particle suspensions with low viscosity by minimizing interaction energy between particles. Once we can prepare highly concentrated suspensions, it is possible that excessive shrinkage and cracking during drying and sintering stage can be avoided.¹

REFERENCES

1. I. A. Aksay, W. Y. Shih, and M. Sarikaya, "Colloidal Processing of Ceramics with Ultrafine Particles," in *Ultrastructure Processing of Advanced Ceramics*, edited by J. D. Mackenzie and D. R. Ulrich (Wiley, New York, 1988), pp. 393-406.
2. H. Abe, "Mechanical Properties of Engineering Ceramics," *Am. Ceram. Soc. Bull.*, 64 (12) 1594-98 (1985).
3. T. J. Fennelly and J. S. Reed, "Compression Permeability of Al_2O_3 Cakes Formed by Pressure Slip Casting," *J. Am. Ceram. Soc.*, 55 (8), 281-282 (1972).
4. F. M. Tiller and L. L. Horng, "Hydraulic Deliquoring of Compressible Filter Cakes," *A.I.Ch.E.* 29(2), 297-305 (1983).
5. F. F. Lange and K. T. Miller, "Pressure Filtration: Consolidation Kinetics and Mechanics," *Am. Ceram. Soc. Bull.*, 66 (10), 1498-1504 (1987).
6. R. J. Akers, "The Compression of Flocculated Sediments," Proceedings of the Filtration Society, *Filtration and Separation*, July/August, 354-356 (1980).
7. T. J. Fennelly and J. S. Reed, "Mechanics of Pressure Slip Casting," *J. Am. Ceram. Soc.*, 55 (5), 264-268 (1972).
8. M. A. Janney, "Plasticity of Ceramic Particulate Systems," Ph.D. Thesis, University of Florida, 1982.
9. H. L. Jakuboukas, "Use of A-B Block Polymers as Dispersants for Non-Aqueous Coating Systems," *J. of Coatings Technology*, 58 [736] 71-82 (1986).
10. E. J. W. Verwey and J. Th. G. Overbeek, *Theory of the Stability of Lyophobic Colloids* (Elsevier, Amsterdam, 1948), pp. 19-20.
11. D. H. Napper, *Polymeric Stabilization of Colloid Dispersions* (Academic Press, New York, 1983).
12. H. C. Hamaker, "The London-van der Waals Attraction Between Spherical Particles," *Physica*, 4 (10), 1058 (1937).

13. J. H. de Boer, "The Influence of van der Waals Forces and Primary Bond on Binding Energy, Strength, and Orientation with Special Reference to Some Artificial Resins," *Trans. Faraday Soc.*, 32, 21 (1936).
14. D. J. Shaw, *Introduction to Colloid and Surface Chemistry*, 3rd ed. (Butterworths, London, 1980).
15. J. W. Hahanty and B. W. Ninham, *Dispersion Forces* (Academic Press, New York, 1973).
16. V. A. Parsegian, "Long-Range van der Waals Forces," *Physical Chemistry: Enriching Topics from Colloid and Surface Science*, IUPAC Commission, 1, (6) Theorex (1975), pp. 27-72.
17. J. Gregory, "The Calculation of Hamaker Constants," *Advan. Colloid Interface Sci.*, 2, 396-417 (1969).
18. J. Visser, "Hamaker Constants, Comparison Between Hamaker Constants and Lifshitz-van der Waals Constants," *Advan. Colloid Interface Sci.* 3 (4), 331-63 (1972).
19. E. F. Adams, "Slip Cast Ceramics," in *High Temperature Oxides, Vol. 5-IV*, edited by A. M. Alper (Academic Press, New York, 1971).
20. B. V. Derjagin and L. Landau, *Acta Phys. Chem.*, URSS 14, 633 (1941).
21. J. Th. G. Overbeek, "Recent Development in the Understanding of Colloid Stability," *J. Colloid Interface Sci.*, 58 (2), 408-422 (1977).
22. E. J. W. Verwey and J. Th. G. Overbeek, *Theory of the Stability of Lyophobic Colloid* (Elsevier, Amsterdam, 1948), p. 95.
23. Wan Y. Shih, I. A. Aksay and R. Kikuchi, "Phase Diagrams of Charged Colloid Particles," *J. Chem. Physics*, 86 (9), 5127-5132, 1987.
24. I. A. Aksay and C. H. Schilling, "Mechanism of Colloidal Filtration," in *Advances in Ceramics, Vol. 9, Forming of Ceramics*, edited by J. A. Mangels (American Ceramic Society, Columbus, Ohio, 1984), pp. 85-93.
25. H. Deeg, "Die Scherbenbildung beim Schlicker-Giessprozess als Diffusions-Problem," *Ber. Dtsch. Keram. Ges.*, 30 (6), 129-38 (1953).

26. A. Dietzel and H. Mostezky, "Vorgänge beim Wasserentzug aus einem Keramischen Schlicker durch die Gipsform (I)," *Ber. Dtsch. Keram. Ges.*, 33 (1), 7-18 (1956).
27. A. Dietzel and H. Mostezky, "Vorgänge beim Wasserentzug aus einem Keramischen Schlicker durch die Gipsform (II)," *Ber. Dtsch. Keram. Ges.*, 33 (3), 73-85 (1956).
28. D. S. Adcock and I. C. McDowall, "The Mechanism of Filter Pressing and Slip Casting," *J. Am. Ceram. Soc.*, 40 (10), 355-62 (1957).
29. E. R. Herman and I. B. Cutter, "The Kinetics of Slip Casting," *Trans. Brit. Ceram. Soc.*, 61, 207-11 (1962).
30. I. A. Aksay and R. Kikuchi, "Structure of Colloidal Solids," in *Science of Ceramic Chemical Processing*, edited by L. L. Hench and D. R. Ulrich (Wiley, New York, 1986), pp. 513-21.
31. C. H. Schilling and I. A. Aksay, "Slip Casting of Advanced Ceramics and Composites," in *Transactions of the Third Canadian University-Industry Council on Advanced Ceramics*, edited by P. S. Nicholson (Canadian Ceramic Society, Willowdale, Ontario, 1987).
32. I. A. Aksay and C. H. Schilling, "Colloidal Filtration Route to Uniform Ultrastructures," in *Ultrastructure Processing of Ceramics, Glasses, and Composites*, edited by L. L. Hench and D. R. Ulrich (Wiley, New York, 1984), pp. 437-439.
33. W.-H. Shih, J. Liu, W. Y. Shih, S. I. Kim, M. Sarikaya, and I. A. Aksay, "Mechanical Properties of Colloidal Gels," in *Processing Science of Advanced Ceramics, Mat. Res. Soc. Symp. Proc.*, Vol. 155, edited by I. A. Aksay, G. L. McVay, and D. R. Ulrich (Materials Research Society, Pittsburgh, Pennsylvania, 1989), pp. 83-92.
34. W. Y. Shih, I. A. Aksay, and R. Kikuchi, "Reversible Growth Model: Cluster-Cluster Aggregation with Finite Binding Energies," *Phys. Rev. A*, 36 (10), 5015-5019 (1987).
35. P. Meakin, "Formation of Fractal Clusters and Networks by Irreversible Diffusion-Limited Aggregation," *Phys. Rev. Lett.*, 51, 1119 (1983).

36. M. Kolb, R. Botet, and R. Jullien, "Scaling of Kinetically Growing Clusters," *Phys. Rev. Lett.*, **51**, 1123 (1983).
37. D. A. Weitz and M. Olivera, "Fractal Clusters Formed by Aggregation of Aqueous Gold Colloids," *Phys. Rev. Lett.*, **52**, 1433 (1984).
38. C. Aubert and D. S. Cannel, "Restructuring of Colloidal Silica Aggregates," *Phys. Rev. Lett.*, **56**, 738 (1986).
39. P. Dimon, S. K. Sinhar, D. A. Wentz, C. R. Safinya, G. Smith, W. A. Varady, and H. M. Lindsay, "Structure of Aggregated Gold Colloids," *Phys. Rev. Lett.*, **57**, 595 (1986).
40. D. A. Weitz, J. S. Huang, M. Y. Lin, and J. Sung, "Limits of the Fractal Dimension for Irreversible Kinetic Aggregation of Gold Colloids," *Phys. Rev. Lett.*, **54**, 1416 (1985).
41. D. W. Schaefer, J. E. Martin, P. Wilzius, and D. S. Cannel, "Fractal Geometry of Colloidal Aggregates," *Phys. Rev. Lett.*, **52**, 2371 (1984).
42. J. C. Rarity and P. M. Pasey, in *On Growth and Form*, edited by H. E. Stanley and M. Ostrowsky (Nijhoff, Dordrecht, 1986), p. 219.
43. P. Sherman, *Industrial Rheology* (Academic Press, New York, 1970).
44. J. D. Ferry, *Viscoelastic Properties of Polymers* (Wiley, New York, 1980).
45. F. R. Eirich, editor, *Rheology - Theory and Applications, Vol. 1* (Academic Press, New York, 1956).
46. T. Murayama, *Dynamic Mechanical Analysis of Polymeric Material* (Elsevier, Amsterdam, 1978).
47. G. V. Vinogradov and A. Ya. Malkin, *Rheology of Polymers: Viscoelasticity and Flow of Polymers*, (Mir Publisher, Moscow; Spring-Verlag, New York, 1980).
48. H. Watanabe, S. Kuwahara and T. Kotaka, "Rheology of Styrene-Butadiene-Styrene Triblock Copolymer in n-Tetradecane Systems," *J. Rheology*, **28** (4), 393-407 (1984).

49. E. V. Gouinlock and R. J. Porter, "Linear Dynamic Mechanical Properties of an SBS Block Copolymer," *Polymer Engineering and Science*, 17 (8), 535-543 (1977).
50. H. Watanabe and T. Kotaka, "Rheological and Morphological Behavior of Styrene-Butadiene Di-Block Copolymer Solutions in Selective Solvents," *J. of Rheology*, 26 (2), 153-179 (1982).
51. C. I. Chung and J. C. Gale, "Newtonian Behavior of Styrene-Butadiene-Styrene Block Copolymer," *J. Polymer Science*, 14, 1149-1156 (1976).
52. H. Rehage and H. Hoffmann, "Viscoelastic Detergent Solutions," *Faraday Discuss. Chem. Soc.*, 76, 363-373 (1983).
53. J. D. F. Ramsay and S. R. Daish, "Structure and Stability of Concentrated Boehmite Sols," *Faraday Discuss. of the Chem. Soc.*, 65, 65-75 (1978).
54. J. P. F. Ramsay, "Colloidal Properties of Synthetic Hectoric Clay Dispersions," *J. Colloid. Interface Sci.*, 109 (2) 441-447 (1986).
55. R. C. Sonntag and W. B. Russel, "Elastic Properties of Flocculated Networks," *J. Colloid. Interface Sci.*, 116 (2) 465-489 (1987).
56. H. Watanabe, S. Kuwahara, and T. Kotaka, "Rheology of Styrene-Butadiene-Styrene Terblock Copolymer in n-Tetradecane Systems," *J. Rheology*, 28 (1), 183-98 (1982).
57. S. Onogi and T. Matsumoto, "Rheological Properties of Polymer Solutions and Melts Containing Suspended Particles," *Polymer Eng. Rev.*, 1 (1), 45-87 (1981).
58. R. Buscall, P. D. A. Mills, J. W. Goodwin, and D. W. Lawson, "Scaling Behavior of the Rheology of Aggregated Networks Formed from Colloidal Particles", *J. Chem. Soc. Faraday Trans.*, 86 (2), 4249-60 (1988).
59. W. D. Brown and R. C. Ball, "Computer Simulation of Chemically Limited Aggregation," *J. Phys. A*, 18, 1517 (1985).
60. W. H. Shih, S. J. Kim, W. Y. Shih, and I. A. Aksay, "Scaling for the Elastic Constant and Yield Behavior of Colloidal Gels," to be published.

61. C. H. Schilling, "Microstructure Development by Colloidal Filtration," M. S. Thesis, University of California, Los Angeles, CA (1983).
62. J. Cesarano III, "Polyelectrolyte Adsorption on α -Alumina Aqueous Suspension Behavior," M.S. Thesis, University of Washington (1985).
63. J. Cesarano III and I. A. Aksay, "Processing of Highly Concentrated Aqueous α -Al₂O₃ Suspensions Stabilized with Polyelectrolytes," *J. Am. Ceram. Soc.*, **71** (12), 1062-67 (1988).
64. B. Tarasevich, "Colloidal Interactions and Packing of Nanometer-Sized Particles; Application to Gel Processing," M. S. Thesis, University of Washington (1988).
65. I. A. Aksay and C. A. Ambarian, "Development of Homogeneity in Si₃N₄ Ceramics by Colloidal Filtration," Report prepared for Garrett Turbine Engine Co., March, 1984.
66. D. Gallagher, "Dispersion in Non-Aqueous Solvents for Enhanced Consolidation," Ph.D. Thesis, University of Washington, (1988).
67. S. I. Kim, W.-H. Shih, and I. A. Aksay, "Structure-Property Relationships in Pressure Filtration," to be submitted for publication.
68. J. Liu, private communication, October 1989.
69. G. Dietler, C. Aubert, D. S. Cannel, and P. Wiltzius, "Gelation of Colloidal Silica," *Phys. Rev. Lett.*, **57** (24), 3117-3120 (1986).
70. P. Meakin, "Particle-Cluster Aggregation with Fractal Particle Trajectories and on Fractal Substrates," in *Kinetics of Aggregation and Gelation*, edited by F. Family and D. P. Landau (Elsevier, Amsterdam, 1984), pp. 91-99.
71. M. Kolb, R. Bofet, and J. Jullien, *Scaling Properties of Growth by Kinetic Clustering of Clusters*, in *Kinetics of Aggregation and Gelation*, edited by F. Family and D. P. Landau (Elsevier, Amsterdam, 1984), pp. 101-109.
72. D. A. Weitz and M. Olivera, "Fractal Structure Formed by Kinetic Aggregation of Aqueous Gold Colloids," *Phys. Rev. Lett.*, **52**, 1-133 (1984).

73. P. Dimon, S. K. Sinha, D. A. Weitz, C. R. Safinya, G. S. Smith, W. A. Varady, and H. M. Lindsay, "Structure of Aggregated Gold Colloids," *Phys. Rev. Lett.*, **57**, 595 (1986).
74. C. Aubert and D. S. Cannel, "Restructuring of Colloidal Silica Aggregates," *Phys. Rev. Lett.*, **56**, 738 (1986).
75. C. Bolle, C. Cametti, P. Codastefano, and P. Tartaglia, "Kinetics of Salt-Induced Aggregation in Polystyrene Lattices Studied by Quasielastic Light Scattering," *Phys. Rev. A*, **35**, 837 (1987).
76. W.-H. Shih, J. Liu, W. Y. Shih, S. I. Kim, M. Sarikaya, and I. A. Aksay, "Electrical Breakdown in Two-Dimensional Cluster-Cluster Aggregated Networks," in *Fractal Aspects of Materials: Disordered Series*, edited by D. A. Weitz, L. M. Sander, and B. B. Mandelbrot (MRS, Pittsburgh, PA, 1988), p. 239.
77. J. Th. G. Overbeek, *Colloid Science*, edited by H. R. Kruyt (Elsevier, Amsterdam, 1952), Vol. 1, p. 267.

APPENDIX: Energy Calculation in Particle Systems

Attractive energy between a pair of plate-like boehmite particles,⁷⁷

$$V_A = -\frac{A}{48\pi} \left\{ \frac{1}{d^2} + \frac{1}{(d+\delta)^2} - \frac{2}{(d+\frac{\delta}{2})^2} \right\}$$

where

A = Hamaker constant (4.2×10^{-20} J)

d = half of the interparticle distance

δ = thickness of plate ($10 \sim 20 \text{ \AA}$)

When $d = 25 \text{ \AA}$, $V_A = -9.23 \times 10^{-26} \text{ (J/\AA}^2\text{)}$.

Attractive energy between a pair of spherical alumina particles.

$$V_A = -\frac{A}{6} \left(\frac{2}{S^2 - 4} + \frac{2}{S^2} + \ln \frac{S^2 - 4}{S^2} \right)$$

where

$$S = 2 + \frac{H}{a}$$

H = distance between two spheres

a = radius of spheres ($\sim 0.12 \text{ }\mu\text{m} = 1200 \text{ \AA}$)

A = Hamaker constant (4.2×10^{-26} J)

when $H = 50 \text{ \AA}$, $V_A = -6.4 \times 10^{-20} \text{ (J)}$

Total attractive energy between particles in 1 cm³ of 5 volume % boehmite suspension:

mean diameter of boehmite $\cong 75 \text{ \AA}$

mean thickness of boehmite $\cong 15 \text{ \AA}$

volume/boehmite particle $\cong 6.627 \times 10^{-8} (\mu\text{m})^3$

total volume of particles/1 cm³ suspension $\cong 0.05 (\text{cm})^3$

total number of particles/1 cm³ suspension $\cong 7.545 \times 10^{17}$

total area of top surface of particles/1 cm³ suspension $\cong 3.33 \times 10^{21} (\text{\AA})^2$.

Therefore, total attractive energy/1 cm³ of 5 volume % boehmite suspension

$$\cong (3.33 \times 10^{21} (\text{\AA})^2) (-9.23 \times 10^{-26} \text{ J} / \text{\AA}^2) \cong -3.07 \times 10^{-4} (\text{J})$$

Total attractive energy between particles in 1 cm³ of 35 volume % alumina (AKP-50) suspension:

mean diameter of alumina $\cong 2400 \text{ \AA}$

volume/alumina particle $\cong 0.0072 (\mu\text{m})^3$

total volume of particles/1 cm³ suspension $\cong 0.35 (\text{cm})^3$

total number of particles/1 cm³ suspension $\cong 4.8354 \times 10^{13}$

Therefore, total attractive energy/1 cm³ of 35 volume % alumina suspension

$$\cong (4.8354 \times 10^{13}) (-6.40 \times 10^{-20} \text{ J}) \cong -3.08 \times 10^{-6} (\text{J})$$

*The distance between particles is assumed to be 50 \AA .